Effect of Foam Density on the Imperfection Sensitivity of Aluminium Foam Sandwich Panels Under In-Plane Compression

A thesis

submitted in fulfilment

of the requirements for the degree

of

Master of Engineering with endorsement in Civil Engineering

at

The University of Waikato

by

Devika Mohan

KO TE TANGATA

THE UNIVERSITY OF
WAIKATO
Te Whare Wānanga o Waikato

2026

Abstract

Aluminium foam sandwich panels are attractive lightweight structural components because they offer a good combination of low mass, stiffness, strength, and energy absorption. However, their in-plane compressive behaviour is still not fully understood, especially when the foam relative density and out-of-plane geometric imperfections are considered together. This study investigates how variations in the combinations of foam relative density and out-of-plane geometric imperfections influence the in-plane compressive response of these panels, with emphasis on strength, collapse mode, and post-buckling behaviour. These findings improve the understanding of the compressive performance and support more reliable use of these panels in lightweight structural applications**.**

Parametric studies were conducted to examine the in-plane compressive response of 200 aluminium foam sandwich panels with varying relative density and initial imperfection [For certain combinations, mode interaction was enhanced, producing a temporary increase in load-carrying capacity. The resulting imperfection-dependent interaction windows do not vary monotonically with either parameter but instead reflect a balance between foam-core stiffness, and imperfection sensitivity. A sensitivity study also showed that plate modulus also has a role in the formation and extend of such mode interaction windows.

To support design decisions, a multi-objective performance framework was developed using imperfection tolerance, deformation mode stability, energy absorption, and mass efficiency. In addition, as a practical aid to similar panel configurations, a FE based predictive equation was developed to predict the normalized peak load in the higher imperfection regime.

Acknowledgement

I would like to begin by expressing my deepest gratitude to God Almighty for His unwavering presence, guidance and strength throughout this journey. His grace has sustained me through the most challenging phases of this research, giving me the perseverance to continue, even when the path seemed uncertain. I am especially grateful for the moments of clarity and insight that came at the right time, enabling me to approach problems from different perspectives and think more critically and creatively. His blessings have been the foundation upon which this work has been completed, and I am truly thankful for his constant support.

I would like to extend my sincere appreciation to my supervisor, Dr. Arthur Fang, for his continuous support, encouragement, and invaluable guidance throughout every stage of this research. His expertise, patience, and thoughtful feedback played a crucial role in shaping the direction and quality of this work. I am truly grateful for the time and effort he dedicated to reviewing my work and providing constructive insights that greatly improved this study. I would also like to express my heartfelt gratitude to Kimi Wang for her timely assistance and guidance. Her support, especially during critical moments of the research, was incredibly helpful and contributed significantly to overcoming various challenges along the way.

Finally, I would like to express my deepest appreciation to my family and friends for their constant support, encouragement, and understanding. Their belief in me has been a constant source of motivation throughout this journey. During both the highs and the lows, they stood by me, inspiring me to keep moving forward and reminding me of the importance of perseverance. Their unwavering support has been instrumental in helping me reach this milestone, and I am truly grateful to have them on my side.

Table of Contents

List of Figures

List of Tables

Glossary

AFS	Aluminium Foam Sandwich
a	Applied imperfection amplitude
t	Total thickness of Al foam sandwich panel
a/t	Normalized Imperfection amplitude in terms of total thickness of panel
ρ^*, ρ	Relative density of Al foam
RF	Reaction force
P	Peak reaction force
P_0	Peak reaction force of sandwich panel without imperfections
P/P_0	Normalized peak reaction force
$U3_{max}$	Maximum out of plane displacement of the sandwich panel
LE12	logarithmic core shear strain in the plane formed by the panel length and thickness directions.
E_f	Modulus of elasticity of Al face plate
E_c	Modulus of elasticity of foam core

Chapter 1

Introduction

1.1.Background

Sandwich panels are widely used in structural engineering because they offer a highly efficient way to achieve high stiffness and strength without adding much weight. In their simplest form, they consist of two relatively strong face sheets separated by a lightweight core material. The face sheets mainly resist bending stresses, while the core transfers shear and provides restraint against local buckling of the faces. This combination makes sandwich panels attractive wherever weight reduction, material efficiency, and good mechanical performance are important design goals. . However, the behaviour of sandwich panels is also affected by several instability-related problems These include compressive buckling, core shear deformation, local face-sheet buckling, face-core debonding, and sensitivity to manufacturing imperfections. These effects can reduce load-carrying capacity, change the collapse mode, and make the structural response less predictable under service or extreme loading.

Compared with other core options, sandwich panels with fibre reinforced polymer (FRP) cores have been studied more extensively than those with metal foam cores. One main reason is that FRP sandwich panels are already widely used in practice in building systems, marine structures, transport components, and protective panels; therefore, they have attracted a large amount of experimental, analytical, and design-oriented research. In contrast, metal foam sandwich panels remain relatively less developed as structural systems and have been examined mainly in relation to compressive behaviour, energy absorption, and crashworthiness. Nevertheless, metal foam sandwich panels offer important advantages because the foam core can actively participate in load transfer and deformation, thereby improving the compressive stability and energy dissipation.

1.2 Aluminium Foam Sandwich Panels

The inherent properties of Al foam sandwich panels, such as low density, good energy absorption, and efficient load-carrying capacity, make them stand out among other metal foam sandwiches. These features make them suitable for structural applications, such as lightweight structures, where the main goal is to reduce mass while maintaining adequate stiffness and collapse resistance. Their favourable strength-to-weight ratio also makes them attractive in crashworthy and deformation-tolerant applications, where the structure needs to dissipate energy in a controlled way rather than fail suddenly.

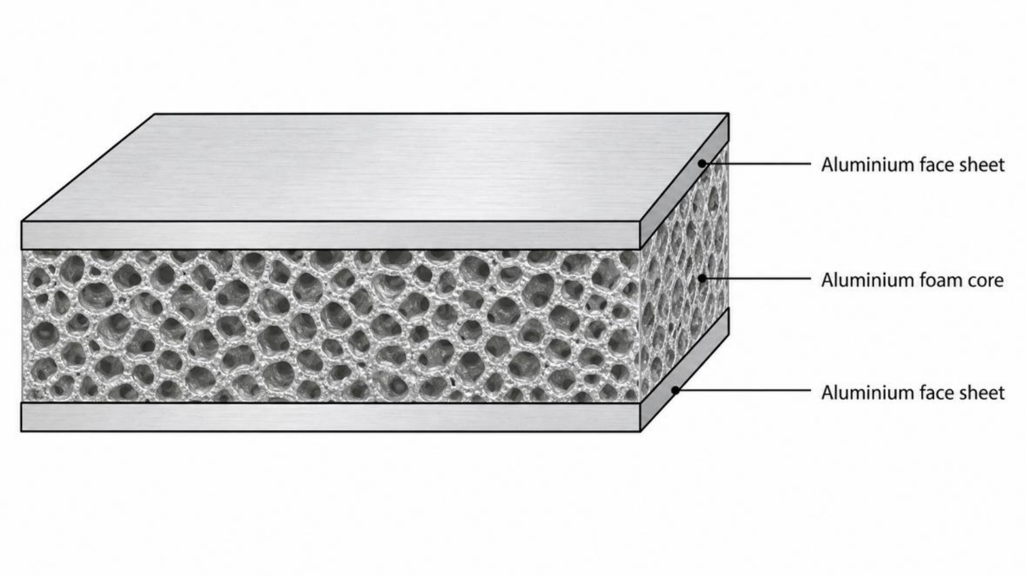

Figure 1.1: Schematic of an aluminium foam sandwich panel showing the aluminium

Although a substantial amount of research has been conducted on aluminium foam sandwich panels, the literature remains concentrated around only a few major themes. The main research on aluminium foam sandwiches remains concentrated on areas such as their manufacturing, core-face interface development, compressive and buckling behaviour, response under ballistic and impact loading, energy absorption capacity, and competitiveness in heat transfer and noise reduction. In particular, the studies look closely at how different production techniques shape the cellular structure of the foam, how the foam structure affects the mechanical performance of the foam, and how the panels behave when they are pushed into regimes where instability, energy absorption, or collapse become key considerations.

Among all these topics, out-of-plane compression and impact responses of the sandwich have been developed the most because they are more closely related to areas such as structural stability, collapse resistance, and energy absorption. In addition, fields including manufacturing routes and studies of basic material behaviour have also been investigated extensively, mainly in the case of review-type and design-oriented papers. Some studies have investigated panels with innovative core architectures and demonstrated that these panels have strong potential as lightweight structural systems.

At the same time, several other important aspects remain underdeveloped. In particular, the detailed interactions between foam density, geometric imperfections, buckling mode transition, and reliable design prediction have not yet been clarified across a broad range of densities. Although existing studies demonstrate that aluminium foam sandwich panels can perform well, fewer studies explain how the structural response changes when the core density varies and when realistic imperfections are included. This creates a clear research gap, especially for studies that aim to move beyond peak load alone and address stability, imperfection sensitivity, and post-buckling behaviour.

1.3 In-Plane Compressive Behaviour

The in-plane compressive strength is an important consideration in structural engineering because sandwich panels may serve as load-bearing members in their own plane in addition to acting as transverse members under bending or out-of-plane compression. Under stable axial loading, the panel should carry the compressive force efficiently while maintaining its stiffness and structural integrity throughout the service range. Therefore, the interaction between the face sheets and core is critical because the core contributes to shear transfer, restrains the face sheets, and enhances overall stability, all of which influence the panel's resistance to axial shortening.

Despite its importance, in-plane compression has received less attention than the more established cases of out-of-plane compression and bending. Out-of-plane behaviour has long been treated as the governing design scenario for sandwich panels; therefore, most experimental and analytical studies have focused on flexural response, local buckling, and collapse under transverse loading. The in-plane response is mechanically more complex because it may involve global instability, local buckling, core shear deformation, and face-sheet interaction simultaneously. Although the in-plane compressive behaviour of polymer, FRP, and other sandwich panels has been studied extensively, corresponding research on metal foam sandwich panels remains limited. Figure 1.2 shows the different failure modes of aluminium foam sandwich panels under in-plane compression.

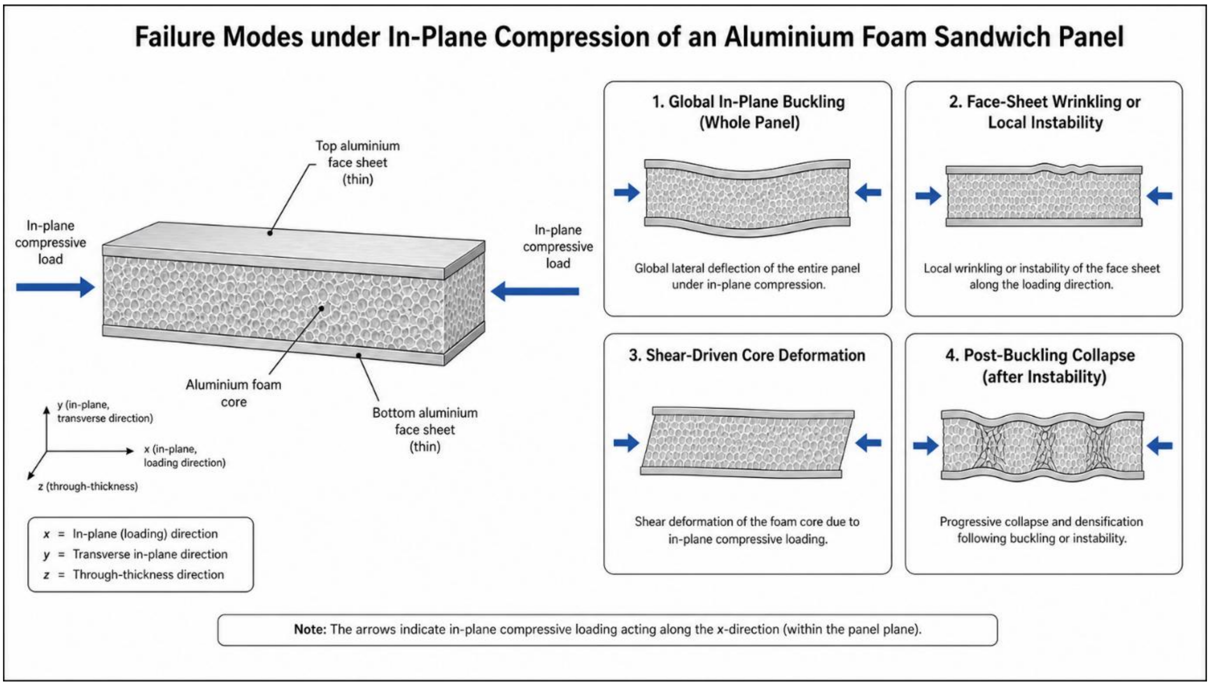

Figure 1.2: Typical failure modes of an aluminium foam sandwich panel under in-plane compression.

More detailed studies on the in-plane compression behaviour of Al foam sandwich panels are needed to provide more knowledge on how variations in the composition of the foam core affect compressive stability, how sensitive the panel is to geometric imperfections, and how far the structure can sustain the load without premature instability or sudden loss of capacity. Although many such studies have been conducted in the case of bending, the effects of such imperfections on in-plane capacity have not been studied sufficiently. This is particularly important for lightweight engineering applications, where the key requirement is not impact resistance but a stable and reliable axial load response. A better understanding of in-plane behaviour would also support the development of design rules for structural components, such as stiffened plates, lightweight panels, and other load-bearing members, which may experience sustained compressive forces during their service.

1.4 Factors affecting in-plane strength

The in-plane compressive strength of aluminium foam sandwich panels is controlled by several linked factors, including foam relative density, core morphology, face sheet properties, core thickness, bonding quality, loading rate and geometric imperfections. Among these, the interaction between core and face sheets are particularly important because they determine the way the load is transferred through the section, the ease with which instability develops, and the manner in which the panel retains its integrity under axial compression. In practice, the in-plane response depends not only on the strengths of the individual materials, but also on how effectively the sandwich behaves as a single structural system.

Some of these influences have already been reasonably well explored in the literature, especially the effects of foam density, loading rate, and basic compressive behaviour. Existing studies have shown that changing the core density can markedly alter the stiffness, load-carrying capacity, collapse characteristics, face-sheet properties and core geometry, which also play a clear role in shaping the overall response. Other aspects are less well resolved, particularly the combined impact of density, geometric imperfections and in-plane compressive stability. In many cases, these variables have been studied one at a time, rather than in combination, so the way they interact to control failure mode and post-buckling behaviour is not yet fully explained.

This gap is important, because a more complete picture of in-plane compression is needed if reliable design guidance is to be developed for lightweight structural applications. Geometric imperfections may not always dominate the average strength, but they can have a strong effect on the collapse path and on stability margins, especially in systems that are highly imperfection-sensitive. For this reason, a detailed study of in-plane compressive behaviour is valuable not only for estimating peak load, but also for understanding how aluminium foam sandwich panels deform, redistribute stresses and remain stable under realistic service conditions

1.5 Manufacturing and geometric imperfections

Aluminium foam sandwich panels almost always contain imperfections arising from both the foam manufacturing process and final assembly stage. Typical examples include variations in pore size, uneven cell distribution, local density gradients, regions of incomplete foaming, face sheet waviness, irregularities in the bond between the core and skins, thickness variations, residual stresses, and geometric deviations introduced during forming, cutting, or handling. Because the structural efficiency of a sandwich panel depends strongly on the interaction between the face sheets and core, these imperfections can have a noticeable influence on load transfer, stiffness, and stability under compression. Even a relatively small departure from the ideal geometry can change the collapse mode, reduce the peak load-carrying capacity and modify the post-buckling response of the sandwich panel.

The role of imperfections has been studied in several different forms, including indentation-type defects, morphological irregularities within the foam core, process-induced defects, and more general geometric imperfections in sandwich structures. These works, all together, show that imperfections can lower structural capacity, trigger earlier localisation of deformation and alter the overall deformation path under compression. However, the combined effect of the imperfection amplitude, foam density and in-plane compressive stability has not yet clarified for aluminium foam sandwich panels over a broad design space. This remains an important research gap, since imperfection sensitivity is often a key factor in stability-driven behaviour and can govern whether a structure fails in a controlled manner or in an undesirable manner.

1.6 Research Gap

Although aluminium foam sandwich panels have been studied for their compressive response, buckling resistance, and energy absorption, the literature does not provide a complete understanding of their structural behaviour under in-plane compression when both geometric imperfections and foam-density variations are present. This is particularly true when both geometric imperfections and foam density variations are present in the structure. Most previous research has treated the problem from a limited perspective, focusing on general sandwich panel behaviour, foam-core morphology, or isolated imperfection effects. Although a few studies have investigated the effects of initial geometric imperfections on the bending behaviour of metal foam sandwich panels, their influence on in-plane compression remains limited**.** Consequently, the coupled influence of face sheets, foam core density, and imperfection severity on stability and collapse behaviour remains insufficiently resolved.

The second limitation is that much of the published work on sandwich panels has been directed toward FRP-core systems or out-of-plane loading cases, whereas aluminium foam sandwich panels under in-plane compressive loading have received comparatively less attention. This is important because in-plane compression is a stability-sensitive problem in which the panel response may simultaneously involve global instability, local buckling, core shear deformation, and face sheet interaction at the same time. Although aluminium foam cores can improve load transfer and energy dissipation, the extent to which they enhance in-plane compressive stability is not clearly established across different densities and panel configurations.

Another important gap concerns the imperfections arising from manufacturing and assembly. Aluminium foam sandwich panels almost inevitably contain pore-size variations, uneven cell distributions, local density gradients, incomplete foaming, face sheet waviness, bonding irregularities, thickness variations, residual stresses and out-of-plane geometric deviations. The literature shows that such imperfections can trigger local wrinkling, promote debonding, reduce stiffness and knock-down buckling loads, and their influence is often highly nonlinear and strongly dependent on defect type, location, and amplitude. Existing studies have examined a wide range of imperfection forms, including face sheet debonds, unbonded truss nodes, indentation-type defects, internal foam damage and as-manufactured core waviness. Such studies have demonstrated that these forms of imperfections can change both the collapse path and observed failure mode in sandwich panels. However, these works typically consider imperfections either in isolation or under out-of-plane or idealised loading conditions. There is still very limited research on the effects of controlled out-of-plane geometric imperfections on aluminium foam sandwich panels. In particular, the combined influence of the imperfection amplitude and foam relative density on the in-plane compressive strength, post-buckling response, and mode transitions remains unclear. These combined effects of density and imperfection amplitude on in-plane behaviour therefore remains insufficiently understood and forms a central focus of the present study

Accordingly, the present study addresses this gap by examining the in-plane compressive behaviour of aluminium foam sandwich panels, with particular attention to the combined effects of foam relative density and out-of-plane geometric imperfections. By focusing on the strength, stability, collapse mode, and post-buckling behaviour, this study aims to develop a clearer scientific basis for predicting the compressive performance of aluminium foam sandwich panels and improving their reliability in lightweight structural applications.

1.7 Novelty and contribution of this thesis

The novelty of this thesis lies in providing a systematic, density-dependent characterisation of in-plane compressive behaviour and imperfection sensitivity in aluminium foam sandwich panels. Unlike most previous studies, which either focus on out-of-plane loading or treat density and imperfections separately, the present work combines ten foam relative densities with a wide range of out-of-plane geometric imperfection amplitudes in a single numerical framework built on validated material models. This makes it possible to identify how density and imperfection amplitude together control peak load, mode interaction, and post-buckling stability under axial compression.

The second contribution is the identification of imperfection-dependent mode interaction windows and the associated deformation regimes of multi-wave, emerging wave, and U-shaped localization across the density-imperfection space. The results show that structural robustness is non-monotonic and maximized at intermediate densities rather than at the highest density alone. This thesis introduces a multi-objective performance framework that incorporates imperfection tolerance, deformation-mode stability, energy absorption, and mass efficiency to support the selection of an optimal range of foam-core densities for design. The thesis also develops a regression-based design equation for the normalized peak load in the higher-imperfection regime

1.8 Thesis Aim

The aim of this study is to investigate the in-plane compressive behaviour of aluminium foam sandwich panels and clarify how foam relative density and out-of-plane geometric imperfections influence their strength, stability, and collapse response.

1.9 Thesis Objectives

The specific objectives of this study are as follows:

1. Examine the in-plane compressive response of aluminium foam sandwich panels with different foam relative densities.
2. Investigate the influence of out-of-plane geometric imperfection amplitudes on compressive strength and stability.
3. Assess how imperfection severity affects collapse mode and post-buckling behaviour.
4. Develop a clearer understanding of how foam density and geometric imperfections control the structural response of the sandwich panel
5. Provide evidence that can support more reliable design and analysis of aluminium foam sandwich panels.
6. Develop and use a multi-objective performance framework that combines imperfection tolerance, deformation-mode stability, energy absorption and mass efficiency, in order to identify a suitable range of foam core relative densities for design
7. Develop and validate a regression-based design equation for the normalized peak load of aluminium foam sandwich panels in the higher-imperfection regime, suitable for use as a design aid within the calibrated density and imperfection range

1.10 Thesis Structure

This thesis is organized into the following chapters. Chapter 1 introduces the background, motivation, research gap, aim, and objectives of this study. Chapter 2 presents the literature review and theoretical background relevant to aluminium foam sandwich panels, in-plane compression, and imperfection sensitivity. Chapters 3 and 4 describe the materials, Abaqus modelling approach, experimental data, and validation of the aluminium foam, aluminium plate, and aluminium foam sandwich models, as well as the analysis methods used in the study. Chapter 5 sets out the parametric study framework and model matrix, clearly distinguishing the validated benchmark model from the extended set of 200 aluminium foam sandwich panel simulations with varying foam relative densities and geometric imperfection amplitudes. Chapter 6 presents the results of the in-plane compressive investigation and discusses the influence of foam density and geometric imperfections on peak load, deformation mode and energy absorption. It also applies a multi-objective performance framework, combining imperfection tolerance, deformation-mode stability, energy absorption and mass efficiency, to identify an optimal range of foam core relative densities for design. Chapter 7 develops and validates a regression-based design equation for peak load carrying capacity in the higher-imperfection regime based on the results obtained from the analysis. Chapter 8 presents the summary, main conclusions derived from the thesis and future prospects of the study.

Chapter 2

Literature Review

This chapter reviews the literature on metallic and aluminium foam sandwich panels, with emphasis on in-plane compression, stability, and imperfection sensitivity. It focuses on how manufacturing route, core morphology, bonding quality, and geometric imperfections affect stiffness-to-weight performance, energy absorption, buckling behaviour, and failure modes in aluminium foam sandwich structures.

The review progresses from general sandwich-panel mechanics to the specific behaviour of aluminium foam sandwich systems. It first considers manufacturing developments and their influence on pore morphology, interface quality, and structural reliability, before outlining the main mechanics and failure modes of sandwich panels. The chapter then discusses forming and laser forming effects, followed by in-plane compression, stability, and debonding. It concludes with a review of imperfection sensitivity, including geometric, morphological, and debonding-related defects, and their influence on buckling and collapse paths.

Together, these sections establish the mechanical and technological background for the present study and identify the research gap addressed in the thesis

2.1. Recent foam and sandwich manufacturing developments

Although metal foam-core sandwich panels have been studied extensively under out-of-plane loading, comparatively few studies have focused on their in-plane compressive behaviour. This gap is partly historical, because foam cores are generally considered weak in in-plane strength and are therefore not primary load carrying members in most sandwich applications. However, recent developments in foam and sandwich manufacturing have begun to challenge this assumption. Emerging processes are improving core uniformity, interface quality, and overall structural performance, suggesting that future foam sandwiches may carry higher in-plane loads more efficiently. Some recent developments relevant to this trend are mentioned below.

A few improvements have been made in the joining and interfacial design of aluminium foam sandwich panels. Graziano et al. [25] joined face sheets to aluminium foam cores using Zn-based fillers by carefully adjusting the solder composition. They found that adding a small fraction of Al to Zn solder can significantly improve the effective stiffness of the sandwich as compared with pure Zn joints. This newly engineered face-core interface can open the door to stiffer and damage-tolerant configurations under both in-plane and out-of-plane loading.

Simultaneously, there is a clear trend away from the classic ‘manufacture the foam core, then cut and bond’ workflow toward more integrated forming routes. Integral forming methods [19] fabricate the foam core and its face sheets in a single forming sequence, which has been shown to produce cores with high porosity, small pore diameters, and relatively homogeneous pore distribution. Quasi-static compression tests on such integral-formed sandwiches indicate more uniform deformation and improved energy absorption, suggesting that controlling pore morphology during the forming process can enhance both performance and repeatability compared with traditional cut-and-bond panels.

Broader reviews of metallic foam processing underline how rich the process landscape has become. The introduction of newer approaches such as additive manufacturing and other advanced forming techniques [24,44], along with existing methods of liquid metallurgy, powder metallurgy, and electrochemical methods, offers a balance of pore control, cell topology, scalability, and defect control. Other emerging technologies, such as freeze casting, electron beam melting , and the use of specialized chemical foaming agents, enable more refined control over the pore structure and relative density of the foam[44]. In addition to these innovations, X ray and electron tomography make it possible to relate morphological imperfections directly to local deformation and damage and help in modelling numerical models that capture these effects more accurately than before.

Another development by Pai Peng et al. [26] is the friction stir welding process used to produce aluminium foam sandwich, which has good sound absorption, high flexural strength and impact resistance than those produced by traditional adhesive or brazing methods

Taken together, these developments show a consistent trend toward more controlled pore morphology, cleaner and stronger interfaces, and more reliable structural performance in aluminium foam sandwiches. As these manufacturing routes mature, they are expected to improve the in-plane compressive performance of foam sandwich panels and reduce the current disparity between the in-plane and out-of-plane load-carrying capacities. This context motivates the present study’s focus on imperfection sensitivity under in-plane compression, since the response of foam sandwiches to small geometric imperfections and process-induced defects must be understood and quantified if their full load-bearing potential is to be realised

2.2 Sandwich panel mechanics and failure mode

Sandwich panels combine thin, stiff face sheets with a lightweight core to achieve high bending stiffness at a low weight. In classical sandwich behaviour, the face sheets primarily carry in-plane normal stresses due to bending, while the core transmits transverse shear and stabilises the faces against local buckling and wrinkling. Failure occurs when one or more of these roles are exceeded, leading to mechanisms such as face yielding, wrinkling, core crushing, debonding at the face–core interface, indentation under local loads, or global and local buckling.

Several studies have examined the development of these mechanisms under different loading conditions and geometries. Work on steel–foam sandwich panels under local buckling, by Narayen Pokharel et al. [36] has shown that conventional effective-width approaches become inaccurate for very slender faces, with breadth-to-thickness ratios above about 100. In that regime, extensive experimental and finite element analyses indicate that local buckling behaviour is more severe than classical formulas predict, and improved design expressions are needed to cover b/t ratios up to around 600. This highlights the sensitivity of face-dominated failure to both face slenderness and the stabilising effect of the core.

Other studies have focused on the influence of the pore structure within metallic foam cores on the bending response. For aluminium foam sandwiches in three-point bending, it has been shown that panels with only a few pore layers can behave mechanically more like dense materials, with limited contribution from the foam architecture (Xiaotong Lu et al. [20]). When the pore diameter is very small, on the order of tenths of a millimetre, shear-type failure tends to dominate, whereas polygonal pores with diameters in the range of a few millimetres can significantly enhance energy absorption. These results show that core morphology affects not only stiffness and strength but also whether failure is governed by shear, crushing, or a more gradual, energy-dissipating mechanism.

Edgewise and in-plane loading introduce additional failure paths, particularly related to instability and debonding. Pier Giovanni et al. [8] conducted studies on steel sandwich panels with polymeric foam cores subjected to edgewise compression. They demonstrated that initial geometric imperfections can trigger earlier buckling and promote debonding between the faces and core. In these cases, relatively small deviations from ideal geometry reduce the load at which instability occurs and change the sequence of damage, reinforcing the idea that sandwich performance under in-plane loading is highly imperfection sensitive.

Fatigue and impact loading further enrich the failure landscapes. According to the work of Fan Dong et al. [21] on composite sandwich panels under three-point bending fatigue, the orientation of the core relative to the panel length has been shown to influence stiffness, strength, and fatigue life. Even though, cores arranged with the loading direction can provide higher strength and stiffness, such orientation may reduce fatigue resistance in comparison with cores that are oriented transversely. Another study [37] proposed damage and failure mode maps, under quasi-static indentation and low-velocity impact to show how variations in core density and face sheet thickness steer the failure path. These studies prove that face sheet thickness is the dominant parameter governing both the ultimate load and the transition between indentation, core crushing, and punching-type failures, whereas core density mainly shifts the specific mode without strongly altering the ultimate capacity.

The support conditions and local stress fields provide another source of complexity. In the paper 'Analysis of failure mechanisms at the supports' by Jolanta Pozorska [23], the test of sandwich panels in bending revealed that the actual compressive stress distributions at the supports can differ markedly from those assumed in simple design formulas. Measured stresses near supports often show local peaks and non-uniform distributions that are not captured by classical sandwich theory, suggesting that localised failure at supports or concentrated load points may occur earlier than global criteria would imply. In parallel, work on sandwich panels with honeycomb cores[22] has clarified how face sheets and the core share load: the faces carry most of the bending stresses, while the honeycomb core resists through-thickness shear and compressive stresses, and simple predictive models for different face and core failure modes have been shown to agree reasonably with experiments.

Taken together, these studies establish a mechanical framework in which the geometry, core morphology, material choice, and imperfections interact to determine the dominant failure mechanism under a given loading mode. However, most of these works have focused on out-of-plane bending, indentation, global buckling in steel, polymer-foam, or composite sandwiches, with only limited emphasis on detailed in-plane compressive behaviour of metallic foam-cored panels. The present study builds on this framework by examining how small initial geometric imperfections in aluminium foam sandwiches influence mode interaction, buckling response, and energy absorption under in-plane compression, thereby extending existing failure-mode understanding into a regime that has received relatively little attention.

2.3 Metal foam and aluminium foam sandwich panels

Sandwich structures with metallic foam cores are often promoted for their high stiffness-to-weight ratio and excellent energy absorption, especially under out-of-plane loading. In these systems, the foam core is intended to carry most of the through-thickness compression and shear, while the face sheets mainly provide bending stiffness and protect the core. Within this broad family, aluminium foam sandwich (AFS) panels are particularly attractive because they combine low density with good specific strength, corrosion resistance, and the possibility of tailoring the core density and cell morphology.

Experimental work on composite metal foam core sandwiches under out-of-plane compression by Jacon Marx et al [14] shows that, in many cases, the deformation is dominated by the foam ,while face sheets contribute relatively little once the core starts to collapse. This type of response emphasizes that the energy absorption capacity and plateau behaviour are controlled primarily by the foam microstructure rather than the face material alone. At the same time, the manner in which the faces are bonded to the core is critical. Comparisons between adhesive bonding and diffusion bonding have shown that diffusion-bonded interfaces can provide much better mechanical performance, with higher strength and more stable deformation. This highlights the importance of bonding quality as a key design parameter in metal foam sandwiches.

The beneficial effects of optimized core-to-face configurations are also clear in foam-filled or architected cores. Studies on sandwich panels with aluminium foam-filled corrugated cores under out-of-plane compression by L.L Yan et al. [15] reported substantial increases in peak reaction force and energy absorption compared with empty or more conventional cores. Similarly, multilayer aluminium foam configurations show that simply stacking foam layers without interlayer plates offers little or no advantage over a monolithic foam and can even reduce the plateau strain and plateau stress [18]. In contrast, multilayer aluminium foam sandwiches with aluminium interlayers can significantly improve the initial collapse stress, plateau stress, and overall absorbed energy. These results underline that load transfer paths and the details of how foam layers and face sheets interact are just as important as the nominal foam density when designing for stiffness-to-weight and energy absorption.

From a modelling and vibration perspective, aluminium foam sandwiches exhibit robustness to variations in core density. Numerical studies that vary the random distribution of core density have found that the overall dynamic response (for example, natural frequencies) is not strongly affected, even though the eigenvectors change (Modelling of Aluminium foam sandwich panel, Vincenzo D'Alessandro et al. [38]). The study suggests that, within certain bounds, the spatial density variation does not affect the global stiffness of the panel, but they can influence deformation patterns and mode shapes. Numerical analysis of the quasi-static compression of panels with varying core and aluminium face sheet thickness showed that increasing the core and face sheet thickness can increase the peak reaction forces and result in greater energy absorption behaviour [17]. This reinforces the classic observation that both the core thickness and face stiffness contribute to the global crushing resistance.

Taken together, the literature indicates that aluminium foam sandwich panels are structurally efficient systems with high specific stiffness and strong energy-absorbing capabilities, only if foam density, core architecture, and bonding quality are carefully controlled. However, most of these studies have focused on out-of-plane compression, bending, vibration, or impact, and rarely explore in detail how aluminium foam sandwiches behave in in plane compression across a range of core densities and imperfection levels. This gap motivates the present work, which examines how initial geometric imperfections interact with foam density to govern buckling behaviour, mode interaction, and energy absorption in aluminium foam sandwich panels under in-plane loading.

2.4 Forming and laser forming of sandwich panels

In many applications, sandwich panels are not left flat after manufacturing but are bent or formed into curved or locally stiffened shapes. These forming operations can introduce curvature, residual stresses, local thinning, and damage at the face–core interface, all of which may change the mechanical response and failure mode of the panel. Studies on hydroforming and incremental forming have shown that if the process is not carefully controlled, defects such as face wrinkling, delamination, and local cracking can occur[27][39]. This shows that forming is not just a shaping step but an important part of the manufacturing process that can strongly affect the final structural performance.

Laser forming has also been proposed as a tool-free method for bending metal foam sandwich panels by creating local thermal gradients in the face sheets. Bucher et al.[27] showed that relatively large bending angles can be achieved when the face–core bond is strong, whereas poor bonding can lead to debonding or local damage instead of controlled bending. Similarly, Contorno et al. [39] found that aluminium foam sandwich panels can be formed into significant curvatures without serious damage when the process is properly designed. Their results also showed that excessive curvature, unsuitable tooling, and weak bonding can cause core crushing, face wrinkling, and partial detachment.

Overall, the literature shows that post-forming and laser forming provide powerful ways to shape foam-cored sandwich panels, but they also introduce additional sources of curvature, residual stress, and interface degradation that can act as imperfections in service. For aluminium foam sandwiches, this is particularly important because the core is relatively compliant and the face–core bond often governs whether damage localises or spreads. In the context of the present work, these findings reinforce the idea that realistically manufactured aluminium foam sandwich panels will contain both geometric and process-induced imperfections. A proper understanding of how such imperfections, together with foam density, influence the in-plane compressive behaviour and buckling response is crucial for the reliable design of AFS components.

2.5. In-plane compression, stability, and debonding

When sandwich panels are loaded in in-plane or edgewise compression, their behaviour is governed by a combination of global buckling, local face instability, core crushing, and face–core debonding. Unlike out-of-plane compression, where the core often dominates, in-plane loading activates the full column-like behaviour of the faces and makes the response highly sensitive to imperfections and interface defects. This section reviews key studies on in-plane compressive response, with a focus on how buckling stability and debonding interact, and why design cannot rely on peak load alone.

Several studies have highlighted the distinction between stable and unstable buckling in sandwich columns. Work on generic sandwich panels under in-plane compression by Anders Lindstorm [30,31] shows that panels failing through unstable, snap-through-type buckling can absorb large amounts of energy but tend to fail catastrophically once instability is triggered. In contrast, panels that fail through more stable, progressive buckling exhibit a smoother load–displacement response and are easier to control in design. This has led to the recommendation that, wherever possible, sandwich panels loaded in in-plane compression should be designed to fail in a stable mode, and that if this is not feasible, intentional trigger features should be used to guide the collapse pattern into a favourable, predictable form. Alongside these qualitative observations, design approaches have been proposed to estimate collapse loads for different sandwich configurations, emphasising that buckling mode shape and stability are as important as nominal strength.

The role of global column buckling was examined using both analytical and numerical methods. Modified Euler-type formulas were developed for steel-metal foam sandwich columns by adjusting the effective flexural stiffness and introducing appropriate reduction factors. These studies by Aditya Vidwans et al. [9] show that, with suitable modifications, classical column buckling theory can predict the load-carrying capacity of steel–foam sandwich panels under axial loading. At the same time, the predicted capacity is sensitive to the assumed geometric imperfection amplitude, and finite element simulations confirm that realistic imperfection shapes and magnitudes can significantly reduce the critical load.

Complementary work on the in-plane compressive strength of steel foam sandwich panels are done by B.W Schafer et al.[2] which extends plate-buckling concepts, such as Winter's effective-width approach, to include shear deformation and foam behaviour, showing that properly designed foam-core sandwiches can outperform solid steel of equal weight over a broad range of slenderness, provided shear effects and reduced core stiffness are treated correctly.

In-plane behaviour is further complicated by the interaction between buckling and debonding at the face–core interface. Experimental campaigns on composite sandwich panels with different face materials and core types [31] have shown that post-buckling failure modes are strongly influenced by the ratio between the fracture toughness of the face–core interface and the bending stiffness of the face sheets. When the interface is relatively weak, local buckling tends to initiate at or near debonded regions, and crack growth from the debond edge often control the final failure. More detailed studies by Yi-Hsin Nieh et al. [33] on debonded composite sandwich structures under in-plane compression have mapped how debond length and face thickness affect the buckling and failure modes: thicker face sheets and shorter debonds increase the buckling load and failure strength, whereas long debonds promote local face buckling and crack propagation. Other work on resin-reinforced foam cores under in-plane compression by Zhiwen Qin et al. [5] links early, small-strain buckling traces to later debonding failure, and shows how machining configuration and core thickness alter both capacity and failure path, with theoretical models providing reasonably accurate failure predictions for certain core geometries.

Core architecture and hybridization offer additional levers for tuning in-plane response. The origami-inspired N core sandwich panels, which combine the features of both I and V cores, were found to have superior load-bearing capacity in in-plane compression compared to conventional trapezoidal cores [7]. Another study on a composite sandwich panel with a locally tight honeycomb core [10] showed a several-fold increase in the specific energy absorption, improved impact load-bearing path, and progressive crushing under in-plane compression rather than sudden collapse. Arameh Eyvazian et al [6] showed that hybrid foam core sandwich columns (where aluminium face sheets are combined with fibre-reinforced layers and resin pins) exhibit higher buckling loads and a marked shift in failure mode from debonding and delamination (which are commonly found in ordinary sandwiches) to Euler-type global buckling and end crushing. These findings collectively show that designers can move from interface-dominated failure towards more stable and predictable buckling and crushing modes by tailoring the core architecture, reinforcing faces, and introducing through-thickness pins.

Taken together, these studies show that in-plane compressive behaviour of sandwich panels cannot be fully characterised by a single peak load. The response depends on the interplay between global and local buckling, interface toughness and debond geometry, core architecture and thickness, and the magnitude and shape of the initial geometric imperfections. Small differences in bonding quality or imperfection amplitude can change the failure path from stable progressive crushing to sudden, unstable buckling or debond-driven collapse. However, most existing work focuses on polymer-foam or steel-foam sandwiches and often treats imperfections in a relatively simple way, without systematically exploring how imperfection level interacts with foam density and energy absorption in metallic foam-cored panels. This motivates the present study's focus on aluminium foam sandwich panels under in-plane compression, where controlled geometric imperfections are used to investigate mode interaction, stability, debond-related behaviour, and their implications for design across a range of core densities.

2.6 Imperfection sensitivity

Real sandwich panels are never perfectly straight. Geometric misalignments, out-of-plane waviness, local debonds, and defects in the foam or truss core all act as imperfections. These imperfections can significantly alter the buckling and collapse of a panel and the load it can carry. The literature on imperfection sensitivity in sandwiches and shell-type structures showed that the effect of imperfections are often highly nonlinear in nature. Small changes in the defect amplitude or location can move the structure from a stable, gradually collapsing response to a sudden, unstable failure.

Several studies have been conducted on sandwich beams and panels under edgewise or in-plane compression emphasize how face-related imperfections and debonds alter both the buckling mode and collapse path. For example, EL-Sayed and S. Sridharan [34], compared fully bonded glass beams with beams in which the face sheet was partially debonded. These tests show that beams are highly sensitive to small wrinkling-type imperfections and slight overall bending; pre-existing debonds make the compressive response much less stable and trigger local face wrinkling and failure at significantly lower loads than in fully bonded beams. This leads to the key message that local face instabilities, combined with imperfect bonding, can dominate failure, even when the global geometry appears almost perfect. Related studies on pyramidal truss-core sandwiches by Russell Biagi et al. [35] with intentionally unbonded nodes show a different but complementary picture: the structures can remain fairly robust in overall compression, but their shear stiffness and shear strength drop sharply, depending on the location of the imperfect nodes. Together, these works show that both the type of imperfection (wrinkling, debonding, unbonded nodes) and its spatial position control whether instability is dominated by local face wrinkling, debond-driven failure, or a more global loss of stiffness.

Beyond sandwich panels, the broader stability literature on frames and shells [11,12] provides a consistent framework for understanding how initial geometric imperfections affect the buckling. In steel frame design [11], for instance, there are proposals for “consistent” definitions of initial imperfections, which stress that both the shape (eigenmode versus simple sway) and amplitude of the assumed imperfection must be chosen carefully to avoid misleading buckling predictions. For orthotropic cylindrical shells and spherical shells under compression, analytical and numerical studies conducted by Marc R. Schultz et al. [40] showed that even small geometric imperfections can reduce the buckling load far below the perfect-shell prediction. Interestingly, in spherical shells with engineered dimple-like defects (study by Anna Lee et al. [12]), there appears to be a “plateau” behaviour: buckling pressure decreases as defect amplitude grows, but beyond a certain size, the buckling load becomes relatively insensitive to further increases in imperfection amplitude. This combination of frame, cylinder, and shell results reinforces the idea that sensitivity to imperfections is not uniform: it can be extremely high at small amplitudes, then saturate, and depends strongly on the chosen imperfection shape.

In sandwich structures, several authors have argued that ignoring imperfections can make classical wrinkling and local instability models either conservative or non-conservative. For example, analyses of face-sheet wrinkling, by Fagerberg, L and Zenkert, D [41] demonstrated that predictions based on perfect geometry can misrepresent the actual failure load if face waviness or small debonds are present. Experimental work by H. Bart-Smith et al. [42] , who deliberately indented metal foam core sandwich panels to introduce local face imperfections, provide a clear illustration: four-point bending tests on these panels show significant stiffness reductions due to debonding and local damage around the indentation, even when the outer geometry seems only slightly disturbed. In parallel to this, numerical studies of open-cell metal foam cores with morphological imperfections such as fractured cell walls or missing cells by Charles Betts et al. [43] show that these internal defects can strongly affect key mechanical properties, such as the Young's modulus, shear modulus, and plateau stress. However, the visible extent of indentation damage does not always reflect internal degradation. Therefore, it is clear from the study that there will always be an error if we try to assess the loss of load-carrying capacity by examining the 'external damage footprint". Together, these results indicate that both external and internal imperfections must be considered when analyzing the effect of imperfections. External face defects may control local wrinkling and debonding, whereas internal foam defects quietly reduce stiffness and strength, even when the damage is not obvious.

Recent studies have moved the imperfection study from idealized imperfections to manufactured imperfections that are measured directly from cores. For example, in honeycomb sandwich panels, researchers such as Adrian X. Rivera et al. [13] use X-ray computed tomography to capture the true imperfections of the core and then categorized them into separate components, such as cell wall errors, in-plane waviness, and out-of-plane waviness. By selectively varying each component, they showed that different imperfection sources produce distinct changes in the flatwise compression behaviour compared with mode-shaped or idealized imperfections. This type of imperfection analysis makes it clear that imperfection sensitivity is not a single scalar property but a response to multiple interacting defect types, each having its own effect on the crushing response, stiffness, and failure mode. When these studies are read alongside beam and truss core studies mentioned earlier, a consistent picture emerges that imperfection effects are often severe when defects are located in highly stressed regions, mild in less critical regions, and are strongly dependent on defect amplitude and pattern.

Despite this growing body of work, important gaps remain for metallic and aluminium foam sandwich panels under in-plane compression. Most existing studies either focus on out-of-plane bending and indentation, where face and core imperfections are introduced locally, or they treat in-plane stability with relatively simple imperfection assumptions, often in steel or composite sandwiches. Systematic studies that combine controlled geometric imperfections with variations in foam relative density and then examine how these factors together shape mode interaction, buckling paths, strength reduction, and energy absorption, are still rare. The present thesis addresses this gap by investigating the combined influence of initial geometric imperfection amplitude and foam relative density on the in-plane compressive response of aluminium foam sandwich panels, with particular attention to changes in buckling mode, collapse stability, and the existence of imperfection-sensitive performance windows

2.7. Summary and Research gap

The literature reviewed in this chapter shows that aluminium and other metal foam sandwich panels are a promising class of lightweight structures. When foam morphology, face–core bonding, and panel architecture are well controlled, these systems can provide high stiffness-to-weight ratios and excellent energy absorption properties. Recent advances in integral forming, joining methods, friction stir welding, and foam fabrication have further improved the core uniformity and interface quality. These developments have strengthened the potential of foam sandwich panels, particularly in applications where structural efficiency is crucial.

The mechanics of these panels are still governed by classical sandwich behaviour, with extensions needed to account for the foam cores and shear effects. This framework remains useful for understanding failure modes, such as local buckling, wrinkling, and core crushing. It also helps to explain how the geometry and material selection influence the dominant collapse path. However, the response becomes more complex when manufacturing defects and post-forming effects are introduced.

A large body of work has examined how the core architecture, face-sheet thickness, and bonding strategy affect the stiffness, strength, and energy absorption under bending, flatwise compression, impact, and vibration. Studies on multilayer foams, corrugated cores, architected cores, and hybrid face configurations have shown that improved load-transfer paths can significantly increase the peak load and absorbed energy. Research on forming and laser forming also shows that manufacturing processes can be used to create useful shapes and local stiffening; however, they can also introduce residual stresses, curvature, and interface damage that later act as imperfections in service.

For in-plane and edgewise compression, the literature shows that the panel response is governed by an interaction between global buckling, local face instability, core crushing, and debonding. Whether collapse occurs progressively or suddenly depends on factors such as the face–core bond quality, face-sheet stiffness, core configuration, and through-thickness reinforcement. Analytical and numerical studies have shown that classical stability concepts can be adapted to foam-core sandwich columns, but the predicted capacity remains highly sensitive to the assumed imperfection shape and amplitude.

The literature on imperfection sensitivity supports this perspective. Geometric and morphological imperfections have been shown to reduce buckling loads and alter collapse paths in sandwich structures, shells, and frames. Local wrinkling, partial debonding, unbonded core nodes, internal foam defects, and as-manufactured waviness all influence the stiffness, strength, and failure mode. Their effects also depend strongly on the defect location and severity.

Despite this progress, important gaps remain in our understanding of aluminium foam sandwich panels. Much of the existing work focuses on out-of-plane loading or on in-plane compression of steel, polymer foam, or composite sandwiches. Imperfections are often treated in a simplified or isolated manner. There appears to be no systematic study that varies both foam relative density and controlled geometric imperfection amplitude, while examining how these two parameters jointly affect mode interaction, stability, strength reduction, and energy absorption under in-plane compression.

This thesis addresses these gaps by examining the in-plane compressive response of aluminium foam sandwich panels using validated material models and prescribed initial geometric imperfections over a range of foam relative densities. The study focuses on how the imperfection amplitude and core density jointly influence the buckling mode transitions, mode interaction, and peak reaction force, and on identifying regimes in which small imperfections either enhance or degrade performance.

Chapter 3

Validation of Aluminium Foam and Aluminium Plate

This chapter validates the material models used for the aluminium foam core and aluminium face sheets. The foam model is verified against uniaxial compression data, and the aluminium sheet model is validated using tensile results reported in the relevant experimental studies. These validated models are then adopted in the subsequent sandwich panel simulations

3.1 Validation of Aluminium Foam

The aluminium foams used for the parametric analyses in this study were characterized using experimental data from the journal paper "Compressive Properties and Energy Absorption of Aluminium Foams with a Wide Range of Relative Densities" by Cheng et al. This experimental work provides quasi-static uniaxial compression data for ten closed-cell aluminium foams fabricated via a modified ALPORAS melt foaming route (pure Al matrix), covering relative densities 0.134 to 0.472 (pore sizes 0.9–3.0 mm).50 mm x 50 mm x 50 mm cube specimens were cast and compressed at the rate of 5mm/min using a WDW-200E universal tester at room temperature. Nominal stress-strain curves were recorded for all ten models, revealing three stages: elastic (linear), plateau (plastic collapse with strain hardening), and densification.

All ten aluminium foam variants ($\rho^* = 0.134$–0.472) from Cheng et al. were calibrated in this study. Nominal stress-strain (σ_n-ϵ_n) curves (shown in Fig. 3 of the journal paper, Yeng Cheng et al. [3]) were digitized using ‘Web Plot Digitizer 4.6 ‘to obtain high-fidelity numerical data points (resolution ~0.001 strain). These digitized curves were then converted into true stress-strain and plastic strain data for use in the foam material calibration, as described in the following subsection.

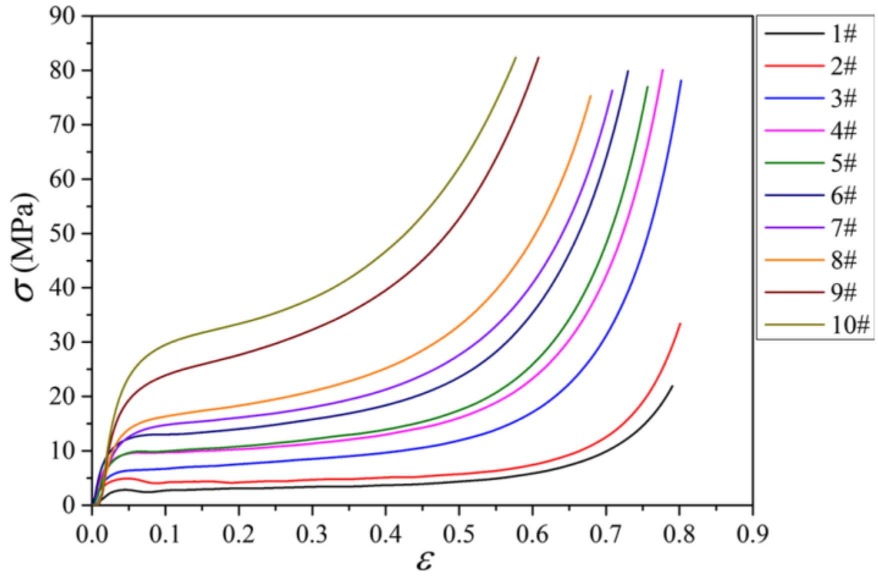

Figure 3.1: Experimental nominal stress-strain curves from Yeng Cheng et al. [3], which were digitized for calibration.

Table 2 Comparison of compressive properties' data of foams with different relative densities

Specimen number	1#	2#	3#	4#	5#
ρ_{rel}	0.134	0.170	0.217	0.250	0.262
E_0, MPa	105	123	190	272	340
σ_p, MPa	2.8	4.9	6.4	9.5	9.6
E_p, MPa	3	4	12	15	17
Specimen number	6#	7#	8#	9#	10#
ρ_{rel}	0.308	0.320	0.355	0.439	0.472
E_0, MPa	508	552	576	817	906
σ_p, MPa	12.2	12.6	14.0	19.3	23.5
E_p, MPa	24	29	38	65	73

Figure 3.2: Table from paper Cheng et al. [3] showing Properties of Aluminium foam

3.1.1 Calibration and Verification of Foam Hardening Data

The crushable foam hardening data were extracted from the uniaxial compression curves reported in Fig. 3 of Cheng et al. [3], which is shown in Fig 3.1, and converted into the form required for the Abaqus crushable foam model. In the Abaqus model, compression was applied by prescribing a negative displacement in the loading direction at the reference point, while the opposite end was fully fixed. Accordingly, the stress-strain and plastic strain data used in the foam hardening table were entered as positive compressive magnitudes

The engineering stress and strain were converted to true stress and true strain using the standard relations:

$$\text{True Stress } \sigma_t = \sigma_n(1+\varepsilon_n)$$

$$\text{True Strain } \varepsilon_t = \ln(1+\varepsilon_n).$$

Where σ_n is the engineering stress, ε_n is the engineering strain.

The elastic true strain and uniaxial plastic strain were then calculated as:

$$\text{Elastic true strain, } \varepsilon_{te} = \sigma_t / E$$

$$\text{Uniaxial plastic strain, } \varepsilon_{tp} = \varepsilon_t - \varepsilon_{te}$$

The elastic moduli E were directly adopted from Table 2 of the paper Yeng Cheng et al. [3].

The true stress–uniaxial plastic strain pairs were first used directly as input for the crushable foam hardening table. However, this direct conversion produced a 50 mm block response that was excessively stiff and transitioned too rapidly into densification, with a limited representation of the plateau region. This indicates that the directly converted hardening table did not reproduce the characteristic crushable-foam response satisfactorily and also led to repeated convergence difficulties in Abaqus during the large-deformation analysis. Therefore, the hardening data were refined by extending the plastic strain range in the plateau and densification regions and adjusting the corresponding yield stress values consistently within the experimental trend.

The refined hardening tables were then verified using a single-element uniaxial compression test, which provided a first-order check of the constitutive response independent of geometric localization and boundary condition effects. The single-element test was used to confirm that the modified hardening law reproduced the target stress–strain response before the same material definition was applied to larger foam block and sandwich panel models. Representative single-element verification plots for relative densities of 0.472 and 0.25 of the Al foam are shown in Fig 3.3 and 3.4, respectively. A small deviation was observed in the initial part of the single-element response. This is acceptable because the single-element model is a highly idealized homogeneous verification case, whereas the 50 mm cube provides a more representative assessment of the bulk foam response under the same material definition. The same hardening table reproduced the elastic region, plateau onset, and subsequent densification of the 50 mm cube response more closely, indicating that the modified hardening law satisfactorily captured the macroscopic foam behaviour.

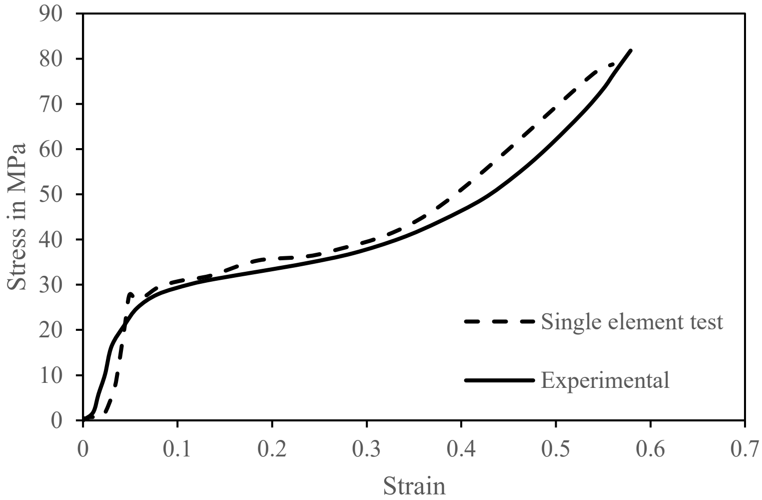

Figure 3.3: Single element test results vs experimental stress strain curve for Al foam of relative density 0.472

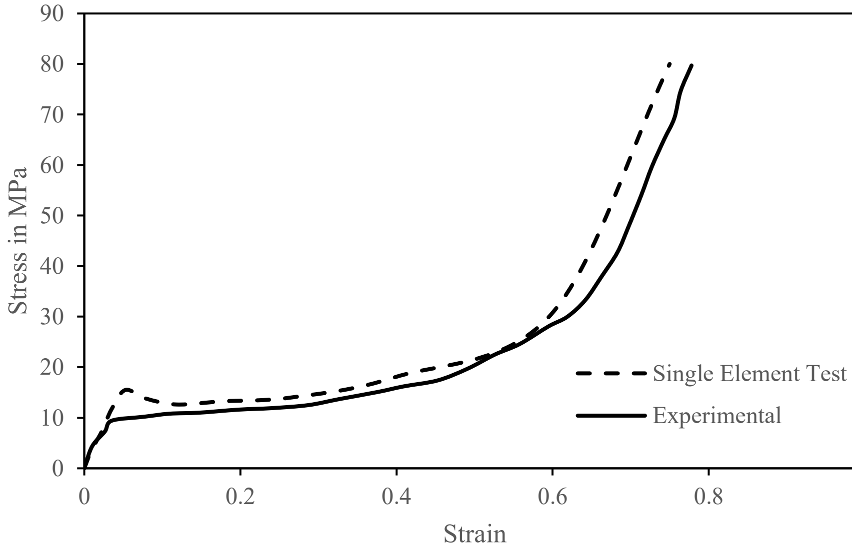

Figure 3.4: Single element test results vs experimental stress strain curve for Al foam of relative density 0.25

3.1.2 Finite Element Modelling

Numerical simulations were performed using Abaqus/Standard (2026) to replicate the uniaxial compression of closed-cell aluminium foam cores (ρ* = 0.134–0.472). This approach emphasizes reproducibility via parametric input files with a common template for geometry, meshing, materials, and analysis. Only relative density dependent properties like modulus of elasticity, density ρ, yield stress, hardening data, and maximum displacement, were varied across the 10 cases.

A 3D prismatic foam core (50 mm cube) was modelled as a deformable solid part, matching the experimental specimen dimensions. A single isotropic elastic-plastic material model (CRUSHABLE FOAM, HARDENING=ISOTROPIC) was assigned uniformly to all elements via a solid section and calibrated for closed-cell Al foam crushing. The density was scaled as the density of solid aluminium multiplied by the relative density value of foam in each case, and the values of Young's modulus were taken directly from Table 2 (Cheng et al.), which follows the Gibson-Ashby ρ^2 scaling, with a fixed Poisson's ratio ν=0.33. The yield behaviour of the foam is defined by the isotropic hardening crushable foam model defined by the compression yield stress ratio, plastic Poisson's ratio, and hardening table. The model comprised a single-part instance, with a reference point kinematically coupled to the top surface for uniform loading.

The boundary conditions and loading were applied within a static general analysis step featuring a non-linear geometry and automatic stabilization to account for large deformations. The bottom surface of the foam core was fully encastred (all translational and rotational degrees of freedom fixed). Compressive loading was imposed via prescribed displacement on the reference point (RP), kinematically coupled to the top surface targeting approximately 80% of the anticipated densification strain (100% of experimental strain was achieved for high-density foams, while for low-density foams, 80% of experimental strain was employed because complete experimental strains could not be attained stably). The lateral translations (U1 and U3) and all rotations at the RP remained free to permit natural barreling and rigid-body motion. The implicit quasi-static loading rate matched the experimental conditions.

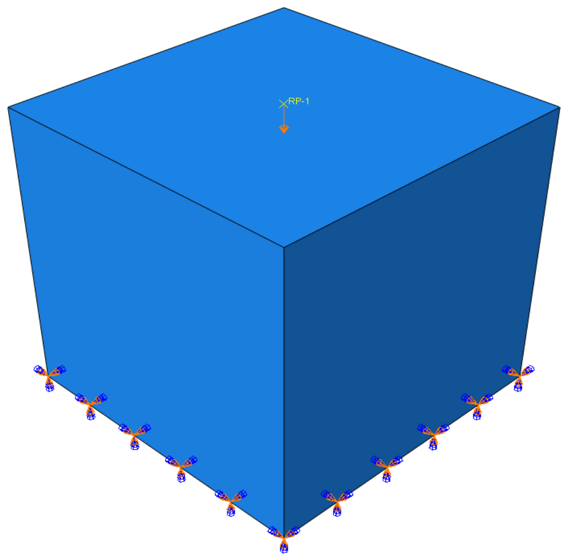

Figure 3.5: Figure Showing Boundary Conditions and Loading for Al foam

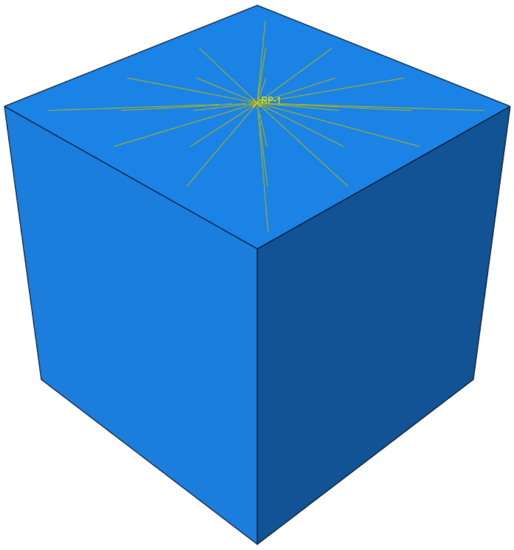

Figure 3.6: Figure Showing Kinematic Coupling on Top Surface of Foam

Meshing employed a structured hexahedral mesh comprising C3D8R 8-node reduced-integration brick elements with approximate 5 mm edge lengths, yielding 1000 elements total (10 layers in height × 10×10 elements per layer). Default hourglass control was utilized, with independent mesh convergence studies confirming adequacy (element aspect ratios <3 and Jacobian determinants >0.6)

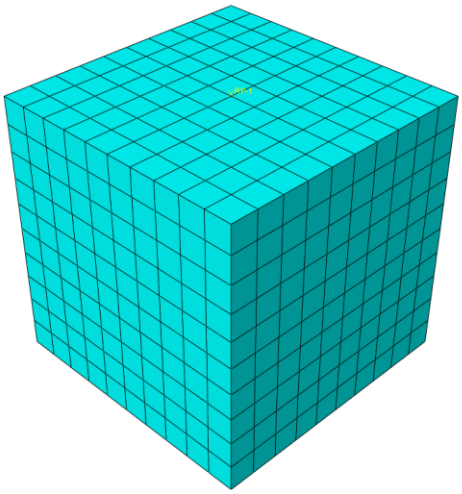

Figure 3.7: Figure Showing Mesh on Al Foam

3.1.3 Numerical Reliability of the Model

The energy balance results for all the ten validated Al foams are listed in Table 3.1. The table reports the final values of the artificial strain energy, internal energy, kinetic energy, and stabilization energy for each case, along with the corresponding energy ratios. These values indicate the extent to which numerical artifacts influence the solutions.

Table 3.1: Energy balance results for the aluminium foam finite element models.

Foam Relative Density	ALLAE (J)	ALLIE (J)	ALLKE (J)	ALLSD (J)	ALLAE/ ALLIE (%)	ALLKE/ ALLIE (%)	ALLSD/ ALLIE (%)
0.134	116.147	318292	0	0.1950	0.036	0	0
0.17	1272.52	521929	0	0.2249	0.24	0	0.017
0.217	112477	2.632E+06	0	7248.73	4.27	0	0.27
0.25	103858	3.163E+06	0	1.08845	3.2	0	0
0.262	113724	2.658E+06	0	1.14012	4.27	0	0
0.308	90344.3	2.353E+06	0	16.1746	3.84	0	0
0.32	101606	3.105E+06	0	3635.82	3.27	0	0.117
0.355	85105.1	2.73E+06	0	0	3.12	0	0
0.439	186.612	2.835E+06	0	0.707505	0.006	0	0
0.472	161.717	3.044E+06	0	0.98579	0.005	0	0

The energy balance results presented above showed that the kinetic energy was negligible for all foam models, whereas the artificial strain energy remained below 5% of the internal energy in all cases. The stabilization energy was also very small compared with the internal energy, indicating that the numerical solutions were stable and suitable for subsequent validation

3.1.3.1 Mesh Convergence Studies

To assess the reliability of the finite element modelling, mesh convergence studies were performed on four representative foam densities, namely, 0.134, 0.262, 0.355, and 0.439. These cases were selected to represent the overall density range of the Al foams investigated in this study. The effect of mesh refinement on the stress response of the models was studied by progressively reducing the global mesh size from 5.0 mm to the minimum feasible mesh size at definite intervals. For the 0.262 and 0.439 foams, the finest mesh that could be solved reliably was 2.5 mm, whereas for the 0.134 and 0.355 foams, the minimum feasible mesh size was 3.0 mm. Refinement below these limits causes the nonlinear solution to lose convergence. For the mesh convergence study, each foam density was compressed only up to a strain level lower than that used in the validation analysis, and the same strain level was maintained for all mesh sizes within each foam density to ensure a consistent comparison.

The stress responses obtained from the coarser meshes were then compared with those from the finest converged mesh for each foam density.

Results for 0.134 Al foam

The mesh convergence study for the Al foam with relative density 0.134 was conducted using mesh sizes of 5.0, 4.5, 3.5, and 3.0 mm. The 3.0 mm mesh was found to be the finest converged mesh for this density, and the stress responses obtained from the coarser meshes were compared with this reference case to assess the effect of mesh refinement. The results of this study are illustrated below.

Table 3.2: Stress response of 0.134 Al foam at different mesh sizes

Mesh Size	Strain	Stress in MPa
3 mm	0.25	3.47
	0.35	3.67
	0.4	3.98
3.5 mm	0.25	3.48
	0.35	3.65
	0.4	3.91
4.5 mm	0.25	3.48
	0.35	3.65
	0.4	3.9
5 mm	0.25	3.47
	0.35	3.67
	0.4	3.9

Table 3.3: Percentage change in stress relative to the 3.0 mm mesh for 0.134 Al foam

Mesh Size	Strain	Change (%)
3.5 mm	0.25	0.28%
	0.35	0.54%
	0.4	1.75%
4.5 mm	0.25	0.28%
	0.35	0.54%
	0.4	2%
5 mm	0.25	0%
	0.35	0%
	0.4	2%

The 0.134 Al foam exhibited good mesh stability overall, with stress changes remaining below 2% for most cases. However, the 4.5 mm and 5.0 mm meshes at 0.40 strain slightly exceeded this limit, indicating a small residual mesh sensitivity at the highest strain.

Results for 0.262 Al foam

The mesh convergence study for the 0.262 Al foam was conducted using mesh sizes of 5.0, 4.5, 3.5, and 2.5 mm. The 2.5 mm mesh was the finest converged mesh for this density, and the stress responses obtained from the coarser meshes were compared with this reference case to assess the effect of mesh refinement. The results of this study are illustrated below.

Table 3.4: Stress response of 0.262 Al foam at different mesh sizes

Mesh Size	Strain	Stress in MPa
2.5 mm	0.25	11.5
	0.45	15.9
	0.65	37.7
3.5 mm	0.25	11.61
	0.45	15.96
	0.65	38.4
4.5 mm	0.25	11.38
	0.45	15.73
	0.65	36.6
5 mm	0.25	11.43
	0.45	15.95
	0.65	37.1

Table 3.5: Percentage change in stress relative to the 2.5 mm mesh for 0.262 Al foam

Mesh Size	Strain	Stress in MPa
3.5 mm	0.25	0.95%
	0.45	0.37%
	0.65	1.80%
4.5 mm	0.25	1.04%
	0.45	1.07%
	0.65	2.91%
5 mm	0.25	0.61%
	0.45	0.31%
	0.65	1.59%

The 0.262 foam exhibited good mesh convergence, with all stress variations remaining below 3% of the 2.5 mm mesh. The largest difference occurred for the 4.5 mm mesh at 0.65 strain, whereas the 3.5 mm and 5.0 mm meshes remained close to the reference solution.

Results for 0.355 Al foam

The mesh convergence study for the Al foam, having relative density of 0.355, was conducted using mesh sizes of 5.0, 4.5, 3.5, and 3 mm. The 3 mm mesh was the finest converged mesh for this density, and the stress responses obtained from the coarser meshes were compared with this reference case to assess the effect of mesh refinement. The results of this study are illustrated below.

Table 3.6: Stress response of 0.355 Al foam at different mesh size

Mesh Size	Strain	Stress in MPa
3 mm	0.4	27.7
	0.5	37
	0.6	58.58
3.5 mm	0.4	27.44
	0.5	36.7
	0.6	58.42
4.5 mm	0.4	28.1
	0.5	36.5
	0.6	58.54
5 mm	0.4	27.5
	0.5	36.5
	0.6	58.14

Table 3.7: Percentage change in stress relative to the 3 mm mesh for 0.355 Al foam

Mesh Size	Strain	Stress in MPa
3.5 mm	0.4	0.94%
	0.5	0.81%
	0.6	0.27%
4.5 mm	0.4	1.44%
	0.5	1.35%
	0.6	0.07%
5 mm	0.4	0.72%
	0.5	1.35%
	0.6	0.75%

The 0.355 Al foam exhibited excellent mesh stability, with stress variations remaining below 1.5% relative to the 3 mm reference mesh. The 3.5, 4.5, and 5.0 mm meshes produced very similar stress responses across the strain range considered, indicating that the model response was largely insensitive to the mesh size.

Results for 0.439 Al foam

The mesh convergence study for the Al foam, with relative density of 0.439, was conducted using mesh sizes of 5.0, 4.5, 3.5, and 2.5 mm. The 2.5 mm mesh was the finest converged mesh for this density, and the stress responses obtained from the coarser meshes were compared with this reference case to assess the effect of mesh refinement. The results of this study are illustrated below.

Table 3.8: Stress response of 0.439 Al foam at different mesh size

Mesh Size	Strain	Stress in MPa
2.5 mm	0.16	28.12
	0.24	30.79
	0.36	35.88
3.5 mm	0.16	28.19
	0.24	30.5
	0.36	35.82
4.5 mm	0.16	28.2
	0.24	30.2
	0.36	35.74
5 mm	0.16	28.1
	0.24	30.5
	0.36	35.74

Table 3.9: Percentage change in stress relative to the 2.5 mm mesh for 0.439 Al foam

Mesh Size	Strain	Stress in MPa
3.5 mm	0.16	0.24%
	0.24	0.94%
	0.36	0.17%
4.5 mm	0.16	0.28%
	0.24	1.90%
	0.36	0.39%
5 mm	0.16	0.07%
	0.24	0.94%
	0.36	0.39%

The 0.439 Al foam also exhibited excellent mesh stability, with stress variations remaining below 2% relative to the 2.5 mm reference mesh. The 3.5, 4.5, and 5.0 mm meshes produced nearly identical stress responses across the strain range considered, indicating that the model response was largely insensitive to the mesh size. Overall, the mesh dependence for this foam density was negligible.

3.1.3.2 Summary of Numerical Reliability Studies

Overall, the numerical reliability assessment confirmed that the finite element model was stable and suitable for further validation. The energy balance showed negligible kinetic energy and a very small stabilization energy, whereas the artificial strain energy remained within acceptable limits for all foam densities. In addition, the mesh convergence studies demonstrated only minor stress variations across the tested mesh sizes, confirming that the model response was largely insensitive to mesh refinement within the considered range.

3.1.4. Results and discussions from Validation of Al Foams

Global response validation was performed by comparing simulated nominal stress–strain curves(σ_n-ε_n) against experimental data from Cheng et al. History Outputs RF(Total reaction force at RP) and U (displacement) were post processes as

Nominal Stress σ_n = RF/A0 (where A0 is 2500 mm^2, specimen cross sectional area)

Nominal Strain ε_n = U/L0 (where L0=50mm is initial height of the specimen)

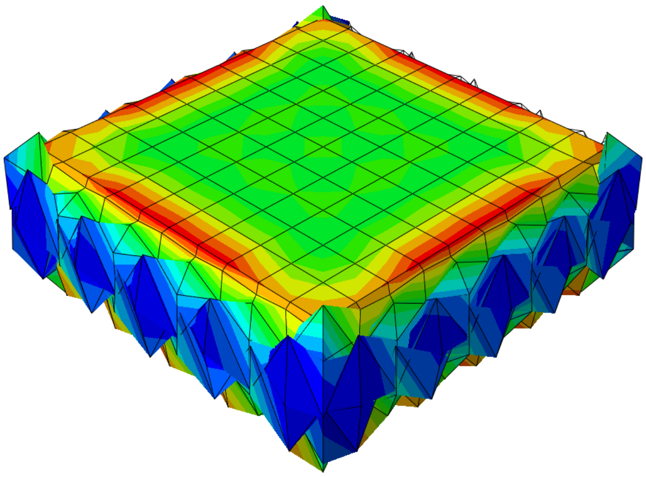

Figure 3.8: Representative Figure Showing Stress Contour on 0.217 Relative Density Al Foam

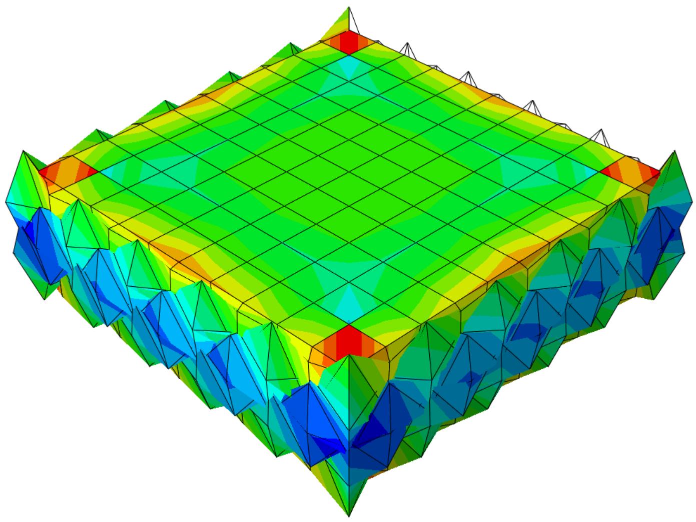

Figure 3.9: Representative Figure Showing Stress Contour on 0.308 Relative Density Al Foam

Figures 3.10 to 3.19 overlay all ten simulated σ_n-ε_n curves with their experimental counterparts, demonstrating acceptable agreement across the yield, plateau, and densification regimes.

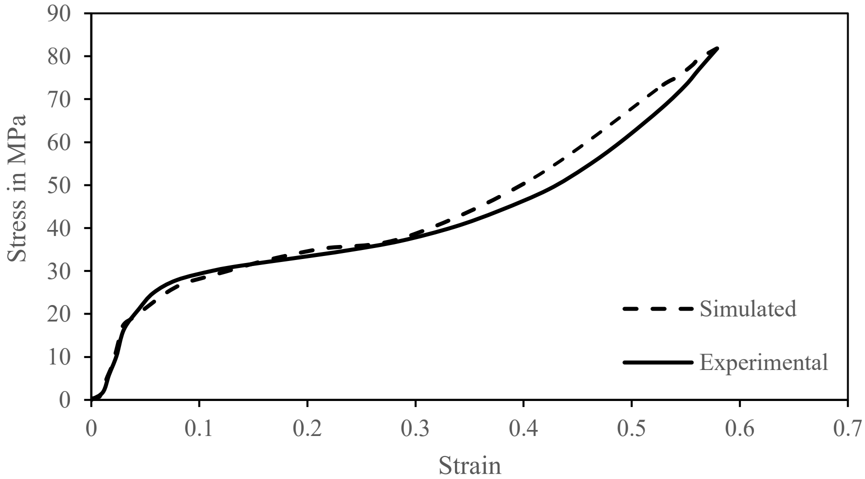

Figure 3.10: Experimental vs Simulated Stress Strain Curve for Al Foam of Relative Density 0.472

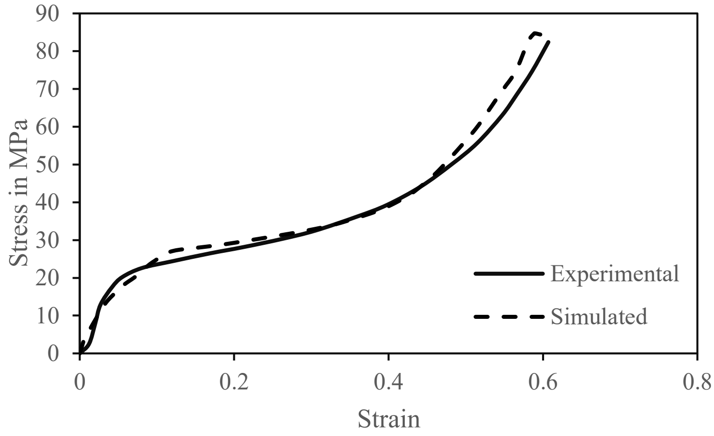

Figure 3.11: Experimental vs Simulated Stress Strain Curve for Al Foam of Relative Density 0.439

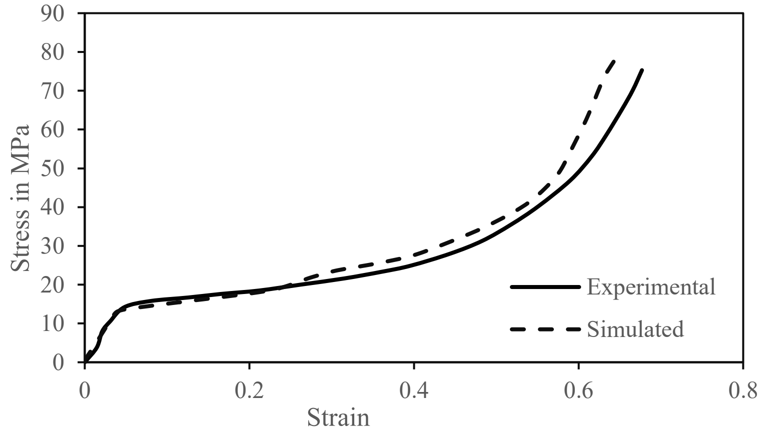

Figure 3.12: Experimental vs Simulated Stress Strain Curve for Al Foam of Relative Density 0.355

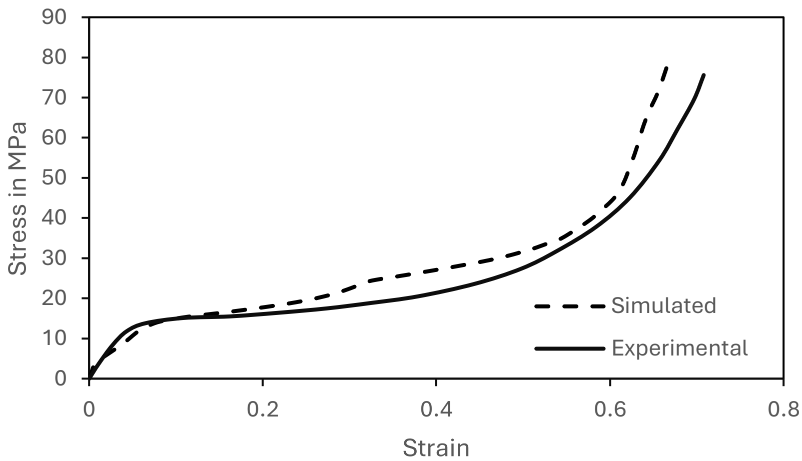

Figure 3.13: Expermental vs Simulated Stress Strain Curve for Al Foam of Relative Density 0.32

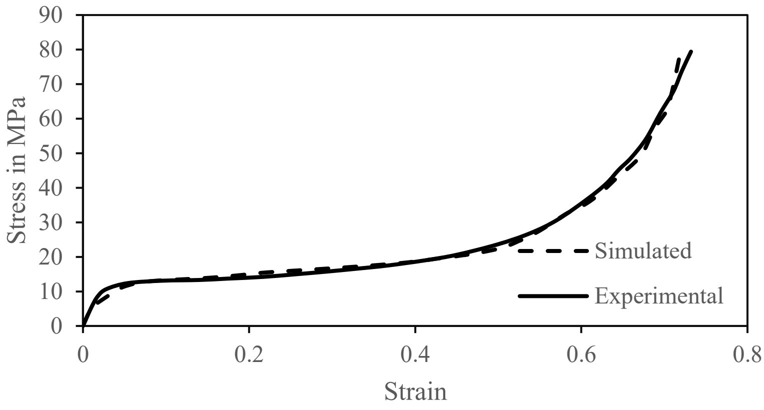

Figure 3.14: Experimental vs Simulated Stress Strain Curve for Al Foam of Relative Density 0.308

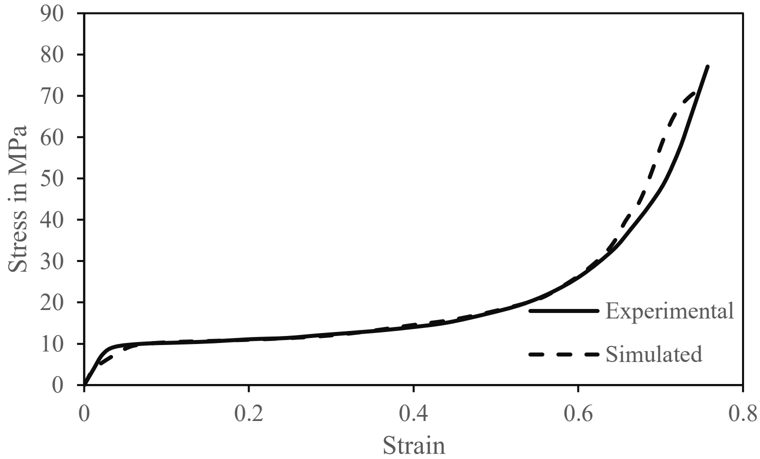

Figure 3.15: Experimental vs Simulated Stress Strain Curve for Al Foam of Relative Density 0.262

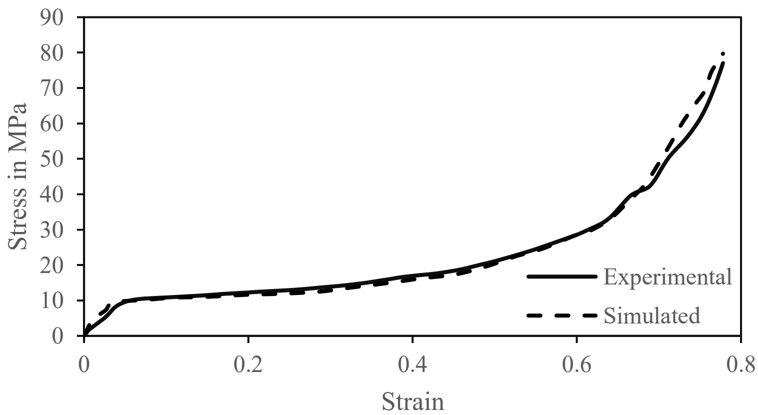

Figure 3.16: Experimental vs Simulated Stress Strain Curve for Al Foam of Relative Density 0.25

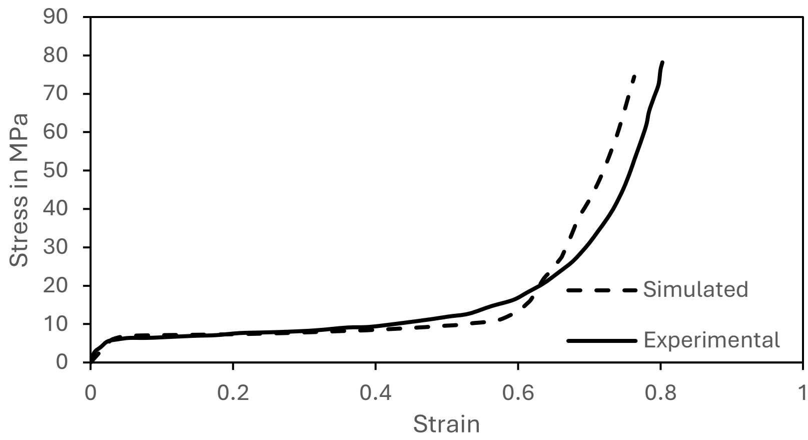

Figure 3.17: Experimental vs Simulated Stress Strain Curve for Al Foam of Relative Density 0.217

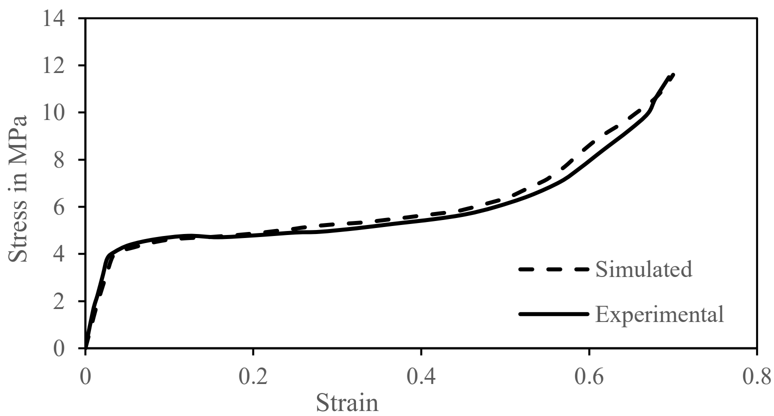

Figure 3.18: Experimental vs Simulated Stress Strain Curve for Al Foam of Relative Density 0.17

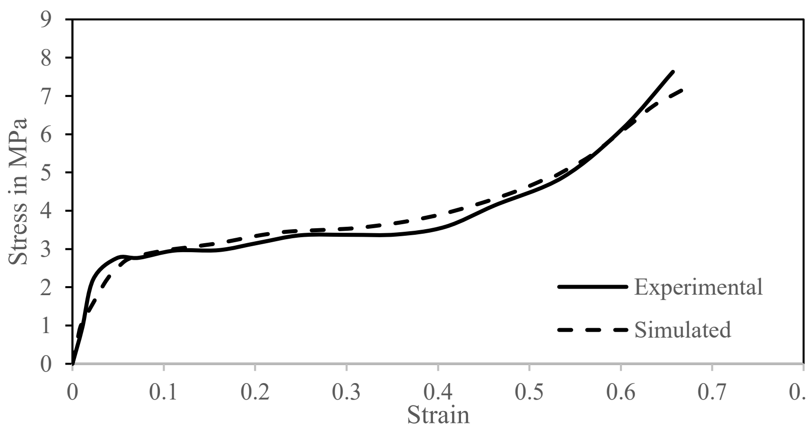

Figure 3.19: Experimental vs Simulated Stress Strain Curve for Al Foam of Relative Density 0.134

To complement the visual comparison presented in Figs. 3.10 to 3.19, a quantitative validation of the simulated and experimental nominal stress–strain responses was performed using three error metrics: root mean square error (RMSE), maximum absolute stress error, and plateau match percentage, and the results are shown in Table 3.1. The RMSE measures the overall deviation between the numerical and experimental curves over the strain range, whereas the maximum absolute stress error identifies the largest pointwise difference between the two responses. In addition, the plateau match percentage was evaluated to assess the accuracy with which the model reproduced the average stress level within the plateau region, which is a key characteristic of the compression behaviour of aluminium foam.

These metrics were obtained by comparing the simulated nominal stress values with the corresponding experimental values at the same nominal strain levels after the interpolation of the experimental curve. The RMSE was calculated over the full overlapping strain range of the numerical and experimental responses, whereas the maximum absolute stress error was determined from the largest local difference between the two curves. The plateau match percentage was calculated as the ratio of the average simulated plateau stress to the average experimental plateau stress over the selected plateau-strain interval. Accordingly, values close to 100% indicate excellent agreement, values above 100% indicate overprediction, and values below 100% indicate underprediction of the plateau response

Table 3.10: Quantitative Validation of Simulated and Experimental Nominal Stress–Strain Responses Using Error Metrics

Relative Density of Foam	RMSE Value in MPa	Max Error in MPa	Plateau %
0.134	1.91	4.91	103.79%
0.17	0.29	0.7	104.56%
0.217	5.5	21.73	85.03%
0.25	2.01	6.53	104.61%
0.262	2.57	11.2	100.42%
0.308	1.11	6.57	98.11%
0.32	4.64	20.24	113.07%
0.355	5.35	19.82	108.88%
0.439	3.42	9.59	105.19%
0.472	1.43	5.08	103.65%

In general, the model showed good predictive capability, with RMSE values ranging from 0.29 to 5.50 MPa, and plateau match values mostly close to 100%. The lowest RMSE was obtained for foam with a relative density of 0.17, whereas the highest RMSE occurred for foam with a relative density of 0.217. The plateau response was captured well for most densities, although the foam with a relative density of 0.217 showed a lower plateau match of 85.03%, indicating some underprediction in the plateau region. Overall, the results confirm that the calibrated crushable foam model reproduces the experimental response with acceptable accuracy over the entire compression range.

3.2 Validation of Aluminum Plate

The material properties of the aluminium sheet used in the validation model were adopted from the experimental study of Roh et al. [4], who investigated the tensile behaviour of the 5052-H32 aluminium alloy under pulsed electric current. In their study, a baseline tensile test was first conducted without the influence of electric current to establish the reference mechanical response of the material. Therefore, the present work uses the material properties corresponding to this baseline condition, that is, the response free from electroplastic effects. The specimens were fabricated from a 2 mm-thick aluminium sheet, with a 9 mm gauge width and a 50 mm gauge length. Uniaxial tension was applied in a universal testing machine by gripping the specimen at both ends and imposing a controlled axial displacement rate while recording the corresponding force and displacement histories to obtain the engineering stress–strain curve reported in the paper.

3.2.1 Calibration of Material Model

The baseline tensile response of the 5052-H32 aluminium alloy, reported without the influence of electric current, was used as the reference for calibration. The baseline engineering stress–strain curve was digitized using 'Web Plot Digitizer' to extract the corresponding engineering stress and strain data points, and the elastic constants were taken as $E = 70.3$ GPa and $\nu = 0.33$, consistent with the standard 5052-H32 material data. The engineering strain values, originally reported in percentage, were first converted into decimal fractions. The resulting engineering stress–strain data were then transformed into true stress, true strain, elastic true strain, and uniaxial plastic strain using the appropriate relations. The true stress–plastic strain pairs up to the maximum point of the curve, prior to the onset of failure, were used as inputs for the plastic material table in Abaqus. Unlike the crushable foam calibration, the aluminium plate material could be represented directly through a conventional elastoplastic formulation using the derived true stress and uniaxial plastic strain data.

3.2.3 Finite Element Modelling

A finite element model of the aluminium tensile specimen was developed in Abaqus 2024 as a three-dimensional solid model. The specimen was discretized using C3D8R elements, which are eight-node linear brick elements with reduced integration and are suitable for simulating the deformation response of the plate under uniaxial tension. The tensile analysis was performed using a static step, and the left end of the specimen was fully fixed in all degrees of freedom, whereas the opposite end was loaded by applying a prescribed displacement in the axial direction at the reference point.

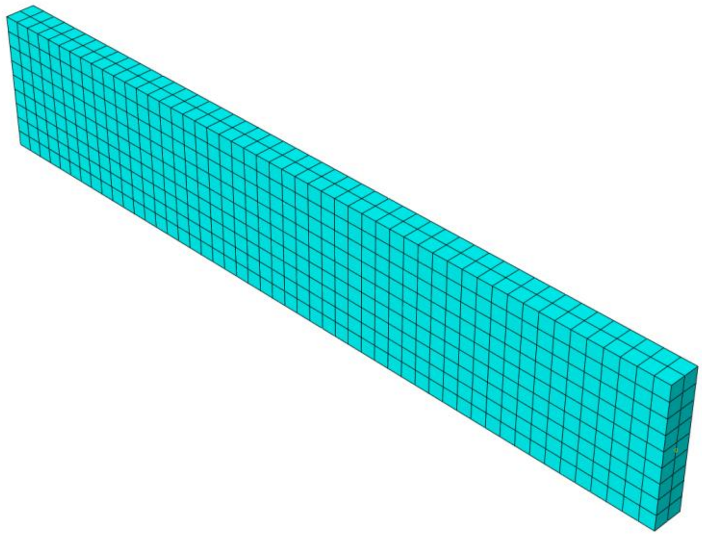

Figure 3.20: Figure showing mesh on Al Plate

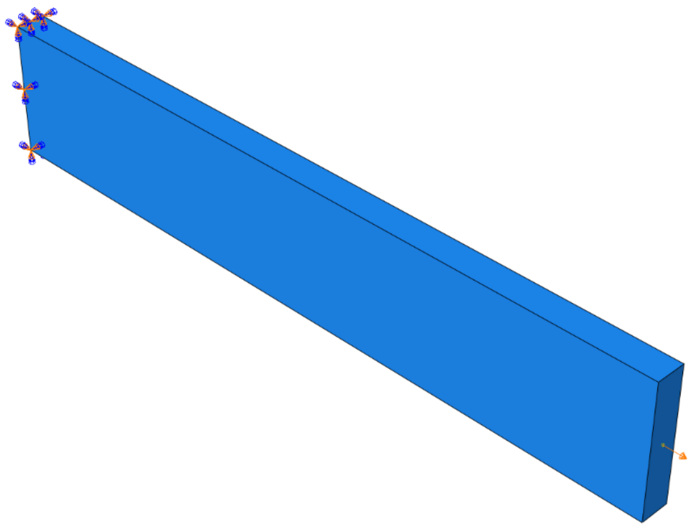

Figure 3.21: Loading and Boundary Conditions

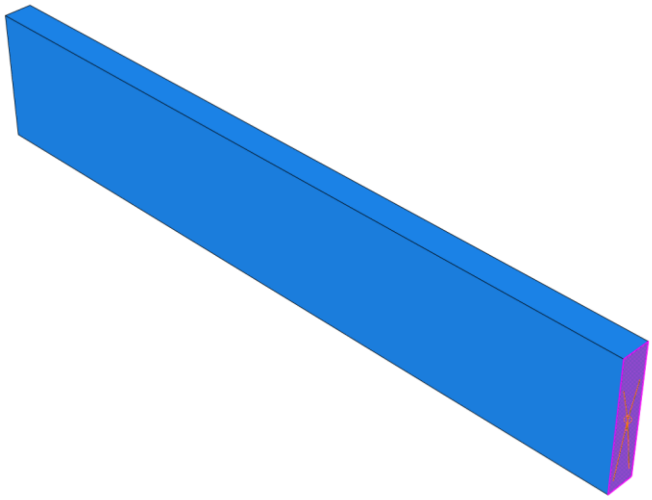

Figure 3.22: Kinematic Coupling on Right Edge

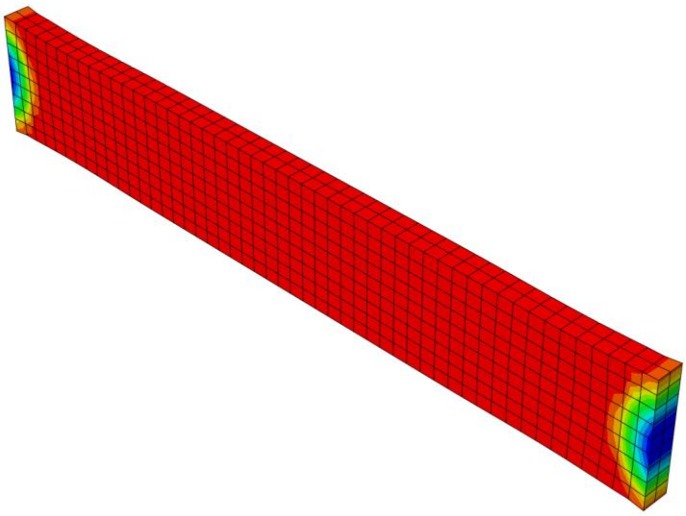

Figure 3.23: Stress Contours on Al Plate

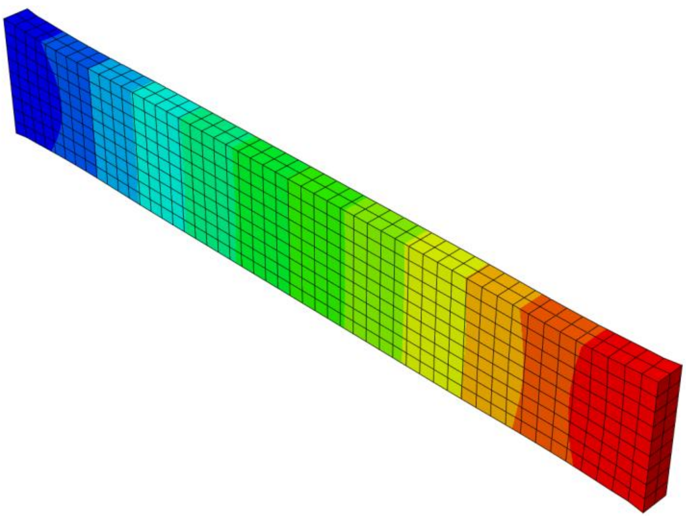

Figure 3.24: Deformation Contours on Al Plate

3.2.4 Results and Discussions

The global stress–strain response was extracted from the history output at the reference point. The reaction force was divided by the specimen cross-sectional area of 9 mm × 2 mm to obtain the stress, whereas the displacement was normalized by the original gauge length of 50 mm to obtain the engineering strain. The resulting simulated stress–strain curve was then compared with the experimental curve, as shown in Fig 3.24.

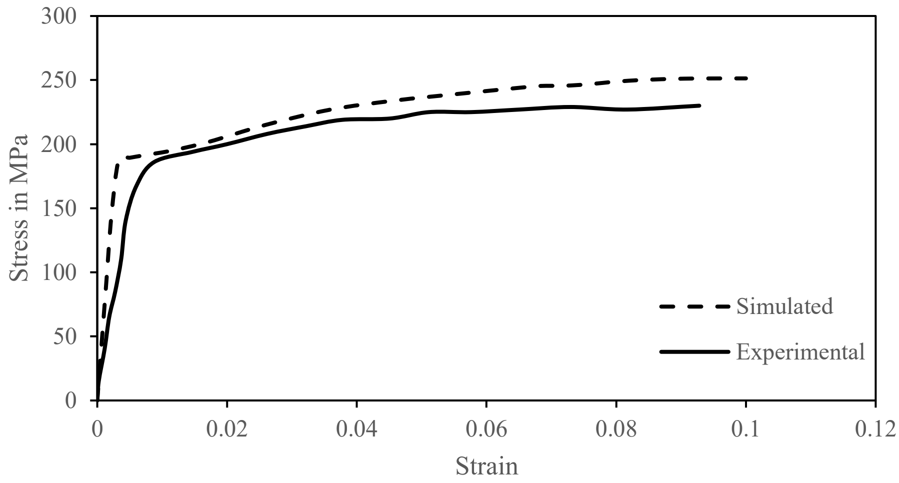

Figure 3.25: Experimental vs. simulated stress-strain curve for Al plate.

The simulated response obtained using a Young's modulus of 70 GPa showed good agreement with the experimental curve in the plastic region, whereas the initial linear segment exhibited a noticeable deviation. Since the initial part of the tensile response is governed primarily by the elastic modulus and Poisson's ratio, this discrepancy indicates that the elastic stiffness represented by the experimental initial slope was lower than the standard value for 5052-H32 aluminium. Therefore, a second analysis was performed using an apparent modulus of 33 GPa extracted from the initial linear portion of the experimental data, and this modified model showed improved overall agreement with the experimental stress–strain response. The comparison graph showing the Abaqus tensile test results for $E = 33$ GPa and $E = 70$ GPa, together with the experimental curve, is presented in Fig 3.25.

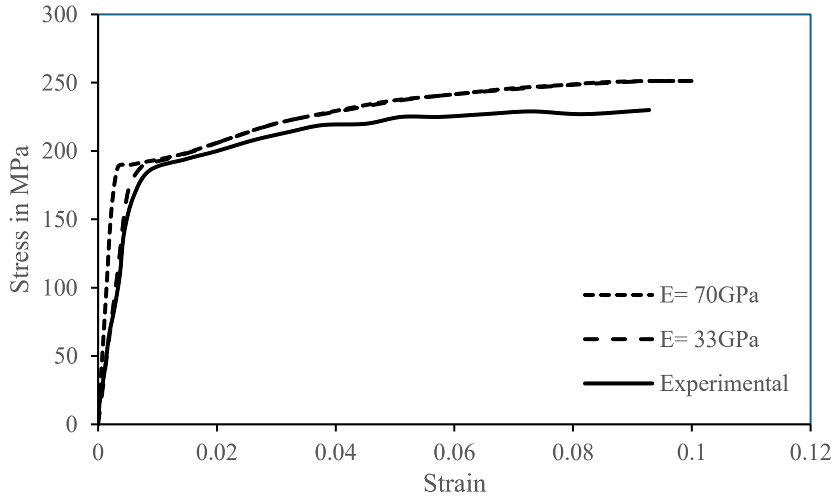

Figure 3.26: Experimental and simulated curves for Al plate with E = 33 GPa and E = 70GPa.

The comparison of the simulated and experimental stress–strain curves shows that both Abaqus analyses, using $E = 33$ GPa and $E = 70$ GPa, reproduce the plastic response almost identically, with the two numerical curves remaining nearly coincident with the experimental data in the post-yield region. The principal difference between the two simulations was confined to the initial linear segment, where the 70 GPa model predicted a steeper elastic response than the experimental curve. Since the initial linear region is governed primarily by the elastic modulus, this discrepancy suggests that the mismatch is associated with the effective elastic response captured during testing rather than the plastic material behaviour. The improved agreement obtained with $E = 33$ GPa indicates that the experimentally measured initial slope was influenced by compliance effects during testing, such as machine seating or grip compliance, which commonly affect small-displacement tensile data. However, because 5052-H32 aluminium is commonly reported to have a Young's modulus of approximately 70 GPa, this standard value was adopted in the final model. The 33 GPa value is therefore interpreted as an apparent calibration modulus derived from the experimental initial slope and was used only for sensitivity assessment, not as the final material property.

3.3 Summary

This chapter presented the validation of the finite element models used in this study. The foam models were first compared with the experimental compression results. The results showed that the numerical simulations could reproduce the overall deformation trend, collapse behaviour, and stress plateau with reasonable accuracy. The aluminium plate model was then validated against the tensile test response reported in the reference study. The comparison showed that the model with the standard Young's modulus captured the plastic response well, whereas the alternative lower-modulus case improved the fit in the initial elastic region. Overall, the validation results demonstrate that the finite element modelling approach is capable of representing the key mechanical behaviour of both the foam sandwich structures and the aluminium plate, and therefore provides a reliable basis for the parametric studies presented in the following chapters.

Chapter 4

Material Calibration and Benchmark Comparison for Aluminium Foam Sandwich Panels

This chapter assesses the finite element model of the aluminium foam sandwich panel under in-plane axial compression through a benchmark comparison with the analytical effective width method proposed by Szyniszewski et al.[2] for steel foam sandwich panels. This method is used here only as a comparative reference, not as the theoretical basis of the thesis. The purpose of this comparison was to determine whether the developed numerical model reproduces a realistic compressive collapse response for aluminium foam sandwich panels.

A direct experimental database for in-plane axial compression of aluminium foam sandwich panels is limited in the published literature. In contrast, the available literature contains more studies on FRP foam sandwiches and out-of-plane loading, whereas only a small number of papers address the in-plane collapse of metallic foam sandwich panels. Therefore, the Schafer/Winter-type effective-width method was selected as a practical reference for material calibration and benchmark comparison. This method provides a useful comparison because it captures the same general structural mechanism relevant to this study: local buckling, effective load-carrying width, and post-buckling strength reduction.

Although the original method was developed for steel foam sandwich panels, it is still relevant here because the present aluminium foam sandwich is governed by the same fundamental mechanisms: face-sheet compression, foam-core support, shear deformation in the core, and imperfectly stable post-buckling response. The material system are different, but their structural mechanics are similar. Therefore, the method was used as a comparative benchmark to test whether the aluminium foam sandwich model behaved in a physically consistent manner, rather than as a universal design rule for all foam sandwiches.

The predicted axial load-carrying capacity was compared with the Abaqus reaction force result, and the deformation and stress patterns were examined against the characteristic response reported in the reference study. This comparison was used as a benchmark-based assessment of the aluminium foam sandwich model and to confirm that it captured the essential structural response required for subsequent analysis.

4.1 Modelling of Aluminium Foam sandwich

An aluminium foam sandwich panel with a length of 500 mm and width of 50 mm was modelled in Abaqus. The material properties of the aluminium foam and face sheets were obtained from previously validated material models. The foam core thickness was 10 mm, and each aluminium face sheet was 2 mm thick, resulting in a total panel thickness of 14 mm.

The finite element model consisted of a 10 mm aluminium foam core bonded between two 2 mm aluminium face sheets. The foam core was modelled using a crushable foam material model with isotropic hardening calibrated from experimental data, whereas the face sheets were modelled using an elastoplastic aluminium material model with multilinear isotropic hardening. The analysis was carried out in two stages: first, a linear eigenvalue buckling analysis was used to extract the first buckling mode shape; second, a nonlinear static Riks analysis was performed to simulate the imperfection-sensitive post-buckling collapse response of the structure.

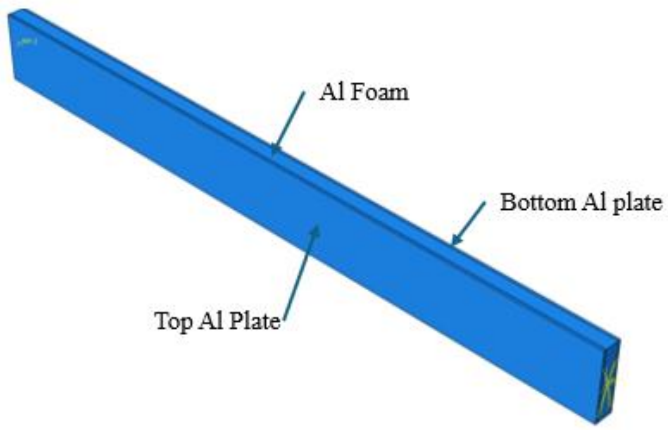

Figure 4.1: Aluminium Foam Sandwich model

4.1.1 Element Type

The model was discretized using 3D 8 node linear brick elements with reduced integration and hourglass control (C3D8R). This element type is suitable for geometrically nonlinear problems involving large deformations, contact, and material nonlinearity. It also reduces the risks of shear and volumetric locking.

4.1.2 Meshing

A structured hexahedral mesh was used across the panel dimensions of 500 mm x 50 mm. A total of 379 and 19 elements were used along the length and width, respectively.. Through the thickness, three elements were assigned to each 2 mm face sheet and 15 elements to the 10 mm foam core. This mesh refinement was selected to capture the through-thickness stress gradients, face-sheet wrinkling, and core crushing while maintaining computational efficiency.

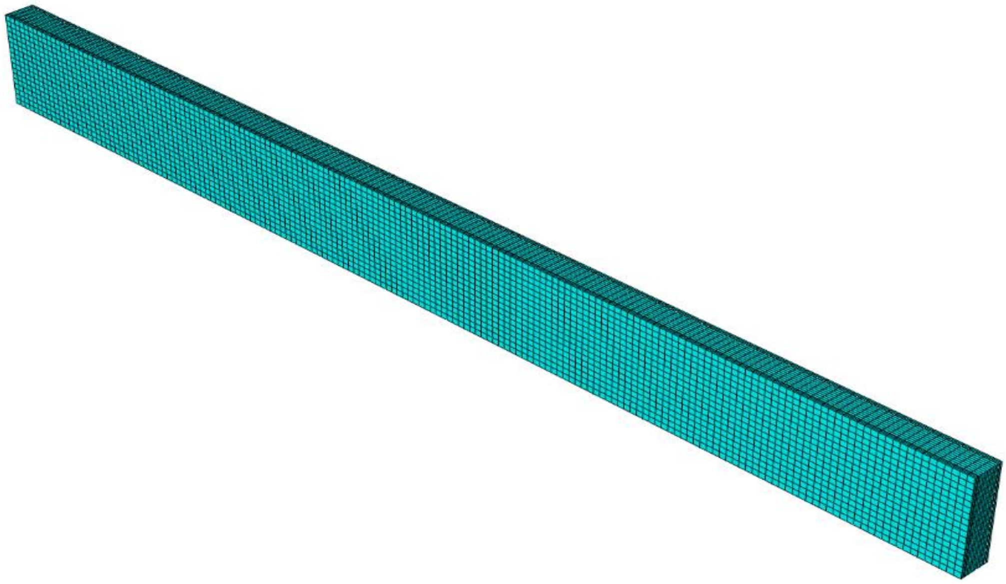

Figure 4..2: Mesh on Al Foams sandwich

4.1.3 Bonding between Foan core and Face sheets

The foam core and face sheets were connected using tie constraints, which enforced perfect bonding at the interface. This idealization ensures continuous load transfer through the sandwich thickness by preventing prevents relative sliding or separation between the core and skins

4.1.4 Loading and Boundary conditions

The buckling step included the necessary boundary conditions at the reference points and control nodes, and the collapse step was performed as a nonlinear static analysis with a displacement control. The load was applied through a reference point coupled to the loading surface using kinematic coupling, and a prescribed axial displacement was imposed to compress the panels. This approach is appropriate for capturing collapse and post-buckling behaviour

4.1.5 Introduction of Imperfection

A geometric imperfection was introduced using the first buckling-mode shape. In the reference steel foam sandwich study, imperfection amplitudes of 0.1t and 0.34t were considered, corresponding to approximately 0.237 mm and 0.796 mm for that panel. However, the present aluminium foam sandwich panel has a much thicker foam core; therefore, a normalized imperfection of the same magnitude would not have the same physical meaning. For this reason, a series of smaller imperfection amplitudes, starting from 0.1 mm, was applied in the finite element analysis to evaluate the load-carrying capacity and imperfection sensitivity of the panel

4.2. Analytical Benchmark Calculation Using the Schafer/Winter Effective-Width Method

The axial compressive capacity of the aluminium foam sandwich panel was estimated using the analytical method proposed by Szyniszewski et al. for steel foam sandwich panels. In this study, the method was used only as an analytical benchmark to assess whether the finite element model produced a realistic compressive response. The calculation was carried out for an equivalent sandwich section, using the total panel thickness t and an equivalent yield stress f_{yp}, rather than as a face-sheet-only design check. The material properties used in the calculation were obtained from previously validated foam and face-sheet models. The panel geometry considered in this calculation had a length of 500 mm, a width of 50 mm, a 10 mm aluminium foam core, and two 2 mm aluminium face sheets. The material properties used are as follows

Poisson's ratio of aluminium foam used $\mu_f = 0.33$

Poisson's ratio of aluminium plate used $\mu_s = 0.33$

Modulus of Elasticity of aluminium foam $E_f = 817$ MPa

Modulus of Elasticity of Al plate $E_s = 70000$ MPa

Yield stress of Al foam $f_{yf}= 15$ Mpa

Yield stress of Al $f_{ys} = 187$ MPa

Thickness of Al plate used $t_s = 2$ mm each

Thickness of Al foam used $t_f = 10$ mm

Length of aluminium foam sandwich panel, a= 500mm

Width of sandwich panel b= 50 mm

The shear modulus of the foam can be calculated as

$$G = \frac{E}{2(1+\mu)} = \frac{817}{2(1+0.33)} = 307.14 \text{ MPa}$$

Calculation of Plate Bending Rigidity

Following Allen's approach, the plate bending rigidity is simplified by accounting for the bending contribution of the face sheets and incorporating the remaining effects into the buckling coefficient k. The modified bending rigidity is calculated as follows:

$$D_P = \frac{E_S\ t_s\,(t_c+t_s)^2}{2(1-\mu_s{}^2)} = \frac{70000\ x\ 2\ x(\,(10+2)^2)}{2(1-(0.33^2))} = \frac{20160000}{1.78} = 11311861.74 \text{ Nmm}$$

Calculation of shear factor r

The shear deformation factor r, which accounts for shear deformation in the foam core, is given by

$$r = \frac{\Pi^2\ E_s\ t_s\ t_c}{2(1-\mu_c^2)G_c\ b^2} = \frac{(3.14^2)x\ 70000\ x\ 2\ x\ 10}{2(1-0.33^2)x\ 307.14x(50^2)} = 10.086$$

Calculation of m and n values

The parameter x_{min} is the aspect ratio at which the plate buckling coefficient reaches its minimum for a given mode number m and shear parameter r. The reference paper provides a graphical estimate of x_{min}(Figure 4.3). Since the present sandwich panel provides a higher value of r than the range shown directly in the published graph, the figure was used as an approximate interpolation tool for this benchmark calculation.

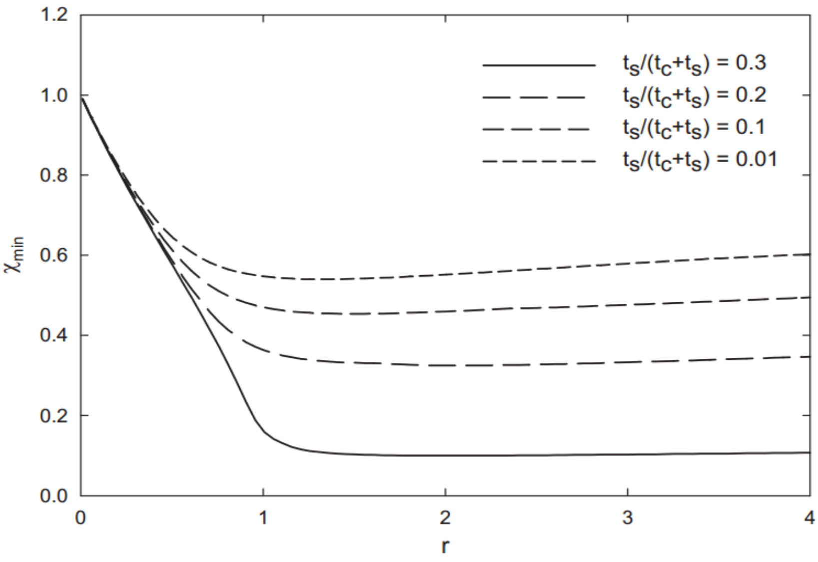

Fig. 6. Graphical representation of closed-form solution for χ_{min}.

Figure 4.3: Graph given in paper S Szyniszewski et al. [2] for finding values of x_{min}

For the present case, x_{min} was taken as 0.39 corresponds to $t_s/(t_c+t_s) = 2/(10+2) = 0.167$

Because the present geometry lies outside the exact range covered by the published graph, $X_{\min}$ was estimated by extrapolating from the nearest available trend. A sensitivity check was then performed at the end of this section to assess the influence of this extrapolation on the final predicted compressive strength

Therefore,

$$m = \frac{a/b}{Xmin} = \frac{500/50}{0.39} = 25$$

The longitudinal half-wave number is expressed as

$$n = 1$$

This indicates that the panel is expected to buckle with approximately 25 transverse waves and one longitudinal wave under axial compression.

Calculation for buckling coefficient, k

From the journal, for a simply supported plate of length a, width b, uniformly compressed on the sides with width b, the plate buckling coefficient 'k' of Allen, including shear deformation is as follows,

$$k = \left(\frac{mb}{a} + \frac{n^2 a}{mb}\right)^2 \left\{\frac{1}{1+r\left(\frac{m^2 b^2}{a^2}+n^2\right)} + \frac{t_s^2}{3(t_c+t_s)^2}\right\}$$

$\frac{mb}{a} + \frac{(n^2)xa}{m\,x\,b} = \frac{25\,x\,50}{500} + \frac{1x1x500}{25\,x\,50}$ =2.5+0.4 = 2.9

$1/(1+r(m^2b^2/a^2+n^2)) = \frac{1}{1+10.086(\frac{25x25x50x50}{(500\,x\,500)}+(1x1))}$ = 0.01349

$t_s^2/3(t_c+t_s)^2 = \frac{2^\wedge 2}{3((10+2)^2)}$ = 0.0093

Therefore k = 2.9^2 x (0.01349 + 0.0093) = 0.19166

Calculation of in plane elastic local plate buckling stress f_{cr}

The in-plane elastic local plate buckling stress is calculated using Eq. 8 from the reference paper,

$$f_{cr} = k\frac{\Pi^2 D_P}{b^2(t_c+2t_s)} = \frac{0.19166\,x\,(\pi^2)\,x\,11311861.74}{(50^2)(10+(2x2))} = 610.74 \text{ N /mm}^2$$

Calculation of equivalent yield stress for the sandwich panel, f_{yp}

The equivalent yield stress for the sandwich panel can be found out by equation 19 in the reference paper

$$f_{yp} = \frac{2t_s f_{ys} + t_c * \min\left(f_{yc}, E_c\left(\frac{f_{ys}}{E_s}\right)\right)}{2t_s + t_c}$$

$E_c(f_{ys}/E_s)$ = 817(187/70000)=2.18 <f_{yf} ,(15)

Therefore,

$$f_{yp} = \frac{(2\,x\,2\,x\,187)+(10x2.18)}{(2x2)+10} = 54.98 \text{ N /mm}^2$$

Effective width calculations

According to equation (21) of the paper Szyniszewski et al. [2] the effective width(b_e) of the panel in carrying the maximum stress is given by

$$b_e = b \text{ if } f_{cr} \geq 2.2f_y \text{ and}$$

$$b_e = b(1-0.22\sqrt{(f_{cr}/f_y)})\sqrt{(fcr/fy)} \text{ if } f_{cr} < 2.2f_y$$

From above, f_{cr} (610.74) > $2.2f_{yp}$ (2.2 x 54.98 =120.956), which means that local elastic buckling does not govern the response prior to yielding. Accordingly, the entire panel width was considered effective, and the effective width was taken as $b_e = b$ in evaluating the axial compressive capacity.

Therefore, $b_e = b = 50$ mm

Calculation of Axial Compressive Strength

The predicted axial compressive strength of the panel is given by equation 22,

$$P_n = b_e t f_y$$

f_y is replaced by f_{yp} and t is the total thickness of the sandwich panel.

$$P_n = 50\text{x } 14 \text{ x } 54.98 = 38430 \text{ N} = 38.4 \text{ kN}$$

The predicted Axial Compressive Strength of Aluminium Foam Sandwich Panel is 38.4 kN

This result was used only as a benchmark prediction for comparison with the Abaqus collapse load. The calculation is not intended to claim that the Schafer/Winter method is the primary design basis of this study, but rather to provide a reasonable reference for assessing the numerical mode.

Sensitivity Check

Because the published Schafer/Winter graph does not extend to the calculated shear deformation ratio range and the present sandwich geometry also lies outside the exact thickness ratio range shown in the figure, $X_{\min}$ was estimated using the closest available trend. To assess the influence of this extrapolation, a sensitivity check was performed by varying $X_{\min}$ within a reasonable range around the baseline estimate

A sensitivity check was performed by varying the estimated $X_{\min}$ within a reasonable bracket around the baseline value. Although the assumed $X_{\min}$ changed the calculated mode number m, buckling coefficient k, and critical stress f_{cr}, the resulting effective width remained unchanged and the predicted axial capacity P_n was constant at 38.4 kN. This indicates that the final outcome is not sensitive to the exact extrapolated value of $X_{\min}$ in the selected range. The results of the sensitivity checks are presented in Table 4.1.

Table 4.1: Effect of variation in the estimated $X_{\min}$ on mode number, buckling coefficient, critical stress, effective width, and axial capacity

	$X_{\min}$	m	k	f_{cr} in N/mm^2	Effective Width	P_n in kN
Baseline	0.39	25	0.1916	610.74	be=b	38.4
Upper Bound	0.43	23	0.1855	591.711	be=b	38.4
Lower Bound	0.35	29	0.207	660.292	be=b	38.4

4.3. Comparison of Analytical and Abaqus Results

The aluminium foam sandwich model was assessed by comparing of the analytical benchmark prediction with the Abaqus results. The reference study by Szyniszewski et al. [2] used the modified effective-width method to predict the axial compressive capacity of steel foam sandwich panels and verified the formulation using finite element analysis. In that study, geometric imperfections of 0.1t and 0.34t were introduced for a much thinner panel than that considered in the present work.

The present aluminium foam sandwich panel had a total thickness of 14 mm, whereas the reference panel had a total thickness of only 2.37 mm. Therefore, directly transferring the same normalized imperfection magnitudes to the present model is inappropriate. For this reason, a series of smaller imperfection amplitudes was applied, starting from 0.1 mm, to evaluate the imperfection sensitivity of the panel. The corresponding peak reaction forces varied with the imperfection amplitude while remaining in a similar overall range, indicating that the model captured the expected collapse behaviour. The Peak Reaction Force obtained over range of imperfections are listed in the Table 4.2 below

Table 4.2: Peak Reaction Force obtained Corresponding to various Imperfections

Imperfection Amplitude (mm)	Peak Reaction Force Obtained in kN
0.15	38.7
0.2	39.4
0.4	38.7
0.45	39
0.5	38.6

The representative RF-U curve obtained for 0.15 mm and 0.5mm are shown in Fig 4.4 and Fig 4.5. The force–displacement curve for the 0.15 mm imperfection showed a clear peak followed by post-buckling softening, which is characteristic of compressive collapse in sandwich structures. For larger imperfection amplitudes, the response becomes more abrupt, with a steeper load rise and a sudden collapse after the peak. This difference indicates that the imperfection magnitude influences the collapse mode, even when the peak load remains similar. Therefore, the influence of the imperfection amplitude is an important factor in the present study, and this effect is examined in more detail later for different relative densities.

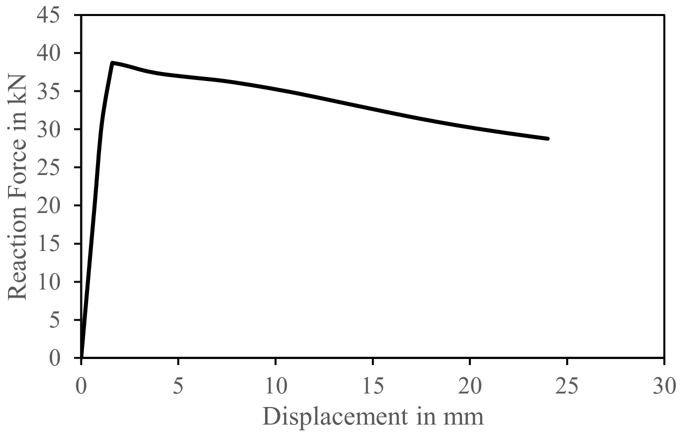

Figure 4.4: Force-displacement graph obtained from Abaqus corresponding to 0.15 mm imperfection

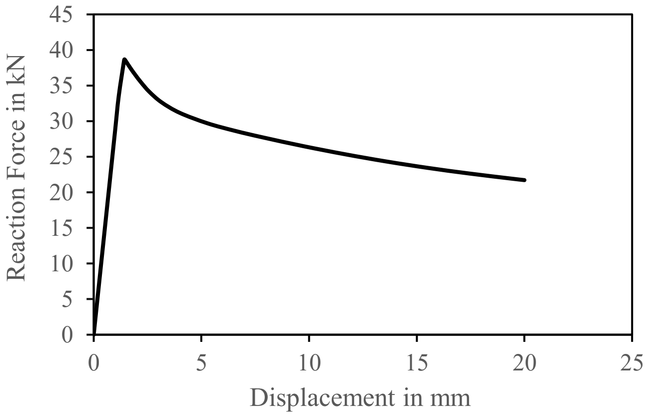

Figure 4.5: Force-displacement graph obtained from Abaqus corresponding to 0.5 mm imperfection

4.4 Qualitative analysis of collapse response and stress distribution

The stress distribution pattern across the width of the aluminium foam sandwich panel under axial compression was compared with the stress distribution reported by Szyniszewski et al., and the results are shown in Fig. 4.7 (a) and (b).

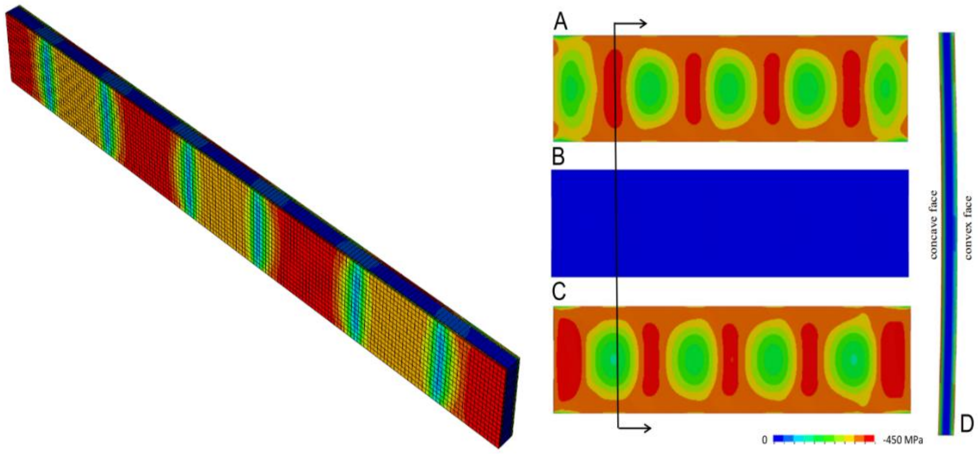

(a) **(b)**

Figure 4.6: (a) stress distribution pattern obtained from Abaqus and (b) shows the stress distribution pattern given in the literature paper S Szyniszewski et al. [2]

The comparison indicates that the stress distribution pattern is reproduced reasonably well. To provide additional support for the benchmark comparison, the von Mises stress contours across the concave face sheet, foam core, and convex face sheet are shown in Fig. 4.7. This Von Mises stress distribution plot was compared with the actual stress distribution plot reported by Szyniszewski et al., as given in Fig. 4.8.

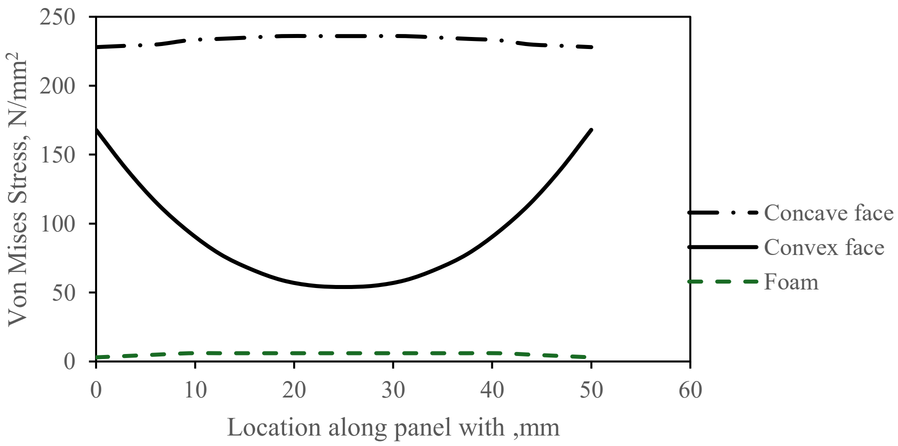

Figure 4.7: Von mises stress distribution across concave face, convex face and foam from aluminium foam sandwich panel

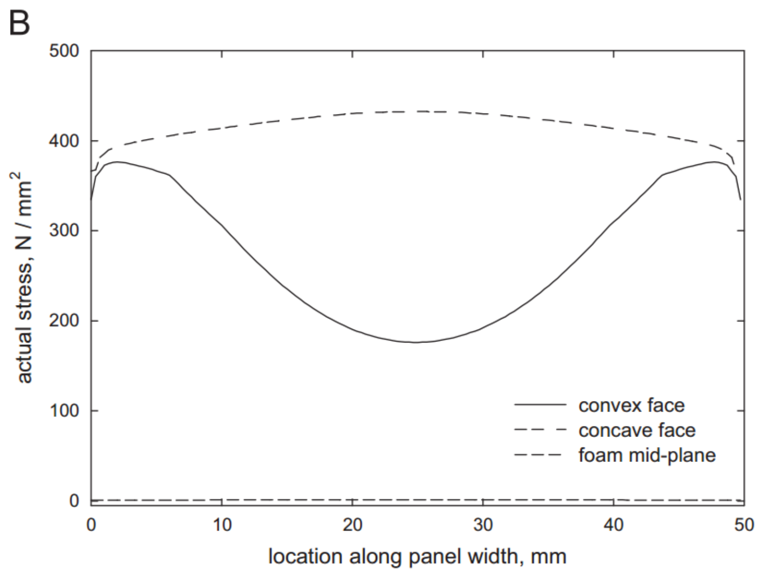

Figure 4.8: Actual stress distribution across concave face, convex face and foam from Steel foam sandwich panel from S Szyniszewski et al. [2]

From Fig. 4.8, most of the axial load is carried by the face sheets, while the foam core remains comparatively lightly stressed. The present Abaqus results show the same general trend, with higher stress concentration in the face sheets and lower stress levels in the foam core. It should be noted that von Mises stress is an equivalent stress measure and does not represent the full stress tensor; therefore, this comparison is made only in a qualitative sense.

The deformation patterns for the 14 mm-thick sandwich panel with small imperfection amplitudes of 0.10 mm and 0.15 mm are shown in Fig. 4.9. The results exhibit a multi-wave-like buckling response, indicating a progressive instability mode under compression. Although no directly comparable experimental axial-compression study on a pure metal-foam sandwich panel was identified, relevant experimental data were found for sandwich panels with honeycomb, polymer, or FRP cores. Caiqi Zhao et al. [46] reported axial-compression tests on an aluminium honeycomb sandwich panel under similar loading and boundary conditions. The panel thickness in that study was 15 mm, which is close to the 14 mm thickness considered in the present work, and the specimen exhibited a small wave-like deformation pattern which is shown in Figure 4.10. This pattern is similar to the predicted FE deformation response (Fig 4.9). Even though, the core material differs, this comparison provides qualitative evidence that the deformation mode obtained in the present model is physically plausible.

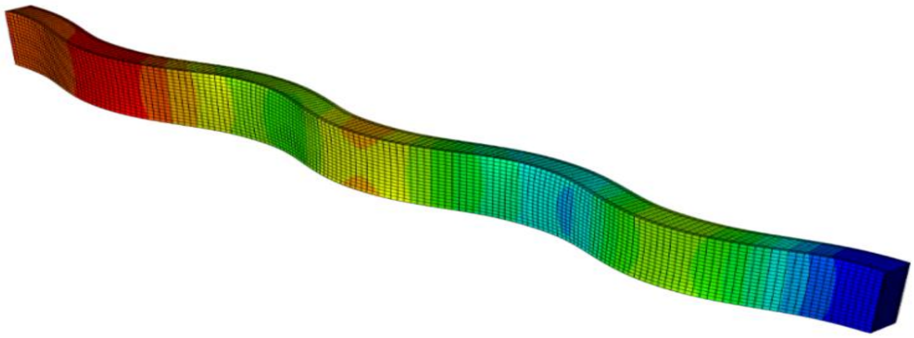

Figure 4.9: FEA deformation pattern of the foam sandwich

Figure 4.10: Experimental deformation pattern of honeycomb sandwich panel under axial compression showing wave-like buckling and local folding from Caiqi Zhao et al. [46]

Overall, the analytical benchmark prediction, Abaqus peak response, deformation pattern, and stress distribution showed reasonable agreement. These comparisons indicate that the finite element model captures the essential response of the selected case, while recognizing that the analytical method is used here only as a benchmark and not as the primary basis of this study.

4.5. Comparison of Analytical and Buckling Mode Shapes

This subsection examines the first buckling mode shape of the $\rho^* = 0.439$ aluminium foam sandwich panel to verify that the finite element model reproduces the correct global instability mechanism, in addition to the peak compressive load and stress distribution. Because the analytical effective-width method was used in this chapter only as a benchmark for the representative high-density configuration, the mode shape comparison was also performed for the same case to provide an additional check on the physical realism of the numerical model.

A comparison was made between the first eigenvalue buckling mode obtained from Abaqus and the corresponding analytical global buckling profile. The Abaqus mode shape was extracted from the linear buckling analysis and plotted along the panel length. The analytical profile was then normalized to the same displacement scale so that the two curves could be compared directly on the same graph, as shown in Figure 4.10. This approach allows the governing deformation pattern predicted by the finite element model to be assessed against an idealized theoretical response.

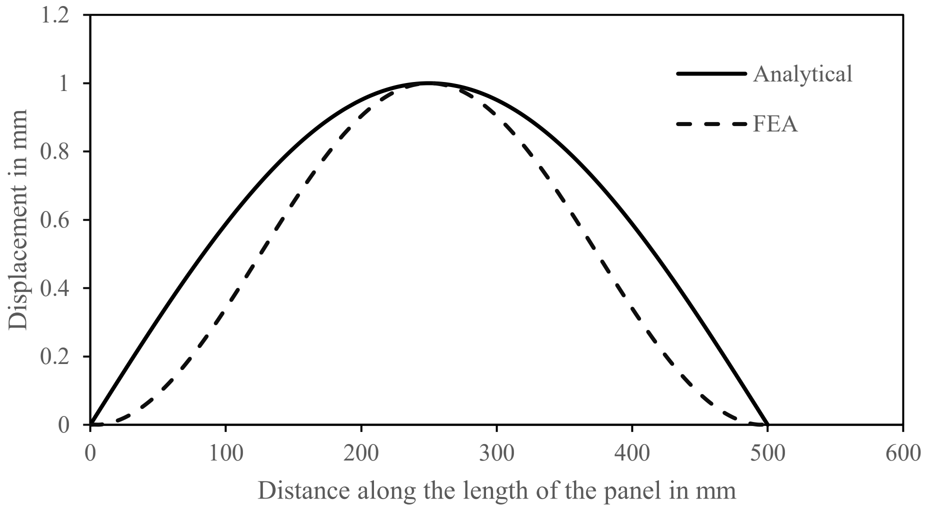

Figure 4.11: Comparison of analytical and FEA buckling mode shape

The comparison shows that both curves follow the same overall single-half-wave deformation shape, confirming that the numerical model captures the expected global-buckling mode. The agreement between the two curves shows that the finite element model can capture the correct instability mechanism of the sandwich panel under in-plane compression. Small differences in local curvature are expected, since the analytical profile is idealised, whereas the numerical result reflects the specific boundary conditions, coupling constraints, and discretised geometry used in the model

This mode shape agreement complements the peak load comparison presented earlier. Together, these two checks confirm not only that the finite element model predicts a realistic collapse load, but also that it reproduces the correct physical mode of failure. Therefore, the model can be considered sufficient for use in the subsequent parametric study on imperfection amplitude and relative density

4.6. Assessment of the Analytical Benchmark and Model Limitations

The model assessment presented in this chapter should be interpreted within its intended scope of application. A benchmark comparison was conducted for one representative aluminium foam sandwich case to confirm the reasonableness of the finite element model before proceeding to a wider parametric study. The Schafer/Szyniszewski effective-width method was used here as a reference framework only. The sandwich panel investigated in this study had a thickness of 14 mm, which was substantially larger than the 2.37 mm panel considered in the source paper. Consequently, the corresponding shear-deformation ratio r lies well beyond the range covered by the published graph, reaching values such as 14.35 for a relative density of 0.355, 15 for 0.32, 16.22 for 0.308, 24.26 for 0.262, and 30.3 for 0.25. This indicates that the graphical procedure needs to be extrapolated outside its calibrated domain and therefore should not be treated as a general predictive tool for the present geometry. Because the published Schafer/Szyniszewski method lies outside its calibrated range for the present sandwich geometry, the analytical comparison is used only as a benchmark for the representative high-density case and is not extended to lower-density configurations**.** Although the paper also provides an equation-based alternative, its iterative nature makes it more cumbersome and more susceptible to compounding errors when applied to a geometry of this type. For this reason, only one representative high-density case was used for benchmark comparison, and the resulting analytical prediction was interpreted cautiously rather than as a universal design basis. The model also assumes perfect bonding between the foam core and face sheets through tie constraints, so possible interfacial debonding is not represented.

4.7. Summary

In this chapter, a benchmark comparison of the aluminium foam sandwich panel model was presented by comparing the Abaqus results with the analytical prediction and the reference study. The close agreement in the peak load, buckling mode, deformation pattern, and stress transfer confirmed that the model captured the essential axial collapse response of the panel.

The chapter also shows that the response is sensitive to the imperfection amplitude, although the peak reaction force remains within a narrow range. This supports the use of the model for the later parametric study on relative density and collapse behaviour.

The comparison should be interpreted within its intended scope, with the main limitations arising from the use of an idealized bonded interface, prescribed imperfections, and qualitative stress comparison. Overall, the chapter established the model as reliable for the selected case and appropriate for subsequent analysis.

Chapter 5

Parametric Study Framework and Model Matrix

The main objective of this stage of the study is to quantify the changes in the compressive response of the sandwich panel when the foam relative density and geometric imperfection amplitude are varied systematically. To achieve this, 200 sandwich panel models were analyzed using the same geometric configuration and modelling assumptions adopted in the validation study. The aluminium face sheets were assigned the previously validated material properties, and the foam core properties were varied across the ten validated foam densities developed earlier in this study. In addition, ten of the 200 models were defined as baseline cases with zero imperfections, allowing the performance of the imperfect models to be assessed relative to an undeformed reference condition. In this way, the study remains consistent with the validated model while extending it to a much wider design space than the original model.

This chapter is deliberately separated from the benchmark comparison works to make a clear distinction that the benchmark models were used to establish confidence in the simulations and it was the parametric study that generates the original research results. The modelling and comparison carried out in the validation chapter are therefore treated as a foundation and reference, while the findings presented in the subsequent chapters constitute the main contribution of this thesis. This structure allows the research to develop in a logical order, starting from model validation and then moving on to a wider investigation of imperfection-sensitive behaviour

A summary table of the model matrix is presented in Table 5.1. This table shows the foam density, imperfection amplitude(a) expressed as in mm, normalized imperfection amplitude in terms of thickness, and the corresponding dimensionless ratio a/t. It also contains the corresponding case identification for all 200 simulations performed. This table forms the reference for the results and discussion chapter, where the effects of imperfection sensitivity on the peak load, collapse mode, and overall structural response are examined in detail.

5.1 Parametric study matrix

The parametric study used 200 aluminium foam sandwich models to examine the effects of foam relative density and imperfection amplitude together on the axial compressive behaviour. The panel geometry, boundary conditions, element type, mesh strategy, and bonding assumptions were kept the same as those in the validated sandwich model, so that the study was built directly on the calibrated configuration. Only the foam density and imperfection magnitude were varied systematically, allowing their specific influence on the structural response to be isolated.

The foam core densities used in the study were the same as the ten aluminium foam models that were previously validated; therefore, the sandwich analysis was grounded in material properties supported by experimental data. For each foam relative density case, several imperfection amplitudes were imposed on the first buckling mode shape, which made it possible to assess the imperfection sensitivity over a wide range of conditions. In addition to these cases, ten baseline models with zero imperfections were included to act as reference specimens for comparison with the imperfect panels. This setup allowed the collapse response to be compared in a controlled and consistent manner across all models. The first buckling mode was adopted as the imperfection shape because it represents the dominant instability pattern under axial compression and provides a practical basis for a controlled parametric study. Other imperfection forms were not included in the present work because they would add complexity and make the interpretation of the results less direct.

The full set of sandwich models considered in this study is presented in Table 5.1. This table includes the relative density of foam in the corresponding sandwich panel, the applied imperfection amplitude in mm, the normalized imperfection value expressed in terms of thickness, and the corresponding dimensionless ratio a/t, together with the specimen ID assigned to each model in the results chapter. Fig 5.1 illustrates the labelling of the specimen used in the parametric study. This matrix forms the basis for subsequent evaluation of peak reaction force, force-displacement behaviour, failure mode and regression behaviour model development.

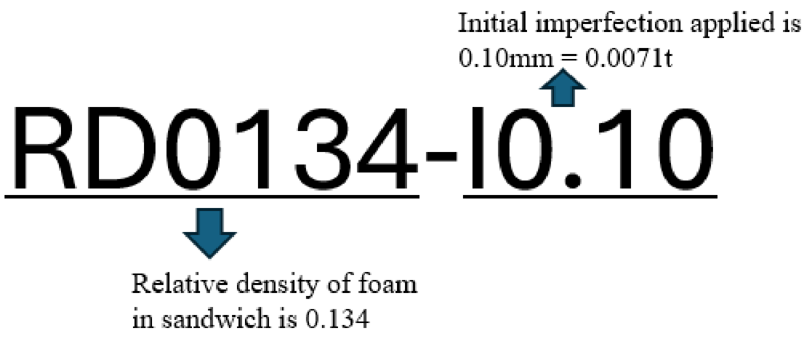

Figure 5.1: Specimen labelling for parametric study.

Table 5.1: Details of specimens used for parametric study

Specimen Number	Specimen ID	Relative Density of Foam	Imperfection Amplitude (a) in terms of total thickness	Imperfection Amplitude (a) in mm	Normalized Imperfection a/t
		Imperfection Models			
1	RD0134-I0.10	0.134	0.0071t	0.1	0.0071
2	RD0134-I0.15	0.134	0.0107t	0.15	0.0107
3	RD0134-I0.20	0.134	0.0143t	0.2	0.0143
4	RD0134-I0.25	0.134	0.0179t	0.25	0.0179
5	RD0134-I0.30	0.134	0.0214t	0.3	0.0214
6	RD0134-I0.35	0.134	0.0250t	0.35	0.0250
7	RD0134-I0.40	0.134	0.0286t	0.4	0.0286
8	RD0134-I0.45	0.134	0.0321t	0.45	0.0321
9	RD0134-I0.50	0.134	0.0357t	0.5	0.0357
10	RD0134-I0.55	0.134	0.0393t	0.55	0.0393
11	RD0134-I0.60	0.134	0.0429t	0.6	0.0429
12	RD0134-I0.65	0.134	0.0464t	0.65	0.0464
13	RD0134-I0.70	0.134	0.0500t	0.7	0.0500
14	RD0134-I0.75	0.134	0.0536t	0.75	0.0536
15	RD0134-I0.80	0.134	0.0571t	0.8	0.0571
16	RD0134-I0.85	0.134	0.0607t	0.85	0.0607
17	RD0134-I0.90	0.134	0.0643t	0.9	0.0643
18	RD0134-I0.95	0.134	0.0679t	0.95	0.0679
19	RD0134-I1	0.134	0.0714t	1	0.0714
20	RD017-I0.10	0.17	0.0071t	0.1	0.0071
21	RD017-I0.15	0.17	0.0107t	0.15	0.0107
22	RD017-I0.20	0.17	0.0143t	0.2	0.0143
23	RD017-I0.25	0.17	0.0179t	0.25	0.0179
24	RD017-I0.30	0.17	0.0214t	0.3	0.0214
25	RD017-I0.35	0.17	0.0250t	0.35	0.0250

26	RD017-I0.40	0.17	0.0286t	0.4	0.0286
27	RD017-I0.45	0.17	0.0321t	0.45	0.0321
28	RD017-I0.50	0.17	0.0357t	0.5	0.0357
29	RD017-I0.55	0.17	0.0393t	0.55	0.0393
30	RD017-I0.60	0.17	0.0429t	0.6	0.0429
31	RD017-I0.65	0.17	0.0464t	0.65	0.0464
32	RD017-I0.70	0.17	0.0500t	0.7	0.0500
33	RD017-I0.75	0.17	0.0536t	0.75	0.0536
34	RD017-I0.80	0.17	0.0571t	0.8	0.0571
35	RD017-I0.85	0.17	0.0607t	0.85	0.0607
36	RD017-I0.90	0.17	0.0643t	0.9	0.0643
37	RD017-I0.95	0.17	0.0679t	0.95	0.0679
38	RD017-I1	0.17	0.0714t	1	0.0714
39	RD0217-I0.10	0.217	0.0071t	0.1	0.0071
40	RD0217-I0.15	0.217	0.0107t	0.15	0.0107
41	RD0217-I0.20	0.217	0.0143t	0.2	0.0143
42	RD0217-I0.25	0.217	0.0179t	0.25	0.0179
43	RD0217-I0.30	0.217	0.0214t	0.3	0.0214
44	RD0217-I0.35	0.217	0.0250t	0.35	0.0250
45	RD0217-I0.40	0.217	0.0286t	0.4	0.0286
46	RD0217-I0.45	0.217	0.0321t	0.45	0.0321
47	RD0217-I0.50	0.217	0.0357t	0.5	0.0357
48	RD0217-I0.55	0.217	0.0393t	0.55	0.0393
49	RD0217-I0.60	0.217	0.0429t	0.6	0.0429
50	RD0217-I0.65	0.217	0.0464t	0.65	0.0464
51	RD0217-I0.70	0.217	0.0500t	0.7	0.0500
52	RD0217-I0.75	0.217	0.0536t	0.75	0.0536
53	RD0217-I0.80	0.217	0.0571t	0.8	0.0571
54	RD0217-I0.85	0.217	0.0607t	0.85	0.0607
55	RD0217-I0.90	0.217	0.0643t	0.9	0.0643
56	RD0217-I0.95	0.217	0.0679t	0.95	0.0679
57	RD0217-I1	0.217	0.0714t	1	0.0714
58	RD025-I0.10	0.25	0.0071t	0.1	0.0071
59	RD025-I0.15	0.25	0.0107t	0.15	0.0107
60	RD025-I0.20	0.25	0.0143t	0.2	0.0143
61	RD025-I0.25	0.25	0.0179t	0.25	0.0179
62	RD025-I0.30	0.25	0.0214t	0.3	0.0214
63	RD025-I0.35	0.25	0.0250t	0.35	0.0250
64	RD025-I0.40	0.25	0.0286t	0.4	0.0286
65	RD025-I0.45	0.25	0.0321t	0.45	0.0321
66	RD025-I0.50	0.25	0.0357t	0.5	0.0357
67	RD025-I0.55	0.25	0.0393t	0.55	0.0393
68	RD025-I0.60	0.25	0.0429t	0.6	0.0429
69	RD025-I0.65	0.25	0.0464t	0.65	0.0464
70	RD025-I0.70	0.25	0.0500t	0.7	0.0500
71	RD025-I0.75	0.25	0.0536t	0.75	0.0536
72	RD025-I0.80	0.25	0.0571t	0.8	0.0571
73	RD025-I0.85	0.25	0.0607t	0.85	0.0607

74	RD025-I0.90	0.25	0.0643t	0.9	0.0643
75	RD025-I0.95	0.25	0.0679t	0.95	0.0679
76	RD025-I1	0.25	0.0714t	1	0.0714
77	RD0262-I0.10	0.262	0.0071t	0.1	0.0071
78	RD0262-I0.15	0.262	0.0107t	0.15	0.0107
79	RD0262-I0.20	0.262	0.0143t	0.2	0.0143
80	RD0262-I0.25	0.262	0.0179t	0.25	0.0179
81	RD0262-I0.30	0.262	0.0214t	0.3	0.0214
82	RD0262-I0.35	0.262	0.0250t	0.35	0.0250
83	RD0262-I0.40	0.262	0.0286t	0.4	0.0286
84	RD0262-I0.45	0.262	0.0321t	0.45	0.0321
85	RD0262-I0.50	0.262	0.0357t	0.5	0.0357
86	RD0262-I0.55	0.262	0.0393t	0.55	0.0393
87	RD0262-I0.60	0.262	0.0429t	0.6	0.0429
88	RD0262-I0.65	0.262	0.0464t	0.65	0.0464
89	RD0262-I0.70	0.262	0.0500t	0.7	0.0500
90	RD0262-I0.75	0.262	0.0536t	0.75	0.0536
91	RD0262-I0.80	0.262	0.0571t	0.8	0.0571
92	RD0262-I0.85	0.262	0.0607t	0.85	0.0607
93	RD0262-I0.90	0.262	0.0643t	0.9	0.0643
94	RD0262-I0.95	0.262	0.0679t	0.95	0.0679
95	RD0262-I1	0.262	0.0714t	1	0.0714
96	RD0308-I0.10	0.308	0.0071t	0.1	0.0071
97	RD0308-I0.15	0.308	0.0107t	0.15	0.0107
98	RD0308-I0.20	0.308	0.0143t	0.2	0.0143
99	RD0308-I0.25	0.308	0.0179t	0.25	0.0179
100	RD0308-I0.30	0.308	0.0214t	0.3	0.0214
101	RD0308-I0.35	0.308	0.0250t	0.35	0.0250
102	RD0308-I0.40	0.308	0.0286t	0.4	0.0286
103	RD0308-I0.45	0.308	0.0321t	0.45	0.0321
104	RD0308-I0.50	0.308	0.0357t	0.5	0.0357
105	RD0308-I0.55	0.308	0.0393t	0.55	0.0393
106	RD0308-I0.60	0.308	0.0429t	0.6	0.0429
107	RD0308-I0.65	0.308	0.0464t	0.65	0.0464
108	RD0308-I0.70	0.308	0.0500t	0.7	0.0500
109	RD0308-I0.75	0.308	0.0536t	0.75	0.0536
110	RD0308-I0.80	0.308	0.0571t	0.8	0.0571
111	RD0308-I0.85	0.308	0.0607t	0.85	0.0607
112	RD0308-I0.90	0.308	0.0643t	0.9	0.0643
113	RD0308-I0.95	0.308	0.0679t	0.95	0.0679
114	RD0308-I1	0.308	0.0714t	1	0.0714
115	RD032-I0.10	0.32	0.0071t	0.1	0.0071
116	RD032-I0.15	0.32	0.0107t	0.15	0.0107
117	RD032-I0.20	0.32	0.0143t	0.2	0.0143
118	RD032-I0.25	0.32	0.0179t	0.25	0.0179
119	RD032-I0.30	0.32	0.0214t	0.3	0.0214
120	RD032-I0.35	0.32	0.0250t	0.35	0.0250
121	RD032-I0.40	0.32	0.0286t	0.4	0.0286

122	RD032-I0.45	0.32	0.0321t	0.45	0.0321
123	RD032-I0.50	0.32	0.0357t	0.5	0.0357
124	RD032-I0.55	0.32	0.0393t	0.55	0.0393
125	RD032-I0.60	0.32	0.0429t	0.6	0.0429
126	RD032-I0.65	0.32	0.0464t	0.65	0.0464
127	RD032-I0.70	0.32	0.0500t	0.7	0.0500
128	RD032-I0.75	0.32	0.0536t	0.75	0.0536
129	RD032-I0.80	0.32	0.0571t	0.8	0.0571
130	RD032-I0.85	0.32	0.0607t	0.85	0.0607
131	RD032-I0.90	0.32	0.0643t	0.9	0.0643
132	RD032-I0.95	0.32	0.0679t	0.95	0.0679
133	RD032-I1	0.32	0.0714t	1	0.0714
134	RD0355-I0.10	0.355	0.0071t	0.1	0.0071
135	RD0355-I0.15	0.355	0.0107t	0.15	0.0107
136	RD0355-I0.20	0.355	0.0143t	0.2	0.0143
137	RD0355-I0.25	0.355	0.0179t	0.25	0.0179
138	RD0355-I0.30	0.355	0.0214t	0.3	0.0214
139	RD0355-I0.35	0.355	0.0250t	0.35	0.0250
140	RD0355-I0.40	0.355	0.0286t	0.4	0.0286
141	RD0355-I0.45	0.355	0.0321t	0.45	0.0321
142	RD0355-I0.50	0.355	0.0357t	0.5	0.0357
143	RD0355-I0.55	0.355	0.0393t	0.55	0.0393
144	RD0355-I0.60	0.355	0.0429t	0.6	0.0429
145	RD0355-I0.65	0.355	0.0464t	0.65	0.0464
146	RD0355-I0.70	0.355	0.0500t	0.7	0.0500
147	RD0355-I0.75	0.355	0.0536t	0.75	0.0536
148	RD0355-I0.80	0.355	0.0571t	0.8	0.0571
149	RD0355-I0.85	0.355	0.0607t	0.85	0.0607
150	RD0355-I0.90	0.355	0.0643t	0.9	0.0643
151	RD0355-I0.95	0.355	0.0679t	0.95	0.0679
152	RD0355-I1	0.355	0.0714t	1	0.0714
153	RD0439-I0.10	0.439	0.0071t	0.1	0.0071
154	RD0439-I0.15	0.439	0.0107t	0.15	0.0107
155	RD0439-I0.20	0.439	0.0143t	0.2	0.0143
156	RD0439-I0.25	0.439	0.0179t	0.25	0.0179
157	RD0439-I0.30	0.439	0.0214t	0.3	0.0214
158	RD0439-I0.35	0.439	0.0250t	0.35	0.0250
159	RD0439-I0.40	0.439	0.0286t	0.4	0.0286
160	RD0439-I0.45	0.439	0.0321t	0.45	0.0321
161	RD0439-I0.50	0.439	0.0357t	0.5	0.0357
162	RD0439-I0.55	0.439	0.0393t	0.55	0.0393
163	RD0439-I0.60	0.439	0.0429t	0.6	0.0429
164	RD0439-I0.65	0.439	0.0464t	0.65	0.0464
165	RD0439-I0.70	0.439	0.0500t	0.7	0.0500
166	RD0439-I0.75	0.439	0.0536t	0.75	0.0536
167	RD0439-I0.80	0.439	0.0571t	0.8	0.0571
168	RD0439-I0.85	0.439	0.0607t	0.85	0.0607
169	RD0439-I0.90	0.439	0.0643t	0.9	0.0643

170	RD0439-I0.95	0.439	0.0679t	0.95	0.0679
171	RD0439-I1	0.439	0.0714t	1	0.0714
172	RD0472-I0.10	0.472	0.0071t	0.1	0.0071
173	RD0472-I0.15	0.472	0.0107t	0.15	0.0107
174	RD0472-I0.20	0.472	0.0143t	0.2	0.0143
175	RD0472-I0.25	0.472	0.0179t	0.25	0.0179
176	RD0472-I0.30	0.472	0.0214t	0.3	0.0214
177	RD0472-I0.35	0.472	0.0250t	0.35	0.0250
178	RD0472-I0.40	0.472	0.0286t	0.4	0.0286
179	RD0472-I0.45	0.472	0.0321t	0.45	0.0321
180	RD0472-I0.50	0.472	0.0357t	0.5	0.0357
181	RD0472-I0.55	0.472	0.0393t	0.55	0.0393
182	RD0472-I0.60	0.472	0.0429t	0.6	0.0429
183	RD0472-I0.65	0.472	0.0464t	0.65	0.0464
184	RD0472-I0.70	0.472	0.0500t	0.7	0.0500
185	RD0472-I0.75	0.472	0.0536t	0.75	0.0536
186	RD0472-I0.80	0.472	0.0571t	0.8	0.0571
187	RD0472-I0.85	0.472	0.0607t	0.85	0.0607
188	RD0472-I0.90	0.472	0.0643t	0.9	0.0643
189	RD0472-I0.95	0.472	0.0679t	0.95	0.0679
190	RD0472-I1	0.472	0.0714t	1	0.0714
		Baseline Models			
191	RD0134-I0	0.134	0	0	0
192	RD017-I0	0.17	0	0	0
193	RD0217-I0	0.217	0	0	0
194	RD025=I0	0.25	0	0	0
195	RD0262-I0	0.262	0	0	0
196	RD0308-I0	0.308	0	0	0
197	RD032-I0	0.32	0	0	0
198	RD0355-I0	0.355	0	0	0
199	RD0372-I0	0.372	0	0	0
200	RD0439-I0	0.439	0	0	0
201	RD0472-I0	0.472	0	0	0

The imperfection amplitudes were selected to span a practical range of out-of-plane deviations relative to the 14 mm total panel thickness, corresponding to normalized imperfections of $a/t = 0.0071$ to 0.0714. This range provides a systematic means of examining imperfection sensitivity from very small geometric deviations to more pronounced imperfections while remaining within the physically plausible limits for the analyzed sandwich panels. Imperfections were introduced using the first buckling mode shape because this mode represents the dominant global instability pattern and provides a consistent basis for comparing the responses of all models. The use of later mode shapes was not considered in the present study, as the objective was to establish a controlled and uniform imperfection representation for the parametric investigation

5.2 Link to the main research

The preliminary objective of this chapter is to establish the transition from model validation to the main parametric investigation. For the selected benchmark case, the previous validation chapters confirmed that the finite element model was capable of reproducing the essential collapse response of the aluminium foam sandwich panel. Based on this foundation, the present study defines a full set of 200 models to examine the combined influence of the relative density of the foam and change in the imperfection amplitudes on the axial compression response of aluminium foam sandwich panels.

The response trends extracted from the 200 simulations were later used to develop a multi-objective performance framework to identify a suitable range of foam core relative density and to develop a regression-based design equation for predicting the compressive behaviour of the aluminium foam sandwich panels within the studied range. In this way, the validation chapter provides confidence in the numerical model, while the present chapter establishes the dataset used for the original analysis and subsequent thesis findings.

Chapter 6

Results and Discussions

This chapter presents the results and discussion of the parametric study on aluminium foam sandwich panels. The effects of foam relative density and geometric imperfection amplitude on the axial compressive response are examined using the model matrix established in Chapter 5. The first section presents the ABAQUS simulation results, followed by a detailed discussion of the observed trends and underlying mechanical behaviour. These findings are then used to develop a multi-objective optimization framework and identify the optimum foam core density.

6.1 Results from Numerical Analysis

To provide a detailed comparison of the nonlinear buckling response across the studied cases, the reaction force behaviour, peak reaction force, deformation pattern, and associated interpretation for each combination of relative density of foam in the sandwich with imperfection amplitude are given in tabular form in the following sections. To facilitate comparison with the analysis of baseline panels, perfect geometries were also analyzed for each set of relative densities. This provides a useful reference for assessing the influence of geometric imperfections on the overall response within a selected relative density. The table highlights the key trends and provides a foundation for subsequent discussions.

In addition to the reaction force response and deformation pattern, several mode indicators were used to characterize the buckling behaviour more precisely, including the initial post-peak softening slope in kN/mm, the core shear strain component $LE13$, the localization length, and the maximum out-of-plane displacement at peak load, $U3_{max}$. For localized U-shaped deformation, the core shear strain (LE13) and $U3_{max}$ were evaluated at the peak load condition, since these values best represent the onset of localized collapse. For multi-wave and emerging-wave deformation modes, the number of half-waves, and the corresponding core shear strain values at the peak and final load steps were used as the principal indicators. These measures provide a more comprehensive basis for comparing the evolution of buckling modes across the different imperfection and density combinations. $LE13$ denotes the logarithmic core shear strain in the plane formed by the panel length and thickness directions.

6.1.1 Aluminium Foam sandwich with 0.134 Relative Density Foam

The influence of the applied initial imperfection amplitude on the structural response of the 0.134 foam sandwich panel under axial compression is summarized in Table 6.1. The table presents the variations in the reaction force response, peak reaction force, deformation pattern, and qualitative interpretation for the full range of imperfection amplitudes considered in this study. The table highlights the sensitivity of the sandwich panels to the initial geometric imperfections, with normalized values in terms of the total thickness of the sandwich panel, provided alongside the corresponding dimensional amplitudes in millimetres for reference.

Table 6.1: Effect of imperfection amplitude on RF behaviour, peak reaction force, and observed deformation mode for 0.134 Al foam sandwich

Imperfection Range	RF Behaviour	Peak RF Values	Deformation Pattern	Interpretation
Without Imperfection	Linear-Plateau-Drop Response	48.5 kN	Regular multi-wave deformation	Distributed buckling with progressive load redistribution before softening
0.0071t (0.1 mm)	Linear response- sudden drop. Initial post peak softening slope of the rf-u curve is -31.26 kN/mm	20.6 kN	U Shaped localization. With u-shape highly confined near centre. Localization length – 251mm, $LE13_{peak\ load}$-0.0698 $U3_{max}$ - 7.46mm	Dominant localized buckling with rapid collapse after the first instability.
0.0107t (0.15 mm)	Linear response: soft plateau: gradual softening. Initial post peak softening slope of the rf-u curve is -2.73 kN/mm	38.3 kN	Multiple wave deformation, 19 short half-waves throughout the length. $LE13_{peak\ load}$-0.003048 $LE13_{collapse}$-0.215	Stable post-buckling redistribution; progressive load sharing across several buckling lobes
0.0143t to 0.0179t (0.2 mm-0.25mm)	Single Peak with Sudden drop. Initial post peak softening slope of the rf-u curve is -65 kN/mm	15 and 19.2 kN	U Shaped localization. With u-shape highly confined near centre. Localization length – 245mm, $LE13_{peak\ load}$-0.06545 $U3_{max}$ - 6.993mm	Early localization into the dominant U-shaped buckling mode, with limited post-buckling redistribution

0.0214t (0.3 mm)	Long Plateau Followed by Gradual Softening. The initial post-peak softening slope of the rf-u curve is -3.61 kN/mm	38.2 kN	Multiple wave deformation, 19 short half-waves throughout the length. $LE13_{peak\ load}$-0.01657 $LE13_{collapse}$-0.09248	Stable post-buckling redistribution; progressive load sharing across several buckling lobes
0.0250t (0.35 mm)	Single Peak with Gradual Drop. The initial post-peak softening slope of the rf-u curve is -15.04 kN/mm	22.6 kN	Emerging wave deformation, five emerging half-waves throughout the length. $LE13_{peak\ load}$-0.06766 $LE13_{collapse}$-0.1743	Localized post-buckling with progressive wave evolution and gradual loss of load-carrying capacity
0.0286t to 0.0714t (0.4 to 1 mm)	Linear RF only; analysis aborted after elastic/post-elastic region	-	Not fully captured	Nonlinear post-buckling response could not be resolved due to numerical termination

Table 6.2 summarizes the peak reaction force responses of the specimens and their corresponding imperfection amplitudes. The inclusion of both $P_{\max}$ and $P_{\max}/P_0$ allows for a direct comparison of the load-carrying capacity relative to the imperfection-free reference case, thereby demonstrating the effect of geometric imperfections on the structural performance of the panel.

Table 6.2: Variation of peak reaction of 0.134 Al foam sandwich panel force across various imperfection amplitude in comparison with imperfection free sandwich panel

Sample ID	Pmax	Pmax/P0	Imperfection Amplitude
RD0134-I0.10	20.6	0.4247	0.0071t
RD0134-I0.15	38.3	0.7897	0.0107t
RD0134-I0.20	15	0.3093	0.0143t
RD0134-I0.25	19.2	0.3959	0.0179t
RD0134-I0.30	38.2	0.7876	0.0214t
RD0134-I0.35	22.6	0.4660	0.0250t

Figure 6.1 shows the variation in the peak reaction force with the imperfection amplitude for the $\rho^* = 0.134$ foam sandwich panel. The corresponding reaction force behavior and deformation patterns for the representative imperfection levels are shown in Figures 6.2 to 6.7,

providing visual evidence of the buckling transition and the associated changes in load-carrying response.

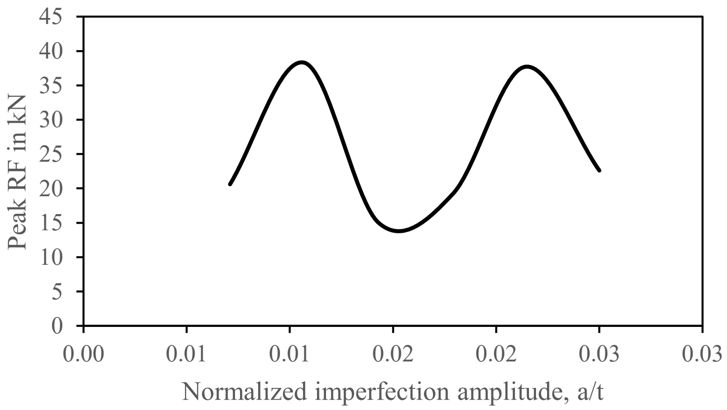

Figure 6.1: Graph showing Variation of Peak Reaction Force with Imperfection Amplitude for 0.134 relative density Al foam sandwich

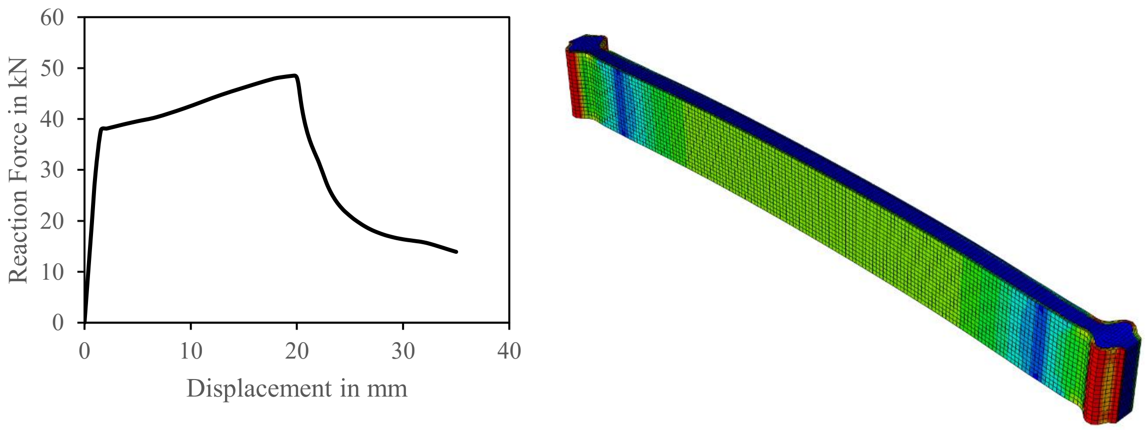

Figure 6.2: Reaction Force-Displacement Graph and Deformation pattern for 0.134 Al foam sandwich panel without imperfection (baseline)

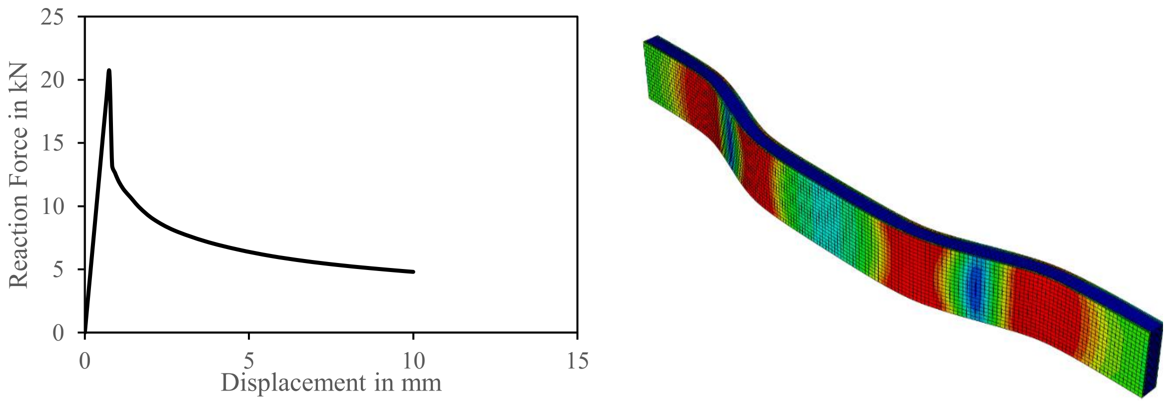

Figure 6.3: Reaction Force-Displacement Graph and Deformation pattern for 0.134 Al foam sandwich panel with 0.0071t imperfection at centre

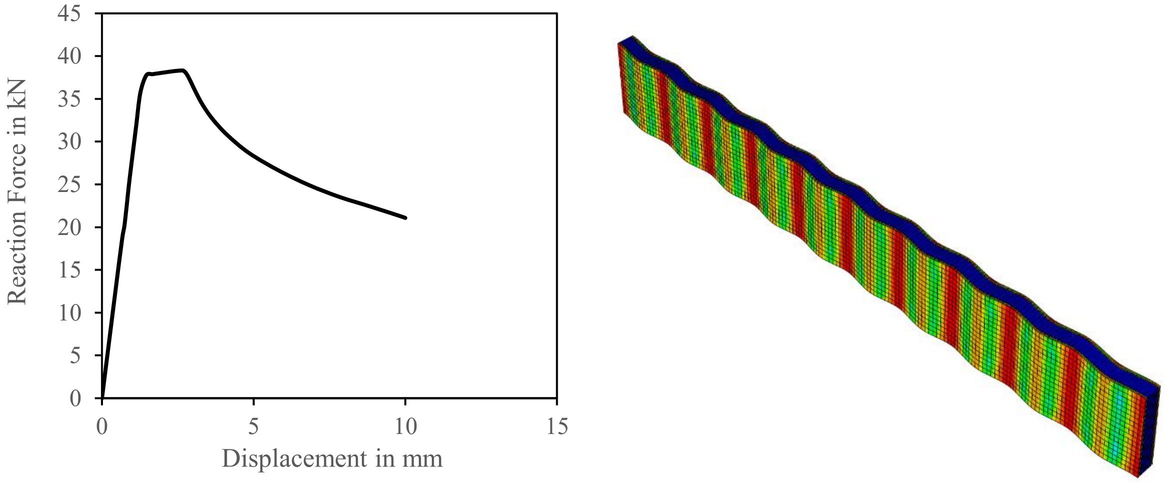

Figure 6.4: Reaction Force-Displacement Graph and Deformation pattern for 0.134 Al foam sandwich panel with 0.00107t imperfection at centre

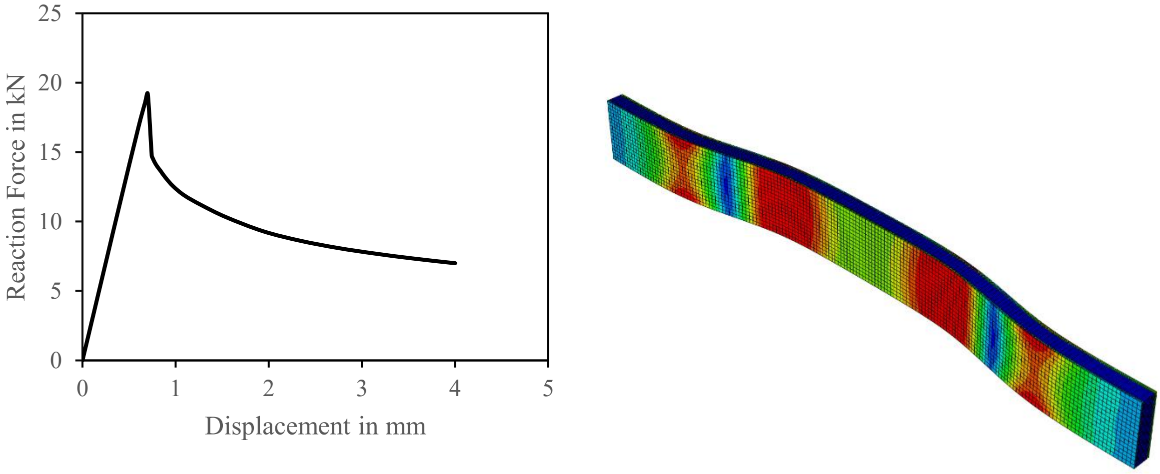

Figure 6.5: Reaction Force-Displacement Graph and Deformation pattern for 0.134 Al foam sandwich panel with 0.0179t imperfection at centre

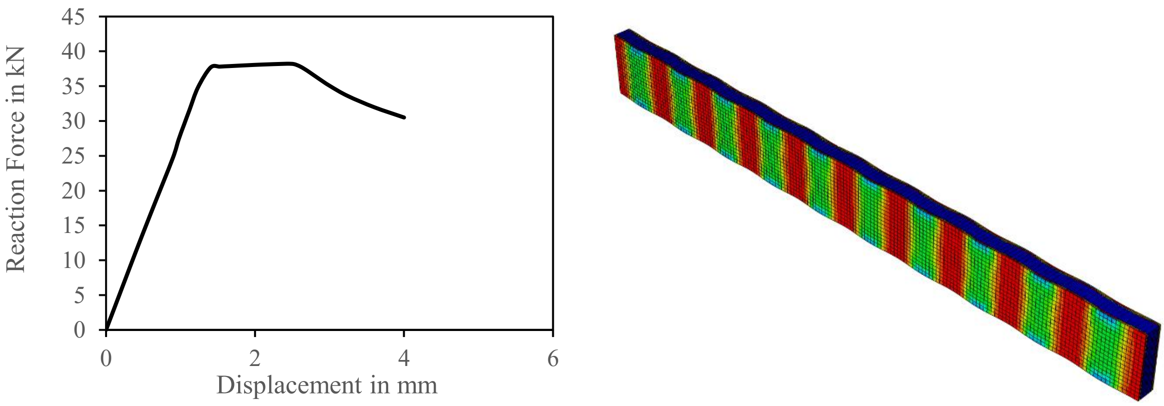

Figure 6.6: Reaction Force-Displacement Graph and Deformation pattern for 0.134 Al foam sandwich panel with 0.0214t imperfection at centre

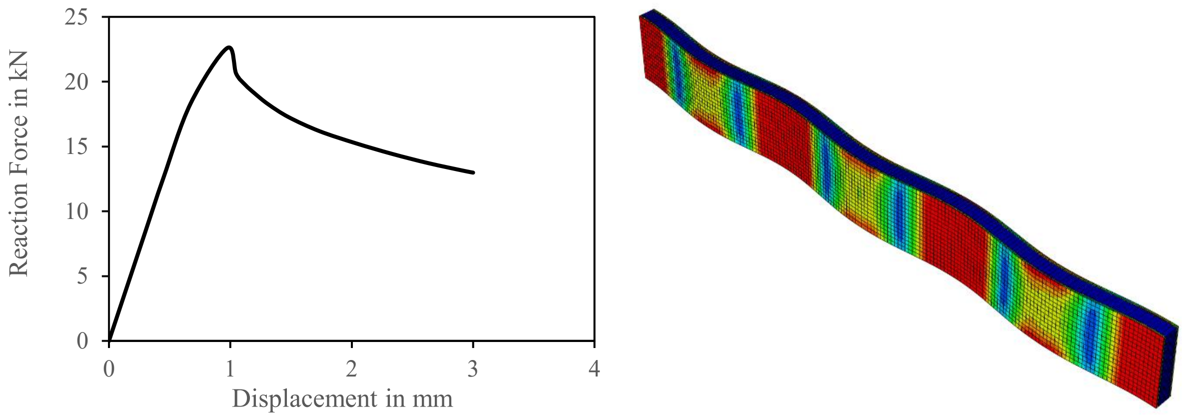

Figure 6.7: Reaction Force-Displacement Graph and Deformation pattern for 0.134 Al foam sandwich panel with 0.025t imperfection at centre

For the 0.134 relative density panel, the results indicate an imperfection-dependent response window in which mode interaction temporarily enhances load-carrying capacity. This is evident at 0.0107t and 0.0214t, where the peak reaction force is relatively high and post-peak softening is delayed. At intermediate and larger imperfection amplitudes, the beneficial interaction weakens and the response becomes progressively more localized. The no-imperfection case serves as the baseline reference, exhibiting a more regular distributed buckling pattern before softening.

6.1.2 Aluminium Foam sandwich with 0.17 Relative Density Foam.

The influence of the applied initial imperfection amplitude on the structural response of the 0.17 foam sandwich panel under axial compression is summarized in Table 6.3.

Table 6.3: Effect of imperfection amplitude on RF behaviour, peak reaction force, and observed deformation mode for 0.17 Al foam sandwich

Imperfection Range	RF Behaviour	Peak RF Values	Deformation Pattern	Interpretation
Without Imperfection	Linear-Plateau-Drop Response	51.7 kN	Regular multi wave deformation with nine half waves throughout the panel	Distributed buckling with progressive load redistribution before softening
0.0071t to 0.0143t (0.1- 0.2 mm)	Piecewise linear response with three slope changes, followed by a single peak and gradual softening with a initial post peak	22.1, 22 and 21.8 kN	U-shape; localized mid-span deformation Localization length-239 mm, $U3_{max}$ - 9.11mm, $LE13_{peak\ load}$- 0.00517	Localized buckling with successive stiffness transitions before post-peak softening

	softening slope of about-6.2 kN/mm			
0.0179t to 0.0250t (0.25-0.35mm)	Linear response with a dominant peak followed by gradual softening with a initial post peak softening slope of about - 5.23 kN/mm	22.9, 22.7 and 22.4 `kN	U-shape; localized mid-span deformation, Localization length-239 mm, $U3_{max}$ -8.89mm, $LE13_{peak\ load}$- 0.05113	Similar localized post-buckling response across this imperfection range, indicating a dominant unstable mode with limited effect of small changes in imperfection amplitude
0.0286t to 0.0714t (0.4-1 mm)	Linear rise to a single peak, followed by gradual post-peak softening of the curve. The initial post peak softening slope increases gradually from - 3.63 kN/mm to - 1.34 kN/mm	Decreases gradually from 22.1 kN to 20.1 kN with increasing imperfection	U-shape; localized mid-span deformation, Localization length-239 mm, $U3_{max}$ -increases from 7.56 to 7.929mm $LE13_{peak\ load}$ - 0.047 approx	Imperfection-driven localization dominates, and the response follows a similar unstable post-buckling path across the range

Table 6.4 summarizes the peak reaction force responses of the specimens and their corresponding imperfection amplitudes.

Table 6.4: Variation of peak reaction force of 0.17 Al foam sandwich panel across various imperfection amplitude in comparison with imperfection free sandwich panel

Sample ID	P_{max} in kN	P_{max}/P_0	Imperfection Amplitude
RD017-I0.10	22.1	0.427466	0.0071t
RD017-I0.15	22	0.425532	0.0107t
RD017-I0.20	21.8	0.421663	0.0143t
RD017-I0.25	22.9	0.44294	0.0179t
RD017-I0.30	22.7	0.439072	0.0214t
RD017-I0.35	22.4	0.433269	0.0250t
RD017-I0.40	22.1	0.427466	0.0286t
RD017-I0.45	21.9	0.423598	0.0321t
RD017-I0.50	21.6	0.417795	0.0357t
RD017-I0.55	21.4	0.413926	0.0393t
RD017-I0.60	21.3	0.411992	0.0429t
RD017-I0.65	21.1	0.408124	0.0464t
RD017-I0.70	21	0.40619	0.0500t
RD017-I0.75	20.8	0.402321	0.0536t
RD017-I0.80	20.7	0.400387	0.0571t
RD017-I0.85	20.5	0.396518	0.0607t

RD017-I0.90	20.4	0.394584	0.0643t
RD017-I0.95	20.3	0.39265	0.0679t
RD017-I1	20.1	0.388781	0.0714t

Figure 6.8 represents the variation in the peak reaction force with the imperfection amplitude for the $\rho^* = 0.17$ foam sandwich panel. The corresponding reaction force behavior and deformation patterns for the representative imperfection levels are shown in Figures 6.9 to 6.13, providing visual evidence of the buckling transition and the associated changes in the load-carrying response.

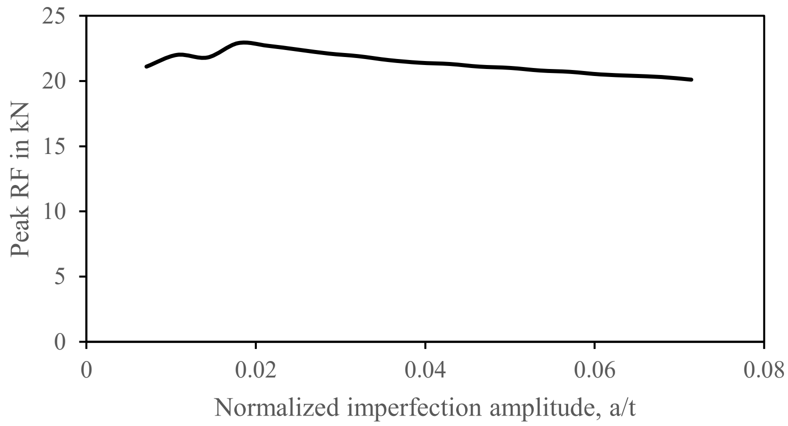

Figure 6.8: Graph showing Variation of Peak Reaction Force with Imperfection Amplitude for 0.17 relative density Al foam sandwich

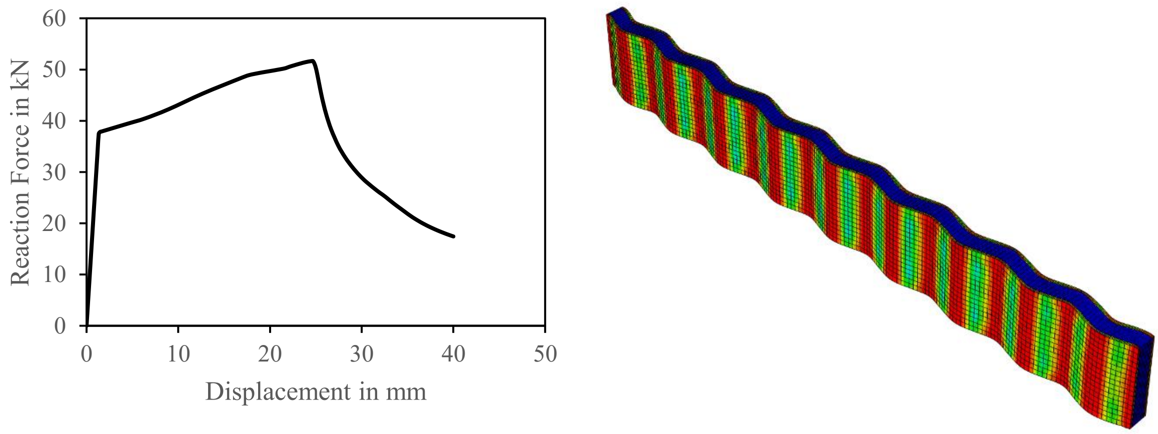

Figure 6.9: Reaction Force-Displacement Graph and Deformation pattern for 0.17 Al foam sandwich panel without imperfection (Baseline)

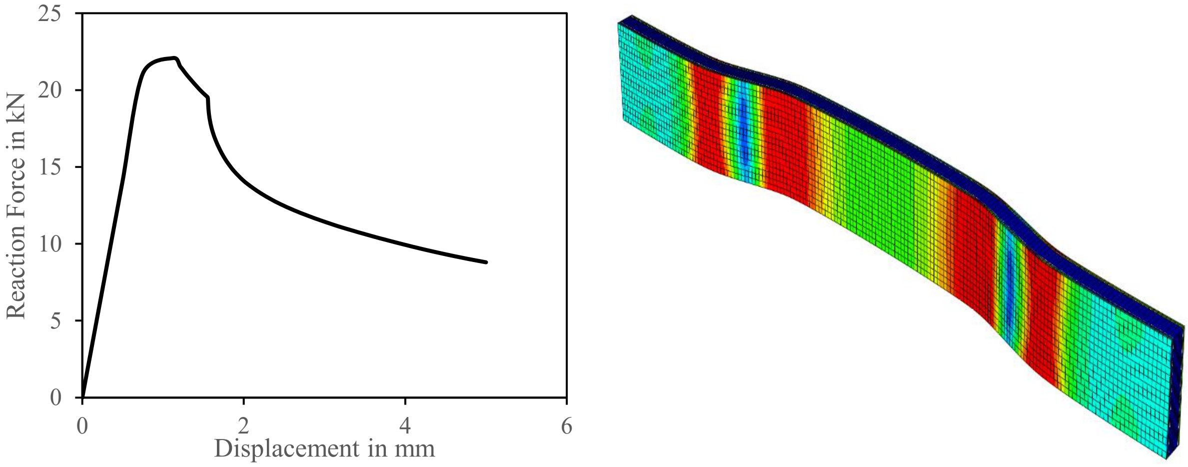

Figure 6.10: Reaction Force-Displacement Graph and deformation pattern for 0.17 Al foam sandwich panel with 0.0071t imperfection at centre

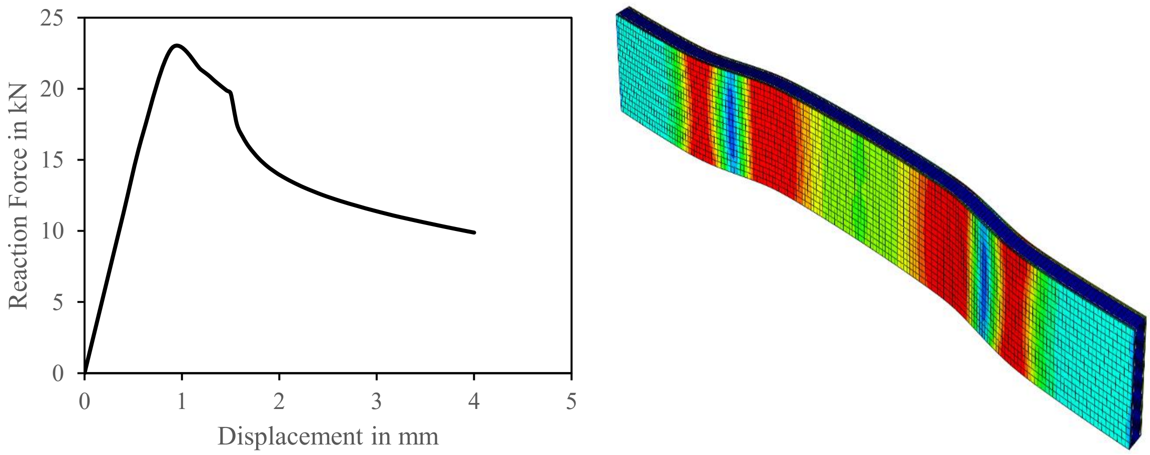

Figure 6.11: Reaction Force-Displacement Graph and deformation pattern for 0.17 Al foam sandwich panel with 0.0179t imperfection at centre

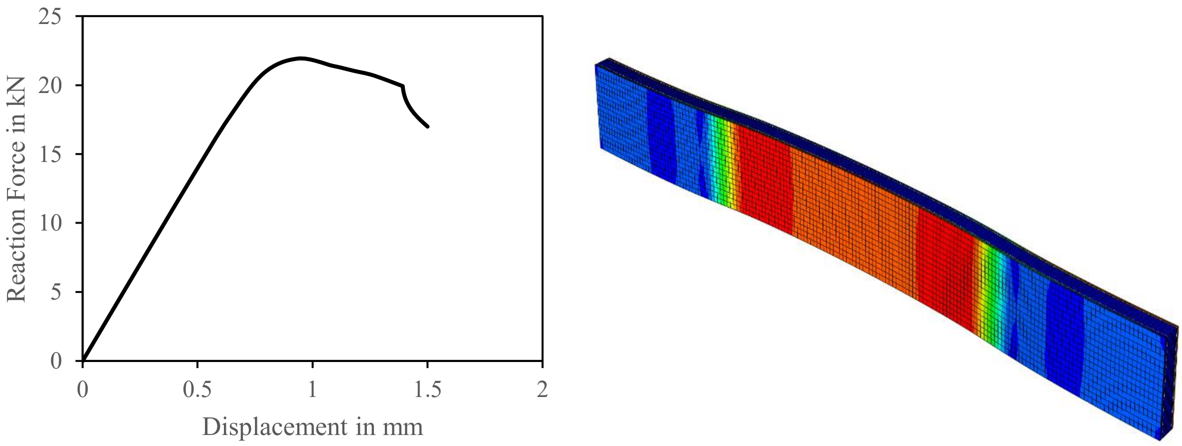

Figure 6.12: Reaction Force-Displacement Graph and Deformation pattern for 0.17 Al foam sandwich panel with 0.0321t imperfection at centre

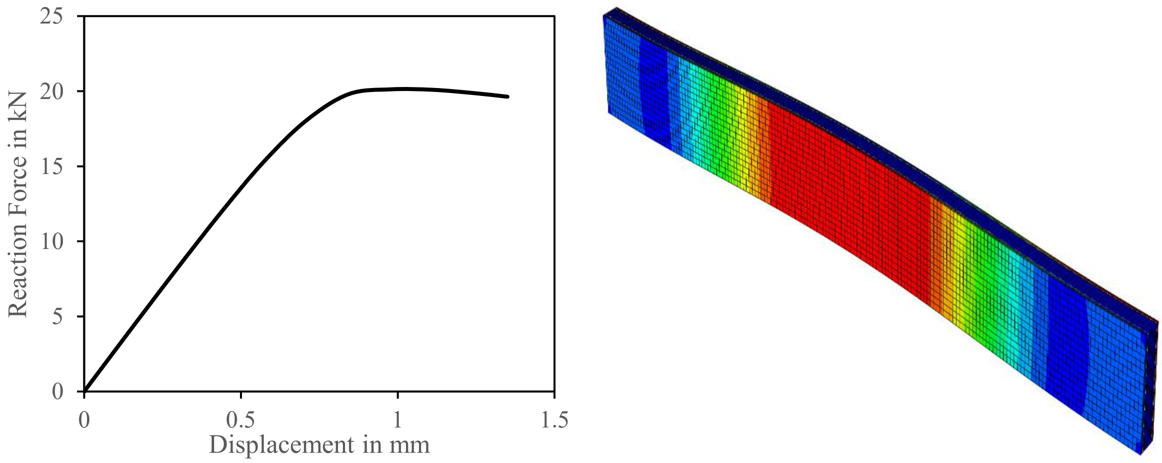

Figure 6.13: Reaction Force-Displacement Graph and deformation pattern for 0.17 Al foam sandwich panel with 0.0714t imperfection at centre

The 0.17 foam sandwich shows a transition from distributed buckling in the imperfection-free case to predominantly localized U-shaped buckling under imperfect conditions. The perfect panel exhibits a linear–plateau–drop response with regular multi-wave deformation and the highest peak load, indicating effective global load redistribution before softening. Once imperfections are introduced, the response is controlled by a persistent localized mode, although the post-buckling path changes slightly with imperfection amplitude. In the lower imperfection range, multiple stiffness transitions suggest some mode interaction and temporary stabilization before peak load. At larger imperfections, the curves become similar and the peak load decreases only marginally, showing that the structure remains relatively insensitive to imperfection amplitude. The normalized peak-load values in Table 6.4 confirm this narrow sensitivity band, with $P_{\max}/P_0$ staying roughly within 0.39–0.44 across the full range.

6.1.3 Aluminium Foam sandwich with 0.217 Relative Density Foam

The influence of the applied initial imperfection amplitude on the structural response of the 0.217 Al foam sandwich panel under axial compression is summarized in Table 6.5.

Table 6.5: Effect of imperfection amplitude on RF behaviour, peak reaction force, and observed deformation mode for 0.217 Al foam sandwich

Imperfection Range	RF Behaviour	Peak RF Values	Deformation Pattern	Interpretation
Without Imperfection	Linear-Plateau-Drop Response	55.3 kN	More localized edge-dominated or end-localized deformation patterns.	Higher relative density delays global instability and promotes a less distributed, more boundary-controlled deformation mode
0.0071t (0.1 mm)	Linear response followed by sudden drop with an initial p,ost peak slope of -39.1 kN/mm	29.7 kN	U-shape; localized mid-span deformation, Localization length-239 mm, $U3_{max}$ - 4.86 mm, $LE13_{peak\ load}$ -0.0179	Early localized U-shaped buckling with abrupt post-buckling instability.
0.0107t to 0.0214t (0.15 to 0.3 mm)	Linear response with a short peak plateau followed by sudden drop, with initial post peak softening around -28.8 kN/mm	28.7, 28.3 and 27.9 kN	U-shape; localized mid-span deformation, Localization length-239 mm, $U3_{max}$ - 4.934 mm, $LE13_{peak\ load}$ - 0.01836	Rapid localization into the dominant buckling mode, with transient strengthening and delayed softening followed by abrupt loss of load-carrying capacity
0.025t to 0.0321t (0.35 to 0.45 mm)	Linear response followed by sudden drop with initial post peak softening around -19 kN/mm	28.7 kN,28.4 kN and 28.1kN	U-shape; localized mid-span deformation, Localization length-239 mm, $U3_{max}$ - 5.45 mm, $LE13_{peak\ load}$ - 0.0202	Rapid localization into the dominant U-shaped mode, with no stable post-buckling redistribution before abrupt loss of capacity
0.0357t to 0.0607t (0.5 to 0.85 mm)	Linear response with a short peak plateau followed by sudden drop, with initial post peak softening slope around (-10.6) kN/mm	Decreases gradually from 27 kN to 25.8 kN with increasing imperfectio n	U-shape; localized mid-span deformation, Localization length-239 mm, $U3_{max}$ – 5mm $LE13_{peak\ load}$ - 0.0201	Rapid localization into the dominant buckling mode, with weakened mode interaction and earlier softening leading to abrupt loss of load-carrying capacity
0.0643t to 0.0714t (0.9 to 1 mm)	Linear response followed by slightly gradual drop, with initial post peak softening slope	26.1 kN,26 kN and 25.8 kN respectivel y	U-shape; localized mid-span deformation, Localization length-239 mm, $U3_{max}$ – 6.66 mm $LE13_{peak\ load}$ – 0.0245	Fully localized buckling with little or no mode interaction and progressive loss of stiffness after peak

around -8.4 kN/mm	

Table 6.6 summarizes the peak reaction force responses of the specimens, along with their corresponding imperfection amplitudes.

Table 6.6: Variation of peak reaction force of 0.217 Al foam sandwich panel across various imperfection amplitudes in comparison with imperfection free sandwich panel

Sample ID	P_{max} in kN	P_{max}/P_0	Imperfection Amplitude
RD0217-I0.10	29.7	0.537071	0.0071t
RD0217-I0.15	28.7	0.518987	0.0107t
RD0217-I0.20	28.3	0.511754	0.0143t
RD0217-I0.25	27.9	0.504521	0.0179t
RD0217-I0.30	27.6	0.499096	0.0214t
RD0217-I0.35	28.7	0.518987	0.025t
RD0217-I0.40	28.4	0.513562	0.0286t
RD0217-I0.45	28.1	0.508137	0.0321t
RD0217-I0.50	27	0.488246	0.0357t
RD0217-I0.55	26.8	0.484629	0.0393t
RD0217-I0.60	26.6	0.481013	0.0429t
RD0217-I0.65	26.5	0.479204	0.0464t
RD0217-I0.70	26.3	0.475588	0.05t
RD0217-I0.75	26.1	0.471971	0.0536t
RD0217-I0.80	26	0.470163	0.0571t
RD0217-I0.85	25.8	0.466546	0.0607t
RD0217-I0.90	26.1	0.471971	0.0643t
RD0217-I0.95	26	0.470163	0.0679t
RD0217-I1	25.8	0.466546	0.0714t

Figure 6.14 represents the variation in the peak reaction force with the imperfection amplitude for the $\rho^* = 0.217$ foam sandwich panel. The corresponding reaction force behaviours and deformation patterns for the representative imperfection levels are shown in Figures 6.15 - 6.20, providing visual evidence of the buckling transition and the associated changes in load-carrying response.

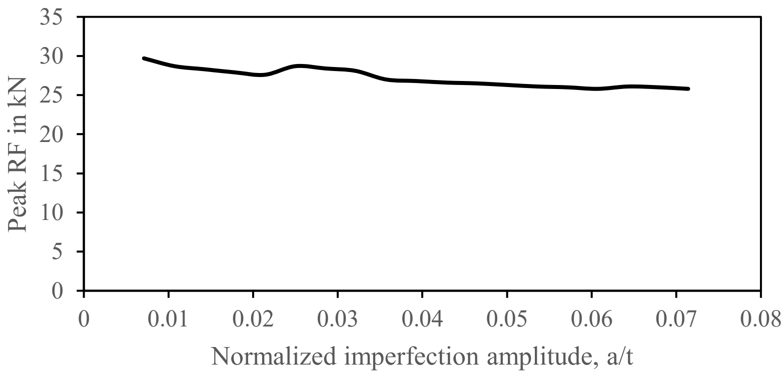

Figure 6.14: Graph showing Variation of Peak Reaction Force with Imperfection Amplitude for 0.217 relative density Al foam sandwich

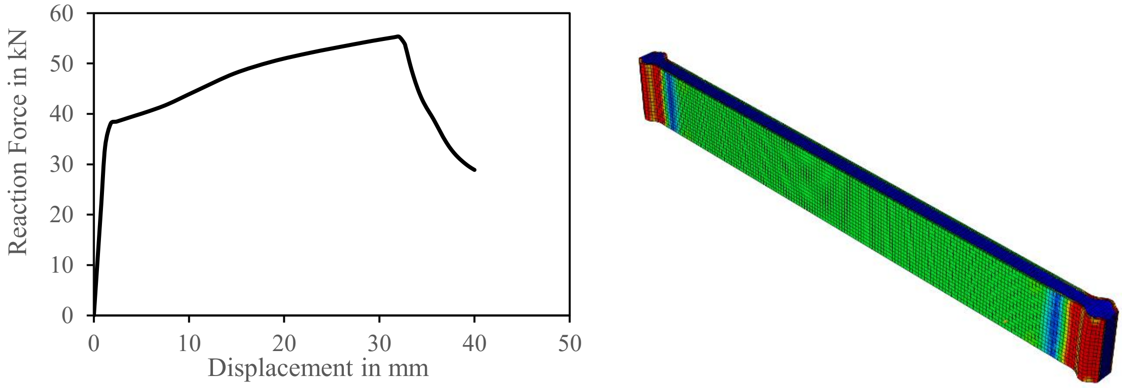

Figure 6.15: Reaction Force-Displacement Graph and Deformation pattern for 0.217 Al foam sandwich panel without imperfection (baseline)

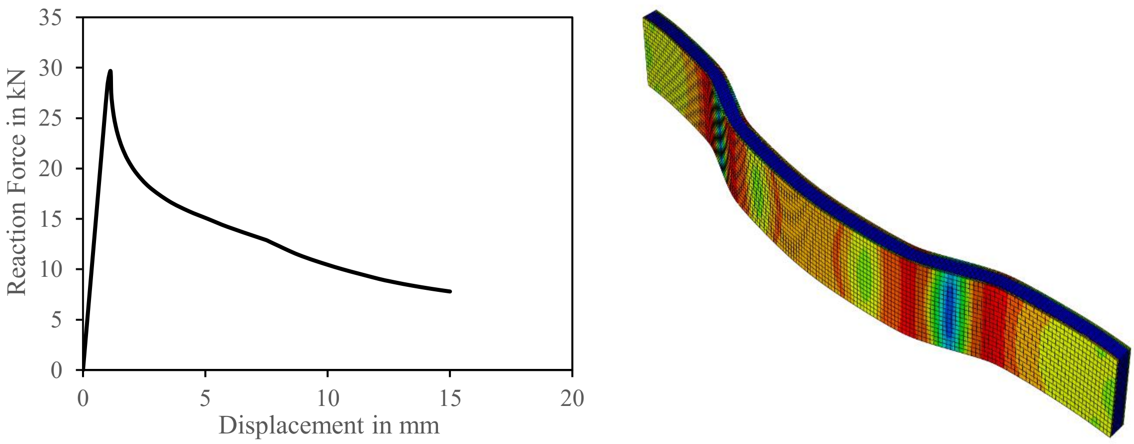

Figure 6.16: Reaction Force-Displacement Graph and Deformation pattern for 0.217 Al foam sandwich panel with 0.0071t imperfection at centre

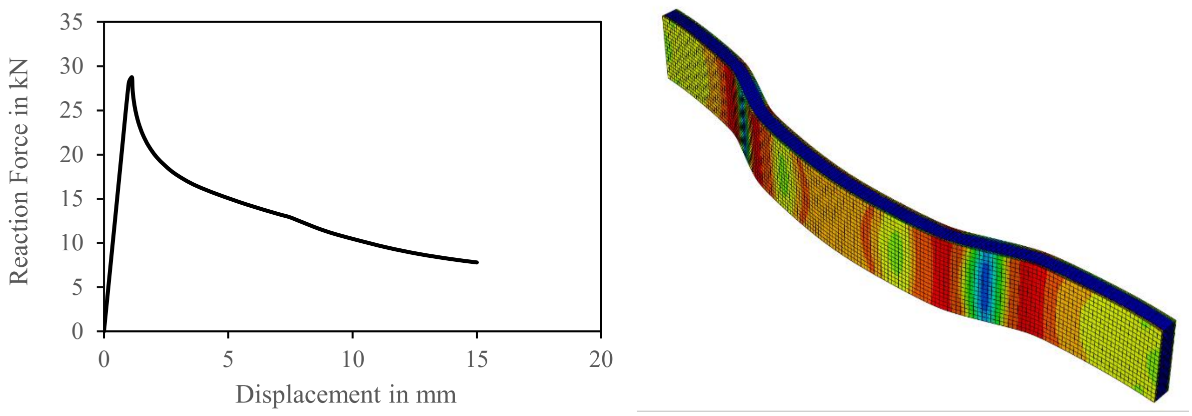

Figure 6.17: Reaction Force-Displacement Graph and Deformation pattern for 0.217 Al foam sandwich panel with 0.0107t imperfection at centre

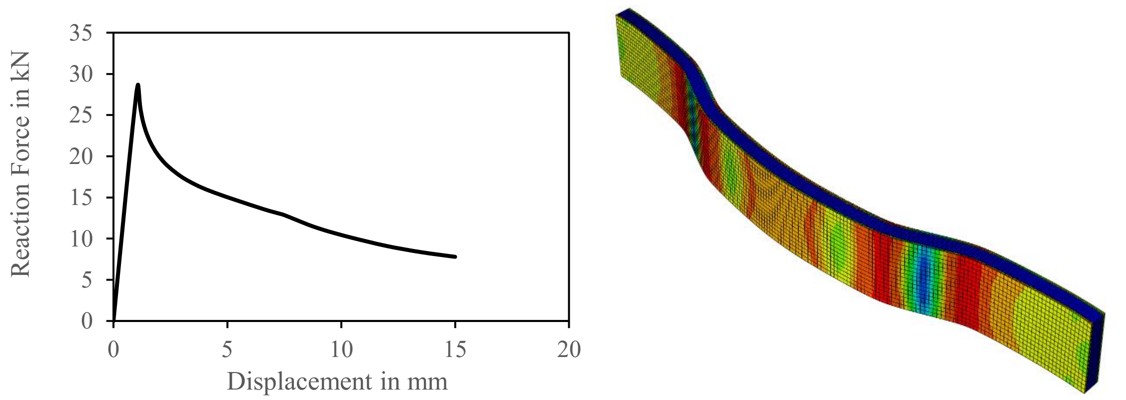

Figure 6.18: Reaction Force-Displacement Graph and Deformation pattern for 0.217 Al foam sandwich panel with 0.025t imperfection at centre

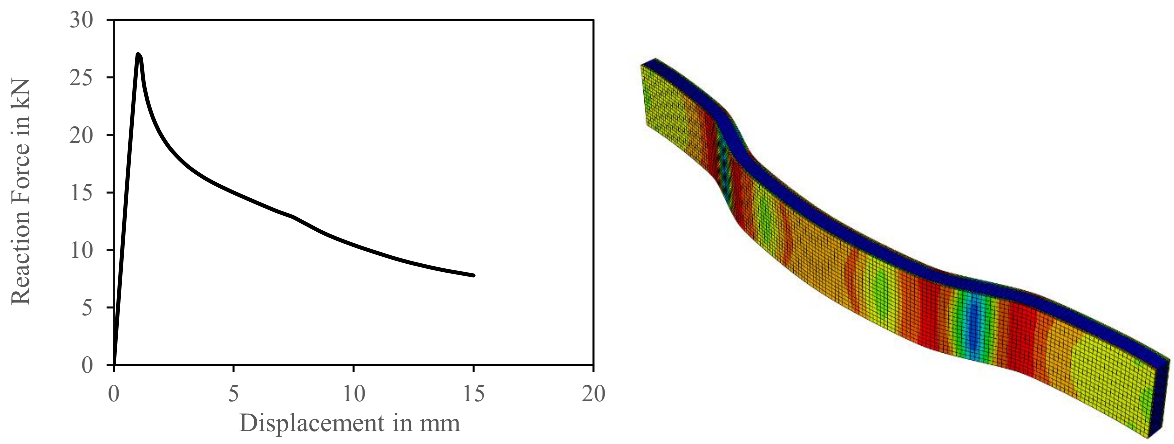

Figure 6.19: Reaction Force-Displacement Graph and Deformation pattern for 0.217 Al foam sandwich panel with 0.0357t imperfection at centre

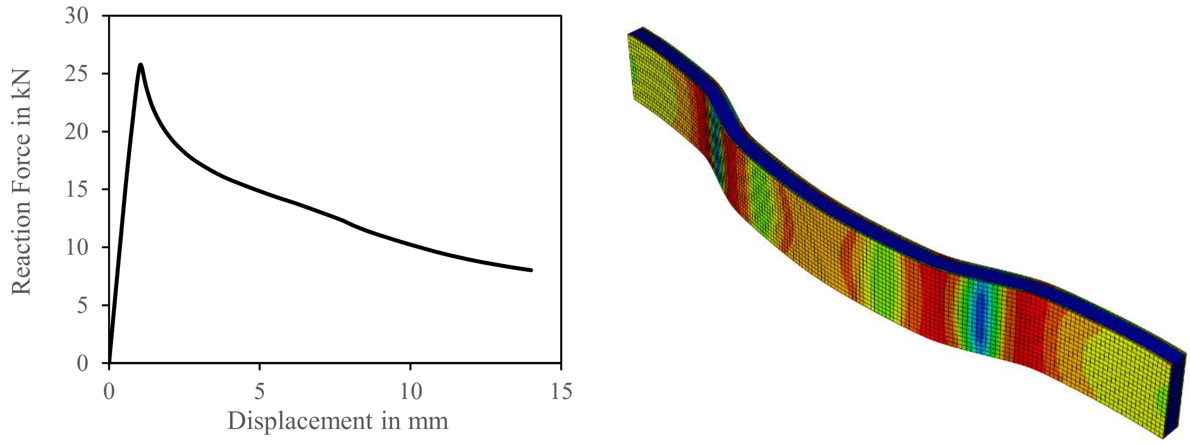

Figure 6.20: Reaction Force-Displacement Graph and Deformation pattern for 0.217 Al foam sandwich panel with 0.0714t imperfection at centre

The 0.217 foam sandwich shows a gradual reduction in normalized peak load as imperfection amplitude increases, although the decrease is less abrupt than in a highly unstable case. The perfect panel exhibits a linear–plateau–drop response with boundary-controlled deformation, while all imperfect panels evolve toward U-shaped localized buckling. Small plateau-like regions in the imperfect curves indicate that mode interaction still occurs, but it is weaker than in the 0.17 foam sandwich and less effective in sustaining post-buckling redistribution. The post-peak softening slope also becomes less negative at larger imperfections, showing that the response becomes more gradual as imperfection amplitude increases. Overall, the panel is moderately imperfection-sensitive: the retained load capacity changes with imperfection amplitude, but the dominant deformation mode remains localized buckling

6.1.4 Aluminium Foam sandwich with 0.25 Relative Density Foam

The influence of the applied initial imperfection amplitude on the structural response of the 0.25 Al foam sandwich panel under axial compression is summarized in Table 6.7.

Table 6.7: Effect of imperfection amplitude on RF behaviour, peak reaction force, and observed deformation mode for 0.25 Al foam sandwich

Imperfection Range	RF Behaviour	Peak RF Values	Deformation Pattern	Interpretation
Without Imperfection	Linear-Plateau rise-Drop Response	59.4 kN	More localized edge-dominated or end-localized deformation pattern,	Higher relative density delays global instability and promotes a less distributed, more boundary-controlled deformation mode

0.0071t to 0.0214t (0.1 to 0.3 mm)	Linear response, broad plateau, and gradual decrease. Initial post peak softening slope is around -0.48 kN/mm	38.2,38,37.9 and 38.2 kN respectively	Multiple wave type deformation. 9 half waves throughout the length. $LE13_{peak\ load}$ - 0.02455 $LE13_{collapse}$- 0.468	Stable progressive buckling with strong load redistribution and sustained post-buckling capacity.
0.025t to 0.0464t (0.35 to 0.65 mm)	Linear rise to peak, followed by abrupt post-peak softening. Initial post peak softening slope is around -58 kN/mm	Peak load reduced from 31.5 kN to 27.7 kN with rise in imperfections	U-shaped global buckling, Localization length-239 mm, $U3_{max}$ -around 4.084 mm, $LE13_{peak\ load}$ - 0.0154	Rapid localization into the dominant buckling mode with little to no post-peak stabilization and abrupt loss of load-carrying capacity
0.05t to 0.0714t (0.7 to 1 mm)	Linear rise to peak, followed by a very short plateau and subsequent softening. Initial post peak softening slope around -10 kN/mm	Peak load reduced from 28.7 kN to 26.4 with rise in imperfections	U-shaped global buckling Localization length-239 mm, $U3_{max}$ -reduced from 6.38 to 4.57 mm with rise in impf's, $LE13_{peak\ load}$ – reduced from 0.02407 to 0.02076	Rapid localization into the dominant buckling mode, with weak post-peak stabilization and limited load redistribution before progressive softening

Table 6.8 summarizes the peak reaction force responses of the specimens and their corresponding imperfection amplitudes.

Table 6.8: Variation of peak reaction force of 0.25 Al foam sandwich panel across various imperfection amplitude in comparison with imperfection free sandwich panel

Sample ID	P_{max} in kN	P_{max}/P_0	Imperfection amplitude
RD025-I0.10	38.2	0.643098	0.0071t
RD025-I0.15	38.1	0.641414	0.0107t
RD025-I0.20	38	0.639731	0.0143t
RD025-I0.25	37.9	0.638047	0.0179t
RD025-I0.30	38.2	0.643098	0.0214t
RD025-I0.35	31.5	0.530303	0.025t
RD025-I0.40	31.6	0.531987	0.0286t
RD025-I0.45	31.4	0.52862	0.0321t
RD025-I0.50	31	0.521886	0.0357t
RD025-I0.55	30.8	0.518519	0.0393t
RD025-I0.60	29.7	0.5	0.0429t
RD025-I0.65	27.7	0.46633	0.0464t

RD025-I0.70	28.7	0.483165	0.05t
RD025-I0.75	27.7	0.46633	0.0536t
RD025-I0.80	27.4	0.461279	0.0571t
RD025-I0.85	27.4	0.461279	0.0607t
RD025-I0.90	27.3	0.459596	0.0643t
RD025-I0.95	27.2	0.457912	0.0679t
RD025-I1	27	0.454545	0.0714t

Figure 6.21 shows the variation in the peak reaction force with the imperfection amplitude for the $\rho^* = 0.25$ foam sandwich panel. The corresponding reaction force behaviours and deformation patterns for the representative imperfection levels are shown in Figures 6.22 to 6.27, providing visual evidence of the buckling transition and the associated changes in the load-carrying response.

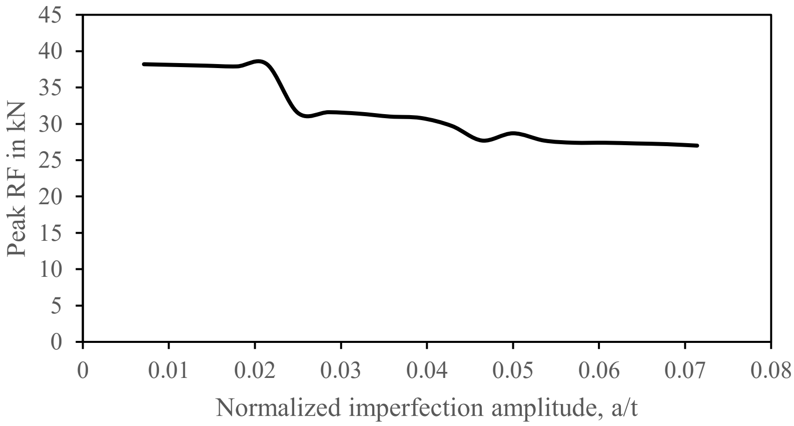

Figure 6.21: Graph showing Variation of Peak Reaction Force with Imperfection Amplitude for 0.25 relative density Al foam sandwich

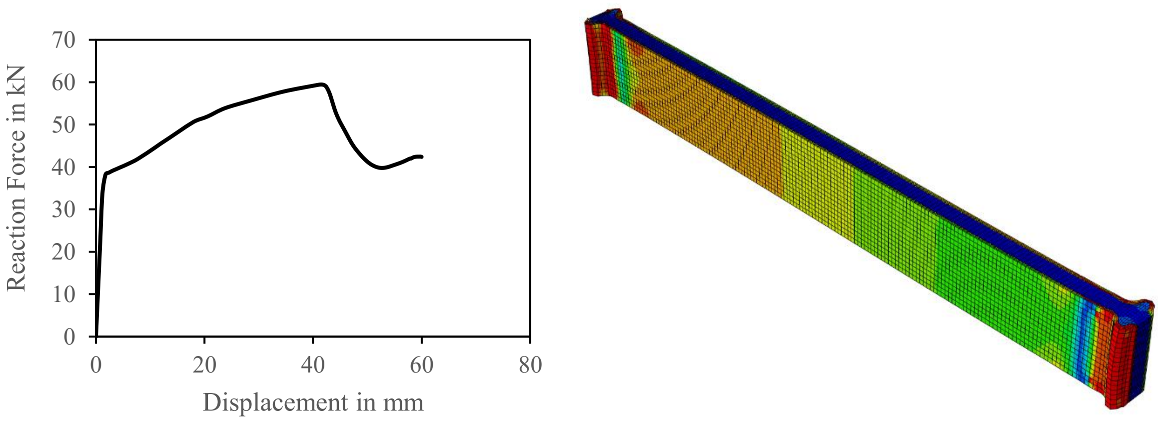

Figure 6.22: Reaction Force-Displacement Graph and Deformation pattern for 0.25 Al foam sandwich panel without imperfection (baseline)

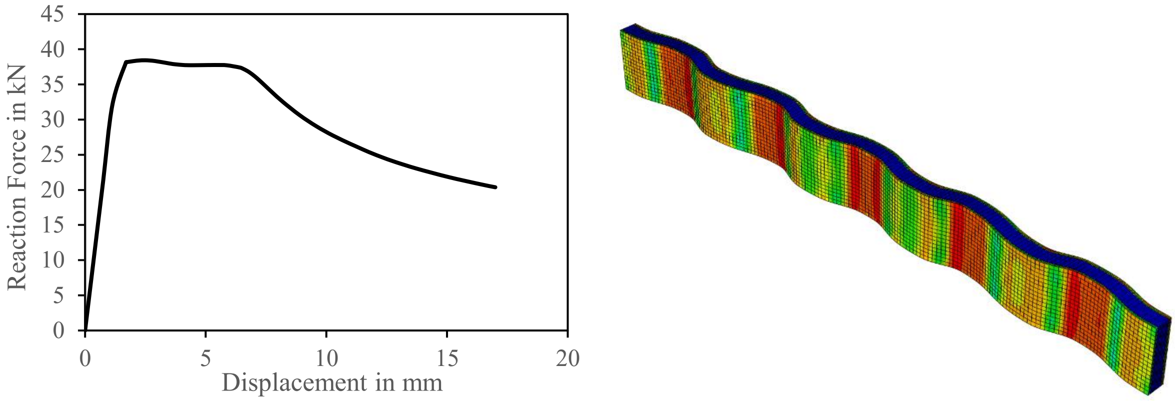

Figure 6.23: Reaction Force Graph and deformation pattern for 0.25 Al foam sandwich panel with 0.0071t imperfection at centre

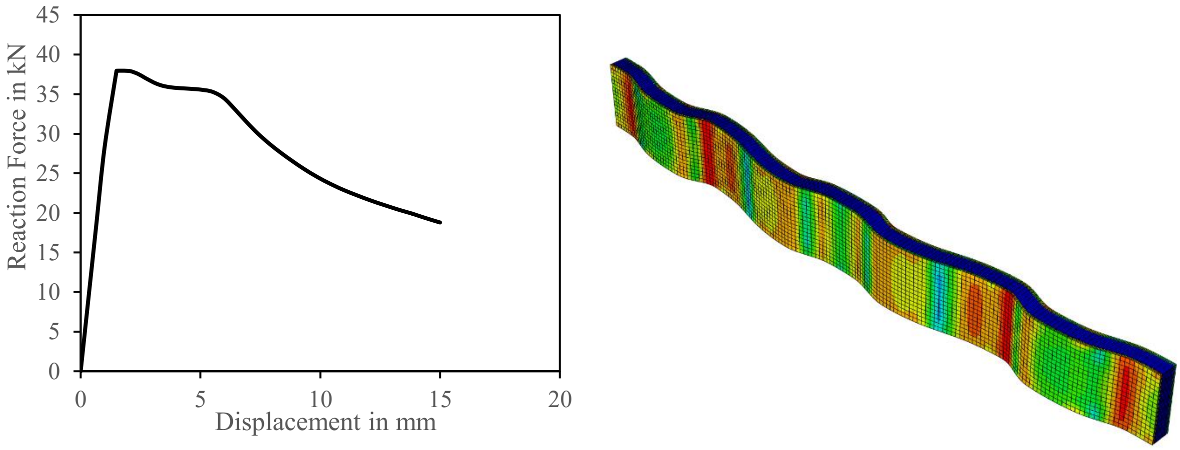

Figure 6.24: Reaction Force Graph and deformation pattern for 0.25 Al foam sandwich panel with 0.0179t imperfection at centre

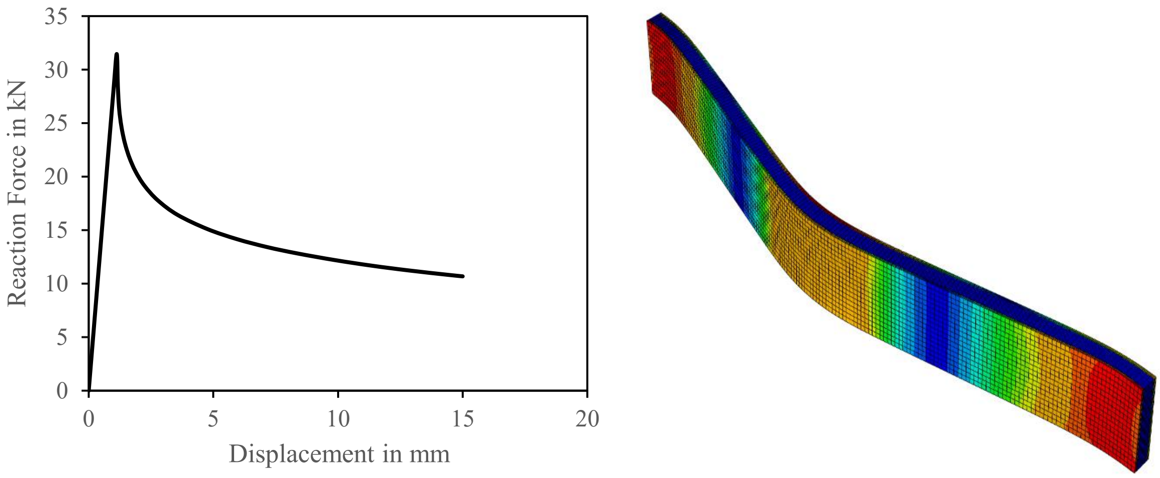

Figure 6.25: Reaction Force-Displacement Graph and Deformation pattern for 0.25 Al foam sandwich panel with 0.025t imperfection at centre

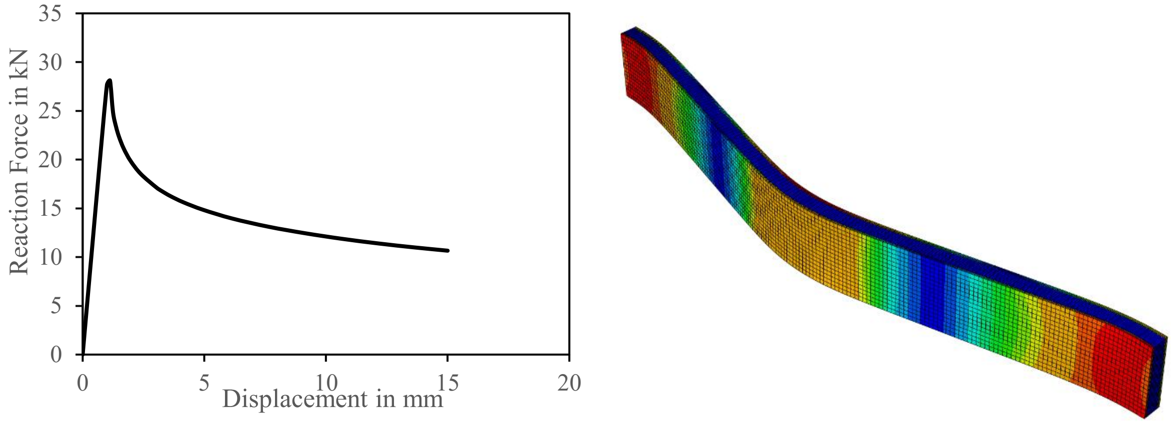

Figure 6.26: Reaction Force Graph and deformation pattern for 0.25 Al foam sandwich panel with 0.05t imperfection at centre

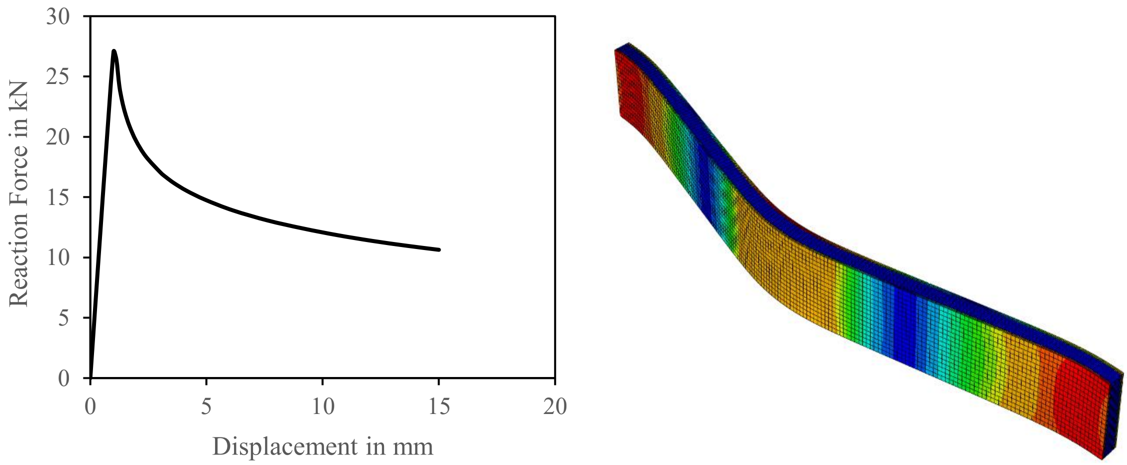

Figure 6.27: Reaction Force-Displacement Graph and deformation pattern for 0.25 Al foam sandwich panel with 0.0714t imperfection at centre

The 0.25 foam sandwich shows a clear imperfection-sensitive response with two distinct regimes. In the perfect case, the panel reaches the highest peak load and deforms in a boundary-controlled, edge-dominated mode, indicating delayed global instability. For low imperfection amplitudes from 0.0071t to 0.0214t, the normalized peak load remains nearly constant, showing a stable load-redistribution window in which multiple-wave buckling and mode interaction are sustained. Once the imperfection amplitude exceeds about 0.025t, the normalized peak load drops noticeably and then decreases gradually with further increase in imperfection, accompanied by a transition to localized U-shaped buckling. In this higher-imperfection regime, mode interaction becomes shorter-lived and less effective, so the response is increasingly governed by imperfection-induced localization rather than distributed buckling. Overall, the 0.25 panel retains a stronger stabilization window at small imperfections than the lower-density panels, but this benefit diminishes once the response enters the localization-dominated regime.

6.1.5 Aluminium Foam sandwich with 0.262 Relative Density Foam

The influence of the applied initial imperfection amplitude on the structural response of the 0.262 Al foam sandwich panel under axial compression is summarized in Table 6.9.

Table 6.9: Effect of imperfection amplitude on RF behaviour, peak reaction force, and observed deformation mode for 0.262 Al foam sandwich

Imperfection Range	RF Behaviour	Peak RF Values	Deformation Pattern	Interpretation
Without Imperfection	Linear-Plateau rise-Drop Response	60.2 kN	More localized edge-dominated or end-localized deformation pattern,	Higher relative density delays global instability and promotes a less distributed, more boundary-controlled deformation mode
0.0071t to 0.0107t (0.1 to 0.15 mm)	A linear rise followed by gradual softening. Initial post peak softening slope is about -1.01 kN/mm	Peak RF values re 37.9 and 38kN respectively	Emerging wave type deformation. Five numbers of Emerging waves throughout the length. $LE13_{peak\ load}$ – 0.00194 $LE13_{collapse}$-0.29	Progressive distributed buckling with continuing load redistribution and no abrupt post-peak instability. The emerging waves suggest the evolution of a distributed buckling pattern rather than a sudden localized collapse
0.0143t (0.2 mm)	A linear rise followed by a pronounced plateau, with no fully developed post-plateau drop within the converged range.	41.8 k N	Onset of instability without a fully developed global buckling shape.	Transitional imperfection case showing strong crush resistance, but the post-peak instability branch was not fully traced
0.0179t (0.25 mm)	A linear rise followed by a plateau and then a gradual drop. Initial post peak softening slope is about -1.29 kN/mm	38.8 kN	Multiple wave type deformation. Seven half-waves throughout the length. $LE13_{peak\ load}$- 0.028 $LE13_{collapse}$ - 0.3196	Relative to the 0.2 imperfection case, the 0.25 case exhibits a similar distributed buckling mechanism, but with reduced plateau strength, indicating weaker sustained resistance despite continued load redistribution
0.0214t (0.3 mm)	Linear rise, short plateau, then immediate drop. Initial post peak softening slope is about -23.7 kN/mm	29.7 kN	U-shaped global buckling, Localization length-239 mm, $U3_{max}$ -4.543 mm, $LE13_{peak\ load}$ - 0.00974	Rapid localization of instability and early loss of stiffness lead to a less stable post-buckling response.

0.025t (0.35 mm)	Linear rise, short plateau, followed by a gradual post-peak drop. Initial post peak softening slope is about -1.66 kN/mm	38.4 kN	Emerging wave type deformation. Seven numbers of half-waves along the length. $LE13_{peak\ load}$ - 0.03867 $LE13_{collapse}$ – 0.285	Three buckle waves develop along the length, indicating progressive mode interaction and distributed instability before softening
0.0286t to 0.0321t (0.4 to 0.45 mm)	A linear rise followed by a sudden drop. Initial post peak softening slope is about -47.8 kN/mm	33.1 and 31.4 kN respectively	U-shaped global buckling, Localization length-246 mm, $U3_{max}$ - 0.059 mm, $LE13_{peak\ load}$ - 0.0002	Rapid U-shaped global buckling with limited post-buckling stability, indicating early loss of stiffness and poor load redistribution.
0.0357t (0.5 mm)	Linear rise, short rising plateau and sudden post-peak drop. Initial post peak softening slope is about -32.51 kN/mm	30.2 kN	U-shaped global buckling, Localization length-239 mm, $U3_{max}$ -4.051 mm, $LE13_{peak\ load}$ - 0.00946	Intermediate U-shaped global buckling with limited but noticeable load redistribution before rapid instability. This may be due to the presence of very weak mode interaction in this imperfection window
0.0393t (0.55 mm)	Linear rise followed by sudden drop Initial post peak softening slope is about -38.76 kN/mm	31.9 kN	U-shaped global buckling, Localization length-239 mm, $U3_{max}$ – 2.96 mm, $LE13_{peak\ load}$ - 0.00794	Rapid U-shaped global buckling with limited post-buckling stability, indicating early loss of stiffness and poor load redistribution.
0.0429t to 0.0714t (0.6 to 1 mm)	Linear rise, short plateau, and immediate collapse. Initial post peak softening changes from -23.6 kN/mm to -8.82 kN/mm	Peak value decreases from 29.5 to 27.9 kN with imperfections	U-shaped global buckling, Localization length-239 mm, $U3_{max}$ – increases from 4.2 to 6.159 mm, $LE13_{peak\ load}$ – increases from 0.00988 to 0.01298	Rapid U-shaped global buckling with weak mode interaction and limited load redistribution, leading to early instability and sudden loss of load-carrying capacity

Table 6.10 summarizes the peak reaction force responses of the specimens, along with their corresponding imperfection amplitudes.

Table 6.10: Variation of peak reaction force of 0.262 Al foam sandwich panel across various imperfection amplitude in comparison with imperfection free sandwich panel

Sample ID	P_{max}	P_{max}/P_0	Imperfection Amplitude
RD0262-I0.10	37.9	0.629568	0.0071t
RD0262-I0.15	38	0.631229	0.0107t
RD0262-I0.20	41.8	0.694352	0.0143t
RD0262-I0.25	38.8	0.644518	0.0179t
RD0262-I0.30	29.7	0.493355	0.0214t
RD0262-I0.35	38.4	0.637874	0.025t
RD0262-I0.40	33.1	0.549834	0.0286t
RD0262-I0.45	31.4	0.521595	0.0321t
RD0262-I0.50	30.2	0.501661	0.0357t
RD0262-I0.55	31.9	0.5299	0.0393t
RD0262-I0.60	29.5	0.490033	0.0429t
RD0262-I0.65	29.2	0.48505	0.0464t
RD0262-I0.70	28.9	0.480066	0.05t
RD0262-I0.75	28.7	0.476744	0.0536t
RD0262-I0.80	28.5	0.473422	0.0571t
RD0262-I0.85	28.3	0.4701	0.0607t
RD0262-I0.90	28.1	0.466777	0.0643t
RD0262-I0.95	27.9	0.463455	0.0679t
RD0262-I1	27.9	0.463455	0.0714t

Figure 6.28 shows the variation in the peak reaction force with the imperfection amplitude for the $\rho^* = 0.262$ foam sandwich panel. The corresponding reaction force behaviours and deformation patterns for the representative imperfection levels are shown in Figures 6.29 - 6.39, providing visual evidence of the buckling transition and the associated changes in the load-carrying response.

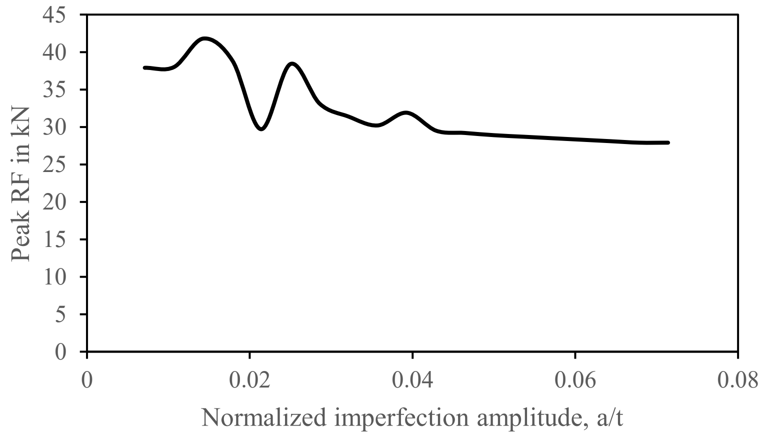

Figure 6.28: Graph showing Variation of Peak Reaction Force with Imperfection Amplitude for 0.262 relative density Al foam sandwich

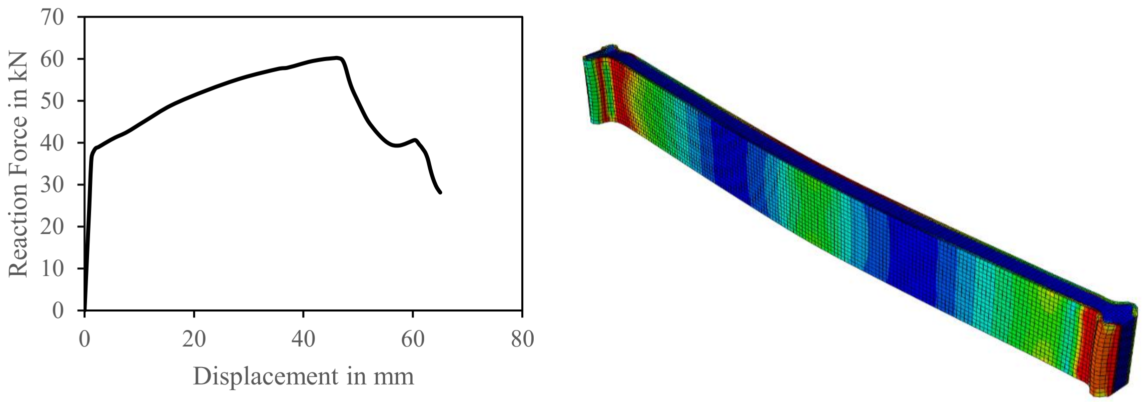

Figure 6.29: Reaction Force-Displacement Graph and deformation pattern for 0.262 Al foam sandwich panel without imperfection (baseline)

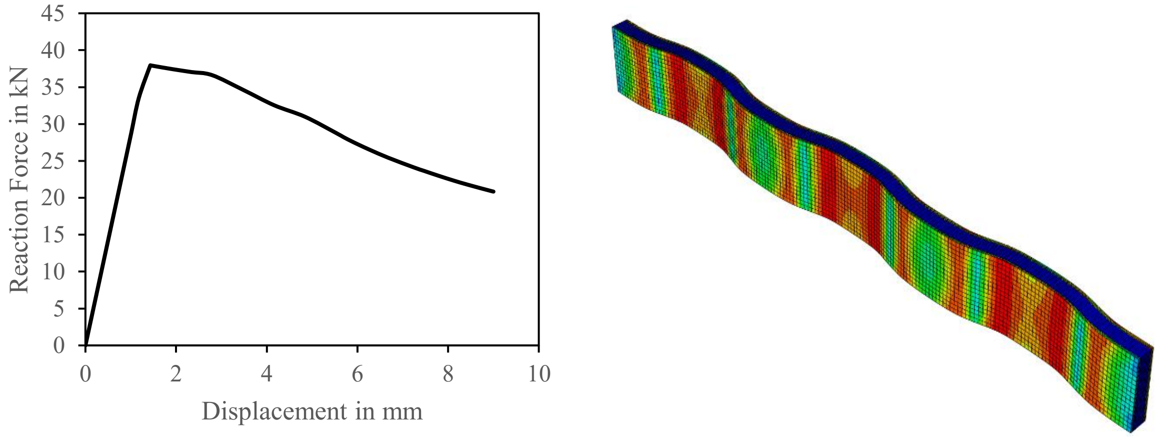

Figure 6.30: Reaction Force-Displacement Graph and deformation pattern for 0.262 Al foam sandwich panel with 0.0071t imperfection at centre

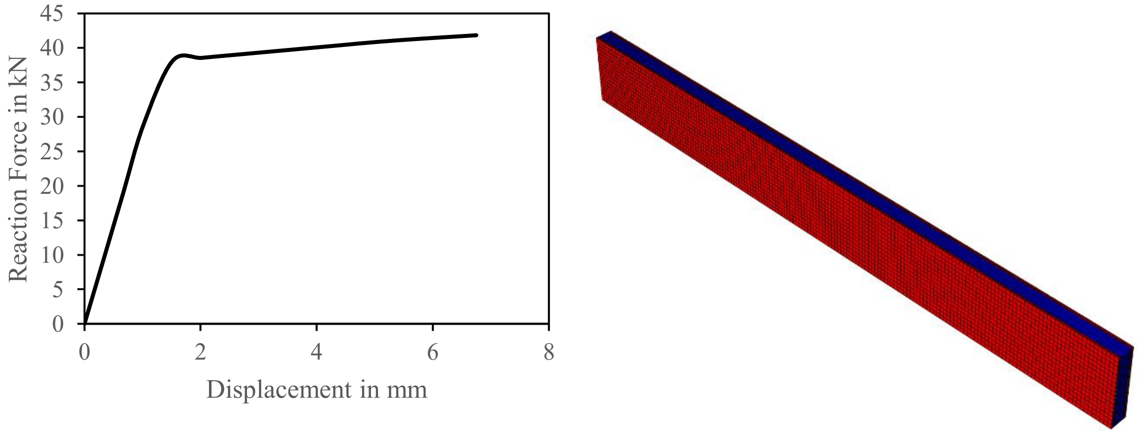

Figure 6.31: Reaction Force-Displacement Graph and deformation pattern for 0.262 Al foam sandwich panel with 0.0143t imperfection at centre

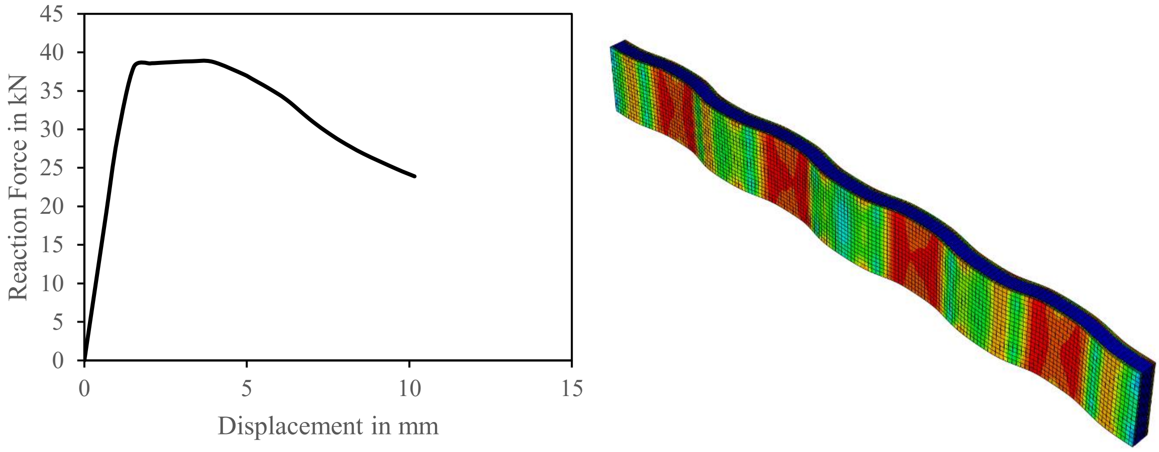

Figure 6.32: Reaction Force-Displacement Graph and deformation pattern for 0.262 Al foam sandwich panel with 0.0179t imperfection at centre

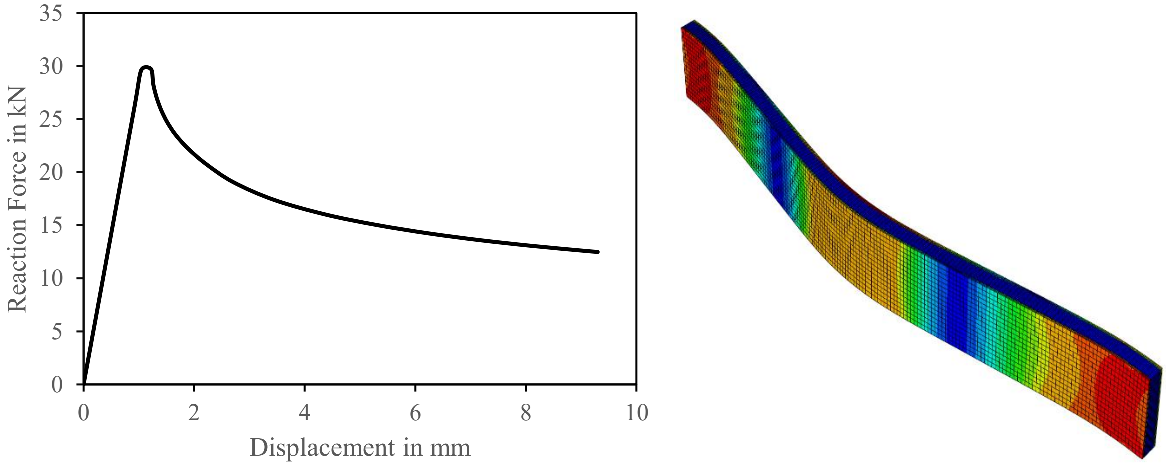

Figure 6.33: Reaction Force-Displacement Graph and deformation pattern for 0.262 Al foam sandwich panel with 0.0214t imperfection at centre

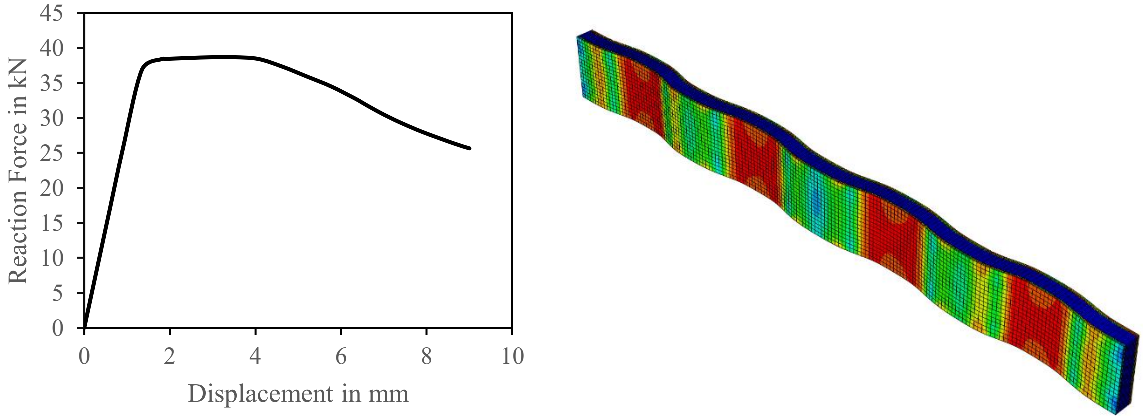

Figure 6.34: Reaction Force-Displacement Graph and deformation pattern for 0.262 Al foam sandwich panel with 0.025t imperfection at centre

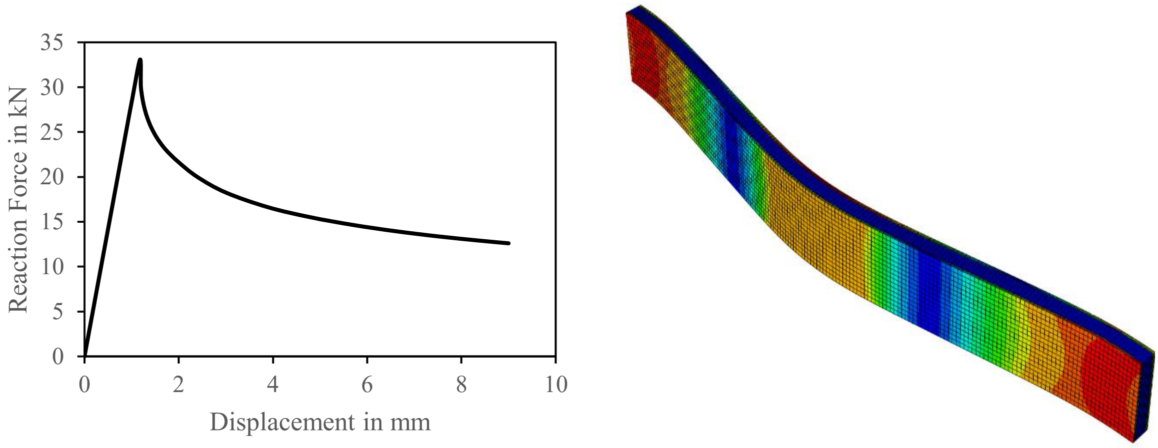

Figure 6.35: Reaction Force-Displacement Graph and deformation pattern for 0.262 Al foam sandwich panel with 0.0286t imperfection at centre

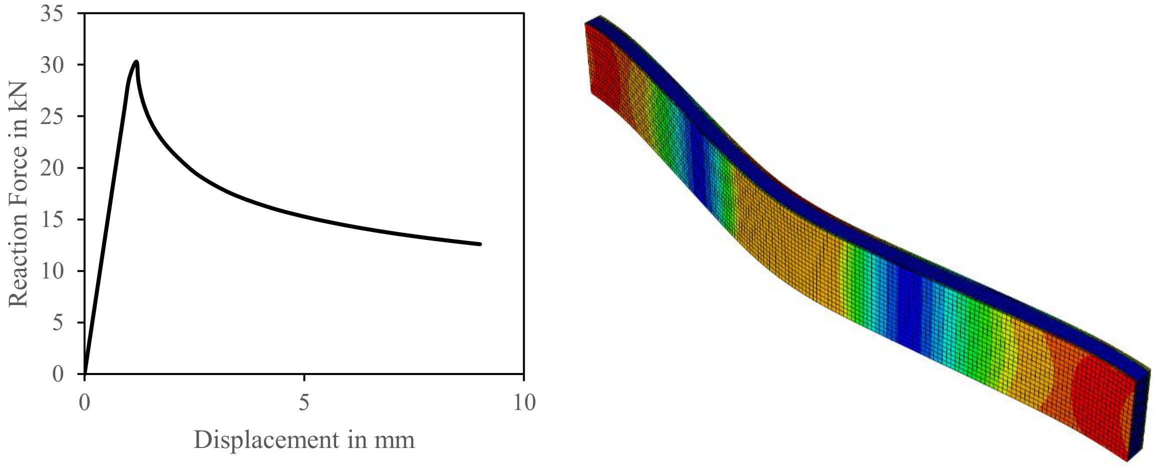

Figure 6.36: Reaction Force-Displacement Graph and deformation pattern for 0.262 Al foam sandwich panel with 0.0357t imperfection at centre

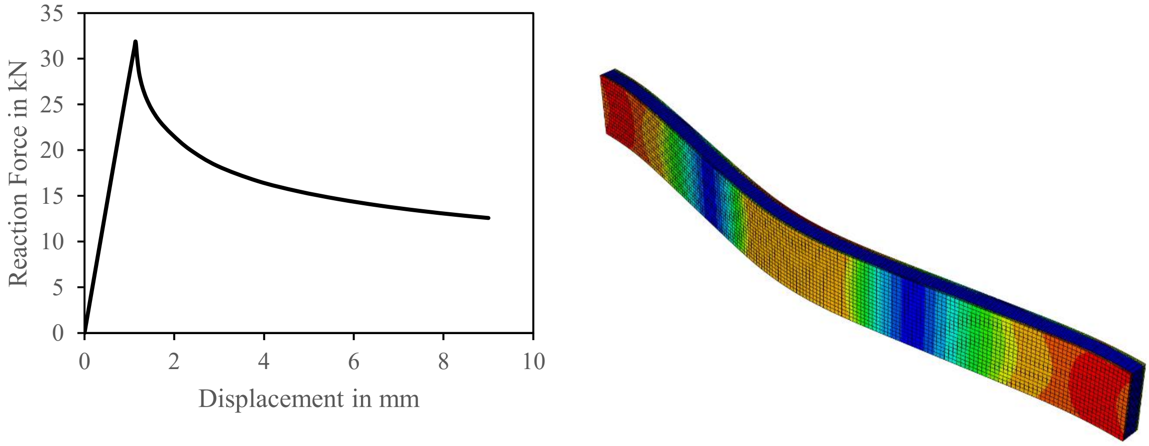

Figure 6.37: Reaction Force-Displacement Graph and deformation pattern for 0.262 Al foam sandwich panel with 0.0393t imperfection at centre

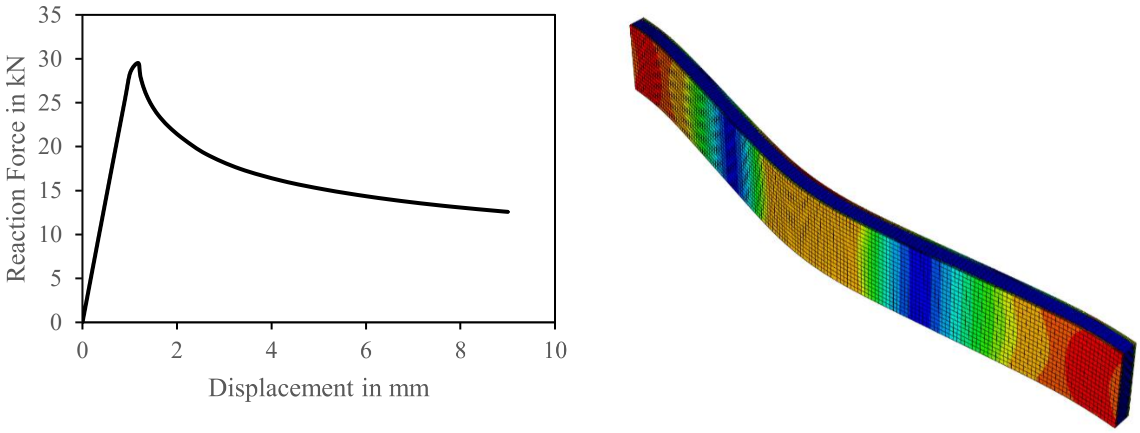

Figure 6.38: Reaction Force-Displacement Graph and deformation pattern for 0.262 Al foam sandwich panel with 0.0429t imperfection at centre

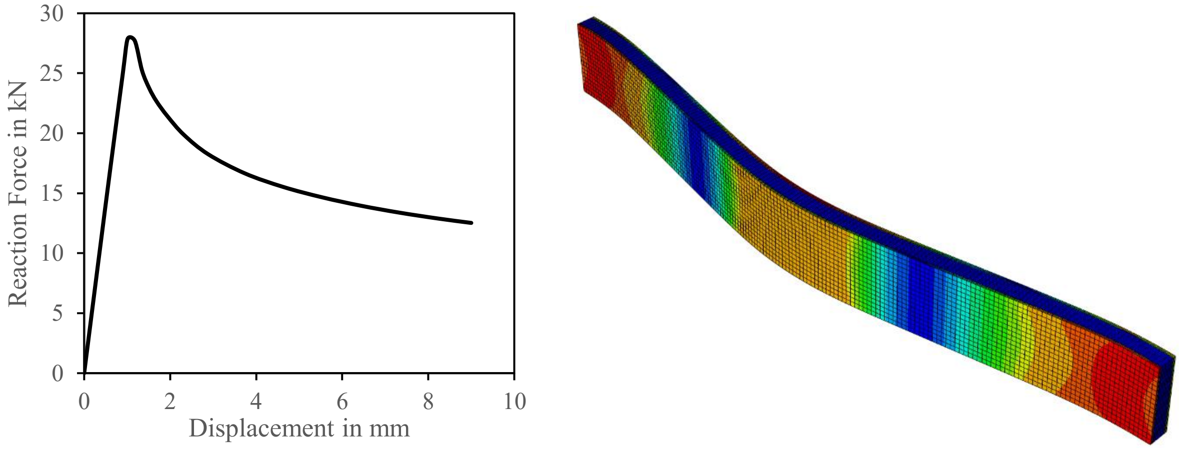

Figure 6.39: Reaction Force-Displacement Graph and deformation pattern for 0.262 Al foam sandwich panel with 0.0714t imperfection at centre

The 0.262 foam sandwich exhibits moderate imperfection sensitivity, with a clear transition in both peak load and deformation mode as imperfection amplitude increases. In the perfect case, the panel is boundary-dominated and reaches the highest peak load, while the imperfect cases initially retain a high fraction of this capacity through temporary load redistribution. At low imperfection amplitudes, the response is governed by distributed or multiple-wave buckling, and the normalized peak load remains relatively high, with a local maximum at 0.0143t. This indicates that mode interaction is active in this range and can temporarily enhance load-carrying efficiency. Beyond approximately 0.0214t, the retained capacity decreases and the response shifts toward imperfection-driven localization, with shorter plateaus, faster post-peak softening, and more direct development of U-shaped buckling. Overall, the 0.262 panel remains more stable than the lower-imperfection-localized cases, but the benefit of mode interaction diminishes as the imperfection amplitude increases.

6.1.6 Aluminium Foam sandwich with 0.308 Relative Density Foam

The influence of the applied initial imperfection amplitude on the structural response of the 0.308 Al foam sandwich panel under axial compression is summarized in Table 6.11.

Table 6.11: Effect of imperfection amplitude on RF behaviour, peak reaction force, and observed deformation mode for 0.308 Al foam sandwich

Imperfection Range	RF Behaviour	Peak RF Values	Deformation Pattern	Interpretation
Without Imperfection	Linear-Plateau rise-Drop Response	63.7 kN	More localized edge-dominated or end-localized deformation pattern,	Higher relative density delays global instability and promotes a less distributed, more boundary-controlled deformation mode
0.0071t to 0.0107t (0.1 to 0.15 mm)	A linear rise followed by an upward plateau and then a gradual softening. Initial post peak softening slope around -0.3 kN/mm	Peak RF value is 47.6 in both cases	Multiple wave type deformation. Seven short half-waves throughout the length. $LE13_{peak\ load}$ – 0.0328 $LE13_{collapse}$ -0.198	Progressive multi-wave buckling with strong mode interaction and effective load redistribution, leading to a sustained post-buckling response before softening
0.0143t (0.2 mm)	Linear rise followed by gradual softening with initial peak softening slope -0.5 kN/mm	44.4 k N	Emerging wave type deformation. Five half-waves throughout the length. $LE13_{peak\ load}$ – 0.0013 $LE13_{collapse}$ -0.5875	Emerging waves indicate progressively distributed buckling and continued stress redistribution, as the panel evolves toward a more stable post-buckling equilibrium path.
0.0179t to 0.0286t (0.25 to 0.4 mm)	Linear rise, upward plateau, then gradual softening with initial peak softening slope around -0.42 kN/mm	47 and 46.9 kN	Multiple wave type deformation. Nine short half-waves throughout the length. $LE13_{peak\ load}$ – 0.08517 $LE13_{collapse}$ -0.174.	Multiple-wave distributed buckling with strong mode interaction; this second imperfection-sensitive window of the sandwich produces temporary stiffness enhancement and improved load-carrying capacity before softening

0.0321t (0.45 mm)	Linear rise followed by gradual post-peak softening with initial peak softening slope around -0.25 kN/mm	38.2 kN	Emerging wave type deformation. Five short half-waves throughout the length. $LE13_{peak\ load}$ – 0.003617 $LE13_{collapse}$ -0.578	The RF response shows linear loading followed by a plateau and gradual post-peak softening, while the emerging waves indicate progressive distributed instability and stress redistribution toward a new post-buckling equilibrium path
0.0357t to 0.0714t (0.5 to 1 mm)	Linear rise followed by sudden drop, with initial post peak softening slope raising from -50 kN/mm to -11 kN/mm	Peak RF value reduces from 33.8 kN to 28.3 kN with increase in imperfection	U-shaped global buckling, Localization length-239 mm, $U3_{max}$ – increases from 2 to 5.217 mm, $LE13_{peak\ load}$ – increases from 0.00408 to 0.008	Rapid U-shaped global buckling with no mode interaction, leading to early instability and sudden loss of load-carrying capacity

Table 6.12 summarizes the peak reaction force responses of the specimens, together with their corresponding imperfection amplitudes.

Table 6.12: Variation of peak reaction force of 0.308 Al foam sandwich panel across various imperfection amplitude in comparison with imperfection free sandwich panel

Sample ID	P_{max} in kN	P_{max}/P_0	Imperfection Amplitude
RD0308-I0.10	47.6	0.74725275	0.0071t
RD0308-I0.15	47.6	0.74725275	0.0107t
RD0308-I0.20	38.3	0.60125589	0.0143t
RD0308-I0.25	47	0.73783359	0.0179t
RD0308-I0.30	46.9	0.73626374	0.0214t
RD0308-I0.35	47.3	0.74254317	0.025t
RD0308-I0.40	46.8	0.73469388	0.0286t
RD0308-I0.45	38.2	0.59968603	0.0321t
RD0308-I0.50	33.8	0.53061224	0.0357t
RD0308-I0.55	32.1	0.50392465	0.0393t
RD0308-I0.60	31.5	0.49450549	0.0429t
RD0308-I0.65	31.1	0.48822606	0.0464t
RD0308-I0.70	29.4	0.46153846	0.05t
RD0308-I0.75	29.2	0.45839874	0.0536t
RD0308-I0.80	29	0.45525903	0.0571t
RD0308-I0.85	28.8	0.45211931	0.0607t
RD0308-I0.90	28.7	0.45054945	0.0643t
RD0308-I0.95	28.5	0.44740973	0.0679t
RD0308-I1	28.3	0.44427002	0.0714t

Figure 6.40 shows the variation in the peak reaction force with the imperfection amplitude for the $\rho^* = 0.308$ foam sandwich panel. The corresponding reaction force behavior and deformation patterns for the representative imperfection levels are shown in Figures 6.41 to 6.47, providing visual evidence of the buckling transition and the associated changes in the load-carrying response.

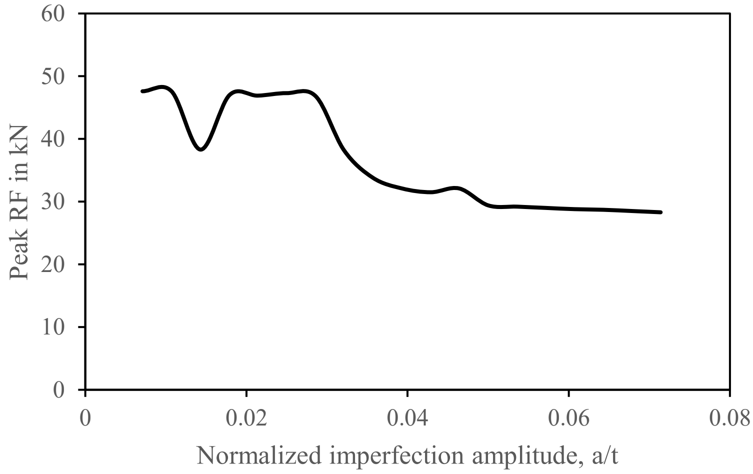

Figure 6.40: Graph showing Variation of Peak Reaction Force with Imperfection Amplitude for 0.308 relative density Al foam sandwich

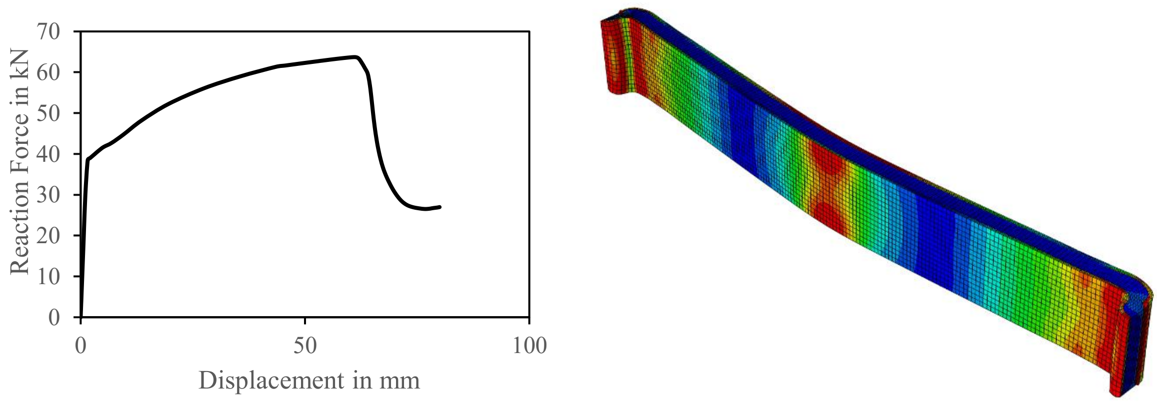

Figure 6.41: Reaction Force-Displacement Graph and Deformation pattern for 0.308 Al foam sandwich panel without imperfection (baseline)

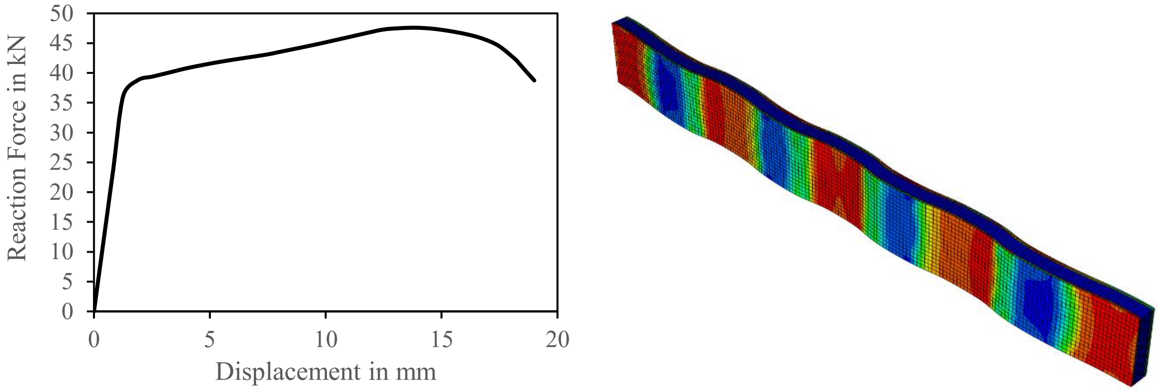

Figure 6.42: Reaction Force Graph and deformation pattern for 0.308 Al foam sandwich panel with 0.0071t imperfection at centre

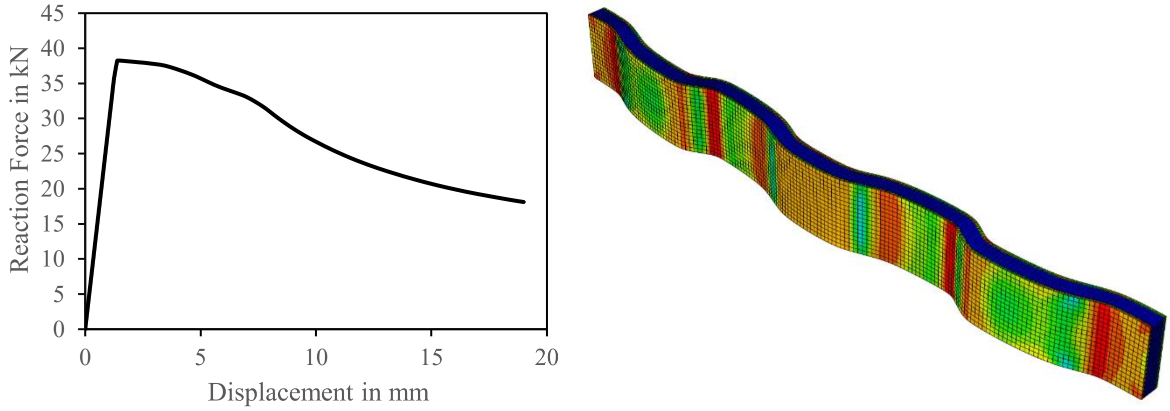

Figure 6.43: Reaction Force-Displacement Graph and Deformation pattern for 0.308 Al foam sandwich panel with 0.0143t imperfection at centre

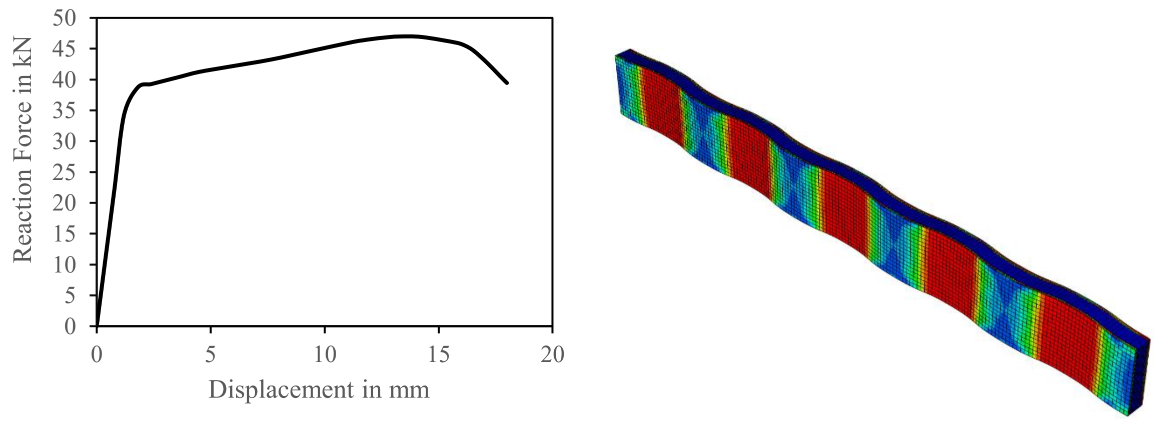

Figure 6.44: Reaction Force-Displacement Graph and Deformation pattern for 0.308 Al foam sandwich panel with 0.0179t imperfection at centre

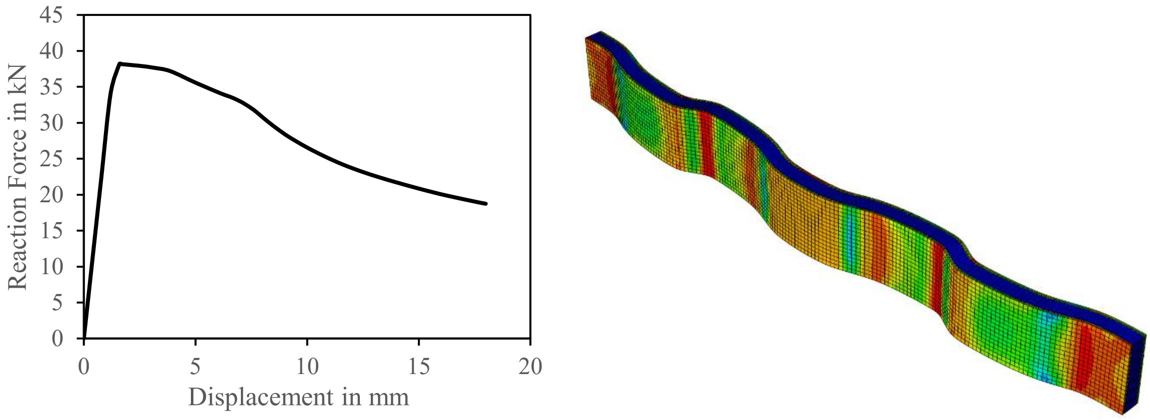

Figure 6.45: Reaction Force-Displacement Graph and Deformation pattern for 0.308 Al foam sandwich panel with 0.0321t imperfection at centre

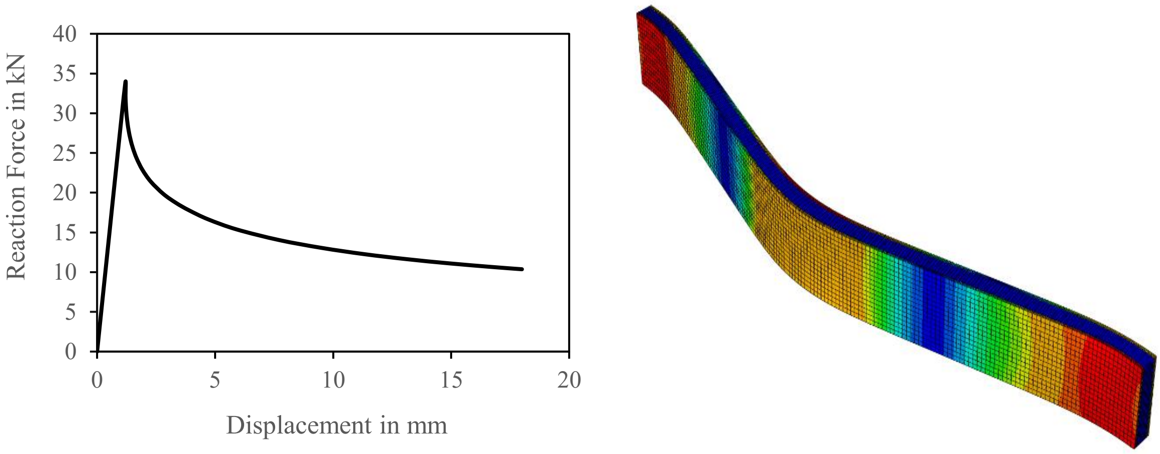

Figure 6.46: Reaction Force-Displacement Graph and Deformation pattern for 0.308 Al foam sandwich panel with 0.0357t imperfection at centre

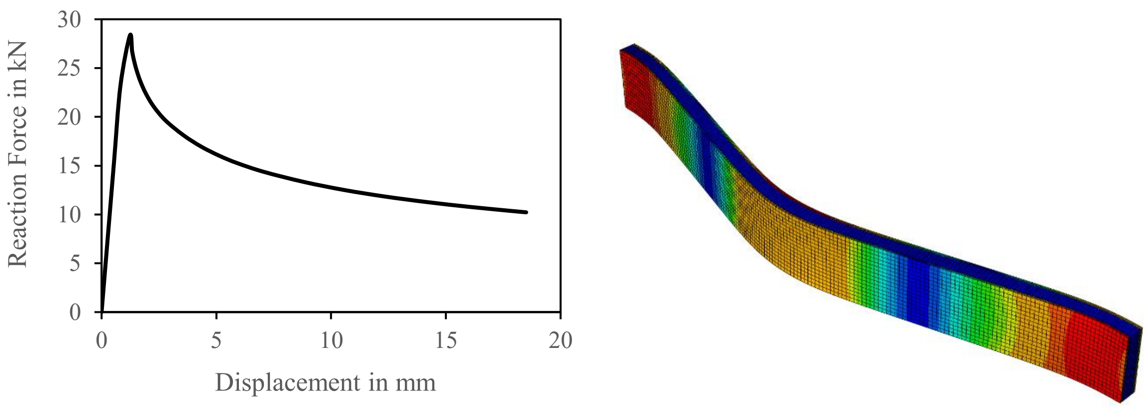

Figure 6.47: Reaction Force-Displacement Graph and Deformation pattern for 0.308 Al foam sandwich panel with 0.0714t imperfection at centre

The 0.308 foam sandwich exhibits a clear imperfection-sensitive buckling response with two distinct regimes. In the perfect case, the panel is boundary-dominated and reaches the highest peak load, indicating delayed global instability. At low imperfection amplitudes, the panel retains a high fraction of its perfect-geometry capacity, with broad plateaus and distributed multi-wave deformation showing that mode interaction remains effective and supports a stable post-buckling path. Beyond a threshold near 0.03t, the normalized peak load drops sharply and then settles into a lower-capacity regime, indicating that the beneficial effect of mode interaction is progressively suppressed and the response becomes increasingly controlled by imperfection-driven localization. The higher-imperfection cases evolve more directly toward U-shaped buckling, with shorter plateaus and faster post-peak softening. Overall, the 0.308 panel shows strong stabilization at low imperfections, but once the threshold is exceeded, the retained capacity decreases more abruptly and the response becomes localization-dominated

6.1.7 Aluminium Foam sandwich with 0.32 Relative Density Foam

The influence of the applied initial imperfection amplitude on the structural response of the 0.32 Al foam sandwich panel under axial compression is summarized in Table 6.13.

Table 6.13: Effect of imperfection amplitude on RF behaviour, peak reaction force, and observed deformation mode for 0.32 Al foam sandwich

Imperfection Range	RF Behaviour	Peak RF Values	Deformation Pattern	Interpretation
Without Imperfection	Linear-Plateau rise-Drop Response	65.2 kN	More localized edge-dominated or end-localized buckling pattern,	Higher relative density delays global instability and promotes a less distributed, more boundary-controlled deformation mode
0.0071t to 0.0179t (0.1 to 0.25 mm)	A linear rise followed by an upward plateau and then a gradual softening. The initial post peak softening slope was around -1.5 kN/mm.	Peak RF value decreases from 42.1 to 41.8 kN with imperfections	Multiple wave type deformation. Nine short half-waves throughout the length. $LE13_{peak\ load}$ – 0.00726 $LE13_{collapse}$ - 0.2603	Multiple-wave distributed buckling with strong mode interaction and effective load redistribution, leading to a sustained post-buckling response before softening
0.0214t to 0.025t (0.3 to 0.35 mm)	Linear rise to peak with a slight pre-peak slope reduction, followed by a	29.6 and 29.4 kN respectively	U-shaped global buckling, Localization length-239 mm,	A linear rise with a brief transitional slope change, indicates weak mode interaction and limited pre-localization load

	collapse. The initial post peak softening slope was around -9 kN/mm.		$U3_{max}$ – 5.561 mm, $LE13_{peak\ load}$ - 0.007297	redistribution before U-shaped global buckling.
0.0286t (0.4 mm)	Linear rise, followed by gradual post-peak softening. The initial post peak softening slope was around -0.20 kN/mm.	38.1 kN	Emerging wave type deformation. Five half-waves throughout the length. $LE13_{peak\ load}$ – 0.002609 $LE13_{collapse}$ - 0.3306	Emerging waves indicate progressive distributed buckling, with the panel redistributing stress along its length and evolving toward a more stable post-buckling equilibrium configuration before gradual softening
0.0321t to 0.0714t (0.45 to 1 mm)	Linear rise followed by sudden drop with initial post peak softening slope incresing from -78 kN/mm to -25 kN/mm	Peak RF value reduces from 34.4 kN to 31.6 kN with increase in imperfection	U-shaped global buckling, Localization length-239 mm, $U3_{max}$ – increases from 0.952 to 3.127 mm, $LE13_{peak\ load}$ – increases from 0.002371 to 0.005622	Rapid U-shaped global buckling with no mode interaction, leading to early instability and sudden loss of load-carrying capacity

Table 6.14 summarizes the peak reaction force responses of the specimens with their corresponding imperfection amplitudes.

Table 6.14: Variation of peak reaction force of 0.308 Al foam sandwich panel across various imperfection amplitude in comparison with imperfection free sandwich panel

Sample ID	P_{max} in kN	P_{max}/P_0	Imperfection Amplitude
RD032-I0.10	42.1	0.645706	0.0071t
RD032-I0.15	42	0.644172	0.0107t
RD032-I0.20	41.9	0.642638	0.0143t
RD032-I0.25	41.8	0.641104	0.0179t
RD032-I0.30	29.6	0.453988	0.0214t
RD032-I0.35	29.4	0.45092	0.025t
RD032-I0.40	38.1	0.584356	0.0286t
RD032-I0.45	34.4	0.527607	0.0321t
RD032-I0.50	34	0.521472	0.0357t
RD032-I0.55	33.4	0.51227	0.0393t
RD032-I0.60	32.3	0.495399	0.0429t
RD032-I0.65	32.2	0.493865	0.0464t
RD032-I0.70	32.2	0.493865	0.05t
RD032-I0.75	32.1	0.492331	0.0536t
RD032-I0.80	32.1	0.492331	0.0571t
RD032-I0.85	32	0.490798	0.0607t

RD032-I0.90	31.9	0.489264	0.0643t
RD032-I0.95	31.8	0.48773	0.0679t
RD032-I1	31.6	0.484663	0.0714t

Figure 6.48 shows the variation in the peak reaction force with imperfection amplitude for the $\rho^* = 0.32$ foam sandwich panel. The corresponding reaction force behavior and deformation patterns for the representative imperfection levels are shown in Figures 6.49 to 6.55, providing visual evidence of the buckling transition and the associated changes in the load-carrying response.

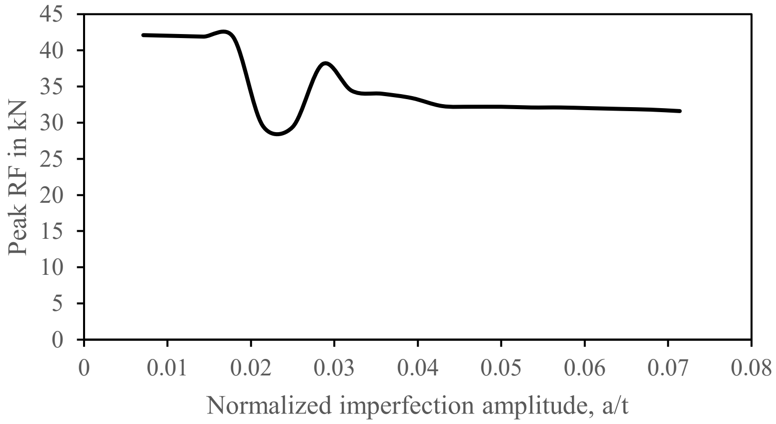

Figure 6.48: Graph showing Variation of Peak Reaction Force with Imperfection Amplitude for 0.32 relative density Al foam sandwich

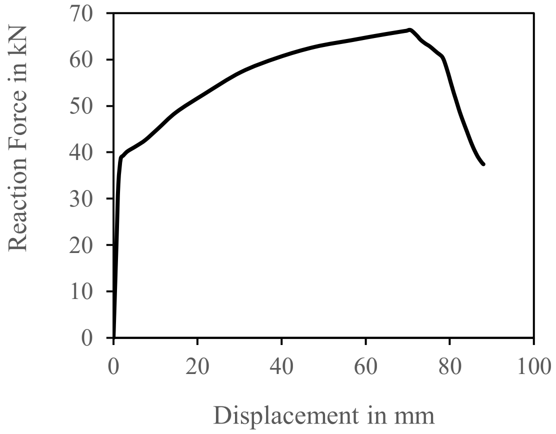

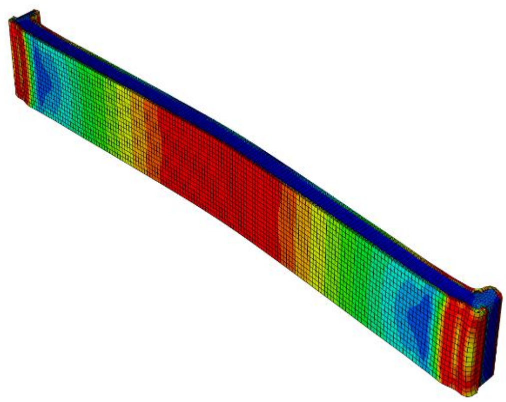

Figure 6.49: Reaction Force Graph and deformation pattern for 0.32 Al foam sandwich panel without imperfection (baseline)

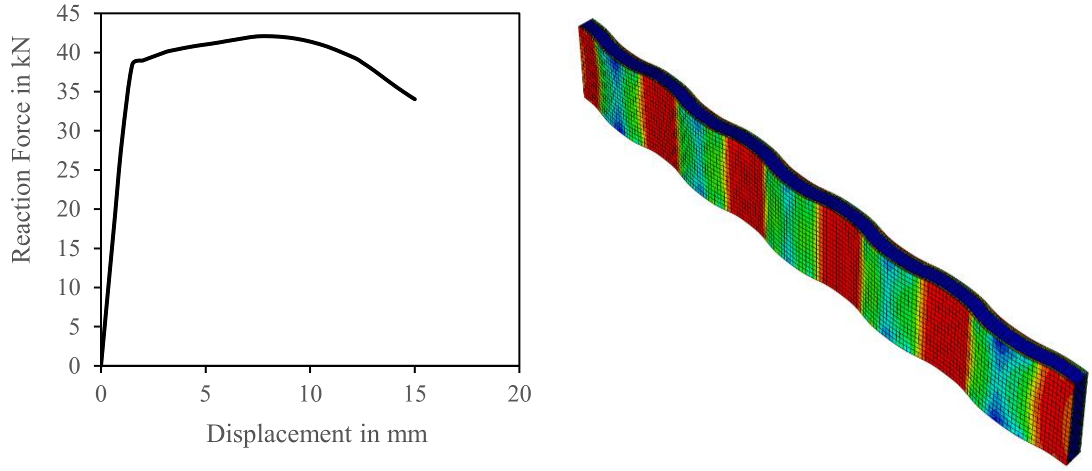

Figure 6.50: Reaction Force Graph and deformation pattern for 0.32 Al foam sandwich panel with 0.0071t imperfection at centre

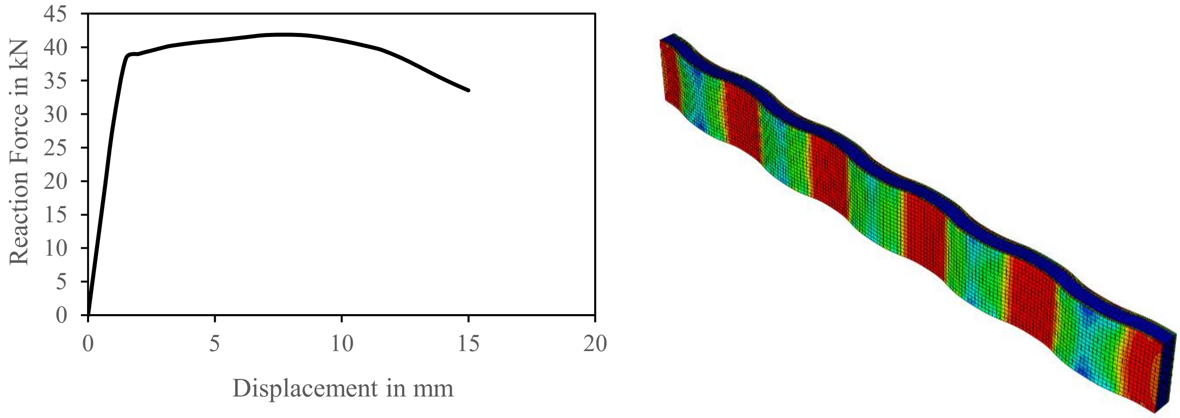

Figure 6.51: Reaction Force Graph and deformation pattern for 0.32 Al foam sandwich panel with 0.0179t imperfection at centre

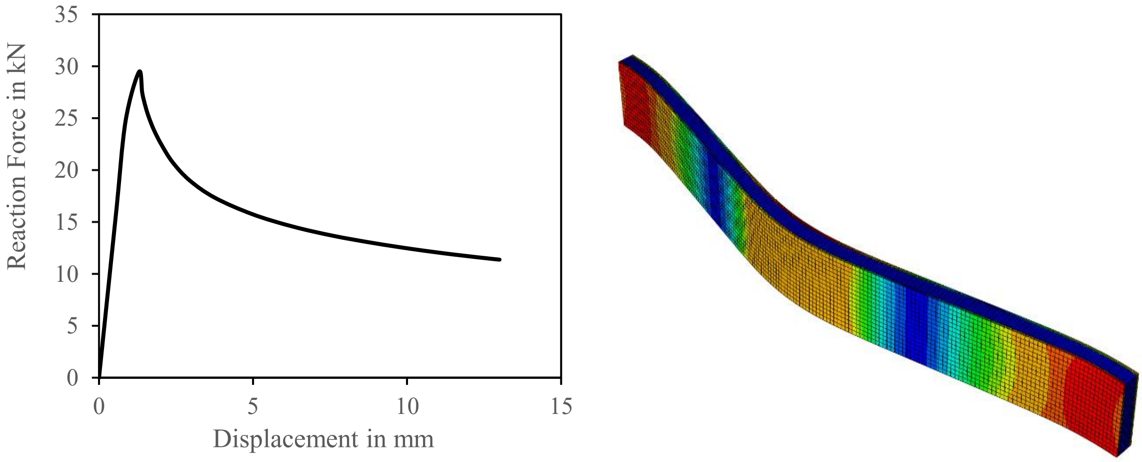

Figure 6.52: Reaction Force Graph and deformation pattern for 0.32 Al foam sandwich panel with 0.025t imperfection at centre

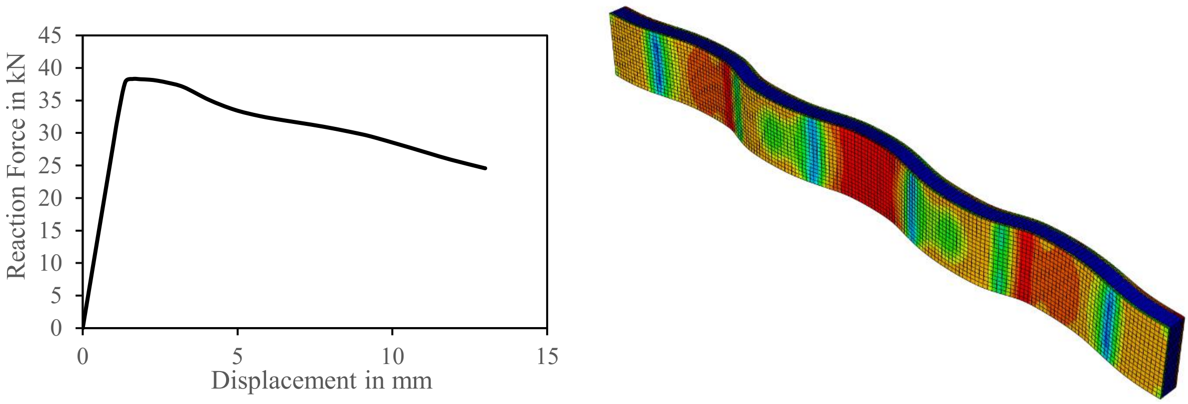

Figure 6.53: Reaction Force Graph and deformation pattern for 0.32 Al foam sandwich panel with 0.0286t imperfection at centre

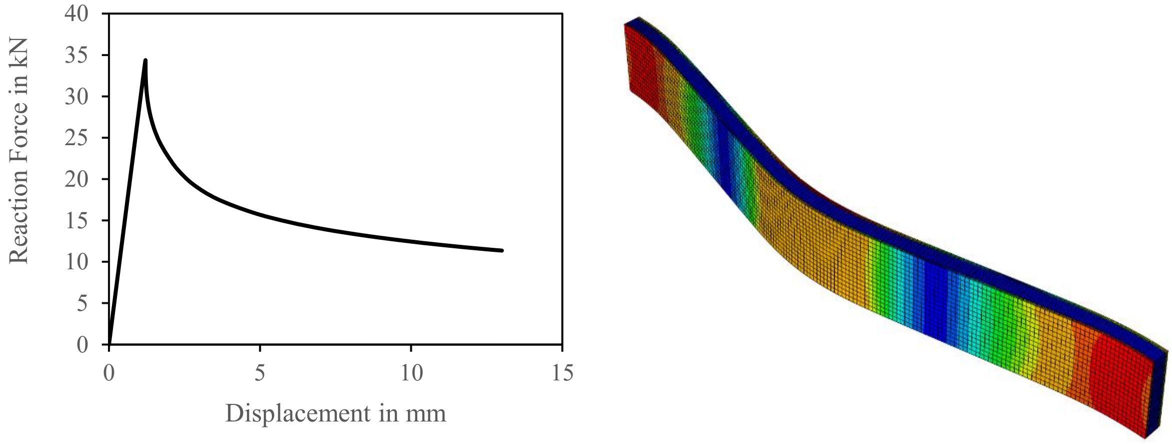

Figure 6.54: Reaction Force Graph and deformation pattern for 0.32 Al foam sandwich panel with 0.0321t imperfection at centre

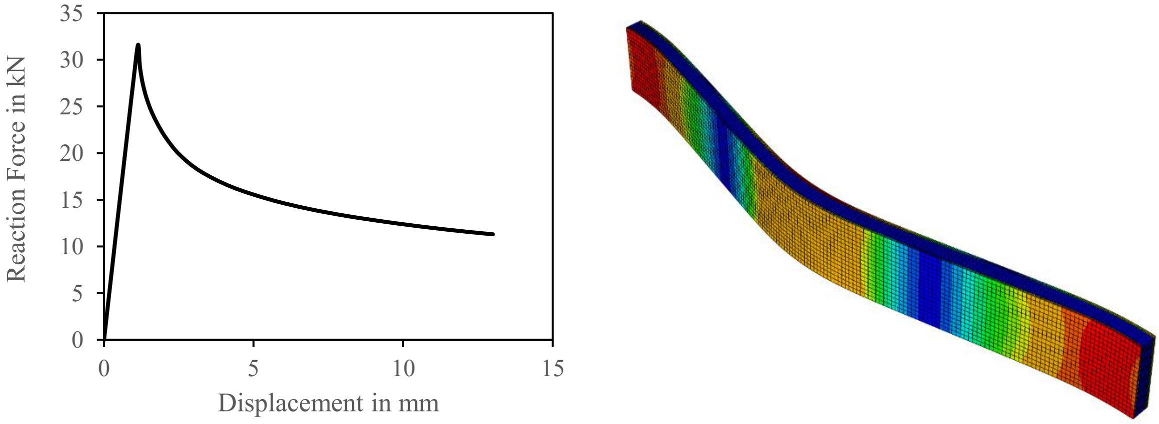

Figure 6.55: Reaction Force-Displacement Graph and Deformation pattern for 0.32 Al foam sandwich panel with 0.0714t imperfection at centre

The 0.32 foam sandwich exhibits a pronounced imperfection-sensitive response, with strong mode interaction only within a limited low-imperfection window. In the perfect case, the panel is boundary-dominated and reaches the highest peak load, indicating delayed global instability. At low imperfection amplitudes, the response is governed by distributed multi-wave buckling with broad plateaus and temporary stiffness recovery, and the normalized peak load remains high. This shows that the panel can still redistribute load effectively and sustain a stable post-buckling path in this range. A clear threshold appears between about 0.0214t and 0.025t, where the normalized peak load drops sharply and the response becomes more localization-driven. Beyond this point, the capacity remains in a lower band, indicating a degraded but relatively stable post-buckling regime governed mainly by imperfection-induced U-shaped localization. Overall, the 0.32 panel retains a strong low-imperfection stabilization window, but the transition to localization becomes sharper once the threshold is exceeded.

6.1.8 Aluminium Foam sandwich with 0.355 Relative Density Foam

The influence of the applied initial imperfection amplitude on the structural response of the 0.355 Al foam sandwich panel under axial compression is summarized in Table 6.15.

Table 6.15: Effect of imperfection amplitude on RF behaviour, peak reaction force, and observed deformation mode for 0.355 Al foam sandwich

Imperfection Range	RF Behaviour	Peak RF Values	Deformation Pattern	Interpretation
Without Imperfection	Linear-Plateau rise-Drop Response	67 kN	More localized edge-dominated or end-localized deformation pattern,	Higher relative density delays global instability and promotes a less distributed, more boundary-controlled deformation mode
0.0071t to 0.0214t (0.1 to 0.3 mm)	A linear rise followed by an upward plateau and then a gradual softening. Initial post peak softening slope is is about -1.05 kN/mm	Peak RF values are 44.8,44.6,44.5 and 44.4 kN respectively	Emerging wave type deformation. Nine half-waves throughout the length. $LE13_{peak\ load}$ – 0.1017 $LE13_{collapse}$ -0.481	Emerging-wave distributed buckling with strong mode interaction and effective load redistribution, leading to a sustained post-buckling response before softening

0.025t to 0.0286t (0.35 to 0.4mm)	Linear rise, stable plateau, and gradual softening. Initial post peak softening slope about -19 kN/mm	39.8 and 39.7 kN respectively	Emerging wave type deformation. Nine half-waves throughout the length. $LE13_{peak\ load}$ – 0.1011 $LE13_{collapse}$ - 0.5154	Emerging waves indicate progressive multi-wave buckling and a transition toward a more stable post-buckling deformation path.
0.0321t to 0.0714t (0.45 to 1 mm)	A linear rise followed by a sudden drop. Initial post peak softening slope increases from -65 kN/mm to -23 kN/mm	Peak RF drops from 34.1 kN to 29.1 kN with increase in imperfection	U-shaped global buckling, Localization length-239 mm, $U3_{max}$ – increases from 2.46 mm to 3.953 mm, $LE13_{peak\ load}$ – increases from 0.00534 to 0.0096	Rapid U-shaped global buckling with no mode interaction , leading to early instability and sudden loss of load-carrying capacity

Table 6.16 summarizes the peak reaction force response of the specimens and their corresponding imperfection amplitudes.

Table 6.16: Variation of peak reaction force of 0.355 Al foam sandwich panel across various imperfection amplitude in comparison with imperfection free sandwich panel

Sample ID	P_{max} in kN	P_{max}/P_0	Imperfection Amplitude
RD0355-I0.10	44.8	0.668657	0.0071t
RD0355-I0.15	44.6	0.665672	0.0107t
RD0355-I0.20	44.6	0.665672	0.0143t
RD0355-I0.25	44.5	0.664179	0.0179t
RD0355-I0.30	44.8	0.668657	0.0214t
RD0355-I0.35	39.7	0.592537	0.025t
RD0355-I0.40	39.8	0.59403	0.0286t
RD0355-I0.45	34.1	0.508955	0.0321t
RD0355-I0.50	33.8	0.504478	0.0357t
RD0355-I0.55	33.4	0.498507	0.0393t
RD0355-I0.60	33.1	0.49403	0.0429t
RD0355-I0.65	32.8	0.489552	0.0464t
RD0355-I0.70	32.4	0.483582	0.05t
RD0355-I0.75	31.3	0.467164	0.0536t
RD0355-I0.80	30.6	0.456716	0.0571t
RD0355-I0.85	30.1	0.449254	0.0607t
RD0355-I0.90	29.8	0.444776	0.0643t
RD0355-I0.95	29.4	0.438806	0.0679t
RD0355-I1	29.1	0.434328	0.0714t

Figure 6.56 represents the variation in the peak reaction force with the imperfection amplitude for the $\rho^* = 0.355$ foam sandwich panel. The corresponding reaction force behavior and deformation patterns for representative imperfection levels are shown in Figures 6.57 to 6.62, providing visual evidence of the buckling transition and the associated changes in load-carrying response

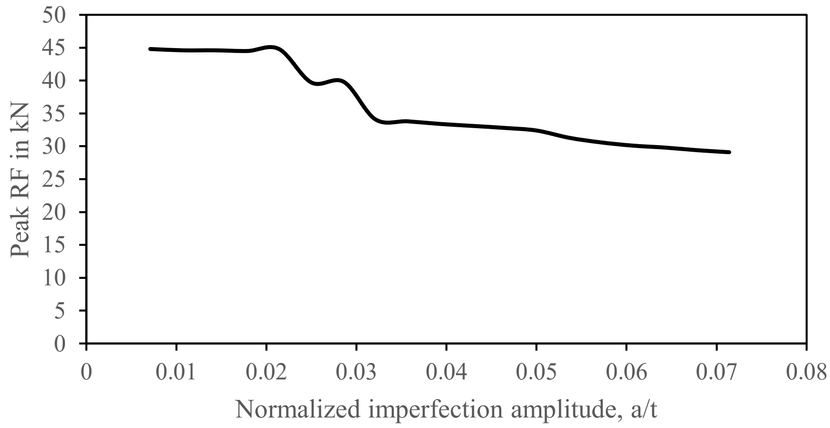

Figure 6.56: Graph showing Variation of Peak Reaction Force with Imperfection Amplitude for 0.355 relative density Al foam sandwich

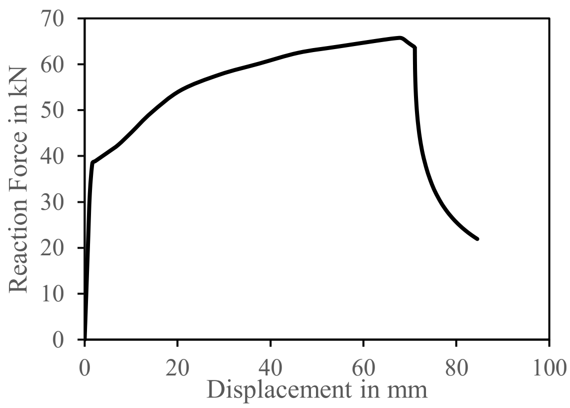

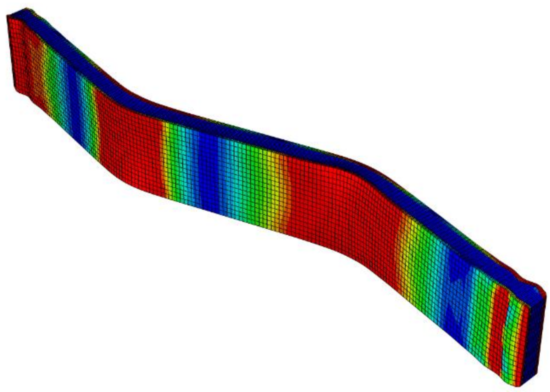

Figure 6.57: Reaction Force-Displacement Graph and Deformation pattern for 0.355 Al foam sandwich panel without imperfection (baseline)

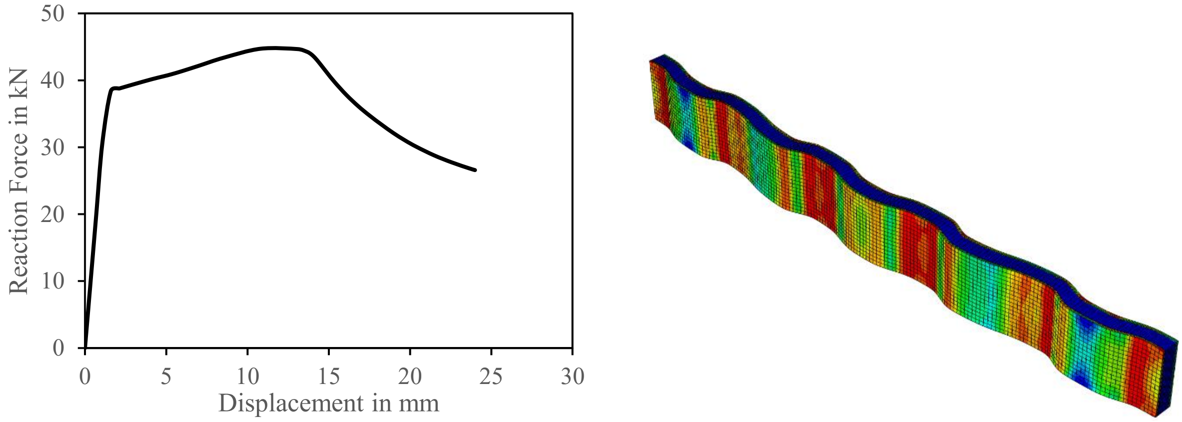

Figure 6.58: Reaction Force-Displacement Graph and Deformation pattern for 0.355 Al foam sandwich panel with 0.0071t imperfection at centre

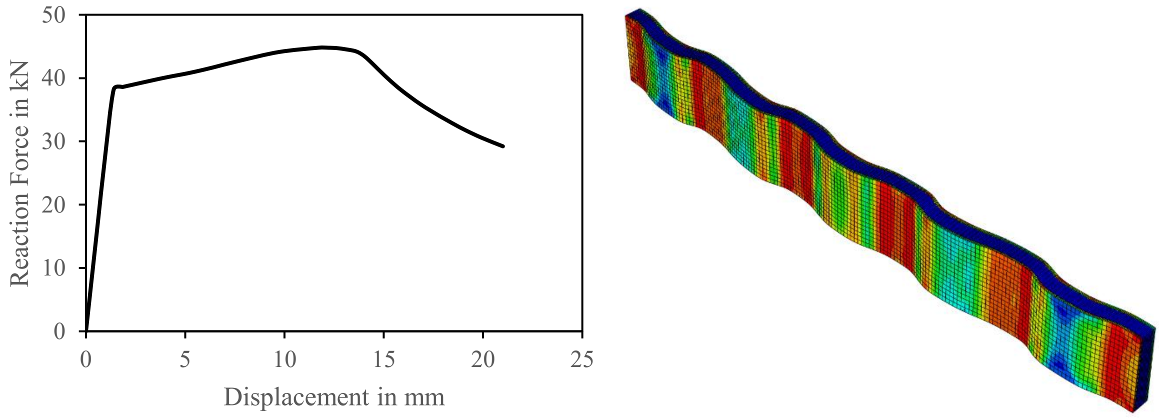

Figure 6.59: Reaction Force-Displacement Graph and Deformation pattern for 0.355 Al foam sandwich panel with 0.0214t imperfection at centre

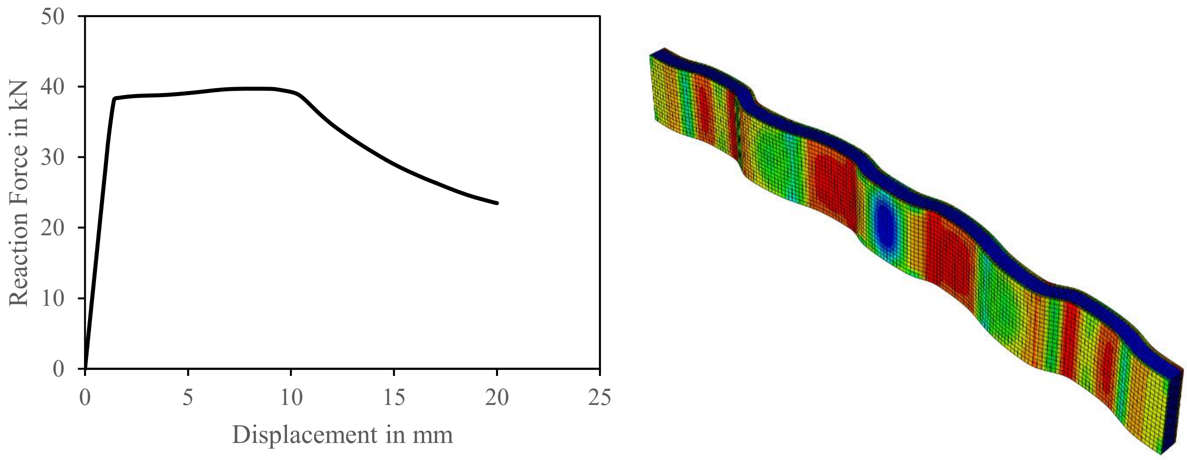

Figure 6.60: Reaction Force-Displacement Graph and Deformation pattern for 0.355 Al foam sandwich panel with 0.025t imperfection at centre

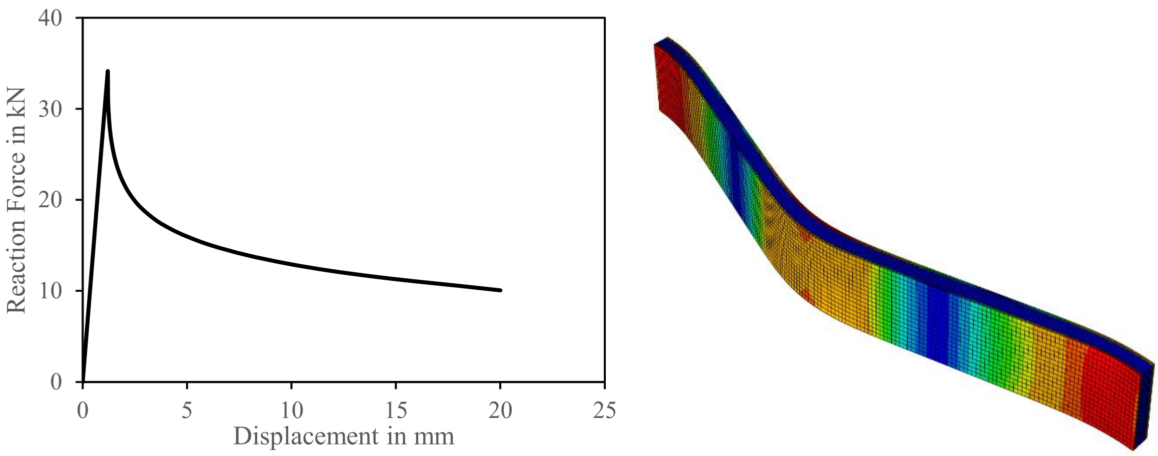

Figure 6.61: Reaction Force -Displacement Graph and Deformation pattern for 0.355 Al foam sandwich panel with 0.0321t imperfection at centre

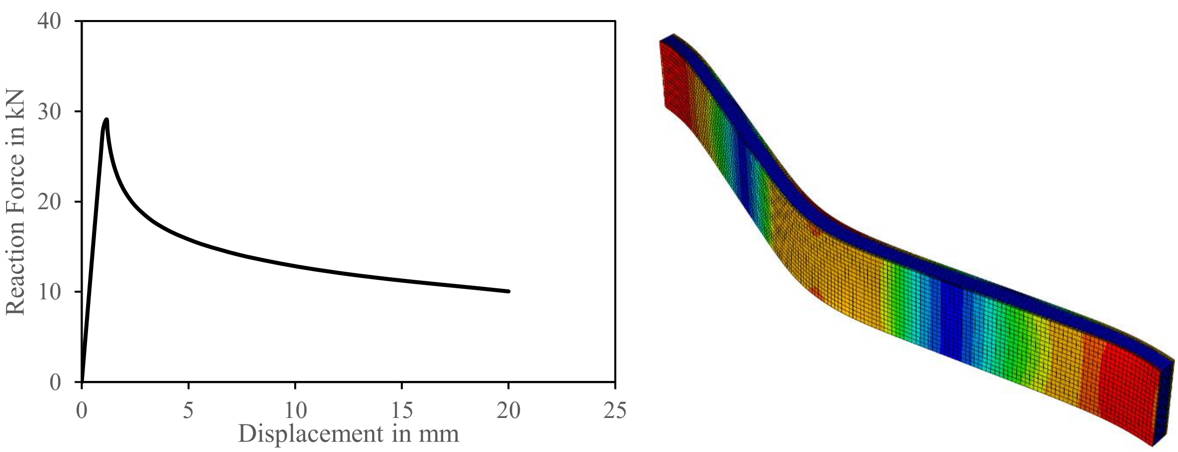

Figure 6.62: Reaction Force-Displacement Graph and Deformation pattern for 0.355 Al foam sandwich panel with 0.0714t imperfection at centre

The 0.355 foam sandwich shows moderate imperfection sensitivity, with a clear transition in buckling behaviour and load-carrying capacity as the imperfection amplitude increases. In the perfect case, the panel exhibits boundary-dominated buckling and reaches the highest peak reaction force, indicating delayed instability. At low imperfection amplitudes, the panel retains about 65–70% of its perfect-geometry capacity and responds through distributed multi-wave buckling with strong mode interaction and effective load redistribution. As the imperfection amplitude increases toward about 0.025t, the normalized peak load drops sharply, marking a transition from distributed buckling to localization-dominated U-shaped instability. Beyond this threshold, the response becomes increasingly controlled by localized buckling, with reduced post-buckling stability and weaker mode interaction. Overall, the 0.355 panel maintains a robust load-carrying capacity in the low-imperfection range, but this beneficial effect diminishes once localization dominates

6.1.9 Aluminium Foam sandwich with 0.439 Relative Density Foam

The influence of the applied initial imperfection amplitude on the structural response of the 0.439 Al foam sandwich panel under axial compression is summarized in Table 6.17.

Table 6.17: Effect of imperfection amplitude on RF behaviour, peak reaction force, and observed deformation mode for 0.439 Al foam sandwich

Imperfection Range	RF Behaviour	Peak RF Values	Deformation Pattern	Interpretation
Without Imperfection	Linear-Plateau rise-Drop Response	77 kN	Regular multi-wave buckling	Localized edge deformation with very short multiple half waves spread throughout the panel
0.0071t (0.1 mm)	A linear rise followed by a short plateau and then an immediate drop. Initial post peak softening slope value is -5.13 kN/mm	39.3 kN	Emerging wave type deformation. Three half-waves throughout the length. $LE13_{peak\ load}$ – 0.002 $LE13_{collapse}$ -0.1057	Emerging waves indicate incipient distributed buckling and early stress redistribution; however, the post-buckling path remains limited and unstable.
0.0107t to 0.0143t (0.15 to 0.2 mm)	Linear rise followed by gradual softening with initial post pek softening slope around -0.42 kN/mm	38.7 kN	Emerging wave type deformation. Five half-waves throughout the length. $LE13_{peak\ load}$ – 0.00225 $LE13_{collapse}$ -0.1678	More half-waves indicate a more distributed post-buckling mode with stronger stress redistribution but not necessarily higher global stability.
0.0179t (0.25 mm)	Single Peak with Sudden drop. Initial post peak softening slope value is -58.8 kN/mm	36.4 kN	U-shaped global buckling, Localization length-233 mm, $U3_{max}$ – 2.2 mm, $LE13_{peak\ load}$ - 0.0025	Early localization into the dominant U-shaped buckling mode, with limited post-buckling redistribution
0.0214t (0.3 mm)	Linear rise, very short plateau, and immediate drop. Initial post peak softening slope value is - 6.5 kN/mm	38.2 kN	U-shaped global buckling, Localization length-233 mm, $U3_{max}$ – 2.969 mm, $LE13_{peak\ load}$ - 0.003399	Very short plateau and sudden drop indicate presence of weakened mode interaction and rapid localization into U-shaped buckling compared

0.025t (0.35 mm)	Linear rise, rising plateau, and gradual softening. Initial post peak softening slope value is -0.16 kN/mm	51.7 kN	Multiple wave type deformation. Nine short half-waves throughout the length. $LE13_{peak\ load}$ – 0.005819 $LE13_{collapse}$ -0.0789	Small multiple waves indicate strong distributed mode interaction and effective load redistribution, producing a stable post-buckling response before a gradual softening.
0.0286t (0.4 mm)	A linear rise followed by gradual softening. Initial post peak softening slope value is -5.2 kN/mm	38.7 kN	Emerging wave type deformation. Five half-waves throughout the length. $LE13_{peak\ load}$ – 0.001902 $LE13_{collapse}$ -0.1562	Gradual softening with emerging waves, showing a transition from strong multi wave interaction to a less developed distributed buckling state
0.0321t to 0.357t (0.45 mm to 0.5mm)	A linear rise was followed by a very short plateau-like behaviour and gradual softening. Initial post peak softening slope value is -0.38 kN/mm	39and 38.6 kN respecti vely	Emerging wave type deformation. Five half-waves throughout the length. $LE13_{peak\ load}$ – 0.00489 $LE13_{collapse}$ -0.1553	Very short plateau with emerging waves, indicating a weak mode-interaction window and a transition from distributed buckling toward localized instability
0.0393t to 0.0714t (0.55 to 1 mm)	A linear rise followed by a sudden drop. Initial post peak softening slope value increasing from around -52 kN/mm to -28 kN/mm	Peak RF value reduces from 33.5 kN to 32 kN with increase in imperfecti -on	U-shaped global buckling, Localization length-239 mm, $U3_{max}$ – increases from 2.047 mm to 2.744 mm, $LE13_{peak\ load}$ – increases from 0.00534 to 0.0096	Rapid U-shaped global buckling with no mode interaction, leading to early instability and sudden loss of load-carrying capacity

Table 6.18 summarizes the peak reaction force responses of the specimens, together with their corresponding imperfection amplitudes.

Table 6.18: Variation of peak reaction force of 0.439 Al foam sandwich panel across various imperfection amplitude in comparison with imperfection free sandwich panel

Sample ID	P_{max} in kN	P_{max}/P_0	Imperfection Amplitude
RD0355-I0.10	39.3	0.51039	0.0071t
RD0355-I0.15	38.7	0.502597	0.0107t
RD0355-I0.20	39.4	0.511688	0.0143t
RD0355-I0.25	36.4	0.472727	0.0179t
RD0355-I0.30	31.7	0.411688	0.0214t
RD0355-I0.35	51.7	0.671429	0.025t

RD0355-I0.40	38.7	0.502597	0.0286t
RD0355-I0.45	39	0.506494	0.0321t
RD0355-I0.50	38.6	0.501299	0.0357t
RD0355-I0.55	33.5	0.435065	0.0393t
RD0355-I0.60	33.5	0.435065	0.0429t
RD0355-I0.65	33.4	0.433766	0.0464t
RD0355-I0.70	33.4	0.433766	0.05t
RD0355-I0.75	33.4	0.433766	0.0536t
RD0355-I0.80	33.3	0.432468	0.0571t
RD0355-I0.85	33.2	0.431169	0.0607t
RD0355-I0.90	32.9	0.427273	0.0643t
RD0355-I0.95	32.4	0.420779	0.0679t
RD0355-I1	32	0.415584	0.0714t

Figure 6.63 shows the variation in the peak reaction force with the imperfection amplitude for the $\rho^* = 0.439$ foam sandwich panel. The corresponding reaction force behavior and deformation patterns for representative imperfection levels are shown in Figures 6.64 to 6.71, providing visual evidence of the buckling transition and the associated changes in load-carrying response

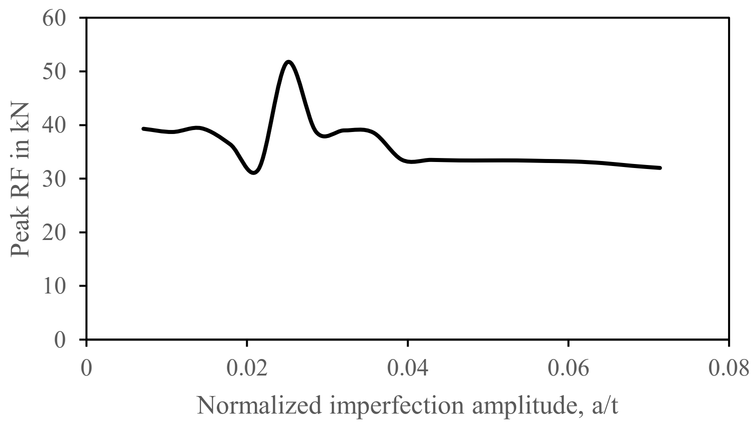

Figure 6.63: Graph showing Variation of Peak Reaction Force with Imperfection Amplitude for 0.439 relative density Al foam sandwich

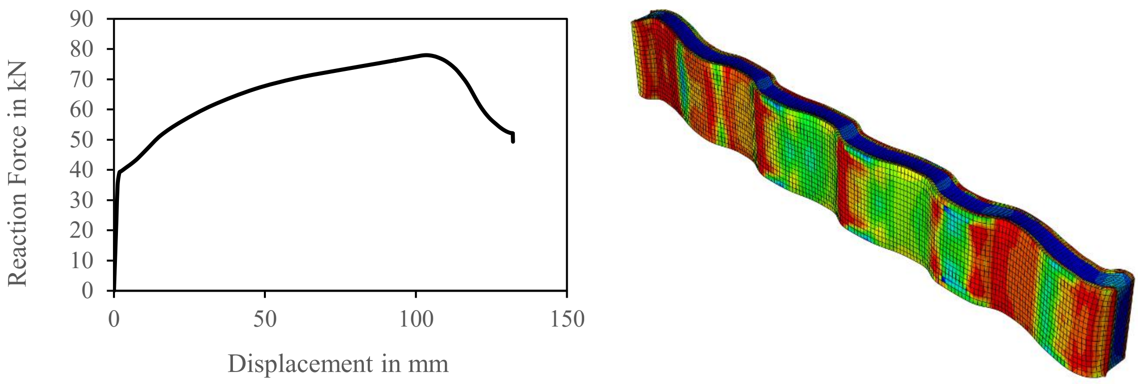

Figure 6.64: Reaction Force-Displacement Graph and Deformation pattern for 0.439 Al foam sandwich panel without imperfection (baseline)

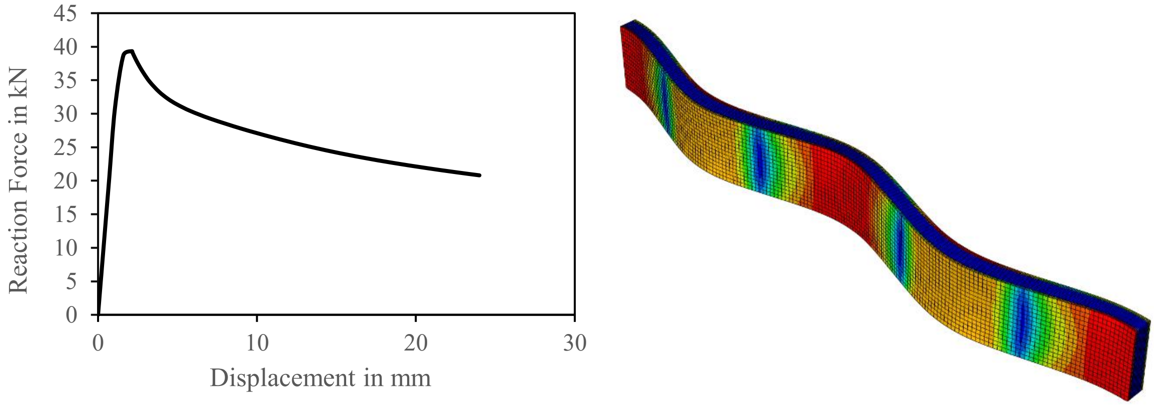

Figure 6.65: Reaction Force-Displacement Graph and Deformation pattern for 0.439 Al foam sandwich panel with 0.0071t imperfection at centre

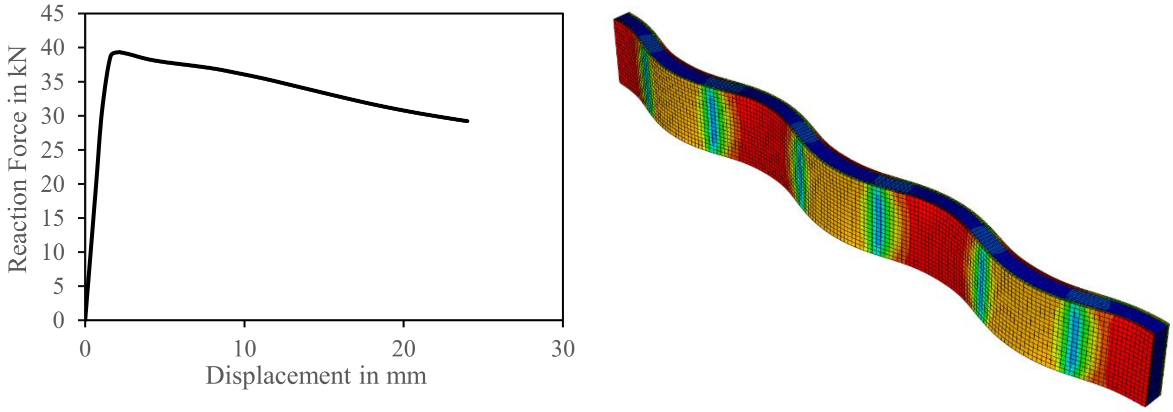

Figure 6.66: Reaction Force-Displacement Graph and Deformation pattern for 0.439 Al foam sandwich panel with 0.0143t imperfection at centre

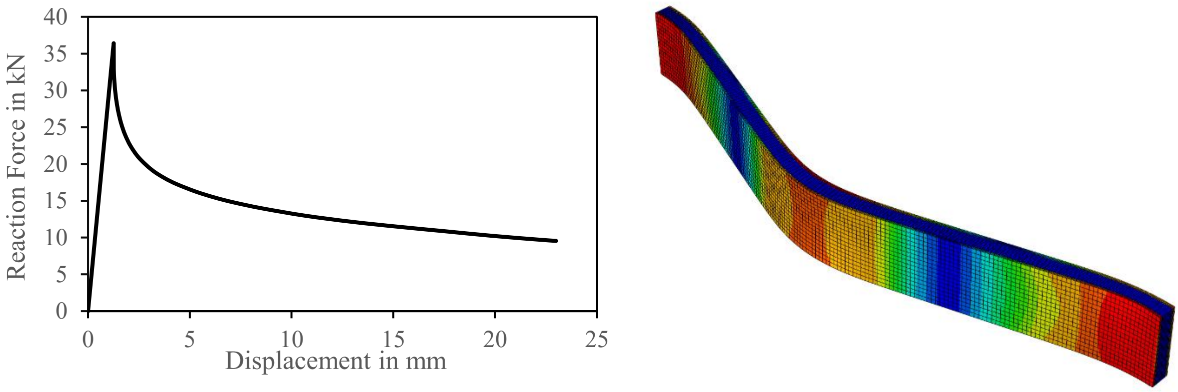

Figure 6.67: Reaction Force-Displacement Graph and Deformation pattern for 0.439 Al foam sandwich panel with 0.0179t imperfection at centre

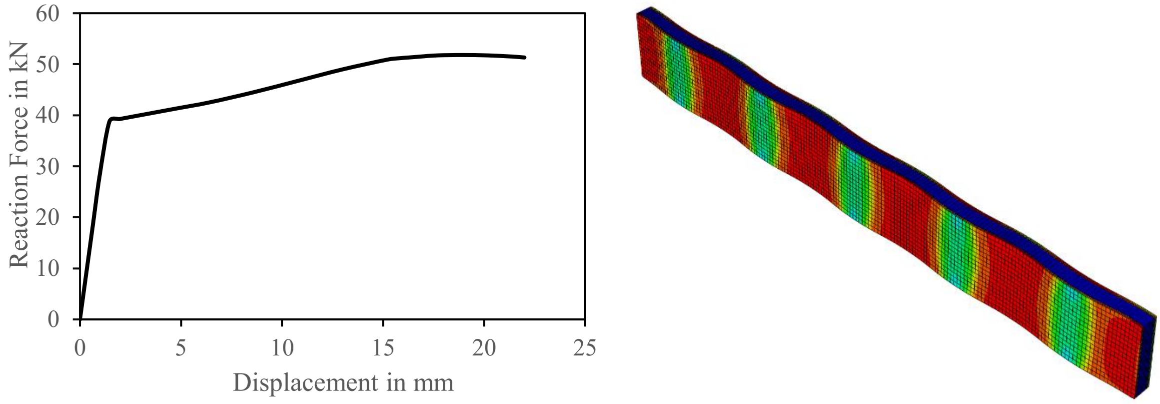

Figure 6.68: Reaction Force-Displacement Graph and Deformation pattern for 0.439 Al foam sandwich panel with 0.025t imperfection at centre

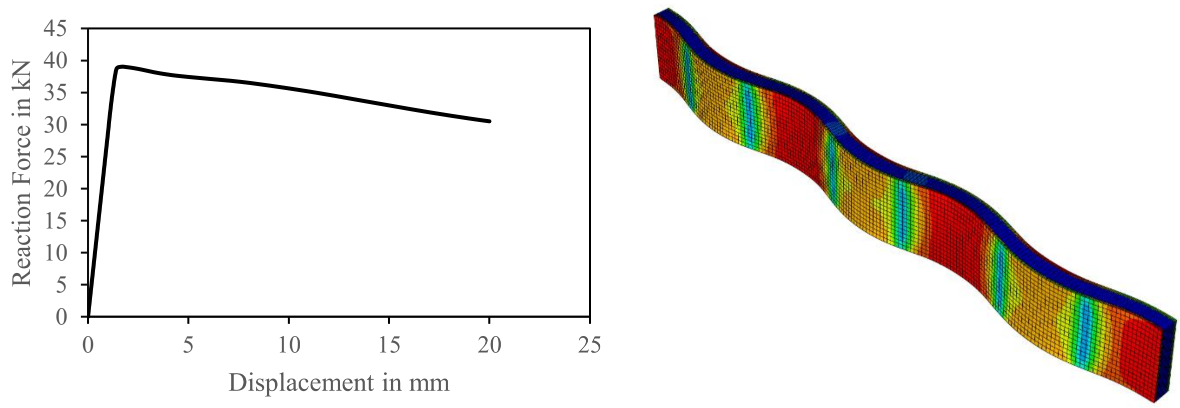

Figure 6.69: Reaction Force-Displacement Graph and Deformation pattern for 0.439 Al foam sandwich panel with 0.0321t imperfection at centre

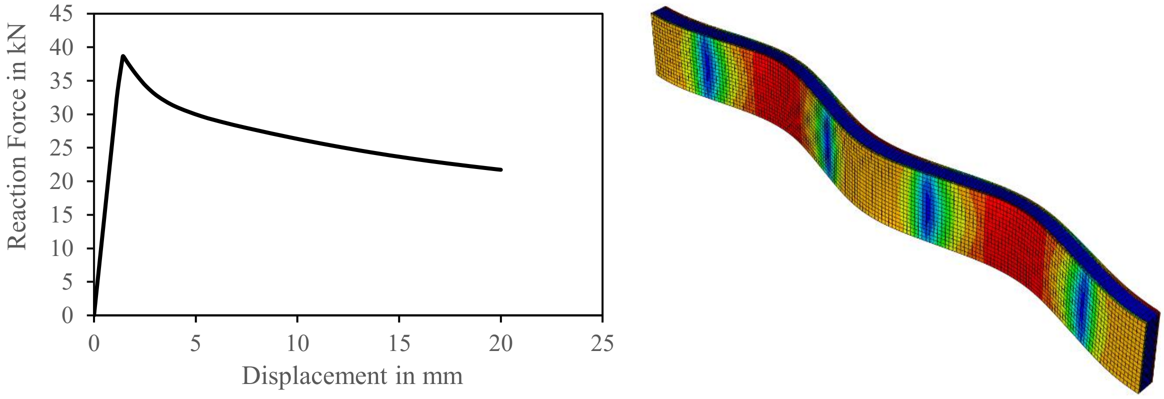

Figure 6.70: Reaction Force-Displacement Graph and Deformation pattern for 0.439 Al foam sandwich panel with 0.0357t imperfection at centre

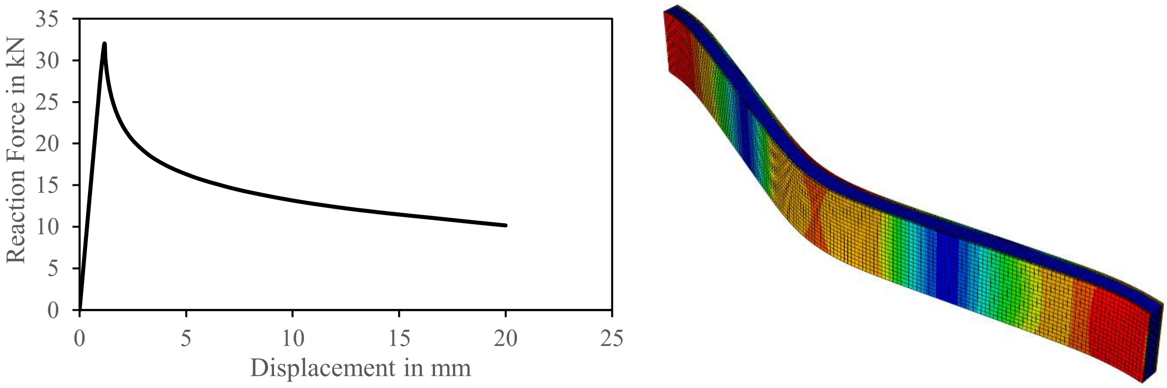

Figure 6.71: Reaction Force-Displacement Graph and Deformation pattern for 0.439 Al foam sandwich panel with 0.0714t imperfection at centre

The 0.439 foam sandwich shows a complex imperfection-sensitive response with a clear transition in both peak load and deformation mode. In the perfect case, the panel is boundary-dominated and reaches the highest peak load, indicating delayed global instability. At low imperfection amplitudes, the panel retains about 50–51% of its perfect-geometry capacity, while the response remains governed by distributed multi-wave buckling and limited load redistribution. A pronounced recovery occurs at around 0.025t, where the normalized peak load rises to 0.671 and the deformation pattern shows strong multi-wave interaction and temporary stiffness enhancement. Beyond this point, the normalized peak load decreases gradually and the response becomes increasingly controlled by U-shaped localization with abrupt softening. Overall, the 0.439 panel exhibits imperfection-sensitive windows at both low and moderate amplitudes, but the beneficial effect of mode interaction diminishes as the imperfection amplitude increases.

6.1.10 Aluminium Foam sandwich with 0.472 Relative Density Foam

The $\rho^* = 0.472$ panel exhibited numerical nonconvergence for all the imperfection amplitudes considered. Consequently, the complete reaction force history and deformation pattern could not be resolved within the current analysis settings. This limitation suggests that the combination of high core stiffness and geometric imperfections leads to a highly unstable post-buckling path that exceeds the convergence capability of the present Riks formulation.

6.2 Initial Buckling Characteristics from Eigenvalue Analysis

Linear buckling analysis was performed prior to the nonlinear collapse analysis for all foam sandwich densities to identify the initial instability characteristics and assess the proximity of competing buckling modes. For all cases, the first three eigenmodes showed a consistent progression from a U-shaped first mode to an S-shaped second mode and a three-half-wave third mode. The eigenvalues and their separation vary with the relative density, providing an initial indication of the buckling sensitivity and the likelihood of mode interaction; however, but they do not determine the final nonlinear response, which is governed by imperfection sensitivity, post-buckling interaction, and mode evolution under compression.

Table 6.19 summarizes the first three eigenvalues for each density, together with the ratios or separations between successive eigenvalues, to indicate the relative closeness of competing buckling modes.

Table 6.19: Initial buckling characteristics from eigenvalue analysis for different foam sandwich relative densities

Relative Density of foam in sandwich	Eigen value of first mode shape(λ1)	Eigen value of second mode shape (λ2)	Eigen value of third mode shape (λ3)	λ2/λ1	λ3/λ1
0.134	0.769	0.87	1.025	1.13	1.34
0.17	0.860	0.985	1.1688	1.145	1.36
0.217	1.1349	1.3648	1.6699	1.2	1.47
0.25	1.3819	1.753	2.2185	1.26	1.6
0.262	1.5372	2.0255	2.6271	1.317	1.7
0.308	1.8046	2.5589	3.4901	1.417	1.93
0.32	1.8563	2.6733	3.6871	1.44	1.98
0.355	1.8822	2.732	3.7902	1.45	2.01
0.439	2.0758	3.2113	4.6797	1.54	2.25
0.472	2.1259	3.3485	4.9525	1.57	2.33

***Note**: Linear buckling eigenvalues were successfully obtained for all densities. Nonlinear Riks analyses for $\rho = 0.134$ (high imperfections) and $\rho^* = 0.472$ (all imperfections) did not converge and were excluded from parametric trends and design recommendations*

Since the mode-shape progression was similar across the studied densities, only representative cases from the 0.217 foam sandwich (Fig. 6.72 to 6.74) are included here.

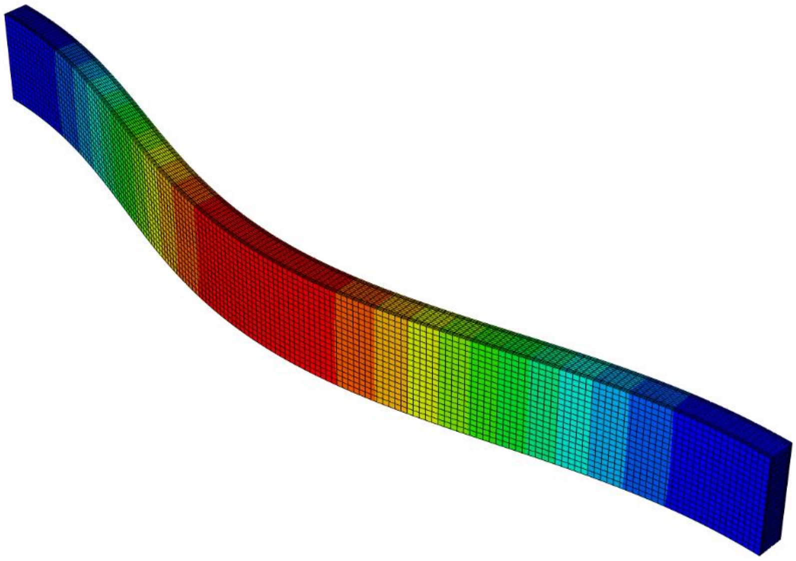

Figure 6.72: First mode shape (U shaped) of 0.217 foam sandwich

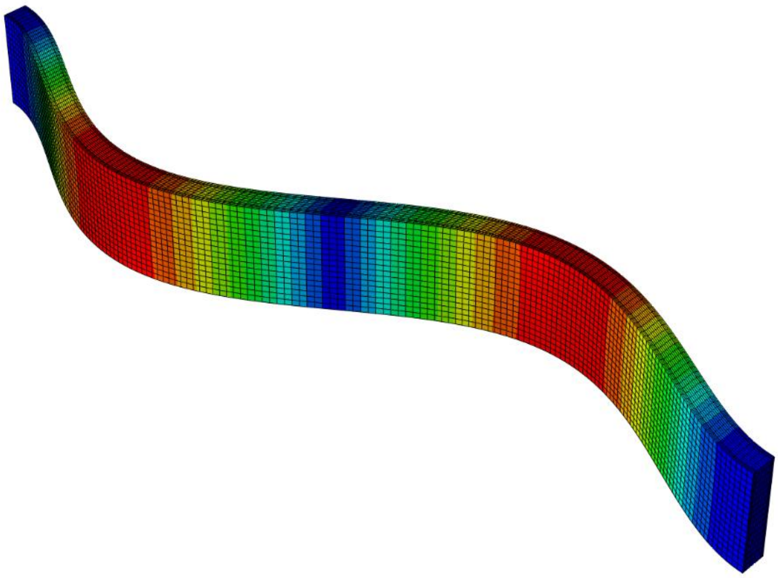

Figure 6.73: Second mode shape (S shaped) of 0.217 foam sandwich

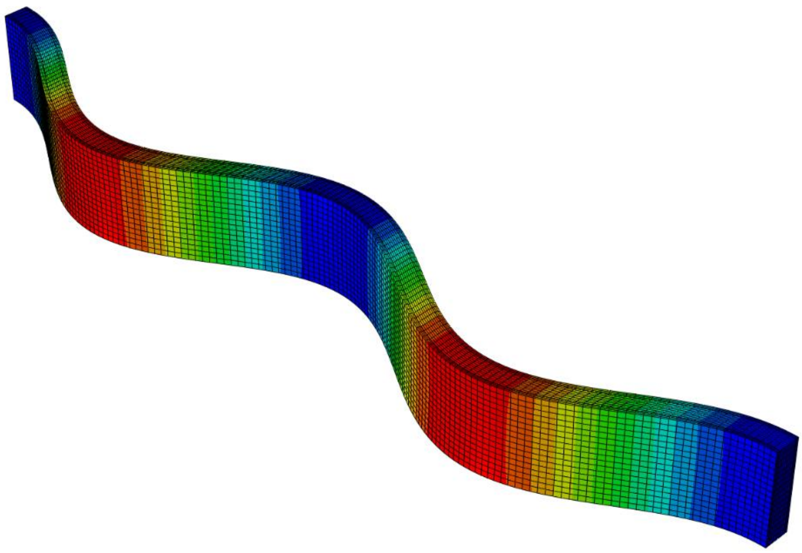

Figure 6.74: Third mode shape (S shaped) of 0.217 foam sandwich

The linear buckling results show that increasing the foam relative density generally raises the critical eigenvalues and increases the separation between the first three modes, indicating a higher initial buckling resistance and reduced proximity of competing modes in the linear stability sense.

The above linear buckling results help explain the imperfection-sensitive behaviour observed in the nonlinear analysis. For the lower relative-density sandwiches, the closer spacing of the first few eigenmodes indicates a stronger potential for mode competition over a broader imperfection range, which is consistent with the presence of mode interaction throughout the imperfection window. For the higher relative-density sandwiches, the higher eigenvalues and larger eigenvalue ratios indicate a stronger dominant buckling mode and greater separation from higher modes. As a result, mode interaction is more pronounced only at lower imperfection amplitudes, whereas larger imperfections suppress distributed deformation and promote rapid localization into U-shaped buckling.

6.3 Discussions

6.3.1 Imperfection-Dependent Mode Interaction Windows

The nonlinear in-plane compression results show that the peak load-carrying capacity is controlled by a competition between global buckling and localized deformation, rather than by imperfection amplitude alone. As the imperfection amplitude increases, the panel does not simply weaken in a monotonic manner; instead, a distinct imperfection-sensitive window appears, most clearly at low imperfection amplitudes between 0.0071t and 0.0286t. Within this range, the initial geometric imperfection is large enough to activate interaction between the primary U-shaped buckling mode and higher-order S-shaped or multi-wave modes, but not so large that the response immediately localizes into a single dominant buckle. The result is a transient redistribution of deformation over several half-waves, which can temporarily delay collapse and, in some cases, produce a higher peak reaction force than neighbouring imperfection casesThe imperfection-dependent mode interaction was identified quantitatively from the percentage deviation of the peak reaction force from the mean stable-region value. Table 6.20 shows the percentage by which the peak reaction force in each case exceeded the mean reaction force in the stable-response region. In the present dataset, the cases corresponding to the imperfection-sensitive regime (highlighted in Table 6.20) are those for which the peak reaction force exceeds the stable-region mean by at least 14 percent; therefore, 14 percent was adopted as the threshold separating the stable-response region from the imperfection-sensitive window. Mechanically, this window represents a regime in which the global buckling mode interacts with emerging local deformation waves, producing additional half-waves, redistributing the strain energy, and altering the collapse path. Outside this range, mode interaction may still occur, but its effect on the peak reaction force is weaker, and the response remains closer to the stable-load trend. Thus, the imperfection-sensitive mode interaction window is defined as the range of normalized imperfection amplitudes a/t for which the peak reaction force satisfies

$$\frac{P_{\max}}{\bar{P}_{\text{stable}}} \geq 1.14$$

where $P_{\max}$ is the peak reaction force for a given case and $\bar{P}_{\text{stable}}$ is the mean peak reaction force in the stable-response region

Table 6.20: Percentage increase of Peak Reaction Force from mean value of stable region

Normalized Imperfection amplitude, a/t	Relative Density of Foam in Sandwich								
	0.134	0.17	0.217	0.25	0.262	0.308	0.32	0.355	0.439
0.0071	12.62	5.74	11.54	**26.02**	**22.14**	**36.72**	**22.61**	**28.81**	**18.7**
0.0107	**53**	5.31	8.46	**25.83**	**22.34**	**36.72**	**22.43**	**28.49**	**14.47**
0.0143	-2	4.44	7.17	**25.63**	**30.12**	**21.35**	**22.24**	**28.49**	**15.98**
0.0179	6.25	9.04	5.84	**25.43**	**23.94**	**35.91**	**22.06**	**28.34**	9.06
0.0214	**52.88**	8.24	4.82	**26.02**	0.639	**35.78**	-10.06	**28.82**	-4.4
0.025	**20.35**	7	8.47	10.28	**23.15**	**36.32**	-10.81	**19.67**	**35.98**

0.0286	-	5.75	7.5	10.57	10.84	**35.64**	**14.48**	**19.87**	**14.47**
0.0321	-	4.88	6.51	10	6.02	**21.15**	5.29	6.48	**15.13**
0.0357	-	3.56	2.7	8.84	2.28	10.89	4.17	5.65	**14.25**
0.0393	-	2.66	1.98	8.25	7.49	6.17	2.45	4.52	1.19
0.0429	-	2.2	1.24	4.85	-0.03	4.38	-0.86	3.65	1.19
0.0464	-	1.27	0.87	-2.02	-1.06	6.17	-1.18	2.77	0.9
0.05	-	0.81	0.11	1.53	-2.11	-2.45	-1.18	1.57	0.9
0.0536	-	-0.14	-0.65	-2.02	-2.82	-3.15	-1.49	-1.88	0.9
0.0571	-	-0.62	-1.04	-3.14	-3.54	-3.86	-1.49	-4.2	0.6
0.0607	-	-1.6	-1.82	-3.14	-4.27	-4.58	-1.81	-5.94	0.3
0.0643	-	-2.11	-0.65	-3.52	-5.02	-4.95	-2.13	-7.01	-0.61
0.0679	-	-2.61	-1.04	-3.89	-5.77	-5.68	-2.45	-8.47	-2.16
0.0714	-	-3.63	-1.82	-4.67	-5.77	-6.43	-3.1	-9.58	-3.44

At the structural level, the window forms when the combined stiffness of the face sheets, foam core, and initial imperfection permits temporary load redistribution before the collapse path locks into localization. In the present study, panels within this range retained approximately 0.60 to 0.70 of the perfect-geometry peak load, showing that geometric imperfection does not only degrade capacity; in certain ranges, it also promotes a more distributed post-buckling response. This effect is broader in the lower-density panels, where mode interaction persists over a wider imperfection range, but it becomes narrower and more concentrated at low imperfection amplitudes in the higher-density panels. Once the imperfection amplitude increases beyond about 0.0321t, the stabilizing effect of mode interaction is lost and the response transitions rapidly to localized U-shaped buckling, accompanied by a sharper reduction in peak load and post-peak stability.

6.3.2 Variation of Mode Interaction with Relative Densities

The Table 6.21 below shows the variation of mode interaction across different tested relative density foam sandwiches

Table 6.21: Variation of mode reactions with imperfection amplitudes across relative density of foam in sandwich

Imperfection	Relative Density of foam in sandwich								
	0.134	0.17	0.217	0.25	0.262	0.308	0.32	0.355	0.439
0.0071t	Absent	Present, but weak	Absent	Strong	Active, but not Strong	Very Strong	Very Strong	Very Strong	Strong
0.0107t	Very Stong	Present, but weak	Weak	Strong	Stronger	Very Strong	Very Strong	Very Strong	Strong
0.0143t	Absent	Present, but weak	Weak	Strong	Very strong	Strong	Very Strong	Strong	Weak

0.0179t	Absent	Moderate	Weak	Strong	Weakens	Very Strong	Very Strong	Strong	Absent
0.0214t	Very Strong	Moderate	Weak	Strong	Weak	Very Strong	Very Weak	Strong	Active. But weak
0.025t	Weak	Moderate	Absent	Weak	Weak	Very Strong	Very Weak	Weake ns	Very Strong
0.0286t	-	Weak	Absent	Weak	Absent	Very Strong	Active, but weak	Weake ns	Weakens
0.0321t	-	Weak	Absent	Weak	Absent	Weak	Absent	Absent	Weak
0.0357t	-	Weak	Weaker	Weak	Active, but weak	Absent	Absent	Absent	Absent
0.0357t	-	Weak	Weaker	Weak	Absent	Absent	Absent	Absent	Absent
0.0429t	-	Weak	Weaker	Weak	Very Weak	Absent	Absent	Absent	Absent
0.0464t	-	Weak	Weaker	Weak	Very Weak	Absent	Absent	Absent	Absent
0.05t	-	Weak	Weaker	Very Weak	Very Weak	Absent	Absent	Absent	Absent
0.0536t	-	Weak	Weaker	Very Weak	Very Weak	Absent	Absent	Absent	Absent
0.0571t	-	Weak	Weaker	Very Weak	Very Weak	Absent	Absent	Absent	Absent
0.0607t	-	Weak	Weaker	Very Weak	Very Weak	Absent	Absent	Absent	Absent
0.0643t	-	Weak	Very Weak	Very Weak	Very Weak	Absent	Absent	Absent	Absent
0.0679t	-	Weak	Very Weak	Very Weak	Very Weak	Absent	Absent	Absent	Absent
0.0714t	-	Weak	Very Weak	Very Weak	Very Weak	Absent	Absent	Absent	Absent

The variation in mode interaction with relative density reflects a change in the balance between core stiffness, introduced initial imperfections, and susceptibility to localization. At low relative density, the foam core provides limited shear support, so the face sheets are less effectively constrained and the buckling response becomes highly dependent on small differences in imperfection amplitude. This is why the $\rho^* = 0.134$ panel shows intermittent behaviour: the structure is too flexible to sustain a consistent multi-wave pattern, so mode interaction appears in some cases but is lost quickly in others as the response shifts toward localization.

The $\rho^* = 0.17$ and 0.217 panels show weaker but more persistent interactions because their cores provide enough stiffness to delay immediate localization, but not enough rigidity to strongly stabilize multi-wave deformation over the full imperfection range. In this density range, the panel response is governed by a competition between distributed buckling and the onset of localized collapse, so the interaction remains present but does not develop into a strong coupled mode over many cases. In mechanical terms, these panels occupy a transitional region in which the core stiffness is sufficient to support some load redistribution, but still too low to maintain robust eigenmode coupling.

By contrast, the $\rho^* = 0.25, 0.262, 0.308, 0.32,$ and 0.355 panels exhibit stronger mode interaction at low imperfection amplitudes because the stiffer core better restrains the face sheets and promotes coupling between the global U-shaped mode and higher-order wave patterns. This enhanced stiffness allows the panel to redistribute compressive load through multiple half-waves before localization becomes dominant. However, as imperfection amplitude increases, the same higher stiffness that supports mode interaction at small imperfections also accelerates the transition to a localized response once the imperfection becomes large enough to break the distributed deformation pattern. As a result, the mode interaction window becomes narrower and shifts toward the low-imperfection regime.

The $\rho^* = 0.439$ panel follows the same general trend, but the interaction is less uniform because the very high core stiffness can both promote and suppress coupling depending on imperfection severity. At small imperfections, the stiffer core supports strong mode interaction, but at larger imperfections the deformation localizes more quickly because the structure loses the ability to sustain distributed buckling

Overall, Table 6.21 demonstrates that mode interactions are not controlled by density alone, but by the combined influence of relative density, imperfection amplitude, and the evolving post-buckling path. Lower-density panels tended to show more intermittent interactions, whereas the higher-density panels generally exhibited stronger interactions at low imperfections but became progressively more localized as the imperfection amplitude increased.

6.3.3 Deformation Patterns and Reaction Force Response

6.3.3.1 Correlation Between Buckling Wave Patterns and RF Behaviour

Across the studied imperfection and density ranges, the reaction force response was governed by how effectively the panel could redistribute compressive load after the onset of buckling. The observed deformation patterns therefore provide a direct indication of the stability of the post-buckling path. When several waves developed along the panel length, the compression load was shared over a wider region, which delayed localization and produced a more stable reaction force response. In these cases, the load rose approximately linearly to the peak value, after which an extended plateau and gradual softening were observed. This behaviour indicates that the panel retained the ability to transfer load between the face sheets and the foam core while multiple buckling modes remained active

Multiple-wave deformation represents the most stable post-buckling response because the global U-shaped mode is not able to dominate immediately. Instead, it interacts with higher-order S-shaped and multi-wave patterns, which distributes curvature and strain energy over the panel length. This mode interaction reduces the tendency for a single localized buckle to form, allowing the panel to sustain load after the peak and to soften gradually rather than collapse abruptly.

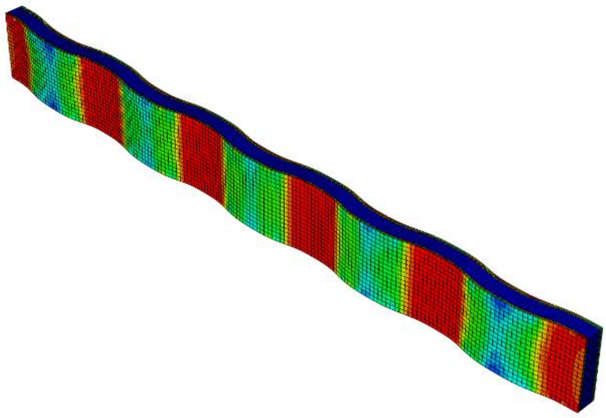

Figure 6.75: Deformation pattern of Sandwich panel with multiple waves

Emerging or evolving waves correspond to an intermediate regime in which mode interaction is present but not yet fully developed. In this case, the buckling pattern begins to spread from the ends toward the centre, showing that the structure is still capable of some load redistribution, but that localization is beginning to compete more strongly with distributed deformation. The associated reaction force response typically shows a peak followed by gradual softening, or a plateau with a delayed drop. Mechanically, this reflects partial coupling between the fundamental and higher-order modes, where the higher modes influence the collapse path but do not fully prevent localization.

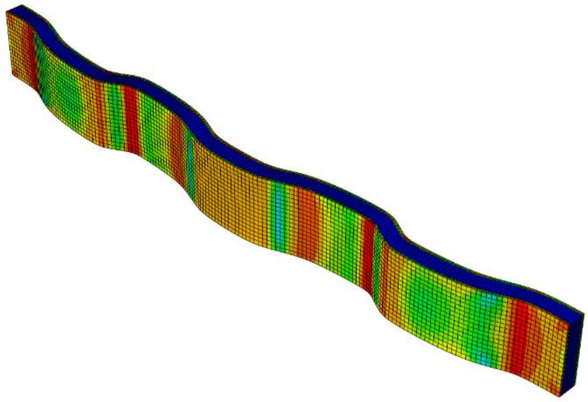

Figure 6.76: Deformation pattern of Sandwich panel with emerging/evolving waves

U-shaped global buckling represents the least stable response because the panel collapses through a single dominant buckle with limited participation of higher-order modes. Once this mode becomes dominant, the deformation concentrates rapidly in the central region and the structure loses its ability to redistribute load effectively. The reaction force therefore rises to a peak, sustains only a short plateau if any, and then drops abruptly. This response indicates that the lowest-energy deformation path has taken over, leading to rapid global instability and minimal post-peak reserve capacity.

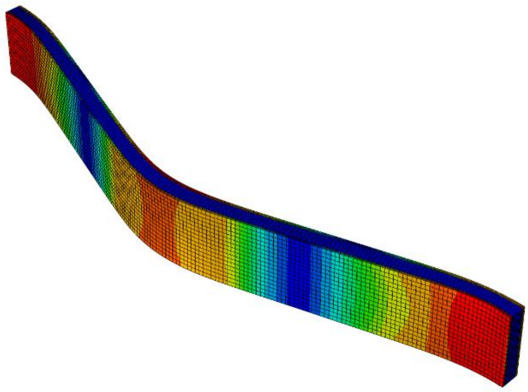

Figure 6.77: Deformation pattern by U shaped global buckling

Overall, the wave morphology and reaction force history are directly linked through the degree of mode interaction and load redistribution. Multiple-wave deformation indicates stable post-buckling behaviour, emerging waves indicate transitional behaviour, and U-shaped localization indicates unstable collapse. This relationship provides a useful basis for interpreting how imperfection amplitude and relative density control buckling performance.

6.3.4 Peak Load-Carrying Capacity Trends

6.3.4.1 Variation of Peak Load-Carrying Capacity with relative density of foam

The peak reaction force increased monotonically with foam relative density from 0.134 to 0.439 because the core stiffness and shear restraint increased with density. A denser foam core provides greater resistance to face-sheet deflection, improves transverse shear transfer, and delays the onset of global buckling, so the panel can sustain a higher compressive load before instability develops. In other words, the increase in peak load is not simply a material-strength effect; it reflects the way the core stiffness controls the stability of the entire sandwich system.

For the perfect-geometry cases, the peak reaction force increased from approximately 48 kN at the lowest density to about 77 kN at the highest density. This trend is consistent with sandwich theory, in which the core relative density governs the transverse shear modulus, and the shear modulus contributes directly to buckling resistance through the shear-flexural interaction of the panel. As the core becomes denser, the face sheets are better supported against out-of-plane deflection, so the structure requires a higher load to trigger the first instability.

The same monotonic increase was also observed when the maximum load within the imperfection-sensitive window was considered. This shows that geometric imperfection changes the detailed collapse path, but it does not alter the fundamental stiffness-driven trend: higher-density foam cores still produce higher load-carrying capacity. However, the mechanical benefit of increasing density should be interpreted together with the mode-interaction results, because higher density increases absolute strength while also influencing how readily the panel transitions to localization after buckling begins

6.3.4.2 Variation of Peak Load-Carrying Capacity with Imperfections

The variation of normalized peak load carrying capacity of Al foam sandwich panel with different relative density foam, with applied initial imperfection amplitude are shown in Fig 6.78.

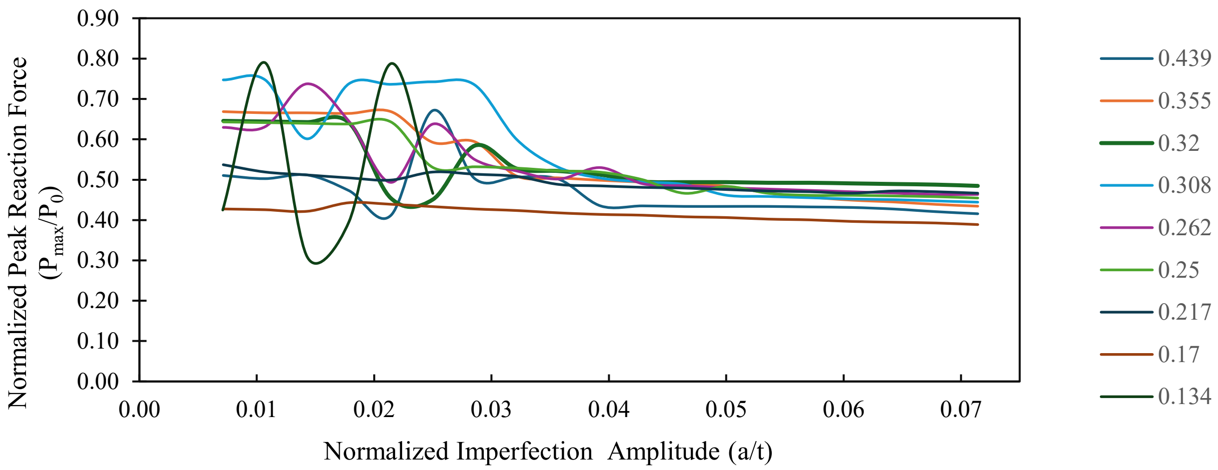

Figure 6.78: Combined variation of normalized peak reaction force with initial imperfection amplitude for aluminium foam sandwich panels of different relative densities.

Figure 6.78 shows that the normalized peak load is governed by how the initial imperfection modifies the load-transfer mechanism within the sandwich section rather than by imperfection amplitude alone. Once buckling begins, the face sheets and foam core no longer act as a uniformly coupled system; instead, the imperfection alters the way compressive load is redistributed through bending of the face sheets and shear transfer in the core.

At $\rho^* = 0.134$, the compliant core provides limited lateral restraint, so even small imperfections can disturb the compressive load path and produce large fluctuations in peak capacity. In this case, the peak load is controlled by whether the section can sustain distributed deformation long enough to delay localization.

At $\rho^* = 0.17$–0.25, the core offers a more balanced stiffness, so the face sheets are sufficiently supported to maintain a more stable load path and the peak load varies only modestly with imperfection amplitude. This indicates that the section is able to redistribute stress before collapse becomes localized.

At $\rho^* = 0.308$–0.439, the sandwich carries higher peak loads because the stiffer core increases the overall flexural and shear resistance of the section; however, once the imperfection is large enough to trigger localization, the same stiffness leaves less capacity for gradual redistribution, so the loss of peak load becomes more pronounced.

Overall, the peak-load trend reflects a competition between shear restraint provided by foam core, face-sheet stability, and the onset of localized buckling, rather than a simple monotonic effect of imperfection amplitude.

6.3.5 Imperfection Sensitivity by Density

The dependence of imperfection sensitivity on density reflects how the foam core modifies the collapse path once buckling has initiated. Unlike Section 6.3.4.1, which addressed the increase in peak load with density, this section examines how strongly the panel response changes when the imperfection amplitude is varied. At $\rho^* = 0.134$, the response is highly imperfection sensitive because the compliant core provides limited restraint to the face sheets, so even small geometric disturbances can alter the way the panel progresses from distributed buckling to localization.

The $\rho^* = 0.17$ and 0.217 panels are less sensitive because the core provides enough shear support to sustain a more gradual post-buckling response, allowing the load to be redistributed before the collapse path becomes fully localized. This gives the section a broader tolerance to imperfection, since the deformation pattern changes less abruptly across the studied range.

For $\rho^* = 0.25$ and above, the response again becomes more imperfection dependent because the stiffer core increases the structural stability margin but also makes the transition from distributed deformation to localization more abrupt once the imperfection exceeds a critical level. In these cases, the panel can carry a higher load, but the route to collapse becomes more condition sensitive, so the exact imperfection amplitude has a stronger influence on the post-buckling path. Overall, the density effect on imperfection sensitivity is non-monotonic: low-density panels are unstable because they cannot sustain redistribution, intermediate-density panels provide the most tolerant response, and higher-density panels regain sensitivity because the stiffer section transitions more sharply once localization begins

The Table 6.22 below shows the normalized peak reaction force, for different relative density foam sandwiches, for corresponding normalized imperfections

Table 6.22: Normalized peak reaction force of sandwich panel of different relative density Al foam across different normalized imperfection amplitudes.

Normalized Imperfection	Relative Density of Foam in Sandwich								
	0.134	0.17	0.217	0.25	0.262	0.308	0.32	0.355	0.439
0.0071	0.4247	0.4275	0.5371	0.6431	0.6296	0.7473	0.6457	0.6687	0.5104
0.0107	0.7897	0.4255	0.5190	0.6414	0.6312	0.7473	0.6442	0.6657	0.5026
0.0143	0.3093	0.4217	0.5118	0.6397	0.6943	0.6013	0.6426	0.6657	0.5117
0.0179	0.3959	0.4429	0.5045	0.6380	0.6445	0.7378	0.6411	0.6642	0.4727
0.0214	0.7876	0.4391	0.4991	0.6431	0.4934	0.7363	0.4540	0.6687	0.4117
0.0250	0.4660	0.4333	0.5190	0.5303	0.6379	0.7425	0.4509	0.5925	0.6714
0.0286	-	0.4275	0.5136	0.5320	0.5498	0.7347	0.5844	0.5940	0.5026
0.0321	-	0.4236	0.5081	0.5286	0.5216	0.5997	0.5276	0.5090	0.5065
0.0357	-	0.4178	0.4882	0.5219	0.5017	0.5306	0.5215	0.5045	0.5013
0.0393	-	0.4139	0.4846	0.5185	0.5299	0.5039	0.5123	0.4985	0.4351
0.0429	-	0.4120	0.4810	0.5000	0.4900	0.4945	0.4954	0.4940	0.4351
0.0464	-	0.4081	0.4792	0.4663	0.4850	0.4882	0.4939	0.4896	0.4338
0.0500	-	0.4062	0.4756	0.4832	0.4801	0.4615	0.4939	0.4836	0.4338
0.0536	-	0.4023	0.4720	0.4663	0.4767	0.4584	0.4923	0.4672	0.4338
0.0571	-	0.4004	0.4702	0.4613	0.4734	0.4553	0.4923	0.4567	0.4325
0.0607	-	0.3965	0.4665	0.4613	0.4701	0.4521	0.4908	0.4493	0.4312
0.0643	-	0.3946	0.4720	0.4596	0.4668	0.4505	0.4893	0.4448	0.4273
0.0679	-	0.3926	0.4702	0.4579	0.4635	0.4474	0.4877	0.4388	0.4208
0.0714	-	0.3888	0.4665	0.4545	0.4635	0.4443	0.4847	0.4343	0.4156

6.3.6 Critical Imperfection Threshold for Buckling Transition

The nonlinear analysis results indicate the presence of a critical imperfection threshold, expressed in terms of the normalized imperfection amplitude. Below this threshold, the panels primarily developed emerging wave or multi-wave buckling patterns, and the reaction force response generally exhibited either a stable plateau or a gradual loss of stiffness. When the normalized imperfection amplitude exceeded this threshold, the deformation was increasingly controlled by a localized U-shaped mode, the contribution of higher-order mode interactions was reduced, and the peak reaction force declined more rapidly. Therefore, the threshold represents the critical point at which the stable mode interaction gives way to dominant localization.

This critical threshold is density-dependent. For the intermediate-density panels ($\rho^* = 0.17–0.262$), no clear transition threshold was observed within the analysed range of $a \leq$

$0.0714t$;these panels maintained distributed or weakly interacting buckling behavior throughout the investigated range, suggesting that the onset of dominant U-shaped localization occurs at significantly higher normalized amplitudes. In contrast, the higher-density panels ($\rho^* = 0.308$–0.439) exhibited a transition to U-shaped deformation at much lower normalized thresholds, typically in the range of $a \approx 0.0286t$–$0.0357t$. This indicates that localization sets in at smaller imperfection amplitudes in the higher-density panels, on the other hand, panels with lower and intermediate core densities retain a more distributed deformation pattern over a much wider range of imperfections.

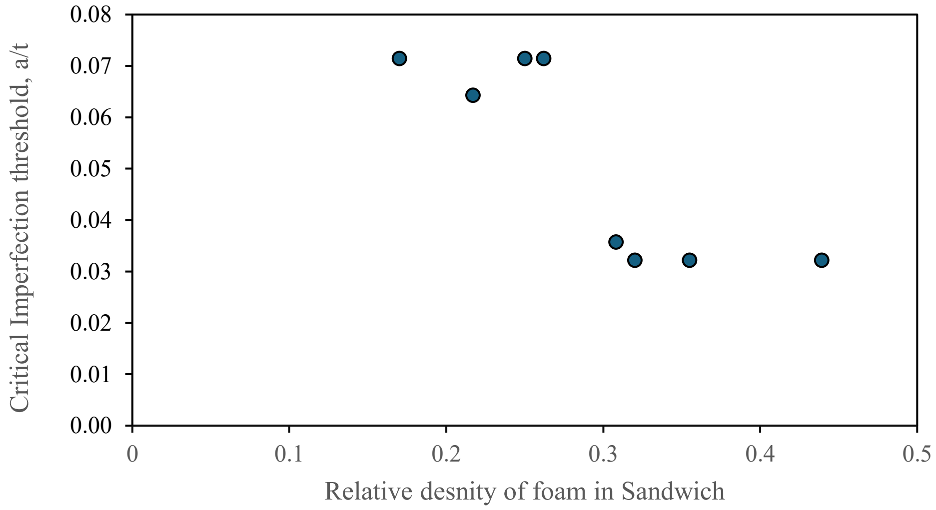

Figure 6.79: Variation of Imperfection Threshold for Buckling Transition of Sandwich Panel with Relative Density of Foam

Overall, the results show that the critical normalized imperfection threshold is not governed by a simple monotonic rule. This reflects the combined influence of the core stiffness, face-sheet restraint, and eigenmode spacing on the post-buckling path. The transition marks a fundamental shift from a distributed instability pattern sustained by active mode coupling to a localized collapse mode governed by the initial geometric perturbation

6.3.7 Density Effects on U-Shaped Localization

The deformation shape within the U-Shaped localized buckling regime varied systematically with the relative density, as observed in the final deformation patterns of the low-density ($\rho^* = 0.134$ to 0.217) and high-density ($\rho^* = 0.25$ and above) foam sandwich panels. The deformation patterns, in localized buckling regime, for sandwich panels with relative densities of 0.134 to 0.217 are shown in Fig 6.80 and for sandwich panels with relative densities 0.25 and above are shown in Fig 6.81. In the low-density case (Figure 6.80), the U-shaped buckling mode was strongly confined to the central region, with little lateral spread toward the panel ends. This suggests a highly localized instability, where the weaker core does not provide sufficient shear stiffness to support significant load redistribution beyond the initial collapse zone. By contrast, in the high-density case (Figure 6.81), the U-shaped localization extended further along the panel length. This deformation pattern indicates that for high-density foam core panels, the stiffer core offers greater shear resistance, delays full collapse at the centre, and allows a larger portion of the face sheets to contribute to the post-buckling load. Although the deformation shapes appear different, both cases show a localization length of approximately 239 mm, suggesting that density mainly affects the intensity and spread of the localized curvature rather than the overall length of the localized region.

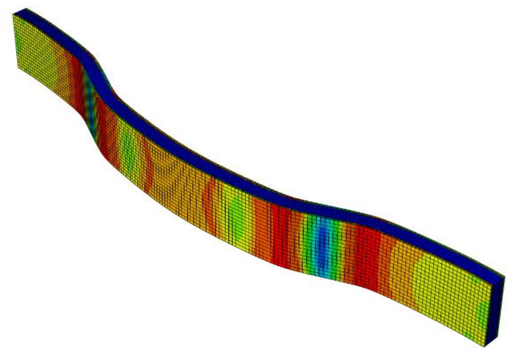

Figure 6.80: U shaped local buckling of low density foam sandwiches

Figure 6.80 captures the end-stage deformation of the low-density panel, where the central U-shape dominates with a sharp curvature and limited end involvement.

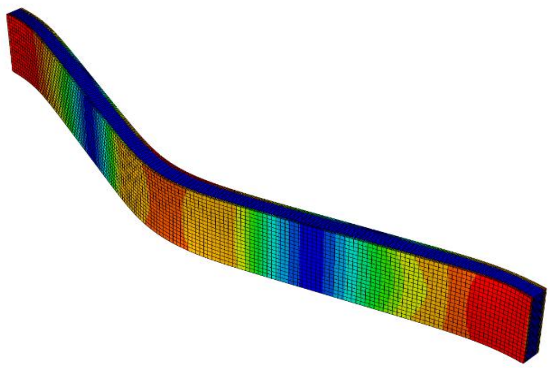

Figure 6.81: U shaped local buckling of higher density foam sandwiches

Figure 6.81 shows the deformation of the higher-density panel at the onset of localization, where a wider U-shaped zone engages a larger portion of the panel length. This behaviour illustrates the density-driven improvement in the post-buckling load redistribution.

6.4 Sensitivity of Collapse Response to Face-Sheet Modulus

A brief sensitivity study was performed to evaluate the effect of reducing the face-sheet elastic modulus from 70 GPa to 33 GPa on the buckling response of the aluminium foam sandwich panels. The aim was to determine whether the plate modulus influences the formation and extent of the imperfection-dependent mode interaction window, in addition to the effects of relative density and imperfection amplitude. The strain-hardening table was kept unchanged, and the analyses were repeated for selected imperfection amplitudes of 0.0071t, 0.0250t, and 0.0321t for aluminium foam sandwich panels with relative densities of 0.134, 0.25, 0.32, and 0.439. These imperfection levels were chosen because they lie within the low-imperfection regime, where imperfection-dependent mode interaction was observed in the baseline $E = 70$ GPa model. To complete the comparison, zero-imperfection models were also developed for all four relative-density cases. The results are given in Table 6.23. The 33 GPa modulus was chosen for comparison because it represents the apparent calibration modulus obtained from the initial linear slope of the previously validated aluminium plate response.

Table 6.23: Effect of imperfection amplitude on RF behaviour, peak reaction force, and observed deformation mode for sandwich panel with face place of E= 33 GPa

Relative Density	Imperfection Amplitude	Peak RF	Rf behaviour	Deformation pattern
0.134	0	46.6 kN	Linear region followed by upward plateau followed by gradual drop	Several halfwaves throughout the panel
0.134	0.0071t	38.5 kN	Linear region followed by a short upward plateau followed by gradual drop. Initial post peak softening slope was -0.37 kN/mm	Multiple wave type buckling.25 small half waves throughout the length of the panel. $LE13_{peak\ load}$ – 0.009828 $LE13_{Collapse}$-0.6371
0.134	0.025t	11.8 kN	Linear region followed by sudden drop. Initial post peak softening slope was -2.59 kN/mm	U shaped localization. $U3_{max}$ – 8.88 mm $LE13_{peak}$ – 0.07597 Localization Length – 245mm
0.134	0.0321t	14.3 kN	Linear region followed by sudden drop. Initial post peak softening slope was -19.8 kN/mm	U shaped localization $U3_{max}$ – 8.66 mm $LE13_{peak\ load}$ – 0.07246

				Localization Length – 299mm
0.25	0	59 kN	Linear region followed by upward plateau followed by gradual drop	Localized edge deformation
0.25	0.0071t	47 kN	Linear region followed by upward plateau followed by gradual drop, with an initial post peak softening slope of -1.53 kN/mm	Maltiple wave deformation, 11 small halfwaves throughout the panel, $LE13_{peak\ load}$ – 0.08412 $LE13_{collapse}$ – 0.6733
0.25	0.025t	22.9 kN	Linear region followed by sudden drop, with an initial post peak softening slope of -5.65 kN/mm	U shaped global buckling $U3_{max}$ – 5.65 mm $LE13_{peak\ load}$ – 0.01939 Localization length – 245 mm
0.25	0.0321t	22.4 kN	Linear region followed by sudden drop, with an initial post peak softening slope of -5.79 kN/mm	U shaped global buckling $U3_{max}$ – 7.396 mm $LE13_{peak\ load}$ – 0.02642 Localization length – 245 mm
0.32	0	64.9 kN	Linear region followed by upward plateau followed by gradual drop	Localized edge deformation
0.32	0.0071t	30.1 kN	Linear region followed by sudden drop, with an initial post peak softening slope of -2.1 kN/mm	U shaped global buckling $LE13_{peak\ load}$ – 0.009316 $U3_{max}$ -7.55 mm Localization length- 238 mm
0.32	0.025t	27.9 kN	Linear region followed by sudden drop, with an initial post peak softening slope of -11.2 kN/mm	U shaped localization $LE13_{peak\ load}$ – 0.01082 $U3_{max}$ -8.098 mm Localization length- 238 mm
0.32	0.0321t	24.2 kN	Linear region followed by sudden drop ,with an initial post peak softening slope of -12.9 kN/mm	U shaped global buckling $LE13_{peak\ load}$ – 0.01563 $U3_{max}$ -10.24 mm Localization length- 238 mm
0.439	0	77.2 kN	Linear region followed by upward plateau followed by gradual drop	Localized edge deformation with very short multiple half waves spread throughout the panel
0.439	0.0071t	52.7 kN	Linear region followed by upward plateau followed by gradual drop, with an initial post peak softening slope of -4.78 kN/mm	Nine well defined half waves throughout the length of the panel $LE13_{peak\ load}$ – 0.05431 $LE13_{collapse}$ – 0.589
0.439	0.025t	24.8 kN	Linear region followed by sudden drop, with an initial post peak softening slope of -12.3 kN/mm	U shaped global buckling $LE13_{peak\ load}$ – 0.01135 $U3_{max}$ - 9.863 mm Localization length- 238 mm,
0.439	0.0321t	28.2 kN	Linear region followed by sudden drop, with an initial post peak softening slope of -24.1 kN/mm	U shaped global buckling $LE13_{peak\ load}$ – 0.0081 $U3_{max}$ -6.93 mm Localization length- 238 mm

To better interpret the influence of face-sheet modulus on the buckling response, the results for $E = 33$ GPa are compared directly with the baseline $E = 70$ GPa cases in the Table 6.24. This comparison highlights whether reducing the modulus changes only the peak reaction force or also alters the deformation mode and the imperfection-sensitive mode interaction window.

Table 6.24: Comparison of peak reaction force, deformation behaviour, and mode transition for aluminium foam sandwich panels with face-sheet modulus of 70 GPa and 33 GPa

Relative density of Foam	Imperfection Amplitude	70 GPa		33 GPa	
		Peak RF	Deformation Pattern	Peak RF	Deformation Pattern
0.134	0	48.5 kN	Multi-wave deformation	46.6 kN	Multi-wave deformation
	0.0071t	20.6 kN	U-Shaped localization	38.5 kN	Multi-wave deformation
	0.025t	22.6 kN	Emerging waves	11.8 kN	U-Shaped Localization
	0.0321t	Non convergence after linear portion	Not fully captured	14.3 kN	U-Shaped Localization
0.25	0	59.4 kN	Localized edge deformation	59 kN	Localized edge deformation
	0.0071t	38.2 kN	Multi-wave deformation	47 kN	Multiple wave deformation
	0.025t	31.5 kN	U-shaped global buckling	22.9 kN	U-Shaped global buckling
	0.0321t	28 kN	U-shaped global buckling	22.4 kN	U Shaped global buckling
0.32	0	65.2	Localized edge deformation	64.9 kN	Localized edge deformation
	0.0071t	47.6 kN	Multiple wave deformation	30.1 kN	U-Shaped global buckling
	0.025t		Multiple wave deformation	27.9 kN	U-Shaped global buckling
	0.0321t	38.2 kN	Emerging waves deformation	24.2 kN	U-Shaped global buckling
0.439	0	77 kN	Multiple wave with localized edge deformation	77.2 kN	Multiple wave with localized edge deformation
	0.0071t	39.3 kN	Emerging wave deformation	52.7 kN	Multiple wave deformation
	0.025t	51.7	Multiple wave deformation	24.8 kN	U Shaped global buckling
	0.0321t	39 kN	Emerging wave deformation	28.2 kN	U Shaped global buckling

The comparison between the 70 GPa and 33 GPa face-sheet modulus cases shows that the effect of modulus reduction is minor in the zero-imperfection condition but becomes increasingly important once geometric imperfections are introduced. For the perfect panels, the peak reaction force remains almost unchanged, indicating that the response is governed mainly by core-dominated global deformation and that the face-sheet modulus plays only a secondary role in the initial stability response. However, when imperfections are present, the face-sheet modulus begins to influence the development of mode interaction, load redistribution, and localization. A reduced modulus weakens the face sheets' ability to restrain the foam core and sustain distributed buckling, so the deformation pattern becomes more sensitive to imperfection amplitude and relative density. This is why the peak reaction force no longer follows the same ordering as in the 70 GPa case, particularly in the imperfection-sensitive regime. A comparison of RF and deformation pattern for 0.134 sandwich with the two face sheet modulus, at 0.025t imperfection, are shown in Fig 6.82 and Fig 6.83 respectively.

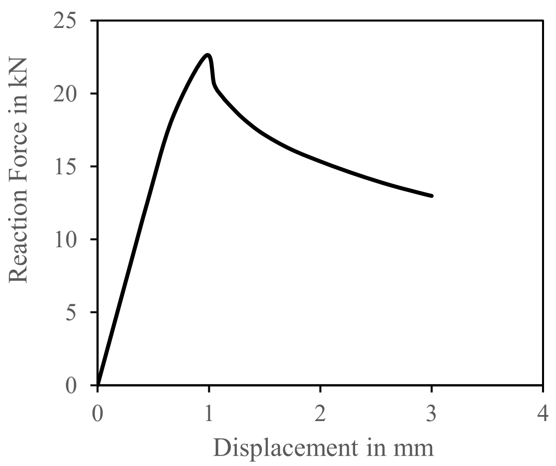

(a) E_f = 70 GPa

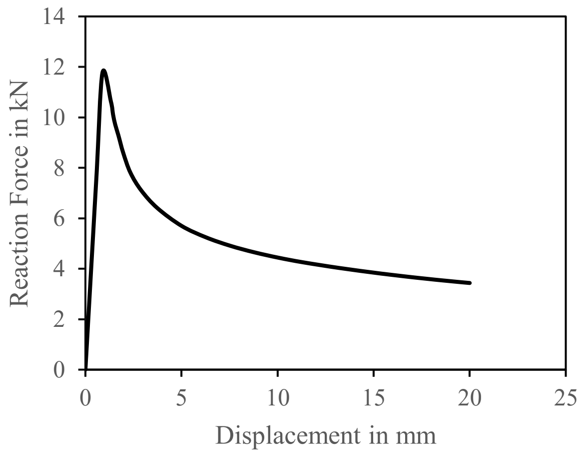

(b) E_f = 33 GPa

Figure 6.82: Comparison of reaction force–displacement response of 0.134 Al foam sandwich with face-sheet modulus of 70 GPa and 33 GPa for 0.025t imperfection

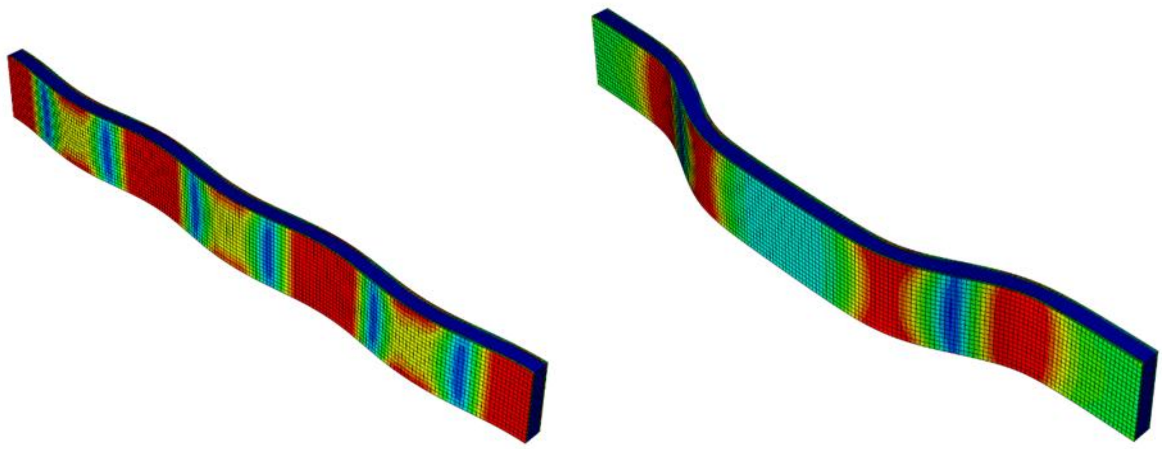

(a) E= 70 GPa (b) E = 33 GPa

Figure 6.83: Comparison of deformation pattern of 0.134 Al foan sandwich with face-sheet modulus of 70 GPa and 33 GPa for 0.025t imperfection

For the 0.134 relative density panel, the absence of convergence issues at $E = 33$ GPa beyond $a = 0.025t$ suggests that lowering the face-sheet stiffness appears to have altered the collapse path and reduced the abruptness of the transition that caused non-convergence in the 70 GPa case. Mechanically, this indicates that the stiffer face sheets in the 70 GPa model were able to sustain stronger interaction with the foam core, which promoted a sharper regime transition into localized instability. When the face-sheet modulus was reduced, the coupled buckling response became less abrupt, allowing the analysis to proceed more smoothly through the post-buckling path. In this sense, the modulus change did not simply reduce strength; it also modified the stability of the collapse mechanism itself.

6.5 Multi-Objective Optimization and Selection of Optimal Foam Core Density

Selecting an optimal foam core for structural sandwich panels is inherently a multi-objective task that requires a balance among the absolute strength, mass efficiency, imperfection sensitivity, and post-buckling stability. Although high density cores can maximise peak load, they are prone to localized failure modes, which can substantially reduce energy absorption and undermine reliability in the presence of manufacturing imperfections

This analysis focused on the normalized imperfection range of 0.0071t to 0.0321t, as this interval captures the key transitions associated with mode coupling. Outside this range, the structural response becomes more monotonic and less sensitive to the initial geometric imperfections, and therefore represents a less critical condition from a design perspective.

6.5.1 Methodology for Performance Evaluation

To facilitate a systematic selection process, the structural performance of the sandwich panels across the investigated relative density range of 0.134 to 0.439 were synthesized into a Multi-Objective Design Selection Matrix (Table 6.26). The metrics presented were derived using the following analytical framework.

1. **Imperfection Tolerance Index (ITI):** This index quantifies the robustness of the panel against initial geometric imperfections. It is calculated as the arithmetic mean of the normalized peak load capacity P_{max}/P_0 across the tested imperfection spectrum 0.0071t to 0.0321t, where P_0 represents the capacity of the near-perfect structure. ITI can be expressed as

$$\text{ITI} = \frac{1}{n}\sum_{i=1}^{n} \frac{P_{max,i}}{P_0}$$

   where $P_{\max,i}$ is the peak load at imperfection level i, P_0 is the peak load of the near-perfect panel, and n is the number of imperfection amplitudes considered.

2. **Deformation Mode Stability:** This rating provides a qualitative measure of the consistency of the buckling mode shape. A ‘High’ rating indicates that the panel maintains a stable and predictable deformation pattern throughout the considered imperfection range, whereas a ‘Low’ rating reflects a greater susceptibility to mode switching or abrupt transitions to a localized U-shaped collapse. this score is based on visual inspection of the deformation patterns shown in section 6.1.

3. **Energy Absorption Potential:** The energy absorption potential was estimated qualitatively from the area under the force–displacement curve. Since the area was assessed visually rather than obtained by numerical integration, it is used here as a comparative indicator only. Panels with a larger sustained plateau region were assigned a higher energy-absorption rating, whereas panels with an early peak and rapid post-peak drop were assigned a lower rating.

4. **Mass Quantification:** Total panel mass (M_{total}), in kg, for each sandwich was calculated as the sum of the aluminium plate masses (constant) and the foam core mass. The mass of foam core (m_{core}) is determined by the product of the volume of the foam core (Vcore) and the mass density of foam for each relative density variant (ρ_{core})

$$M_{total} = m_{core} + m_{face\ sheets}$$

where,

$$m_{core} = \rho_{core} * V_{core}$$

In Table 6.25, the raw regime-by-regime performance data are presented for each relative density. This table provides direct evidence from which the final design recommendations are established. The design recommendations are based on the observed response over the governing imperfection interval (listed in Table 6.25) rather than an isolated peak value or a single deformation pattern.

The raw data show that the influence of the imperfection amplitude is strongly dependent on the density. Lower densities, such as $\rho^* = 0.134$, show frequent transitions between multi-wave response and U-shaped localization, indicating unstable mode interactions and poor robustness. Intermediate densities, particularly in the range $\rho^* = 0.25$ to 0.355, exhibit more persistent multi-wave or evolving-wave responses over wider portions of the critical regime, which are associated with improved stability and energy absorption potential. In contrast, the highest density, $\rho^* = 0.439$, tends to shift toward localized deformation over part of the regime despite its greater mass, indicating that an increase in density does not automatically lead to superior structural robustness.

Table 6.25: Raw regime by regime performance data for each relative density foam sandwich

Relative Density of Foam in Sandwich	Imperfection Sensitivity Regime	Dominant Deformation Mode	Deformation Stability Rating	Energy Absorption	Pmax/P0 over the regime	Average Pmax/P0 over the total sensitivity regime	Mass in kg
0.134	0.0071	U Shaped Localization	Low	Low	0.4247	0.5292	0.361
	0.0107	Multi-waves		High	0.7897		
	0.0143 to 0.01179	U Shaped Localization		Low	0.3526		
	0.0214	Multi-waves		High	0.7876		
	0.0259	Evolving Waves		Medium	0.466		
0.17	0.0071 to 0.0321	U Shaped Localization	High	High		0.4311	0.385
0.217	0.0071 to 0.0321	U Shaped Localization	High	Low		0.5149	0.416
0.25	0.0071 to 0.0214	Multi-waves	Low	High	0.641	0.572	0.439
	0.0250 to 0.0321	U Shaped Localization		Low	0.5303		
0.262	0.0071 to 0.0107	Emerging Waves	Low	High	0.6304	0.6132	0.447
	0.0143	No fully developed global buckling		High	0.6943		
	0.0179	Emerging Waves		High	0.6445		
	0.0214	U Shaped Localization		Low	0.4934		

	0.0250	Multi-waves		High	0.6379		
	0.0286 to 0.0321	U Shaped Localization		Low	0.5357		
0.308	0.0071 to 0.0107	Multi-waves	Moderate	High	0.7473	0.6955	0.475
	0.0143	Emerging Waves		Medium	0.6013		
	0.0179 to 0.0286	Multi-waves		High	0.7378		
0.32	0.0071 to 0.0179	Multi-waves	Low	High	0.6434	0.5601	0.486
	0.0214 to 0.0250	U Shaped Localization		Low	0.4525		
	0.0286	Emerging Waves		Medium	0.5844		
0.355	0.0071 to 0.0214	Emerging Waves	Moderate	High	0.666	0.6296	0.51
	0.0250 to 0.0286	Emerging Waves		High	0.5932		
0.439	0.1 mm	Emerging Waves	Low	Moderate	0.5104	0.51265	0.566
	0.15 to 0.2 mm	Emerging Waves		Moderately High	0.5071		
	0.25 mm	U Shaped Localization		Low	0.4727		
	0.3 mm	U Shaped Localization		Low	0.4117		
	0.35 mm	Multi-waves		High	0.6714		
	0.4 mm	Emerging Waves		High	0.5026		

6.5.2 Design recommendation for foam core selection

Figure 6.84 presents the failure mode map derived from the finite element results. This map shows the dominant deformation response of the Al foam sandwich panel as a function of the relative density and normalized imperfection amplitude. The map identifies three distinct response regions: including localized U-shaped buckling, emerging-wave transition, and distributed multi-wave buckling. The boxed regions indicate approximate imperfection-dependent mode interaction windows, where mode interactions are the strongest. Of all the investigated densities, $\rho^* = 0.308$ lies in the most favorable region because it sustains distributed multiwave deformation over the critical imperfection range, whereas densities above 0.355 shift more rapidly toward localization-dominated collapse

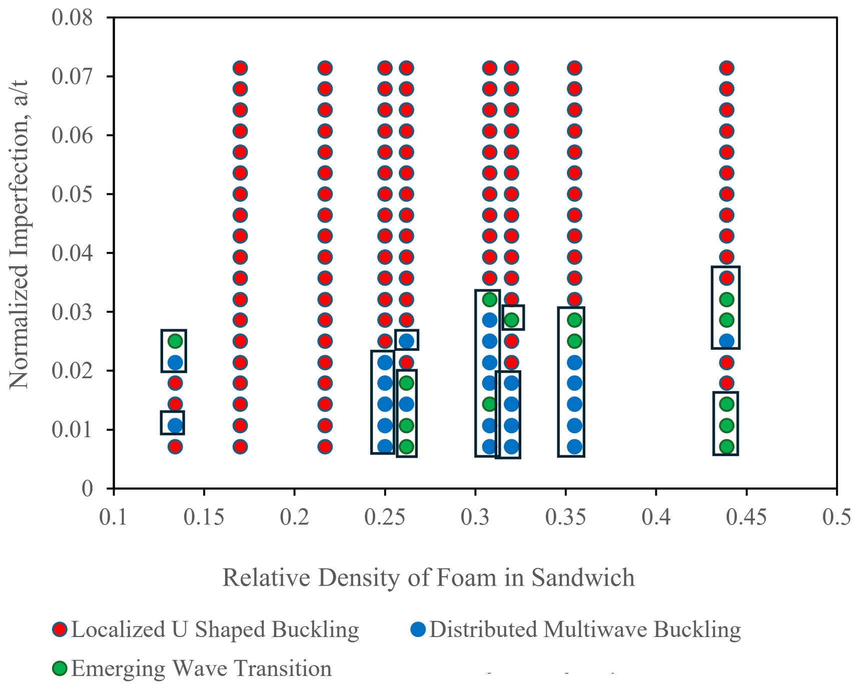

Figure 6.84: Failure mode map for sandwich panels

The detailed results from Table 6.25 were summarized into a decision matrix, as given in Table 6.26, to translate the raw performance trends to a practical design outcome. This matrix enables the rational selection of the core density by simultaneously considering multiple performance criteria, including imperfection tolerance, deformation mode stability, energy absorption potential, and mass efficiency.

Table 6.26: Multi-Objective Design Selection Matrix

Relative Density ρ^*	Mass (kg)	Imperfection Tolerance Index (ITI)	Deformation Mode Stability	Energy Potential	Design Recommendation
0.134	0.361	0.5292	Low (Unstable)	Low	Not Recommended
0.17	0.385	0.4311	High	Medium	Baseline Structure
0.217	0.416	0.5149	High	Medium	Baseline Structure
0.25	0.439	0.572	Moderate (Mixed)	Med-High	Secondary Candidate
0.262	0.447	0.6132	Moderate (Mixed)	Med-High	Baseline Structure
0.308	0.475	0.6955	High (Multi-wave)	Highest	Primary Recommendation
0.32	0.486	0.5601	Low (U-prone)	Low-Med	Alternative
0.355	0.51	0.6296	Moderate (Emerging)	High	Robust Structure
0.439	0.566	0.5127	Low (Localized)	Low-Med	High-Load Only

The data indicate a non-monotonic performance trend, with the structural efficiency and robustness maximized at intermediate relative densities. In particular, the configuration with $\rho^* = 0.308$ is identified as the preferred design option. Although this density involves a modest increase in mass (0.475 kg) compared with the lower-density variants, it provides the highest imperfection tolerance index (ITI = 0.6955) and sustains a stable multi-wave deformation mode over the highly sensitive imperfection range of $a/t = 0.0071$ to 0.0321.

This combination of mode-shape robustness and highest energy potential establishes $\rho^* = 0.308$ as the Pareto-optimal solution, offering superior reliability for structural applications where manufacturing imperfections are unavoidable. In contrast, despite having greater mass, relative densities above 0.355 show a pronounced tendency toward unstable, localized U-shaped collapse. This renders them less suitable for crashworthiness or energy-absorbing applications.

6.6. Numerical Limitations of the Parametric Study

During the parametric study, two numerical limitations were identified at the extremes of the investigated density ranges. For the lowest density panel, $\rho^* = 0.134$, the analysis could be completed only up to an imperfection amplitude of 0.0250t; beyond this value, the Riks procedure terminated before a full post-buckling response could be obtained. This indicates that the model became increasingly difficult to stabilize as the response progressed to stronger localization. At the opposite extreme, the highest-density panel, $\rho^* = 0.472$, did not converge for any of the imperfection amplitudes considered from a/t = 0.0071 to 0.0714. Consequently, no reliable reaction force history or deformation pattern could be extracted for this configuration within the present numerical framework. These limitations suggest that the extreme density cases entered highly unstable post-buckling regimes that exceeded the convergence capacity of the analysis settings adopted in this study.

In addition, the model assumes perfect bonding between the foam core and face sheets through the tie constraints. This idealization may overestimate the stiffness, peak strength, and post-buckling stability if interfacial slip or debonding occurs in practice. The imperfection modelling was also simplified by using only a single eigenmode to generate the initial geometric perturbation. The first buckling mode was selected because it represents the dominant instability pattern of the panel under axial compression and provides a practical basis for a controlled parametric study. Real sandwich panels may exhibit combined-mode imperfections, local face-sheet waviness, or random imperfection fields, which can alter the stability response and broaden peak-load sensitivity. However, these additional imperfection forms were not considered in the present work because they would introduce further modelling complexity and make the interpretation of the collapse response less direct. In addition, the one-year duration of the research programme required the study to remain focused on the most influential imperfection shape. Therefore, the reported trends should be interpreted as representative of the idealized numerical model rather than as a complete description of all possible physical imperfections. Nevertheless, the present framework can be extended in future work to include higher-order, mixed, and random imperfection modes to examine mode interactions and their effect on collapse behaviour in greater detail.

Chapter 7

Proposed Equation for Peak Load Carrying Capacity

This chapter develops a regression based equation for the normalized peak load of aluminium foam sandwich panels under axial compression from the mechanically smoother higher-imperfection regime identified in the previous chapter. The purpose of the equation is not to replace the finite element study, but to provide a simplified expression that reflects the governing post-buckling behaviour when the response is controlled by progressive deformation rather than abrupt mode switching. In this regime, peak load varies in a more regular way with foam relative density, imperfection amplitude, and stiffness ratio, making a response-surface type equation physically meaningful for as a predictive tool.

7.1 Regime Separation Based on Peak Reaction Force

Although the full finite element database comprised 200 analysed models, only the higher-imperfection subset, excluding unconverged and baseline models, was used in the final regression analysis. This separation was required because the low-imperfection response is governed by a different mechanical process from the higher-imperfection response. At low imperfection amplitudes, the panel behaviour is dominated by strong mode interaction, regime transition, and sudden changes in collapse path, so the peak reaction force does not evolve in a sufficiently smooth manner for a single global quadratic equation to represent it reliably. This regime is controlled by discrete switching between deformation modes rather than by gradual post-buckling softening.

To examine this regime quantitatively, the low-imperfection subset was assessed using both exponential and quadratic forms, and the results are presented in Table 7.1. The exponential model resulted values of $R^2 = 0.259$ and adjusted $R^2 = 0.220$, whereas the quadratic model improved these values to $R^2 = 0.449$ and adjusted $R^2 = 0.354$. Although the quadratic form performed better, the fit remained moderate, and several regression terms were statistically weak. This suggests that the low-imperfection regime is governed by a distinct imperfection-sensitive mechanism rather than a simple continuation of the higher-imperfection trend. Accordingly, the low-imperfection region is retained in this study as a separate behavioural regime, while the final proposed equation is calibrated only for the higher-imperfection range ($a/t \geq 0.0321$).

Although small imperfections are practically relevant in real structures, the low-imperfection regime was not incorporated into the final equation because its response is strongly affected by regime transition and mode interaction, making it unsuitable for representation using the same global quadratic model. Therefore, the equation developed in this section is restricted to the higher-imperfection regime, whereas the low-imperfection region remains a distinct behavioural domain.

Table 7.1: Comparison of regression performance for the low-imperfection and higher-imperfection regime

Regime	Model Form	R Square	Adjusted R Square	Comment
a/t<0.0321	Exponential	0.259	0.22	Poor Fit
a/t<0.0321	Quadratic	0.449	0.354	Better, still not robust
a/t≥0.0321	Final Quadratic	0.888	0.876	Adopted for final equation

7.2. High-Imperfection Regime Model Development

Based on the regime separation established in the previous section, the higher imperfection subset was selected to develop the final quadratic predictive equation equation. This subset exhibited a sufficiently regular response to support regression-based modelling, and the resulting equation was evaluated using the 96-case calibration set. Mechanically, this is the regime in which the sandwich panel has already passed the most unstable mode-transition region, so the peak load is governed more by the combined stiffness of the section and the progressive post-buckling response than by abrupt switching between collapse modes.

The response variable used in the regression was the normalized peak reaction force extracted from the Abaqus reaction force history, whereas the predictor variables were the foam relative density, normalized imperfection amplitude (a/t), and stiffness ratio ($E_{Face\ sheet}/E_{Foam}$). These variables were selected because they represent the main mechanical controls on the panel response: foam relative density governs the restraint and shear support provided by the core, normalized imperfection amplitude measures the severity of the geometric disturbance that drives localization, and stiffness ratio captures the balance between face-sheet resistance and foam support during buckling. The relative density values used in the final regression database were 0.17, 0.217, 0.25, 0.262, 0.308, 0.32, 0.355, and 0.439. The lowest density, 0.134, was excluded because no clear peak RF was obtained beyond the linear region for imperfection amplitudes above a/t = 0.0250. The selected finite element results formed the basis for the proposed regression equation. In mechanical terms, the equation represents the smoother post-buckling domain where load redistribution is still possible, so the peak reaction force can be approximated by a continuous function of density, imperfection severity, and stiffness balance.

7.2.1 Choice of Regression Model Form

To identify an appropriate regression form for the higher-imperfection regime, several candidate models were examined and compared based on their statistical fit and physical consistency. The selection criteria included the coefficient of determination, adjusted coefficient of determination, significance of the regression terms, and the ability of the model to represent the observed response trend within the calibrated range of values. This comparison was necessary because the post-buckling response of the sandwich panel is not governed by a single linear stiffness relationship, but by a coupled interaction between core density, imperfection severity, and the redistribution of load after buckling begins. The quadratic form was selected because the higher-imperfection regime exhibited a smooth but nonlinear variation in the peak reaction force with respect to the relative density, imperfection amplitude, and stiffness ratio. In this regime, the response is governed by progressive deformation and gradual changes in the load-carrying capacity rather than abrupt regime switching; therefore, a second-order polynomial is suitable for capturing both the curvature and interaction effects. From a sandwich-mechanics perspective, this is consistent with the fact that the core density controls face-sheet restraint, the imperfection amplitude controls how quickly localization develops, and the stiffness ratio reflects the balance between face-sheet support and foam compliance. These coupled effects naturally produce a curved response surface rather than a straight-line trend.

Although the low-imperfection subset showed limited predictive consistency for both tested forms, the higher-imperfection data were better represented by a quadratic response surface. This form provided a better balance between the statistical performance and mechanical interpretability; therefore, it was adopted for final equation. In other words, the quadratic model was not chosen only because it fitted the data better, but because it also reflects the underlying mechanics of the smoother post-buckling regime in which the panel response evolves continuously rather than through abrupt mode changes.

7.2.3 Regression Analysis Procedure

The proposed FE-based predictive equation equation was developed using multiple regression analysis in Microsoft Excel, based on the selected finite element database. The dependent variable was the normalized peak reaction force (P/P_0), whereas the independent variables were the foam relative density, normalized imperfection amplitude, and stiffness ratio (E_f/E_c). A quadratic response surface was fitted using the terms intercept, $\rho, \frac{a}{t}, \frac{E_f}{E_c}, \rho^2, (\frac{a}{t})^2, (\frac{E_f}{E_c})^2, p\frac{a}{t}$, $\rho\frac{E_f}{E_c}$ and $\frac{a}{t}\frac{E_f}{E_c}$, so that both the individual effects and the interaction between the three variables could be captured. The regression coefficients were obtained by fitting the selected FE results to the assumed polynomial form, and the significance of each term was assessed using its p-value. Terms with low p-values were considered statistically significant contributors to the model, while the overall quality of the regression was evaluated using R^2, adjusted R^2, and the Significance F value. The final model was selected by balancing the statistical fit, significance of the coefficients, and practical simplicity, with preference given to the equation that provided a strong fit without unnecessary complexity. This approach ensured that the resulting equation was both statistically defensible and suitable for use as a compact expression.

Table 7.2 lists the finite element cases selected for the regression and the corresponding governing variables used in the calibration database. The squared and interaction terms required for the quadratic response surface were generated from these variables during the fitting procedure. The fitted model was then evaluated using Excel summary statistics and p-values of the regression coefficients.

Table 7.2:Finite element calibration cases and governing variable

Specimen ID	Relative Density of foam (ρ)	Normalized Imperfection (a/t)	E_f/E_f	P/P_0
RD017-I0.45	0.17	0.0321	569.110	0.424
RD017-I0.5	0.17	0.0357	569.110	0.418
RD017-I0.55	0.17	0.0393	569.110	0.414
RD017-I0.6	0.17	0.0429	569.110	0.412
RD017-I0.65	0.17	0.0464	569.110	0.408
RD017-I0.7	0.17	0.0500	569.110	0.406
RD017-I0.75	0.17	0.0536	569.110	0.402
RD017-I0.8	0.17	0.0571	569.110	0.400
RD017-I0.85	0.17	0.0607	569.110	0.397
RD017-I0.9	0.17	0.0643	569.110	0.395
RD017-I0.95	0.17	0.0679	569.110	0.393
RD017-I1	0.17	0.0714	569.110	0.389

RD0217-I0.45	0.217	0.0321	368.420	0.508
RD0217-I0.5	0.217	0.0357	368.420	0.488
RD0217-I0.55	0.217	0.0393	368.420	0.485
RD0217-I0.6	0.217	0.0429	368.420	0.481
RD0217-I0.65	0.217	0.0464	368.420	0.479
RD0217-I0.7	0.217	0.0500	368.420	0.476
RD0217-I0.75	0.217	0.0536	368.420	0.472
RD0217-I0.8	0.217	0.0571	368.420	0.470
RD0217-I0.85	0.217	0.0607	368.420	0.467
RD0217-I0.9	0.217	0.0643	368.420	0.472
RD0217-I0.95	0.217	0.0679	368.420	0.470
RD0217-I1	0.217	0.0714	368.420	0.467
RD025-I0.45	0.25	0.0321	257.350	0.529
RD025-I0.5	0.25	0.0357	257.350	0.522
RD025-I0.55	0.25	0.0393	257.350	0.519
RD025-I0.6	0.25	0.0429	257.350	0.500
RD025-I0.65	0.25	0.0464	257.350	0.466
RD025-I0.7	0.25	0.0500	257.350	0.483
RD025-I0.75	0.25	0.0536	257.350	0.466
RD025-I0.8	0.25	0.0571	257.350	0.461
RD025-I0.85	0.25	0.0607	257.350	0.461
RD025-I0.9	0.25	0.0643	257.350	0.460
RD025-I0.95	0.25	0.0679	257.350	0.458
RD025-I1	0.25	0.0714	257.350	0.455
RD0262-I0.45	0.262	0.0321	205.880	0.522
RD0262-I0.5	0.262	0.0357	205.880	0.502
RD0262-I0.55	0.262	0.0393	205.880	0.530
RD0262-I0.6	0.262	0.0429	205.880	0.490
RD0262-I0.65	0.262	0.0464	205.880	0.485
RD0262-I0.7	0.262	0.0500	205.880	0.480
RD0262-I0.75	0.262	0.0536	205.880	0.477
RD0262-I0.8	0.262	0.0571	205.880	0.473
RD0262-I0.85	0.262	0.0607	205.880	0.470
RD0262-I0.9	0.262	0.0643	205.880	0.467
RD0262-I0.95	0.262	0.0679	205.880	0.463
RD0262-I1	0.262	0.0714	205.880	0.463
RD0308-I0.45	0.308	0.0321	137.790	0.600
RD0308-I0.5	0.308	0.0357	137.790	0.531
RD0308-I0.55	0.308	0.0393	137.790	0.504
RD0308-I0.6	0.308	0.0429	137.790	0.495
RD0308-I0.65	0.308	0.0464	137.790	0.488
RD0308-I0.7	0.308	0.0500	137.790	0.462
RD0308-I0.75	0.308	0.0536	137.790	0.458
RD0308-I0.8	0.308	0.0571	137.790	0.455
RD0308-I0.85	0.308	0.0607	137.790	0.452
RD0308-I0.9	0.308	0.0643	137.790	0.451
RD0308-I0.95	0.308	0.0679	137.790	0.447
RD0308-I1	0.308	0.0714	137.790	0.444

RD032-I0.45	0.32	0.0321	126.810	0.528
RD032-I0.5	0.32	0.0357	126.810	0.521
RD032-I0.55	0.32	0.0393	126.810	0.512
RD032-I0.6	0.32	0.0429	126.810	0.495
RD032-I0.65	0.32	0.0464	126.810	0.494
RD032-I0.7	0.32	0.0500	126.810	0.494
RD032-I0.75	0.32	0.0536	126.810	0.492
RD032-I0.8	0.32	0.0571	126.810	0.492
RD032-I0.85	0.32	0.0607	126.810	0.491
RD032-I0.9	0.32	0.0643	126.810	0.489
RD032-I0.95	0.32	0.0679	126.810	0.488
RD032-I1	0.32	0.0714	126.810	0.485
RD0355-I0.45	0.355	0.0321	121.530	0.509
RD0355-I0.5	0.355	0.0357	121.530	0.504
RD0355-I0.55	0.355	0.0393	121.530	0.499
RD0355-I0.6	0.355	0.0429	121.530	0.494
RD0355-I0.65	0.355	0.0464	121.530	0.490
RD0355-I0.7	0.355	0.0500	121.530	0.484
RD0355-I0.75	0.355	0.0536	121.530	0.467
RD0355-I0.8	0.355	0.0571	121.530	0.457
RD0355-I0.85	0.355	0.0607	121.530	0.449
RD0355-I0.9	0.355	0.0643	121.530	0.445
RD0355-I0.95	0.355	0.0679	121.530	0.439
RD0355-I1	0.355	0.0714	121.530	0.434
RD0439-I0.45	0.439	0.0321	85.680	0.506
RD0439-I0.5	0.439	0.0357	85.680	0.501
RD0439-I0.55	0.439	0.0393	85.680	0.435
RD0439-I0.6	0.439	0.0429	85.680	0.435
RD0439-I0.65	0.439	0.0464	85.680	0.434
RD0439-I0.7	0.439	0.0500	85.680	0.434
RD0439-I0.75	0.439	0.0536	85.680	0.434
RD0439-I0.8	0.439	0.0571	85.680	0.432
RD0439-I0.85	0.439	0.0607	85.680	0.431
RD0439-I0.9	0.439	0.0643	85.680	0.427
RD0439-I0.95	0.439	0.0679	85.680	0.421
RD0439-I1	0.439	0.0714	85.680	0.416

7.3. Proposed equation

Based on the regression analysis of the selected higher-imperfection finite element database, the following quadratic equation is proposed for predicting the normalized peak reaction force P/P_0 of aluminium foam sandwich panels under axial compression. The equation was obtained from the 96-case calibration set and included the linear, quadratic, and interaction terms required to represent the observed nonlinear trend within the validated range.

$$\frac{P}{P_0} = -1.363 + 10.34\rho - 8.385\frac{a}{t} + 0.00927\frac{E_f}{E_c} - 11.57\rho^2 + 49.27\left(\frac{a}{t}\right)^2 - 6.56 \times 10^{-6}\left(\frac{E_f}{E_c}\right)^2$$

$$+2.577\rho\frac{a}{t} - 0.02738\rho\frac{E_f}{E_c} + 0.00388\frac{a}{t}\frac{E_f}{E_c} \qquad [1]$$

In this equation,

$\frac{P}{P_0}$ is the normalized peak reaction force, where P is the peak reaction force obtained from the finite element analysis and P_0 is the reference peak reaction force of the corresponding perfect geometry panel,

ρ denotes the relative density of the foam core,

$\frac{a}{t}$ denotes the normalized imperfection amplitude,

$\frac{E_f}{E_c}$ denotes the stiffness ratio of the face sheet to that of the foam core.

The terms ρ^2, $(a/t)^2$, and $\left(E_f/E_c\right)^2$ represent the quadratic effects of the three governing variables, whereas $\rho(a/t)$, $\rho(E_f/E_c)$, and $\left(a/t\right)(E_f/E_c)$ represent the interaction effects between the variables.

The equation is valid for the selected density range and for normalized imperfection amplitudes $a/t \geq 0.0321$, which correspond to the high-imperfection regime used in the regression analysis. The equation should not be applied outside this range, particularly in the lower-imperfection regime, where the response is highly non-monotonic and not well represented by a single smooth surface.

7.4. Statistical Fit of the Model

The adequacy of the proposed quadratic regression model was evaluated using the Excel summary output obtained from 96 selected finite element cases. The model produced a coefficient of determination of $R^2 = 0.887818$ and an adjusted $R^2 = 0.876078$, indicating that the fitted equation explains a large proportion of the variation in the normalized peak reaction force within the calibrated higher-imperfection regime. The standard error of 0.01334 was small relative to the range of predicted values, suggesting that the model reproduced the finite element results with limited scatter. In addition, the Significance F value of 5×10^{-37} confirms that the overall regression is significant.

The coefficient table indicates that the main linear terms and several quadratic and interaction terms contributed meaningfully to the response surface. In particular, the coefficients associated with the relative density, normalized imperfection amplitude, stiffness ratio, ρ^2, $(a/t)^2$, $\left(E_f/E_c\right)^2$, $\rho(E_f/E_c)$, and $\left(a/t\right)\left(E_f/E_c\right)$ are statistically significant at the 95% confidence level, whereas the $\rho(a/t)$ interaction term is comparatively weaker. This suggests that the response is governed primarily by the combined effects of the density, imperfection amplitude, and stiffness ratio, with the curvature and interaction effects captured by the second-order polynomial form.

The fitted coefficients also exhibited physically consistent trends. The positive coefficient of ρ indicates that an increase in the foam relative density generally increases the peak load, while the negative coefficient of a/t indicates that larger imperfections reduce the load-carrying capacity. The quadratic terms reflect the nonlinear curvature of the response surface, and the interaction terms indicate that the effect of one variable depends on the level of another variable. Overall, the high R^2, low standard error, significant regression F-test, and physically reasonable coefficient signs indicate that the proposed equation provides a strong and defensible fit to the selected finite element data.

The regression statistics and coefficients are presented in Tables 7.3 and 7.4.

Table 7.3: Regression Statistics

Statistic	Value
Multiple R	0.942240942
R Square	0.887817993
Adjusted R Square	0.876078015
Standard Error	0.013342528
Observations	96
F	75.62348315
Significance F	5.00E-37

Table 7.4: Regression Coefficients

Term	Coefficient	Standard Error	t Stat	P-value
Intercept	-1.3626256	0.500649801	-2.721714	0.00786045
ρ	10.33613842	2.3721424	4.357301	3.63E-05
a/t	-8.384922443	1.567255932	-5.350066	7.1723E-07
Ef/Ec	0.009271226	0.002244355	4.1309097	8.35E-05
ρ^2	-11.57232518	2.499403179	-4.630035	1.286E-05
(a/t)^2	49.27045633	10.10437986	4.8761485	4.9062E-06
(Ef/Ec)^2	-6.56004E-06	1.4738E-06	-4.451109	2.5485E-05
ρ*(a/t)	2.577019065	2.903079759	0.8876846	0.37718637
ρ*(Ef/Ec)	-0.027385546	0.006623638	-4.134517	8.2398E-05
(a/t)*(Ef/Ec)	0.003877906	0.001497192	2.5901202	0.01126707

Although the fitted response surface includes a positive coefficient for the $(a/t)^2$ term, this reflects the local curvature in the polynomial fit rather than a non-physical increase in strength with increasing imperfections. A physical plausibility check was performed by comparing the predicted normalized peak reaction force with the corresponding perfect panel value. Across the entire calibrated dataset, all predicted P/P_0 values remained below 1, indicating that the proposed regression equation does not predict a load-carrying capacity greater than that of the perfect panel within the validated range. This confirms that the fitted surface is consistent with the expected physical behaviour of imperfection-sensitive sandwich panels.

7.5. Comparison of FE and Predicted Peak Reaction Force

The accuracy of the proposed equation was further assessed by comparing the finite element predictions with the corresponding values obtained from the final quadratic model for the 96-case calibration set.

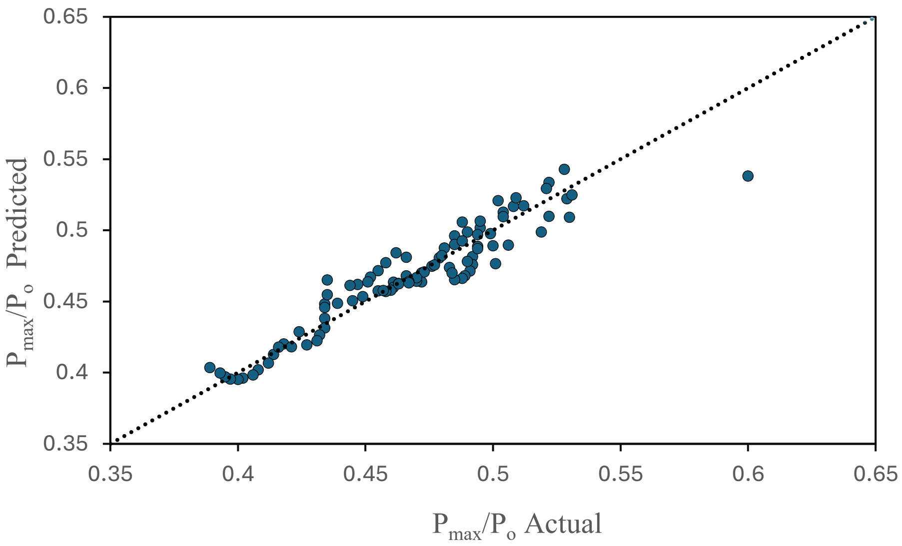

Figure 7.1: Comparison of FE peak load and predicted load for the regression validation cases with a 1:1 reference line

Figure 7.1 compares the finite element and predicted normalized peak reaction forces for the 96-case calibration set. It should be noted that the finite element peak reaction force represents the structural response of the analysed model and should not be interpreted directly as the design strength. The data points lie close to the 1:1 line, indicating that the proposed quadratic equation reproduces the overall FE trend well across the calibrated higher-imperfection regime. The close clustering of the points around the diagonal indicates a good agreement between the model predictions and finite element results.

A detailed comparison between the finite element peak reaction force and the corresponding values predicted by the quadratic regression model is provided in Table 7.5. The residuals were generally small, and the mean predicted-to-actual ratio remained close to unity. This indicates a good overall agreement between the model and FE results. The scatter in the residuals was limited for most specimens, with absolute percentage errors typically remaining below 5%. The maximum deviation occurs for specimen RD0308-I0.45, where the absolute percentage error reaches 10.323%, but it is still an isolated case rather than a systematic trend

In terms of conservatism, the residuals were nearly balanced, with 50 positive and 46 negative residuals. This indicates a very slight overall conservative tendency, as the model underpredicts the FE peak reaction force in a marginally larger number of cases than it overpredicts it. The magnitude of the deviations remained small, and the larger errors were mainly associated with cases near the transition region, where the response was more sensitive to the imperfection amplitude and panel stiffness ratio. Overall, the table confirms that the proposed equation reproduces the FE peak reaction force with acceptable accuracy and limited scatter across the calibrated range.

Table 7.5: Comparison of FE peak load, predicted load, residual, and percentage error for regression validation cases.

Specimen ID	Actual P/P_0	Predicted P/P_0	Residual	Absolute Percentage Error (%)
RD017-I0.45	0.424	0.429	-0.00472	1.114
RD017-I0.5	0.418	0.420	-0.00208	0.499
RD017-I0.55	0.414	0.413	0.00128	0.308
RD017-I0.6	0.412	0.407	0.00536	1.301
RD017-I0.65	0.408	0.402	0.00605	1.483
RD017-I0.7	0.406	0.398	0.00761	1.876
RD017-I0.75	0.402	0.396	0.00590	1.468
RD017-I0.8	0.4	0.395	0.00490	1.226
RD017-I0.85	0.397	0.395	0.00167	0.421
RD017-I0.9	0.395	0.397	-0.00184	0.465
RD017-I0.95	0.393	0.400	-0.00662	1.685
RD017-I1	0.389	0.404	-0.01455	3.742
RD0217-I0.45	0.508	0.517	-0.00871	1.714
RD0217-I0.5	0.488	0.506	-0.01770	3.627
RD0217-I0.55	0.485	0.496	-0.01098	2.263
RD0217-I0.6	0.481	0.488	-0.00653	1.357
RD0217-I0.65	0.479	0.481	-0.00154	0.321
RD0217-I0.7	0.476	0.475	0.00139	0.293
RD0217-I0.75	0.472	0.470	0.00205	0.434
RD0217-I0.8	0.47	0.467	0.00335	0.712
RD0217-I0.85	0.467	0.465	0.00248	0.531
RD0217-I0.9	0.472	0.464	0.00834	1.767
RD0217-I0.95	0.47	0.464	0.00592	1.260
RD0217-I1	0.467	0.466	0.00129	0.276
RD025-I0.45	0.529	0.522	0.00697	1.317
RD025-I0.5	0.522	0.510	0.01221	2.340
RD025-I0.55	0.519	0.499	0.02018	3.889
RD025-I0.6	0.5	0.489	0.01088	2.175
RD025-I0.65	0.466	0.481	-0.01492	3.202
RD025-I0.7	0.483	0.474	0.00925	1.916
RD025-I0.75	0.466	0.468	-0.00185	0.397
RD025-I0.8	0.461	0.463	-0.00234	0.508
RD025-I0.85	0.461	0.460	0.00104	0.225
RD025-I0.9	0.46	0.458	0.00214	0.465
RD025-I0.95	0.458	0.457	0.00097	0.211
RD025-I1	0.455	0.457	-0.00246	0.540
RD0262-I0.45	0.522	0.533	-0.01150	2.202

RD0262-I0.5	0.502	0.521	-0.01864	3.714
RD0262-I0.55	0.53	0.509	0.02094	3.950
RD0262-I0.6	0.49	0.499	-0.00876	1.788
RD0262-I0.65	0.485	0.490	-0.00497	1.025
RD0262-I0.7	0.48	0.482	-0.00219	0.456
RD0262-I0.75	0.477	0.476	0.00131	0.276
RD0262-I0.8	0.473	0.471	0.00241	0.510
RD0262-I0.85	0.47	0.467	0.00340	0.723
RD0262-I0.9	0.467	0.464	0.00311	0.666
RD0262-I0.95	0.463	0.462	0.00054	0.117
RD0262-I1	0.463	0.462	0.00071	0.153
RD0308-I0.45	0.6	0.538	0.06194	10.323
RD0308-I0.5	0.531	0.525	0.00632	1.190
RD0308-I0.55	0.504	0.513	-0.00858	1.702
RD0308-I0.6	0.495	0.502	-0.00676	1.365
RD0308-I0.65	0.488	0.492	-0.00446	0.913
RD0308-I0.7	0.462	0.484	-0.02215	4.794
RD0308-I0.75	0.458	0.477	-0.01912	4.175
RD0308-I0.8	0.455	0.472	-0.01651	3.629
RD0308-I0.85	0.452	0.467	-0.01500	3.319
RD0308-I0.9	0.451	0.464	-0.01277	2.831
RD0308-I0.95	0.447	0.462	-0.01481	3.314
RD0308-I1	0.444	0.461	-0.01714	3.859
RD032-I0.45	0.528	0.543	-0.01471	2.786
RD032-I0.5	0.521	0.529	-0.00829	1.591
RD032-I0.55	0.512	0.517	-0.00515	1.005
RD032-I0.6	0.495	0.506	-0.01128	2.279
RD032-I0.65	0.494	0.497	-0.00294	0.595
RD032-I0.7	0.494	0.489	0.00541	1.095
RD032-I0.75	0.492	0.482	0.01048	2.130
RD032-I0.8	0.492	0.476	0.01613	3.278
RD032-I0.85	0.491	0.471	0.01968	4.008
RD032-I0.9	0.489	0.468	0.02095	4.285
RD032-I0.95	0.488	0.466	0.02195	4.499
RD032-I1	0.485	0.465	0.01967	4.056
RD0355-I0.45	0.509	0.523	-0.01375	2.702
RD0355-I0.5	0.504	0.510	-0.00558	1.108
RD0355-I0.55	0.499	0.498	0.00131	0.262
RD0355-I0.6	0.494	0.487	0.00692	1.402
RD0355-I0.65	0.49	0.478	0.01202	2.453
RD0355-I0.7	0.484	0.470	0.01412	2.917
RD0355-I0.75	0.467	0.463	0.00394	0.843
RD0355-I0.8	0.457	0.458	-0.00066	0.144
RD0355-I0.85	0.449	0.453	-0.00436	0.970
RD0355-I0.9	0.445	0.450	-0.00533	1.198
RD0355-I0.95	0.439	0.449	-0.00958	2.183
RD0355-I1	0.434	0.448	-0.01411	3.251
RD0439-I0.45	0.506	0.489	0.01656	3.273

RD0439-I0.5	0.501	0.477	0.02445	4.881
RD0439-I0.55	0.435	0.465	-0.02993	6.881
RD0439-I0.6	0.435	0.455	-0.01960	4.505
RD0439-I0.65	0.434	0.446	-0.01177	2.712
RD0439-I0.7	0.434	0.438	-0.00395	0.911
RD0439-I0.75	0.434	0.431	0.00259	0.597
RD0439-I0.8	0.432	0.426	0.00572	1.325
RD0439-I0.85	0.431	0.422	0.00875	2.029
RD0439-I0.9	0.427	0.420	0.00749	1.754
RD0439-I0.95	0.421	0.418	0.00296	0.703
RD0439-I1	0.416	0.418	-0.00184	0.442

The residuals, defined as the finite element load minus the normalized predicted reaction force, remained relatively small for most cases, and the corresponding absolute percentage errors were generally low. This indicates that the regression equation captures the overall trend of the FE response with a limited bias across the calibrated domain. The scatter observed at higher load levels does not suggest a systematic over- or under-prediction, but rather reflects the strong nonlinear sensitivity of the response near the mode-transition region. In particular, the larger errors (`10.32%) at the 0.308 panel with $a/t = 0.0321$ and the 0.439 panel (6.66%) with $a/t = 0.0393$ are physically reasonable because, as discussed in Section 6.2, these cases lie close to the transition between distributed mode interaction and localized U-shaped buckling. In this region, small changes in the imperfection amplitude can cause noticeable shifts in the peak Reaction Force; therefore, isolated deviations from the regression prediction are expected. Overall, the close alignment with the 45-degree line, together with the small residuals in most cases, demonstrates that the proposed equation provides a satisfactory representation of the FE peak load response within the calibrated domain.

7.6. Residual Analysis of the Regression Model

Residual analysis was performed to evaluate the adequacy of the proposed regression equation and to determine whether the prediction errors exhibited any systematic patterns. The residuals were plotted against the predicted normalized peak reaction force, foam relative density, and normalized imperfection amplitude to assess whether the model reproduced the response consistently across the calibrated range. The three residual plots are shown in Figs. 7.2 to 7.4.

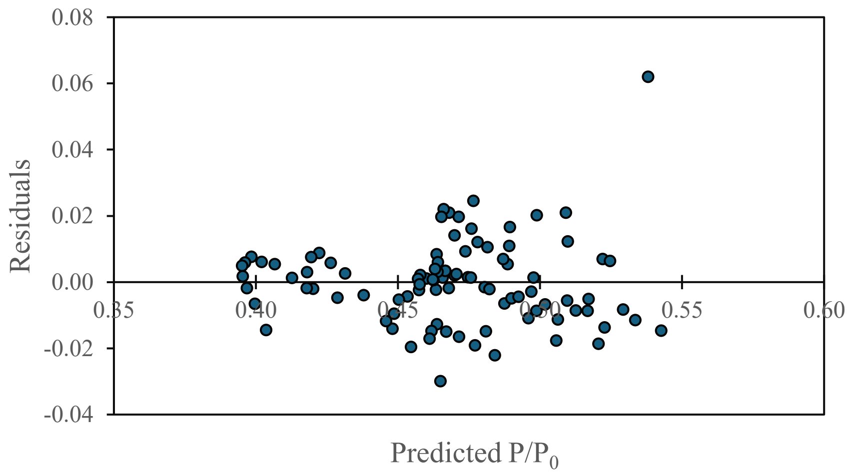

Figure 7.2: Residuals versus normalized predicted peak reaction force.

The residuals versus the predicted normalized peak reaction force plot shows a broadly scattered distribution about the zero line. This indicates that the prediction error does not consistently increase or decrease with the predicted response; therefore, no strong load-dependent bias is evident. Although a small amount of local clustering was visible, the overall pattern remained sufficiently random, suggesting that the model fit was acceptable.

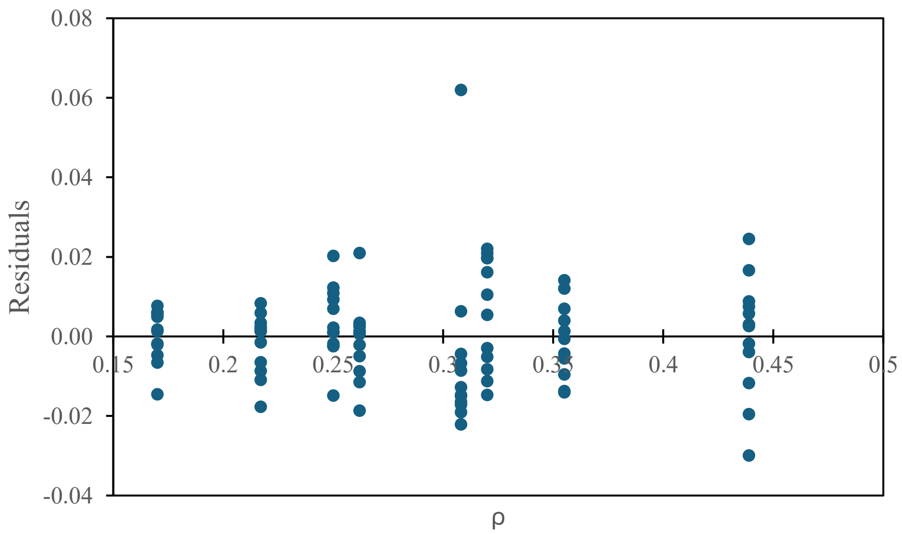

Figure 7.3: Residuals versus relative density of foam in sandwich

The residuals versus relative density plot also remained centered near zero, with some grouping at specific density levels. This suggests that the effect of relative density was captured satisfactorily by the proposed equation. Importantly, the plot did not show a clear increasing or decreasing trend with density, indicating that there was no strong evidence of a systematic bias associated with this variable.

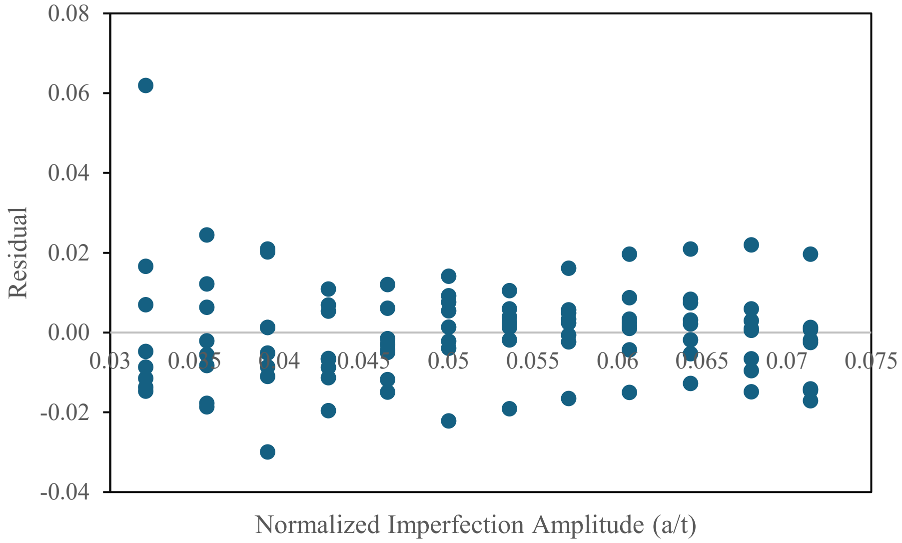

Figure 7.4: Residuals versus normalized imperfection amplitude

Similarly, the residuals versus normalized imperfection amplitude plot displayed a scatter around zero without a distinct monotonic pattern. A few larger residuals appeared near the lower and upper ends of the imperfection range, but these did not form a consistent trend. This suggests that the regression model captures the overall effect of the imperfection amplitude well while still allowing for small local discrepancies.

Overall, the three residual plots indicate that the proposed regression equation is acceptable within the range studied. The residuals were mostly randomly scattered around zero, with only mild grouping in certain regions, and no strong systematic trend was observed. Accordingly, the model is suitable for prediction within the calibrated domain, although only small local deviations remain.

7.7. Cross-Validation of the Regression Model

A five-fold cross-validation procedure was performed to assess the predictive robustness of the proposed regression equation. In each fold, four subsets of the finite element database were used to fit the regression model, and the remaining subset was withheld for the validation. This procedure provides an independent check on the model by assessing its performance using data that were not used during calibration.

Table 7.6: Summary of 5-Fold Cross Validation Results for the Regression Analysis

	Fold 1	Fold 2	Fold 3	Fold 4	Fold 5
Mean Predicted to Actual Ratio	1.000	1.003	1.005	0.991	1.004
Coefficient of Variation	0.027	0.022	0.027	0.032	0.034
RMSE	0.012	0.011	0.013	0.018	0.016
MAPE(%)	2.181	1.676	2.214	2.051	2.898

The validation results for the five folds are summarized in Table 7.6. The mean predicted-to-actual ratio remained very close to 1.0 in all cases, ranging from 0.991 to 1.005, which indicates that the regression model produced predictions with little systematic bias. The coefficient of variation also remained low, between 0.022 and 0.034, indicating that the prediction scatter was limited and broadly consistent across the folds. In addition, the RMSE values were small, ranging from 0.011 to 0.018, which confirms that the prediction errors were low in magnitude. The variation in the MAPE values between 1.676% and 2.898% demonstrates that the model achieved good predictive accuracy over all five validation sets.

Overall, the cross-validation results show that the proposed regression equation is stable and reliable within the available data range. Although minor variations exist between the folds, no fold exhibited poor predictive behaviour. Fold 2 yielded the best performance based on the RMSE and MAPE. Fold 5 showed a slightly higher error but remained within an acceptable range. These results confirm that the proposed equation generalizes well and is suitable for practical prediction within the calibrated higher-imperfection regime.

7.7 Discussion of Multicollinearity

During the variable selection process for the regression model, correlation analysis revealed a strong linear relationship between relative density (ρ) and stiffness ratio, with a correlation coefficient of $r = -0.876$. This indicates substantial multicollinearity between these predictor variables, suggesting they share overlapping information regarding the foam stiffness properties. This correlation is physically expected, as relative density inherently reflects the material stiffness of the aluminium foam to some extent.

To determine whether the stiffness ratio should be retained despite the multicollinearity issue, a reduced model is developed, including only normalized imperfection (a/t) and relative density (ρ) as predictor variables. This reduced model was then compared with the full model which included stiffness ratio too as predictor variables and the results are presented in Table 7.7 and 7.8.

Table 7.7 presents the regression statistics for both models. The full model with stiffness ratio demonstrates superior statistical performance with an R^2 value of 0.8878 compared to 0.8051 for the reduced model, representing a 10.3% improvement in explained variance. Similarly, the adjusted R^2 increases from 0.7943 to 0.8761, confirming that the additional variable contributes meaningful predictive information beyond what is explained by relative density alone. The standard error is reduced by 22.7% (from 0.0172 to 0.0133), indicating more precise predictions

Table 7.7: Regression Statistics Comparison – Full Model vs Reduced Model

Statistics	Full Model (with Stiffness Ratio)	Reduced Model (without Stiffness Ratio)	Percentage Difference
Multiple R	0.942240942	0.89726	+5%
R Square	0.887817993	0.80508	+10.3%
Adjusted R Square	0.876078015	0.79425	+3%
Standard Error	0.013342528	0.01719	-22.7%
Significance F	5.00E-37	1.90306E-30	Both are significant

The predictive performance and stability of both models were further evaluated using 5-fold cross-validation, with results summarized in Table 7.8. The full model demonstrates substantially lower prediction errors, with a mean RMSE of 0.0140 compared to 0.0238 for the reduced model, representing a 41.2% reduction in error magnitude. Similarly, the mean absolute percentage error (MAPE) is reduced by 46.5% (from 4.12% to 2.20%), indicating that predictions from the full model are, on average, closer to the actual values.

The coefficient of variation (CV) across folds is notably lower for the full model (0.028) compared to the reduced model (0.052), indicating greater prediction stability and consistency across different data subsets. This difference becomes particularly evident when examining fold-by-fold performance

Table 7.8: Five Fold Cross Validation Results Comparison

Fold	RMSE (Full)	RMSE (Reduced)	MAPE % (Full)	MAPE % (Reduced)	COV (Full)	COV (Reduced)
1	0.012	0.022	2.181	3.424	0.027	0.043
2	0.011	0.018	1.676	3.506	0.022	0.039
3	0.013	0.015	2.214	2.635	0.027	0.032
4	0.018	0.018	2.051	3.309	0.032	0.039
5	0.016	0.046	2.898	7.757	0.034	0.105
Mean	0.014	0.0238	2.2	4.126	0.028	0.052

A critical observation is the dramatically degraded performance of the reduced model in Fold 5, where RMSE increases from 0.016 to 0.046 (2.9× higher) and MAPE increases from 2.898% to 7.737% (2.7× higher). This substantial performance variation indicates that the reduced model is unstable and may overfit to certain data subsets, whereas the full model maintains consistent predictive accuracy across all folds.

Based on the comprehensive comparison of regression statistics and cross-validation results, it is found that the full model including stiffness ratio was better as the final proposed equation despite the multicollinearity concern (r = -0.876). The decision is justified by the following key findings.

1. **Superior predictive accuracy**: The full model achieves 10.3% higher R^2 and 41.2% lower RMSE
2. **Better prediction precision**: MAPE is reduced by 46.5% (2.20% vs 4.12%)
3. **Enhanced stability**: CV across folds is 46% lower (0.028 vs 0.052)
4. **Robustness**: The full model maintains consistent performance across all folds, while the reduced model shows significant degradation in Fold 5

The stiffness ratio adds independent predictive information beyond relative density alone, likely capturing additional mechanical behavior of the aluminum foam sandwich panels under compression that is not fully represented by relative density. This suggests that while relative density reflects foam stiffness to some extent, the stiffness ratio provides supplementary information related to the panel's structural response

7.7.1. Limitation and Interpretation Caution

The multicollinearity between relative density and stiffness ratio (r = -0.876) presents a limitation in the physical interpretation of the regression equation. Due to this correlation, the individual regression coefficients for these two variables should not be over-interpreted as representing completely independent physical effects. The coefficient values reflect the correlated nature of the predictor variables, and attributing distinct mechanical meanings to each coefficient separately may be misleading.

However, this limitation does not compromise the predictive capability of the equation. The full model provides accurate predictions of normalized load capacity with R^2 = 0.888 and MAPE = 2.20%, which is adequate for FE-based predictive use within the calibrated range.

When discussing the physical significance of the proposed equation, the combined effect of relative density and stiffness ratio should be considered rather than interpreting each coefficient independently.

7.8. Procedure for peak load prediction

To facilitate the practical use of the proposed regression equation, a procedure is presented for predicting the normalized peak load of aluminium foam sandwich panels within the calibrated higher-imperfection regime. The proposed equation is valid for the specific panel geometry and loading configuration considered in this study. The parameter ranges over which the equation is valid are as follows: relative density from 0.17 to 0.439, normalized imperfection amplitude from 0.0321 to 0.0714, and stiffness ratio from 85.68 to 569.11. This equation should not be extrapolated beyond these limits without further validation.

The procedure is as follows,

1. Determine the panel parameters required by the equation, namely the relative density of the foam, the imperfection amplitude, and the stiffness ratio E_f/E_c.
2. Confirm that the selected values lie within the calibrated range of the proposed equation.
3. Substitute the corresponding normalized variables into the final quadratic expression for P/P_0.
4. Compute the predicted normalized peak load using the equation.
5. If required, convert the normalized prediction back to the peak load by multiplying by the reference load P_0.
6. Use the predicted value for interpretation only within the validated range of the model.

This procedure provides a direct and transparent method for applying the proposed equation without requiring additional numerical analysis. It also ensures that the equation is used consistently with the behavioural regime for which it was developed.

7.8.1. Worked example

As an illustration, consider the sandwich panel RD0355-I0.55 with the following properties:

- Relative density, $\rho = 0.355$

- Imperfection amplitude, $\frac{a}{t} = \frac{0.55}{14} = 0.0393$
- Stiffness ratio, $E_f/E_c = 121.53$

Substituting these values into the proposed equation yields:

$\frac{P}{P_0}$= -1.363+10.34 x 0.355 – 8.385 x 0.0393 + 0.00927 x121.53 – 11.57 x 0.355^5 + 49.27 x0.0393^3 -6.56 x 10^{-6} x 121.53^2 +2.577 x 0.355 x 0.0393 – 0.02738 x 0.355 x 121.53 + 0.00388 x0.0393 x 121.53

$$\frac{P}{P_0} = -1.363 + 3.6717 - 0.3295755 + 1.1263851 - 1.4596 + 0.0761 - 0.0969 + 0.03595 - 1.18062 + 0.018924$$

$$= 0.499$$

Therefore, for the above sandwich panel, the normalized peak reaction force obtained from the equation is 0.499, which means that the predicted peak reaction force is 49.9% of the peak reaction force of the perfect panel.

If the peak reaction force of the perfect panel is known, the corresponding peak reaction force for the panel with the considered imperfection can be obtained as follows:

$$P = (P/P_0)\, P_0$$

Here, the peak reaction load carrying capacity of the panel i.e peak reaction force of the panel in perfect condition (no imperfectios) is known as 67 kN. Therefore peak load carrying capacity of of the given panel is

$$P = 0.499 \times 67 = 33.43\ kN$$

This demonstrates how the proposed equation can be used to estimate the normalized peak reaction force and, subsequently, the corresponding peak load of the sandwich panel. It should be noted that this value represents the predicted finite element peak load under the analysed loading condition, rather than a code-based design strength

7.9. Discussion of Model Applicability and Limitations

The proposed regression equation is intended as a FE-based predictive approximation for aluminium foam sandwich panels that deform through the same mechanical regime studied in this thesis. Its validity is therefore limited not only by the numerical calibration range, but also by the structural mechanism that governs the response. The equation represents the higher-imperfection post-buckling regime, where the panel response evolves in a relatively smooth and continuous manner as a consequence of stiffness balance, load redistribution, and gradual localization. It should not be used where the governing collapse mechanism changes, because a single response surface cannot represent different buckling processes with the same reliability.

The proposed regression equation is applicable only to the specific panel geometry and loading configuration considered in this study. The equation was developed for aluminium foam sandwich panels with rectangular geometry, having a face-sheet thickness of 2 mm and a core thickness of 10 mm. The panel dimensions were 500 mm × 50 mm.The boundary conditions employed in the finite element models consisted of simply supported constraints on all four edges, wherein transverse displacement was restrained while allowing rotation about the edge axes. The loading type applied was quasi-static uniaxial compressive loading, representative of axial compression scenarios encountered in structural applications.

The sandwich panels were constructed using closed-cell aluminium foam as the core material, fabricated via a modified ALPORAS melt foaming route with pore sizes ranging from 0.9 to 3.0 mm (Cheng et al. [3]). The face sheets were made from 5052-H32 aluminium alloy (Roh et al. [4]). Changes in foam processing, pore structure, density distribution, or face-sheet alloy would modify the face-core interaction and could shift the panel into a different buckling regime. For that reason, the equation should not be applied to other foam systems or other face-sheet materials without further validation.

The equation was calibrated using finite element results covering the following parameter ranges: relative density (ρ) from 0.17 to 0.439, normalized imperfection amplitude (a/t) from 0.0321 to 0.0714, and stiffness ratio from 85.68 to 569.11. Within this calibrated domain, the model provides reliable estimates of the normalized peak reaction force for aluminium foam sandwich panels in the higher-imperfection regime. Since the dependent variable P/P_0, imperfection amplitude a/t, and stiffness ratio are all dimensionless, the proposed equation is expressed in non-dimensional form for these variables. Therefore, the coefficients are empirical regression constants for the calibrated dataset, rather than unit-based physical constants.

The model behaviour was physically consistent within the validated domain. Increasing the foam relative density generally led to a higher predicted peak reaction force, whereas increasing the imperfection amplitude lowered it. The stiffness ratio also affects the response through the interaction terms of the regression equation. Although the fitted surface contains a positive quadratic term in the imperfection amplitude, this does not imply that the strength increases with larger imperfections; instead, it represents the local curvature in the fitted response surface and remains consistent with the overall decreasing trend observed within the calibrated range.

A further physical plausibility check confirmed that all the predicted normalized peak reaction force values remained below unity for the entire calibration database. This indicates that the regression equation does not predict a load-carrying capacity greater than that of the corresponding perfect panel within the validated range of the panel. This is consistent with the expected behaviour of imperfection-sensitive sandwich panels, in which geometric imperfections reduce the structural capacity rather than enhance it.

For some low-density cases, the fitted quadratic surface showed a slight local curvature near the upper end of the imperfection range, even though the finite element data continued to decrease more clearly with increasing imperfection amplitude. This does not indicate an unphysical trend in the model but rather reflects the compromise inherent in fitting a single global regression surface to the full database. Because the predicted values remained below the perfect panel response and the deviation was confined to the edge of the validated range, the equation was considered appropriate for use within the calibrated domain.

Overall, the proposed equation is best understood as a mechanics-based predictive tool for a specific aluminium foam sandwich system operating in a specific post-buckling regime. It is useful because it captures the smooth higher-imperfection response where peak load varies in a predictable way with core density, geometric imperfection, and stiffness ratio. It should not be extrapolated beyond that domain, since the governing collapse mechanism changes and the same regression form can no longer represent the sandwich mechanics with confidence.

Chapter 8

Summary & Conclusion

8.1 Summary

This study examined the non-linear buckling and post-buckling behaviour of sandwich panels under axial compression. The finite element models of the foam and aluminium plate were first validated against experimental data, while the aluminium foam sandwich model was calibrated and assessed through comparison with analytical benchmark predictions, with additional consideration of buckling mode, deformation pattern, and stress distribution. It was found that the simulations reproduced the main deformation trends, stress distribution patterns, and global mechanical response with reasonable accuracy. After calibration and benchmark comparison, the influence of foam relative density and geometric imperfection amplitude on the in-plane compression of sandwich panels was examined through a parametric finite element study**.** The results showed that both parameters had a pronounced effect on the reaction force response, deformation mode evolution, buckling interaction, and overall compressive load-carrying capacity of the panels. The analyses further showed that these responses are strongly governed by imperfection-dependent mode interaction in a limited low-imperfection range, where distributed multi-wave buckling and load distribution along the panel can occur.

Linear buckling analysis identified the dominant instability modes and showed that the spacing between the first few eigenmodes increased with the relative density. This suggests a stronger mode separation in the higher-density panels and helps explain the differences observed in the nonlinear response. The nonlinear analysis showed that small imperfections may promote distributed buckling and stable post-buckling behaviour, whereas larger imperfections generally trigger localization into a U-shaped deformation pattern accompanied by a rapid reduction in load-carrying capacity.

An imperfection-dependent mode interaction window was also identified, within which the panels could redistribute the load more effectively and sustain higher reaction forces. This can be defined quantitatively chosen by the performance criterion, within which the panel can sustain higher reaction forces and exhibit more stable post-buckling behaviour. Outside this window, the deformation became increasingly localized, and the post-buckling response became less stable and transited towards U-shaped localization. In addition, the monotonic increase in the peak reaction force with relative density confirmed that denser foam cores provide greater compressive strength. However, the effect of imperfection sensitivity is not monotonic with relative density. Instead, the intermediate density panels showed the most favourable balance between strength, stability, and imperfection tolerance.

In the localized buckling regions, the spatial extent of the deformation was influenced by the relative density. The panels with lower foam densities exhibited a more confined U-shaped localization concentrated near the central region, whereas the higher-density panels exhibited a wider U-shaped deformation extending further toward the panel ends. This indicates that the relative density affects not only the magnitude of the peak reaction force but also the development and spread of the localized buckling mode along the length of the panel.

The parametric study also showed numerical limits at the density extremes, with the 0.134 panel terminating beyond a 0.35 mm imperfection and the 0.472 panel failing to converge within the analysed imperfection range.

A multi-objective performance framework was introduced to compare the relative densities using several criteria simultaneously, including an Imperfection Tolerance Index (based on $P_{\max}/P_0$), deformation-mode stability, energy absorption potential and mass. By condensing the parametric results into a failure-mode map and a design selection matrix, the analysis showed that structural robustness and efficiency are maximised at intermediate densities, with ρ* = 0.308 emerging as the primary recommendation and ρ* ≈ 0.25–0.355 identified as a favourable density band for design. The lowest and highest densities were found to be less attractive due to either poor robustness to imperfections or a stronger tendency towards localised U-shaped collapse.

In the final stage of the work, a regression-based predictive equation was developed for the normalized peak reaction force in the higher-imperfection regime. Using the finite element database for eight relative densities and a range of imperfection amplitudes and stiffness ratios, a quadratic response surface was calibrated that provides a compact prediction of peak load within the smoother, stable part of the response space. The low-imperfection regime, where strong mode interaction produces irregular behaviour, was deliberately excluded from this equation and retained as a separate behavioural domain.

8.2 Conclusions

The in-plane buckling response of aluminium foam sandwich panels is governed by a competition between stiffness-driven load support and imperfection-driven localization. Foam-core relative density does not simply increase strength in a uniform way; it changes the way the sandwich section distributes compressive load after buckling begins, and therefore changes whether the panel remains in a distributed post-buckling state or collapses through a localized deformation path.

A key mechanical finding is that increasing foam density raises the compressive load-carrying capacity, but it also alters the stability of the buckling path. Higher-density panels can sustain larger loads, yet their stiffer cores make the post-buckling response more condition sensitive once the initial imperfection becomes large enough to disrupt the coupled deformation pattern. Lower-density panels, by contrast, are less capable of carrying load, but their response is more diffuse and less sharply dependent on the exact imperfection amplitude. The important point is that strength and imperfection tolerance do not increase together in a simple monotonic way.

The results also imply that geometric imperfection is not just a flaw that reduces capacity. In a limited low-imperfection range, it can activate interaction between the primary buckling mode and higher-order deformation waves, allowing the panel to redistribute strain energy and delay localization. This behaviour defines an imperfection-sensitive mode interaction window, beyond which the deformation path shifts toward U-shaped localization and the peak load drops more sharply. The practical implication is that imperfection influences not only the magnitude of the response, but also the instability mechanism itself.

The deformation mode is therefore a better indicator of performance than peak load alone. Multiple-wave and emerging-wave responses correspond to more effective load redistribution and greater post-buckling stability, whereas U-shaped localization indicates a concentrated collapse mechanism with limited reserve capacity. This means that panel performance must be judged using both strength and stability, rather than peak load in isolation.

Another important outcome is that imperfection sensitivity varies non-monotonically with density. Intermediate core densities provide the best balance between restraint and deformability, giving the most stable post-buckling response over the studied range. The lowest-density panels are too flexible to maintain stable redistribution, while the highest-density panels, although stronger, tend to localize more abruptly once the imperfection becomes large enough to destabilize the coupled buckling path. For the present configuration, $\rho^* = 0.308$ offered the best overall compromise between imperfection tolerance, deformation stability, energy absorption, and mass efficiency.

A brief sensitivity study on the face-sheet elastic modulus further confirmed that the buckling response is governed by the coupled action of face-sheet stiffness, core restraint, and geometric imperfection. Reducing the face-sheet modulus from 70 GPa to 33 GPa had only a limited effect in the perfect-geometry cases, where the response remained largely core-dominated. However, under imperfect conditions, the lower modulus altered the development of mode interaction and delayed or softened the transition to localized collapse in several cases, particularly for the lower-density panels. This shows that the face-sheet modulus influences not only the magnitude of the peak load, but also the stability of the post-buckling path and the sharpness of the mode transition

The regression-based equation developed in this thesis should be viewed as a practical consequence of these mechanics, not as the central result. Its role is to provide a usable estimate of peak load within the calibrated higher-imperfection regime, where the response is smoother and more predictable. The main contribution of the thesis is therefore the physical explanation of how density and imperfection together control the transition from distributed multi-wave buckling to localized U-shaped collapse.

Overall, this thesis closes an important gap in the understanding of aluminium foam sandwich panels under in-plane compression by showing that their response is governed by the coupled effects of density, imperfection, and post-buckling mode interaction. The principal conclusion is that the most mechanically efficient panel is not simply the strongest one, but the one that best balances load-carrying capacity with stable deformation and imperfection tolerance.

8.3 Future Work

Future studies can extend this study in several directions. This study focuses on analytical work; however, the experimental testing of the sandwich panel with initial geometric imperfections analysed in this study can be valuable for further validation of the numerical trends observed in this work. The imperfection modelling considered in the study is simple as only the first eigen model is considered. Future studies can extend this by considering combined modes, local face-sheet imperfections, or random imperfection fields.

Future studies can also examine other loading conditions, such as bending, impact, cyclic loading, or combined compression and bending, to investigate the behaviour of the observed imperfection dependent sensitive windows and mode interactions, under the considered low imperfection regime. Since the present study focuses exclusively on axial compression, these additional cases would assess the broader structural performance of aluminium foam sandwich panels. In addition, further research can investigate different face-sheet materials, core geometries, or graded foam densities to identify designs with improved strength, stability, and imperfection tolerance.

References

[1] Dassault Systèmes. Abaqus Analysis User's Guide. Version 6.14. Dassault Systems Providence, RI, USA, 2014

[2] S Szyniszewski, B.H Smith, B.W Schafer, J.F Hajjar et al. (2012 December), Local buckling strength of steel foam sandwich panels, Thin-Walled Structures, 59, 11-19. Elsevier

[3] Yeng Cheng, Yanxiang Li, Xiang Chen, Xu Zhou and Ningzhen Wang (2018 July), Compressive properties and energy absorption of aluminum foams with a wide range of relative densities, JMEPEG 27: 4016-4024

[4] Jae-Huh Roh, Jeong-Jin Seo, Sung-Tae Hing, Moon-Jo Kim et al. (2014 February), The mechanical behavior of 5052-H32 aluminum alloys under a pulsated electric current, International Journal of Plasticity 58,84-99. Elsevier

[5] Zhiwen Qin, Xiaofei Song, Caicai Liao, Lu Yu et al. (2024), In-plane compressive responses and failure behaviors of composite sandwich plates with resin reinforced foam core, Heliyon 10, e26679

[6] Arameh Eyvazian, Seyed Ahamad Tahizadeh, Abdel Magid Hamouda et al. (2021), Buckling and crushing behaviour of foam core hybrid composite sandwich columns under quasi static edgewise compression, Journal of Sandwich Structures and Materials, Vol 23(7) 2643-2670

[7] Jian Deng, Xia Zhao, Zengxian Wang, Yufei Guo, Chenjun Ding et al. (2026), Mechanical behavior and failure mechanisms of all-composite N-core sandwich plates under in-plane compression, Thin-Walled Structures,227,115005. Elsevier.

[8] Pier Giovanni Benzo, Joao M Pereira, Jose Sena Cruz (2023), Structural response of steel sandwich panels with PUR foam subjected to edgewise compression: Experimental, numerical and analytical considerations, Construction and Building Materials, 409, 134009. Elsevier.

[9] Aditya Vidwans, Patrizia Trovalusci, Nicolas Fantuzzi and Jose A.F.O Correia (2023), Application of column buckling theory to steel aluminium foam sandwich panels, Structures, 54, 607-617. Elsevier.

[10] Shanshan Shi, Xin Zhou, Jiansen Zhang, Bingzhi Chen and Zhi Sun (2023), In-plane compressive response of composite sandwich panels with local tight honeycomb cores, Composite Structures, 314, 116970. Elsevier.

[11] Harry Slack, Fiona Walport, Hou Un Chan, M Ahamer Wadee and Leroy Gardner (2024), A consistent approach to the definition of initial geometric imperfections for in-plane stability design of steel moment frames, Structures, 65, 106596. Elsevier.

[12] Anna Lee, Francisco Lopez Jimenez, Joel Marthelot, John W. Hutchinson and Pedro M. Reis (2016 November), The Geometric role of precisely engineered imperfections on the critical buckling load of spherical elastic shells, Journal of Applied Mechanics, Vol 83, 111005-1.

[13] Adrian X Rivera, Satchi Venkataraman, Hyonny Kim, Evan Pineda and Andrew Bergan (2020), Sensitivity analysis of geometric imperfection sources in honeycomb cores on flatwise compression behavior, In AIAA SciTech Forum, American Institute of Aeronautics and Astronautics.

[14] Jacob Marx and Afsaneh Rabiei (2020 August), Study on the Microstructure and compression of composite metal foam core sandwich panels, Metallurgical and Materials Transactions, Volume 51A, 5187.

[15] L.L Yan, B.Yau, B Han, C.Q Chen, Q.C Zhang and T.J Lu (2013 July), Compressive strength and energy absorption of sandwich panels with aluminum foam filled corrugated cores, Composite Science and Technology, 86, 142- 148.Elsevier.

[16] LL Yan, B Yu, B Han, QC Zhang, TJ Lu and BH Lu (2020), Effects of aluminum foam filling on the low velocity impact response of sandwich plates with corrugated cores, Journal of Sandwich & Materials, Vol. 22(4) 929-947.

[17] Muataz Hazza F. Al Hazza, Nor Amalina Endut, Erry Y.T.Adesta et al. (2019 March), Numerical analysis of aluminum foam sandwich subjected to compression loading, International Journal of Recent Technology and Engineering (IJRTE), ISSN: 2277-3878, Volume-7, Issue -6S.

[18] Cheng-Xu Ren, Zheng-Fei Hu, Cheng Yao and Fan Mo (2019 August), Experimental study on the quasi-static compression behavior of multilayer aluminium foam sandwich structure, Journal of Alloys and Compounds 810, 151860. Elsevier.

[19] Zichen Zhang, Haomin Feng, Tao Xu, Wei Xin, Jian Ding, Nannan Liu et al. (2021 December), Compressive performances of integral forming aluminum foam sandwich, Composite Structures, 283, 115090.Elsevier.

[20] Xiaotong Lu, Lei Jing, Wenhao Zhou, Hui Yang, Pingyun Yuan et al. (2024 January), Pore structure and deformation correlation of an aluminum foam sandwich subject to three point bending, Materials, 17, 567.

[21] Fan Dong, Yazhi Li, Xin Qi, Weijie Ma, Chunping Zhou et al. (2024 October), Failure behavior and damage model of composite sandwich panels under three point bending fatigue load, Thin-Walled Structures ,205, 112570. Elsevier.

[22] Mehdi Nakisa, Fatemeh Behrouzi and Ahamad Mobasher Amini (2016 October), Different failure mode assessment to improve the sandwich composite panel stiffness with honeycomb core for marine structures application, Jurnal Teknologi 78:11, 183-189, eISSN 2180-3722.

[23] Jolanta Pozorska and Zbigniew Pozorski (2017), Analysis of the failure mechanism of the sandwich panel at the supports, Procedia Engineering 177, 168-174. Elsevier.

[24] Ahmed Hassan and Ibrahim Abdullah Alnaser (2024), A review of different manufacturing methods of metallic foams, ACS Omega 9, 6280-6295.

[25] Graziano Ubertalli, Monica Ferraris and Muhammad Kashif Bangash (2017 February), Joining of AL-6016 TO Al-Foam using Zn-based joining materials, Composites: Part A 96, 122-128. Elsevier.

[26] Pai Peng, Kuaishe Wang, Wen Wang, Liying Huang, Ke Qiao, Qianying Che et al. (2018 October), High performance aluminium foam sandwich prepared through friction stir welding, Materials Letters 236, 295-298, Elseveir.

[27] Tizian Bucher, Mini Zhang, Chang Jun Chen, Ravi Verma, Wayne Li et al. (2019 May), Laser forming of metal foam sandwich panels: Effect of panel manufacturing method, Journal of Manufacturing Science and Engineering, Vol. 141, 051006-1.

[28] Chao Yan, Xiaowei Xu, Tianli Wang, Yishengi Li et al. (2022 October), Effect of resin pins on the failure behavior of foam core sandwich beams under three-point loading, ACS Omega, 7, 37834-37845.

[29] Jinhua Zhang, Li Chen, Hao Wu, Qin Fang et al. (2019 April), Experimental and mesoscopic investigation of double layer aluminum foam under impact loading, Composite Structures, 214, 110859. Elsevier.

[30] Anders Lindstrom (2009), In-plane compressive response of sandwich panels, Doctoral thesis, KTH Royal Institute of Technology, School of Engineering Sciences, Department of Aeronautical and Vehicle Engineering, Stockholm.

[31] Anders Lindstrom (2007), Strength of sandwich panels loaded in in-plane compression, Licentiate thesis, KTH Royal Institute of Technology, School of Engineering Sciences, Department of Aeronautical and Vehicle Engineering, Stockholm.

[32] Pawel Jasion and Krzysztof Magnucki (2013), Global buckling of a sandwich column with metal foam core, Journal of Sandwich Structures and Materials, Vol 15(6) 718-732.

[33] Yi-Hsin Nieh, Yen-Kun Lai and Jia-Lin Tsai (2015), Characterizing failure behaviors of debonded composite sandwich structures under compressive loading, Journal of Sandwich Structures and Materials, Vol 17(5) 578-594.

[34] S EL-Sayed and S. Sridharan (2002 January), Imperfection-sensitivity of integral and debonded sandwich beams under compression, Journal of Sandwich Structures and Materials, Vol 4, 1099-6362/02/01 0049-21.

[35] Russell Biagi and Hilary Bart-Smith (2006 December), Imperfection sensitivity of pyramidal core sandwich structures, International Journal of Solids and Structures 44, 4690-4706. Elsevier.

[36] Narayan Pokharel and Mahen Mahendran (2003 August), Finite Element Analysis and design of sandwich panels subject to local buckling effects, Thin-Walled Structures, 42, 589-611. Elsevier.

[37] Zhu Shengqing and Chan Gin Boay (2013 February), Damage and failure mode maps of composite sandwich panel subjected to quasi-static indentation and low-velocity impact, Composite Structures, 101, 204-214. Elsevier.

[38] Vicenzo D Alessandro, Giuseppe Petrone, Sergio De Rosa et al. (2014), Modelling of aluminium foam sandwich panels, Smart Structures and Systems, Vol 13, No 4, 615-636.

[39] D. Contorno, L. Filice, L. Fratini and F. Micari (2006), Forming of aluminum foam sandwich panels: Numerical simulations and experimental tests, Journal of Materials Processing Technology, 117, 364-367.Elsevier.

[40] Marc R Schultz and Michael P Nemeth (2009), Buckling imperfection sensitivity of axially compressed orthotropic cylinders, In 50th AIAA/ASME/ASCE/AHS/ASC Structures, Structural Dynamics and Materials Conference, American Institute of Aeronautics and Astronautics.

[41] Linus Fagerberg and Dan Zenkert (2005), Imperfection induced wrinkling material failure in sandwich panels, Journal of Sandwich Structures and Materials, 7(3), 195-219, SAGE Publications.

[42] H. Bart-Smith, J.W. Hutchinson, N.A. Fleck and A.G. Evans (2002), Influence of imperfections on performance of metal foam core sandwich panels, International Journal of Solis and Structures 39, 4999-5015. Elsevier.

[43] Charles Betts, Daniel Balint and Jianguo Lin (2013), The effect of morphological imperfections on damage in 3D FE analysis of open-cell metal foam core sandwich panels, International Journal of Mechanical Sciences, 75, 377-387, Elsevier.

[44] Louis Philippe Lefebvre, John Banhart and David c. Dunand (2008), Porous metals and metallic foams: Current status and recent developments, Advanced Engineering Materials,10, No 9.

[45] Pai Peng, Kuaishe Wang, Wen Wang, Liying Huang, Ke Qiao et al. (2018 October), High-performance aluminium foam sandwich prepared through friction stir welding, Materials Letters, 236, 295-298. Elsevier.

[46] Caiqi Zhao, Weidong Zheng, Jun Ma et al. (2016 June),The lateral compressive buckling performance of aluminum honeycomb panels for long-span hollow core roofs, Materials, 9, 444